

University of Alberta
Department of Civil &
Environmental Engineering



Structural Engineering Report No. 252

Experimental and Numerical Analysis of FRP Sheets Bonded to Concrete

by

A.M.S. Kamel

A.E. Elwi

J.J.R. Cheng

January, 2003

Experimental and Numerical Analysis of FRP Sheets Bonded to Concrete

by

A.M.S. Kamel

A.E. Elwi

J.J.R. Cheng

Structural Engineering Report 252

Department of Civil and Environmental Engineering

University of Alberta

Edmonton, Alberta

January 2003

ABSTRACT

This thesis investigates the bond behaviour of fibre reinforced polymer (FRP) sheets externally bonded to concrete structures. External bonding of FRP sheets is one of the techniques used to restore deteriorating reinforced concrete structures. The primary mode of failure related to the use of FRP is debonding of the sheets from the concrete surface. Progress in understanding the mechanisms of stress transfer and bond failure that result from the use of externally bonded FRP plates and sheets is necessary to develop sound design codes.

Two experimental test series using pull-apart test method and a modified push-apart test method proposed in this study were conducted. The effects of different parameters, such as the bond length, width, and anchor sheets, on the bond behaviour between FRP sheets and concrete were investigated.

A parametric study investigating the main parameters affecting the bond behaviour was conducted using both two and three-dimensional nonlinear finite element models. The numerical models showed satisfactory agreement with the test results. Trend relationships were produced from the parametric study.

Three conventional bond test methods in addition to the modified push-apart test method were analysed using numerical models. Two bond test methods were recommended as standard test methods. A conversion standard between the different

methods was also proposed based on a comparison between the test methods using numerical analysis and experimental results obtained from this study and from the literature.

Two regression analysis based models were developed to predict the effective bond lengths and the bond capacity of FRP sheets bonded to concrete. Test results from the current study and the literature were used to derive the equations and compare their accuracy compared to existing equations. The results show that the proposed equations are more accurate and reliable than those proposed in the literature.

Acknowledgements

Funding for this research was provided by the Natural Sciences and Engineering Research Council of Canada (NSERC) and the Canadian Network of Centres of Excellence on Intelligent Sensing for Innovative Structures (ISIS Canada). Mitsubishi Canada Ltd. Provided the CFRP material and epoxy used for preparation of the test specimens.

TABLE OF CONTENTS

ACKNOWLEDGMENT

ABSTRACT

TABLE OF CONTENTS

LIST OF TABLES

LIST OF FIGURES

LIST OF SYMBOLS

1. INTRODUCTION	1
1.1. Background	1
1.2. Scope	2
1.3. Objectives	2
1.4. Thesis Outline	3
2. LITERATURE REVIEW	6
2.1 Introduction	6
2.2 Fibre Reinforced Polymers (FRP)	6
2.2.1 Types of Fibres	7
2.2.2 Types of Matrix	8
2.2.3 Forms of FRP Materials	8
2.2.4 Advantages of Using FRP	9
2.2.5 Disadvantages and Limitations of using FRP	9
2.3 Adhesive Used to Bond FRP Sheets to Concrete	10
2.4 Strengthening of Reinforced Concrete Beams	11
2.4.1 Flexural Strengthening of RC Beams	11
2.4.2 Shear Strengthening of RC Beams	12
2.5 Possible Failure Mechanisms	14
2.5.1 Failure Mechanisms for Beams Strengthened in Flexure	14
2.5.2 Failure Mechanisms for Beams Strengthened in Shear	16
2.6 Conventional Bond Test Methods	17
2.6.1 Direct Tension Bond Tests	17

2.6.2	Bending Bond Tests.....	17
2.6.3	Shear Bond Tests.....	18
2.6.3.1	Direct Pull Bond Tests.....	18
2.6.3.2	Indirect Pull-Apart Tests.....	18
2.6.3.3	Indirect Push-Apart Tests.....	19
2.7	Factors Affecting Bond Behaviour.....	20
2.7.1	FRP Sheet Bond Length.....	20
2.7.2	FRP Sheet Bond Width.....	22
2.7.3	FRP Sheet Stiffness.....	23
2.7.4	Concrete Strength.....	23
2.7.5	Concrete Surface Preparation.....	24
2.7.6	Type of Test Conducted.....	25
2.7.7	Anchorage Details.....	25
2.8	Bond Strength Models.....	28
2.8.1	Empirical Models.....	28
2.8.2	Fracture Mechanics Based Models.....	30
2.8.3	Design Proposed Models.....	32
2.9	Summary.....	34
3	EXPERIMENTAL PROGRAM.....	43
3.1	Introduction.....	43
3.2	Modified Push-Apart Test.....	43
3.2.1	Specimen Description.....	43
3.2.2	Test set-up and Instrumentation.....	44
3.2.3	Variables Studied.....	45
3.3	Pull-Apart Test.....	45
3.3.1	Specimen Description.....	46
3.3.2	Test set-up and instrumentation.....	46
3.3.3	Variables studied.....	47
3.4	Material Properties.....	48
3.4.1	Concrete.....	48

3.4.2	CFRP Sheets	49
3.4.3	Epoxy	50
3.4.4	Steel	50
3.5	Bonding the FRP Sheets	50
4	TEST RESULTS, OBSERVATIONS, AND DISCUSSION	62
4.1	Introduction and Overview	62
4.2	Failure Mechanism.....	63
4.2.1	Modified Push-Apart Test Failure Mechanism	63
4.2.2	Pull-Apart Test Failure Mechanism.....	64
4.2.3	Anchor Sheets	65
4.3	Load Transfer Process.....	66
4.3.1	Load Transfer Along the CFRP Sheet Length.....	66
4.3.2	Load Transfer Across the CFRP Sheet Width.....	69
4.4	Bond Length.....	72
4.4.1	General Discussion	72
4.4.2	Effective Length Evaluation.....	73
4.5	Bond Width	74
4.6	Test Method.....	76
4.7	L/W Ratio	77
4.8	Anchor Sheet Configuration	78
4.8.1	Anchor Sheet Location Relative to the Tested Sheet	79
4.8.2	Anchor Distance from Crack.....	80
4.8.3	Anchor Extension Beyond Tested Sheet.....	80
5.	NUMERICAL MODEL.....	116
5.1.	Introduction and Overview	116
5.2.	Geometric Modeling.....	117
5.2.1.	2D Models	117
5.2.2.	3D Models	118
5.3.	Boundary Conditions and Loading	119
5.3.1	Boundary Conditions and Loading of 2D Models	120

5.3.2. Boundary Conditions and Loading of 3D Models	120
5.4. Material Properties	121
5.4.1. Concrete.....	121
5.4.2. CFRP	123
5.4.3. Adhesive.....	124
5.4.4. Steel	125
5.5. Concrete-CFRP Sheet Interface.....	125
5.6. Analysis Procedures	127
5.7. Verification	128
5.7.1. 2D Model Verification.....	129
5.7.2. 3D Model Verification.....	130
6. PARAMETRIC STUDY	160
6.1 Introduction	160
6.2 FRP Sheet Bond Length Effect.....	161
6.3 FRP Sheet Bond Width Effect.....	166
6.3.1 General.....	166
6.3.2 The Effect of FRP Sheet Width to Concrete Width Ratio.....	168
6.4 FRP Sheet Stiffness Effect.....	172
6.5 Concrete Strength Effect.....	173
7 COMPARISON BETWEEN BOND TEST METHODS	200
7.1 Introduction and Overview	200
7.2 Direct Pull Bond Test.....	201
7.3 Pull-Apart Test	203
7.4 Push-Apart Test.....	205
7.5 Modified Push-Apart Test.....	207
7.6 Comparison Between the Bond Tests.....	209
7.6.1 Specimen Preparation	210
7.6.2 Test Serviceability and Execution	210
7.6.3 Test Stability	210
7.6.4 Relationship Between Test Methods.....	211

8.	FRP SHEET BOND MODEL	242
8.1.	Introduction and Overview	242
8.2.	Design Implementations of the Analytical Model	242
8.3.	Design Model	244
8.3.1.	Effective Bond Length Model	244
8.3.2.	Bond Capacity Model	246
9	SUMMARY, CONCLUSIONS, AND RECOMMENDATIONS	264
9.1	Summary	264
9.2	Conclusions	265
9.2.1	Conclusions from the Experimental Analysis	265
9.2.2	Conclusions from the Numerical Analysis	266
9.3	Recommendations	268
10	REFERENCES	270

LIST OF TABLES

Table 3-1 Modified push-apart test variables.....	52
Table 3-2 Modified push-apart concrete compression and split cylinder test results... .	52
Table 3-3 Pull-apart test concrete compression and tensile split cylinder test results.....	53
Table 3-4 Pull-apart test variables.....	53
Table 3-5 Push-apart test concrete mix for 1.0 m ³	54
Table 3-6 Pull-apart test concrete mix for 1.0 m ³	54
Table 3-7 Material properties.....	54
Table 4-1 Push-apart bond test specimens' details and results	81
Table 4-2 Pull-apart bond test specimen's details and results.....	81
Table 6-1 Main material properties used in the parametric study.....	176
Table 6-2 Models with FRP sheet bond lengths varying with bond width.....	177
Table 6-3 Models with bond lengths varying with sheet stiffness, Et.....	178
Table 6-4 Models with bond lengths varying with concrete strength.....	179
Table 6-5 Models with various concrete width and FRP bond length.....	180
Table 6-6 3D models with various concrete width and FRP bond widths.....	180
Table 6-7 2D models with various E and t values but with the same Et product.....	180
Table 7-1 Material properties used in all models.....	214
Table 8-1 Effective bond length comparison details	251
Table 8-2 Test vs. predicted effective bond length summary	252
Table 8-3 Summary of comparison with all test results	253

1. INTRODUCTION	1
1.1. Background.....	1
1.2. Scope	2
1.3. Objectives.....	2
1.4. Thesis Outline	3
2. LITERATURE REVIEW	6
2.1 Introduction.....	6
2.2 Fibre Reinforced Polymers (FRP).....	6
2.2.1 Types of Fibres	7
2.2.2 Types of Matrix	8
2.2.3 Forms of FRP Materials	8
2.2.4 Advantages of Using FRP	9
2.2.5 Disadvantages and Limitations of using FRP.....	9
2.3 Adhesive Used to Bond FRP Sheets to Concrete	10
2.4 Strengthening of Reinforced Concrete Beams.....	11
2.4.1 Flexural Strengthening of RC Beams	11
2.4.2 Shear Strengthening of RC Beams.....	12
2.5 Possible Failure Mechanisms	14
2.5.1 Failure Mechanisms for Beams Strengthened in Flexure.....	14
2.5.2 Failure Mechanisms for Beams Strengthened in Shear.....	16
2.6 Conventional Bond Test Methods.....	17
2.6.1 Direct Tension Bond Tests	17
2.6.2 Bending Bond Tests.....	17
2.6.3 Shear Bond Tests	18
2.6.3.1 Direct Pull Bond Tests.....	18
2.6.3.2 Indirect Pull-Apart Tests.....	18
2.6.3.3 Indirect Push-Apart Tests	19
2.7 Factors Affecting Bond Behaviour.....	20
2.7.1 FRP Sheet Bond Length	20
2.7.2 FRP Sheet Bond Width	22

2.7.3	FRP Sheet Stiffness	23
2.7.4	Concrete Strength	23
2.7.5	Concrete Surface Preparation	24
2.7.6	Type of Test Conducted	25
2.7.7	Anchorage Details	25
2.8	Bond Strength Models	28
2.8.1	Empirical Models.....	28
2.8.2	Fracture Mechanics Based Models	30
2.8.3	Design Proposed Models.....	32
2.9	Summary	34
3	EXPERIMENTAL PROGRAM.....	43
3.1	Introduction	43
3.2	Modified Push-Apart Test	43
3.2.1	Specimen Description.....	43
3.2.2	Test set-up and Instrumentation	44
3.2.3	Variables Studied.....	45
3.3	Pull-Apart Test.....	45
3.3.1	Specimen Description.....	46
3.3.2	Test set-up and instrumentation	46
3.3.3	Variables studied.....	47
3.4	Material Properties	48
3.4.1	Concrete	48
3.4.2	CFRP Sheets	49
3.4.3	Epoxy	50
3.4.4	Steel.....	50
3.5	Bonding the FRP Sheets	50
4	TEST RESULTS, OBSERVATIONS, AND DISCUSSION	62
4.1	Introduction and Overview	62
4.2	Failure Mechanism.....	63
4.2.1	Modified Push-Apart Test Failure Mechanism	63

4.2.2 Pull-Apart Test Failure Mechanism.....	64
4.2.3 Anchor Sheets.....	65
4.3 Load Transfer Process.....	66
4.3.1 Load Transfer Along the CFRP Sheet Length.....	66
4.3.2 Load Transfer Across the CFRP Sheet Width.....	69
4.4 Bond Length.....	72
4.4.1 General Discussion.....	72
4.4.2 Effective Length Evaluation.....	73
4.5 Bond Width.....	74
4.6 Test Method.....	76
4.7 L/W Ratio.....	77
4.8 Anchor Sheet Configuration.....	78
4.8.1 Anchor Sheet Location Relative to the Tested Sheet.....	79
4.8.2 Anchor Distance from Crack.....	80
4.8.3 Anchor Extension Beyond Tested Sheet.....	80
5. NUMERICAL MODEL.....	116
5.1. Introduction and Overview.....	116
5.2. Geometric Modeling.....	117
5.2.1. 2D Models.....	117
5.2.2. 3D Models.....	118
5.3. Boundary Conditions and Loading.....	119
5.3.1. Boundary Conditions and Loading of 2D Models.....	120
5.3.2. Boundary Conditions and Loading of 3D Models.....	120
5.4. Material Properties.....	121
5.4.1. Concrete.....	121
5.4.2. CFRP.....	123
5.4.3. Adhesive.....	124
5.4.4. Steel.....	125
5.5. Concrete-CFRP Sheet Interface.....	125
5.6. Analysis Procedures.....	127
5.7. Verification.....	128

5.7.1. 2D Model Verification.....	129
5.7.2. 3D Model Verification.....	130
6. PARAMETRIC STUDY.....	160
6.1 Introduction.....	160
6.2 FRP Sheet Bond Length Effect.....	161
6.3 FRP Sheet Bond Width Effect.....	166
6.3.1 General.....	166
6.3.2 The Effect of FRP Sheet Width to Concrete Width Ratio.....	168
6.4 FRP Sheet Stiffness Effect.....	172
6.5 Concrete Strength Effect.....	173
7 COMPARISON BETWEEN BOND TEST METHODS.....	200
7.1 Introduction and Overview.....	200
7.2 Direct Pull Bond Test.....	201
7.3 Pull-Apart Test.....	203
7.4 Push-Apart Test.....	205
7.5 Modified Push-Apart Test.....	207
7.6 Comparison Between the Bond Tests.....	209
7.6.1 Specimen Preparation.....	210
7.6.2 Test Serviceability and Execution.....	210
7.6.3 Test Stability.....	210
7.6.4 Relationship Between Test Methods.....	211
8. FRP SHEET BOND MODEL.....	242
8.1. Introduction and Overview.....	242
8.2. Design Implementations of the Analytical Model.....	242
8.3. Design Model.....	244
8.3.1.Effective Bond Length Model.....	244
8.3.2 Bond Capacity Model.....	246
9 SUMMARY, CONCLUSIONS, AND RECOMMENDATIONS.....	264

LIST OF TABLES

Table 3-8 Modified push-apart test variables.....	52
Table 3-9 Modified push-apart concrete compression and split cylinder test results.....	52
Table 3-10 Pull-apart test concrete compression and tensile split cylinder test results.....	53
Table 3-11 Pull-apart test variables.....	53
Table 3-12 Push-apart test concrete mix for 1.0 m ³	54
Table 3-13 Pull-apart test concrete mix for 1.0 m ³	54
Table 3-14 Material properties.....	54
Table 4-1 Push-apart bond test specimens' details and results	81
Table 4-2 Pull-apart bond test specimen's details and results.....	81
Table 6-1 Main material properties used in the parametric study.....	176
Table 6-2 Models with FRP sheet bond lengths varying with bond width.....	177
Table 6-3 Models with bond lengths varying with sheet stiffness, Et.....	178
Table 6-4 Models with bond lengths varying with concrete strength.....	179
Table 6-5 Models with various concrete width and FRP bond length.....	180
Table 6-6 3D models with various concrete width and FRP bond widths.....	180
Table 6-7 2D models with various E and t values but with the same Et product.....	180
Table 7-1 Material properties used in all models.....	214
Table 8-1 Effective bond length comparison details	251
Table 8-2 Test vs. predicted effective bond length summary	252
Table 8-3 Summary of comparison with all test results	253

LIST OF FIGURES

Figure 2-1 Typical failure stress of unidirectional GFRP with respect to axis orientation	35
Figure 2-2 Typical stress vs. strain relationship for different types of fibres	35
Figure 2-3 Flexure strengthened in RC beams	36
Figure 2-4 Load vs. deflection, flexural strengthened beams with and without FRP	36
Figure 2-5 Shear strengthened RC beams	37
Figure 2-6 Load vs. deflection, shear-strengthened beams with and without FRP	38
Figure 2-7 Possible failure mechanisms of RC beams strengthened in flexure	38
Figure 2-8 Direct tension bond test (a) elevation (b) plan view	39
Figure 2-9 Bond strength-compressive strength	39
Figure 2-10 Bending bond test (a) elevation (b) bottom plan view	40
Figure 2-11 Direct pull-apart bond test set-up	40
Figure 2-12 Direct pull-apart bond test specimen free body diagram	41
Figure 2-13 Pull-apart bond test (a) set-up (b) free body diagram, plan view	41
Figure 2-14 Push-apart bond test (a) set-up (b) free body diagram	42
Figure 2-15 Anchoring methods for shear strengthening	42
Figure 3-1 Orthographic of the modified push-apart test	55
Figure 3-2 Modified push-apart test steel form and cage details	55
Figure 3-3 Modified push-apart test (a) plan view (b) side view	56
Figure 3-4 Modified push-apart test set-up and instrumentation	56
Figure 3-5 S-series strain gauge locations on CFRP sheets and concrete	57
Figure 3-6 Pull-apart forms and reinf. (a) without spiral (b) with spiral	57
Figure 3-7 Pull-apart specimen (a) Steel form (b) bars alignment arrangement	58
Figure 3-8 Pull-apart specimen dimensions, details, and anchor configurations	59
Figure 3-9 Pull-apart test set-up and instrumentation	60
Figure 3-10 Concrete girder strengthened in flexure and shear with FRP sheets	60
Figure 3-11 Strain gauge locations and sheet dimensions for P9 to P13	61
Figure 4-1 Crack propagation and failure zone formation sketch	82
Figure 4-2 Schematic sketch of the failure zone plan view in the push-apart tests	82
Figure 4-3 Push-apart failure surface (a) concrete (b) CFRP sheet	82
Figure 4-4 Side view of pull-apart specimen showing crack opening	83

Figure 4-5 Typical post failure mode for specimens P1 through P13, accept for specimen P3 (a) side view (b) CFRP sheet surface (c) concrete surface.....	83
Figure 4-6 Specimen P3 failure mode.....	83
Figure 4-7 Specimen P15 failure mode.....	84
Figure 4-8 Typical failure, anchor (a) above sheet (b) below sheet.....	84
Figure 4-9 Failure mode (a) Specimen P17 (b) Specimen P24.....	84
Figure 4-10 Average strain distributions for specimen S1.....	85
Figure 4-11 Average strain distributions for Specimen S2.....	85
Figure 4-12 Average strain distributions for Specimen S3.....	86
Figure 4-13 Average strain distributions for Specimen S4.....	86
Figure 4-14 Average strain distributions for Specimen S5.....	87
Figure 4-15 Strain distributions at centre of sheet for specimen P9.....	87
Figure 4-16 Strain distribution at centre of sheet for specimen P10.....	88
Figure 4-17 Strain distributions at centre of sheet for specimen P11.....	88
Figure 4-18 Strain distributions at centre of sheet for specimen P12.....	89
Figure 4-19 Strain distributions at centre of sheet for specimen P13.....	89
Figure 4-20 Load vs. transfer length for S-series specimens with $w = 150$ mm ..	90
Figure 4-21 Load vs. transfer length for P-series specimens with $w = 150$ mm ..	90
Figure 4-22 Average bond stress in sheet centre vs. relative load for S5.....	91
Figure 4-23 Schematic sketch deriving incremental average bond stress.....	91
Figure 4-24 Average bond stress in sheet centre vs. relative load for P10.....	92
Figure 4-25 Strain distributions along the sheet width of S1 at crack location	92
Figure 4-26 Strain distributions along half the sheet width of S2 at 0, 15, 30, and 45 mm from the crack location	93
Figure 4-27 Strain distributions along the sheet width of S3 at crack location	94
Figure 4-28 Strain distributions along the sheet width of S4 at crack location	94
Figure 4-29 Strain distributions along the sheet width of S5 at crack location	95
Figure 4-30 Strain distributions across the width of P9 at crack location.....	95
Figure 4-31 Strain distribution across the width of P10 at crack location.....	96
Figure 4-32 Strain distributions across the width of P11 at crack location.....	96
Figure 4-33 Strain distributions across the width of P12 at crack location.....	97
Figure 4-34 Strain distributions across the width of P13 at crack location.....	97

Figure 4-35 CFRP sheet width vs. strain difference between the edge and centre of the sheet at the crack location	98
Figure 4-36 Strain distributions in the sheet centre and edge along its length at various load levels in S4	98
Figure 4-37 Average bond stresses along width vs. relative load level for S1	99
Figure 4-38 Average bond stresses across width vs. relative load level for S4....	99
Figure 4-39 Average bond stresses across width vs. relative load level for S2....	100
Figure 4-40 Average bond stresses across width vs. relative load levels for P10	100
Figure 4-41 Average bond stresses across width vs. relative load level for P11 ..	101
Figure 4-42 Load vs. displacement curves for specimens with $w = 150$ mm.....	101
Figure 4-43 Load vs. displacement for specimens with $w = 150$ mm	102
Figure 4-44 Strain distributions along the sheet centre at 20 kN, $w = 150$ mm ...	102
Figure 4-45 Strain distributions along the sheet centre at 20 kN, $w = 150$ mm ...	103
Figure 4-46 Response for specimens with same sheet width, $w = 100$ mm	103
Figure 4-47 Load vs. bond length for specimens with $w = 100$ mm	104
Figure 4-48 Response for specimens with $L = 150$ mm.....	104
Figure 4-49 Response for specimens with $L = 150$ mm.....	105
Figure 4-50 Load vs. width and Load vs. average bond strength for P-series specimens with $L = 150$ mm.....	105
Figure 4-51 Strain distributions along the sheet centre, S-series, $L = 150$ mm	106
Figure 4-52 Strain distributions along the sheet centre, P-series, $L = 150$ mm	106
Figure 4-53 Response comparison for specimens with $w = 150$ mm	107
Figure 4-54 Strain distributions at centre of sheet for specimens P9 and S2.....	107
Figure 4-55 Strain distributions at centre of sheet for specimens P10 and S3.....	108
Figure 4-56 Strain distributions at centre of sheet for specimens P11 and S5.....	108
Figure 4-57 Response for specimens with the same bond area.....	109
Figure 4-58 Strain distributions along the sheet centre, same bond area.....	109
Figure 4-59 Response for specimens with $a = 0$ and $b = 75$ mm	110
Figure 4-60 Response for specimens with $a = 25$ mm and $b = 75$ mm.....	110
Figure 4-61 Response for specimens with $a = 50$ mm and $b = 75$ mm.....	111
Figure 4-62 Response for specimens with $a = 75$ mm, $b = 75$ mm.....	111
Figure 4-63 Response for specimens with $a = 25$ mm, $b = 50$ mm.....	112
Figure 4-64 Response for specimens with $a = 25$ mm, $b = 25$ mm.....	112

Figure 4-65 Effect of distance from crack “a” , anchor on top and b = 75 mm....	113
Figure 4-66 Effect of distance from crack “a” , anchor below sheet and b=75 mm.....	113
Figure 4-67 Anchor distance from crack, b = 75 mm.....	114
Figure 4-68 Effect of anchor extension beyond sheet “b” when the anchor is above the sheet and a = 25 mm	114
Figure 4-69 Effect of anchor extension beyond sheet “b” when the anchor is below the sheet and a = 25 mm	115
Figure 4-70 Anchor spacing for specimens with a = 25 mm	115
Figure 5-1 Modified push-apart specimen plan view and symmetry lines	132
Figure 5-2 Pull-apart specimen elevation and symmetry lines	132
Figure 5-3 2D modified push-apart model mesh, loading, and boundary conditions.	133
Figure 5-4 Half the 2D pull-apart model mesh, loading, and boundary conditions	133
Figure 5-5 Modified push-apart specimen (a) planes of symmetry (b) modeled part	134
Figure 5-6 Pull-apart specimen (a) planes of symmetry (b) modeled part	134
Figure 5-7 Modified push-apart 3D model	135
Figure 5-8 Pull-apart test mesh, loading, and boundary conditions	136
Figure 5-9 Concrete yield and failure surfaces in plain stress	136
Figure 5-10 Calculation of the displacement at which a linear loss of strength after cracking gives zero stress.....	137
Figure 5-11 Uniaxial behaviour of plain concrete (ABAQUS, 1998)	137
Figure 5-12 Stress-strain behaviour for CFRP and steel	138
Figure 5-13 2D modified push-apart model.....	138
Figure 5-14 Strain contour in load direction for modified push-apart model.....	139
Figure 5-15 2D pull-apart mesh, boundary conditions, and deformed shape.....	139
Figure 5-16 Load-displacement curves experimental and 2D model of S1.....	140
Figure 5-17 Load-displacement experimental and 2D model of S2	140
Figure 5-18 Load-displacement experimental and 2D model of S3	141
Figure 5-19 Load-displacement experimental and 2D model of S4	141
Figure 5-20 Load-displacement experimental and 2D model of S5	142
Figure 5-21 Load-displacement for experimental and 2D model of P9.....	142
Figure 5-22 Load-displacement for experimental and 2D model of P10.....	143
Figure 5-23 Load-displacement for experimental and 2D model of P11.....	143
Figure 5-24 Load-displacement for experimental and 2D model of P12.....	144

Figure 5-25 Load-displacement for experimental and 2D model of P13.....	144
Figure 5-26 Strain distributions for experimental and 2D model of S1.....	145
Figure 5-27 Strain distributions for experimental and 2D model of S2.....	145
Figure 5-28 Strain distributions for experimental and 2D model of S3.....	146
Figure 5-29 Strain distributions for experimental and 2D model of S4.....	146
Figure 5-30 Strain distributions for experimental and 2D model of S5.....	147
Figure 5-31 Strain distributions for experimental and 2D model of P9.....	147
Figure 5-32 Strain distribution for experimental and 2D model of P10.....	148
Figure 5-33 Strain distributions for experimental and 2D model of P11.....	148
Figure 5-34 Strain distributions for experimental and 2D model of P12.....	149
Figure 5-35 Strain distributions for experimental and 2D model of P13.....	149
Figure 5-36 Load-displacement for experimental and 3D model of S1.....	150
Figure 5-37 Load-displacement for experimental and 3D model of S3.....	150
Figure 5-38 Load-displacement for experimental and 3D model of S4.....	151
Figure 5-39 Load-displacement for experimental and 3D model of S5.....	151
Figure 5-40 Load-displacement for experimental and 3D model of P9.....	152
Figure 5-41 Load-displacement for experimental and 3D model of P10.....	152
Figure 5-42 Load-displacement for experimental and 3D model of P11.....	153
Figure 5-43 Load-displacement for experimental and 3D model of P12.....	153
Figure 5-44 Load-displacement for experimental and 3D model of P13.....	154
Figure 5-45 Strain distributions across sheet width of S1 at the crack location ...	154
Figure 5-46 Strain distributions across half sheet width of S2 at crack.....	155
Figure 5-47 Strain distributions across sheet width of S3 at the crack location ...	155
Figure 5-48 Strain distributions across sheet width of S4 at the crack location ...	156
Figure 5-49 Strain distributions across sheet width of S5 at the crack location ...	156
Figure 5-50 Strain distributions across the width of P9 at crack location.....	157
Figure 5-51 Strain distribution across the width of P10 at crack location.....	157
Figure 5-52 Strain distributions across the width of P11 at crack location.....	158
Figure 5-53 Strain distributions across the width of P12 at crack location.....	158
Figure 5-54 Strain distributions across the width of P13 at crack location.....	159
Figure 6-1 Load-displacement response for models with $L = 150$ mm.....	181
Figure 6-2 Bond length-ultimate load at different w values.....	181
Figure 6-3 Effective length-Bond width relationship.....	182

Figure 6-4 Average bond strength-bond length at different w values.....	182
Figure 6-5 Average effective bond strength-bond length, various w values	183
Figure 6-6 Bond length-ultimate load at different Et values	183
Figure 6-7 Effective length-stiffness for w = 100 mm	184
Figure 6-8 Load-displacement, modified push-apart models, L = 200 mm	184
Figure 6-9 Bond length-ultimate load, various f'_c	185
Figure 6-10 Bond length-Average bond strength, various f'_c	185
Figure 6-11 Bond length-Average effective bond strength, various f'_c	186
Figure 6-12 Bond width-ultimate load at different L values	186
Figure 6-13 Ultimate load per width vs bond length at various bond widths	187
Figure 6-14 Bond width-bond strength at different L values	187
Figure 6-15 Bond width-bond strength at different L values, $L_e = 110$ mm	188
Figure 6-16 Load-Displacement, various w_c , w = 200 and L =50 mm.....	188
Figure 6-17 Load-Displacement, various w_c , w = 200 and L = 150 mm.....	189
Figure 6-18 Strain E11 contour lines (a) isometric view for $w/w_c = 0.7$ (b) elevation view for $w/w_c = 0.7$ (c) elevation view for $w/w_c = 1.0$	190
Figure 6-19 Strain distribution across the concrete width	191
Figure 6-20 Stress distribution across the concrete width at ultimate load.....	191
Figure 6-21 Strain distribution across bond width, 15 kN.....	192
Figure 6-22 Strain distribution across bond width, $P/P_u = 0.5$	192
Figure 6-23 Strain distribution across bond width, $P/P_u = 0.7$	193
Figure 6-24 Strain distribution across bond width, $P/P_u = 1.0$	193
Figure 6-25 Strain difference-bond width response, $w_c = 200$ mm	194
Figure 6-26 Strain distribution across FRP sheet width at 15 kN	194
Figure 6-27 FRP stiffness vs. ultimate load at various bond lengths	195
Figure 6-28 FRP stiffness vs. average bond strength at various bond lengths	195
Figure 6-29 Effective FRP stiffness vs. bond length relationship.....	196
Figure 6-30 Concrete strength vs. ultimate load at various bond lengths	196
Figure 6-31 Strain distribution for various f'_c values.....	197
Figure 6-32 Concrete strength vs. ultimate load at various bond lengths	197
Figure 6-33 Load-displacement response, pull-apart models, L = 200 mm	198
Figure 6-34 Concrete strength vs. ultimate load, push-apart model	198

Figure 6-35 Strain distribution for various f'_c at ultimate load, pull-apart model.....	199
Figure 7-1 Direct pull bond test.....	215
Figure 7-2 Load-displacement for direct pull tests with various unbonded lengths.....	216
Figure 7-3 Development of principal stresses in direct pull specimen	217
Figure 7-4 Load-displacement for direct pull models	218
Figure 7-5 Load level-displacement for direct pull models	218
Figure 7-6 Strain distribution for direct pull models, $w = 25$ mm	219
Figure 7-7 Strain distribution for direct pull models, $w = 150$ mm	219
Figure 7-8 Pull-apart bond test.....	220
Figure 7-9 Load-displacement for pull-apart models	221
Figure 7-10 Normilized load-displacement response for pull-apart models.....	221
Figure 7-11 Strain distribution for pull-apart models, $w = 25$ mm	222
Figure 7-12 Strain distribution for pull-apart models, $w = 150$ mm	222
Figure 7-13 Push-apart bond test.....	223
Figure 7-14 Load-displacement push-apart tests, unbonded sheet lengths.....	223
Figure 7-15 Load-displacement for push-apart models.....	224
Figure 7-16 Normilized load-displacement response for push-apart models	224
Figure 7-17 Strain distribution for push-apart models, $w = 25$ mm.....	225
Figure 7-18 Strain distribution for push-apart models, $w = 150$ mm.....	225
Figure 7-19 Modified push-apart test.....	226
Figure 7-20 Load-displacement response for models with $L = 150$ mm.....	227
Figure 7-21 Normilized load-displacement response for models with $L = 150$ mm.....	227
Figure 7-22 Strain distribution for modified push-apart models, $w = 25$ mm.....	228
Figure 7-23 Strain distribution for modified push-apart models, $w = 150$ mm.....	228
Figure 7-24 Load-displacement for modified push-apart tests, various arm widths	229
Figure 7-25 Load-displacement behaviour for modified push-apart with arm widths ranging from 40 to 100 mm	229
Figure 7-26 Load-displacement behaviour for modified push-apart with arm widths ranging from 100 to 300 mm.....	230
Figure 7-27 Strain distribution along the concrete arm in modified push-part model with 40 mm arm width	230
Figure 7-28 Stress distribution along the concrete arm for modified push-part model with 40 mm arm width	231

Figure 7-29 Strain distribution in perpendicular direction to loading for modified push-apart model with 300 mm arm width	231
Figure 7-30 Stress distribution across outer concrete for modified push-part model with 300 mm arm width	232
Figure 7-31 Load-displacement for all bond tests, $w = 25$ mm	232
Figure 7-32 Load-displacement for all bond tests, $w = 50$ mm	233
Figure 7-33 Load-displacement for all bond tests, $w = 100$ mm	233
Figure 7-34 Load-displacement for all bond tests, $w = 150$ mm	234
Figure 7-35 Ultimate load vs. bond width for $L = 150$ mm	234
Figure 7-36 Ultimate load per width vs. bond width for $L = 150$ mm.....	235
Figure 7-37 Ultimate load per width vs. bond width, pull-apart tests.....	235
Figure 7-38 Ultimate load per width vs. bond length, direct pull tests	236
Figure 7-39 Ultimate load per width vs. bond length, pull-apart tests.....	236
Figure 7-40 Ultimate load per width vs. bond length, push-apart tests	237
Figure 7-41 Ultimate load per width vs. bond length, modified push-apart test	237
Figure 7-42 Strain distribution for models with FRP width of 25 mm at $0.6 P_u$	238
Figure 7-43 Strain distribution for models with FRP width of 25 mm at $0.8 P_u$	238
Figure 7-44 Strain distribution for models with FRP width of 25 mm at $0.9 P_u$	239
Figure 7-45 Strain distribution for models with $w = 25$ mm at ultimate load	239
Figure 7-46 Strain distribution for models with $w = 150$ mm at ultimate load	240
Figure 7-47 Strain distribution for models with FRP width of 25 mm at 4 kN.....	240
Figure 7-48 Strain distribution for models with FRP width of 150 mm at 24 kN.....	241
Figure 8-1 Schematic sketch and derivation of development length	256
Figure 8-2 Effective length-stiffness for $w = 100$ mm (Section 6.2)	256
Figure 8-3 Effective length-stiffness for $w = 100$ mm	257
Figure 8-4 Effective length-Bond width relationship (Section 6.2).....	257
Figure 8-5 Effective length vs. square root of bond width relationship.....	258
Figure 8-6 Test vs. predicted effective length.....	258
Figure 8-7 Concrete compressive strength vs. ultimate load (Section 6-5)	259
Figure 8-8 Ultimate load vs. FRP sheet bond width (Section 6.3.1).....	259
Figure 8-9 Ultimate load vs. Bond length (Section 6.2).....	260
Figure 8-10 Ultimate load vs. bond area	260
Figure 8-11 Ultimate load test to predicted values, Equation 8-7	261

Figure 8-12 Ultimate load vs. square root of stiffness (Section 6-4)	261
Figure 8-13 Ultimate load test to predicted ratio vs $\sqrt{E_p t_p} / wL_e$, all tests	262
Figure 8-14 Ultimate load test to predicted values, Equation 8-9	262
Figure 8-15 Ultimate load test to predicted values, Equation 8-10	263
Figure 8-16 Ultimate load test to predicted values, Equation 8-11	263

b_p	Width of the bonded plate, mm
c	Length of initial failure, mm
c_f	Constant
d_1	Distance of the metal sheet edge from the concrete surface, mm
E	Modulus of Elasticity, MPa
E_1	Modulus of elasticity in main direction in the plane of sheet, MPa
E_2	Modulus of elasticity in secondary direction in the plane of sheet, MPa
E_a	Young's modulus of adhesive, MPa
E_c	Young's modulus for concrete, MPa
E_c	Modulus of elasticity of the concrete, MPa
E_p	Modulus of elasticity of FRP, MPa
f	Critical interface stress criterion, MPa
f'_c	Concrete compressive strength, MPa
F_1	Forces in the composite material plate at gauge 1, kN
f_{ct}	Tensile strength of concrete, MPa
f_{cy}	Concrete compressive yield stress, MPa
f_{su}	Steel ultimate strength, MPa
G_{12}	Shear modulus in 1-2 plan, N.mm/mm ²
G_f	Fracture energy, N.mm/mm ²
g_i	Strain value at point i
I_p	Moment of inertia of FRP plate, mm ⁴
k	Length factor
k_p	Width ratio or geometric factor
L	Bond length, mm

L'	Unbonded FRP sheet, mm
L_e	Effective bond length, mm
L_{ea}	Anticipated effective length, mm
P	Applied load, kN
P_u	Ultimate load or bond capacity, kN
R	Average bond resistance, MPa
t_a	Thickness of adhesive, mm
t_c	Thickness of the concrete, mm
t_p	FRP sheet thickness, mm
u_o	Displacement, mm
w	FRP sheet bond width, mm
w_c	Concrete specimen width, mm

Greek Symbols

ν	Poisson's ratio
ν_c	Poisson's ratio for concrete
ΔL	Distance between gauges, mm
ν_s	Poisson's ratio for steel
ψ	Coefficients obtained from curve fitting the test results
ϵ_{cp}	Concrete absolute plastic strain
ϵ_{sp}	Steel plastic strain at ultimate strength
ϕ	Angle of failure surface
σ	Critical normal stresses, MPa

- σ_f Limiting normal stress failure value, MPa
- σ_n Observed normal stress carried across the interface, MPa
- τ Critical interface shear, MPa
- τ_b Average bond strength
- τ_f Limiting shear stress failure value, MPa
- τ_n Observed shear stress carried across the interface, MPa

1. INTRODUCTION

1.1. Background

A common rehabilitation solution used to repair concrete bridges employs steel plates bonded and/or mechanically fastened to the concrete surface. One of the main advantages of the steel plating rehabilitation method is that all work can be carried out from beneath the superstructure and it is not necessary to disturb the deck or perform substantial drilling. However, the weight of the plates makes the bonding work difficult. Generally they must be held in place under pressure until cure is complete, to ensure a good bond. The proper formation of joints was a problem, due to the limited delivery lengths of the plates. Also of prime concern is the possibility of corrosion at the steel-concrete interface due to moisture migration at this sensitive location, which in turn leads to the deterioration of the bond at the steel-concrete interface. The problem is even more severe for bridges where de-icing chemicals are commonly used in cold seasons.

An effective way of eliminating the corrosion problem is to replace the steel plates with corrosion-resistant synthetic materials. In the last 20 years a new family of materials has gained increasing exposure in civil engineering applications, namely Fibre Reinforced Polymer (FRP) materials. These materials, which were originally developed and applied in aeronautics, space, and sports and recreation industries, possess certain properties that make them superior to steel in some respects. The FRP-strengthening technique has found wide acceptance among researchers and engineers today in many parts of the world, and is no longer considered to be a new technique for certain types of strengthening jobs (Triantafillou 1998).

Although FRP sheets have been widely applied to rehabilitate and upgrade concrete columns, beams and slabs, no rational design method with FRP sheets has yet been established. This is because complete understanding of the effects bonded FRP materials have on the performance of structural systems has not yet been achieved.

Recent developments in composite material technologies, with numerous new fibres and resin systems emerging in the construction industry, require not only a basic knowledge of the material properties of each new product but also their interfacial behaviour when applied as external reinforcement. The local bond strength when delamination occurs and the average bond strength are likely dependent on many factors such as the FRP bonded length, width, and sheet stiffness as well as concrete strength and surface condition. To develop rehabilitation procedures for concrete structures involving externally applied FRP sheets, a good understanding of the behaviour and strength of the bond is necessary.

1.2. Scope

Unidirectional FRP sheets externally bonded to concrete are investigated in this research with the stress condition being tensile stress in the direction of the fibres. The failure mode investigated is the bond failure at the crack location.

Numerous bond stress curves and equations are proposed in the literature. Each describe well the data from which they were defined. However, there is large discrepancy and scatter between these curves. The expected reason is the different bond test methods and loading arrangements used to study the bond behaviour.

Several researchers have proposed different models to predict the bond strength and the effective length. The models can be classified into three categories: empirical models based on regression analysis of test data, fracture mechanics based models, and design models, which use simplified assumptions. A model needs to be recommended or a new model proposed based on the evaluation of the proposed models in the literature, an extensive parametric study, and the test results existing in the literature. This is the thrust of the investigation reported in this thesis.

1.3. Objectives

There are five main objectives in this thesis. The first is to have a better understanding of the bond behaviour between fibre reinforced polymer (FRP) sheets and

concrete. This was accomplished by investigating the role of the main parameters affecting the bond behaviour through experimental and numerical analyses. The parameters studied were the FRP sheet bond length, bond width, stiffness, and concrete strength. For practical implementation of the configuration and detailing of the bonded sheets, the anchor requirements for FRP sheets were also investigated experimentally.

The second objective is to produce charts showing the effect of the main parameters on the bond behavior and to propose guidelines for design purposes. This is to be done by producing a numerical model of the debonding type failure that accurately predicts the load-displacement behavior and the strain distribution in the bonded FRP sheets. The charts showing the effect of the different parameters on the bond behavior are then produced through an extensive parametric study.

The third objective is to develop a rational standard test method for FRP sheets bonded to concrete. This objective arose from the literature review that showed that the type of bond test method used in predicting the bond behaviour had an effect on the test results. This is to be done by analyzing the various conventional bond test methods using numerical models and evaluating the advantages and drawbacks of each method. Based on the investigation, a standard test method is recommended.

A fourth objective is to develop regression analysis based models predicting the effective bond lengths and the ultimate bond capacity of FRP sheets bonded to concrete.

1.4. Thesis Outline

Chapter 2 presents an overview of the FRP material, the advantages and disadvantages of using the material, and the forms in which they are manufactured. The strengthening schemes for flexure and shear and the possible failure mechanisms are also presented. A lack of understanding of the bond behaviour is seen through a discussion of the effects of the parameters proposed by previous research. Reviewing the different conventional bond test methods used in different bond research points out the need to develop a rational standard test method for FRP sheets bonded to concrete. Finally the

existing bond strength and FRP effective length models are discussed. This also shows the need to evaluate the existing models and propose or develop a model, that gives more reliable results.

Two experimental test series were conducted in this research using two different types of bond test methods. One series used a modified push-apart test and the other used a pull-apart test. A detailed description of each test specimen is presented in Chapter 3. The test set-up, instrumentation, and the property of the materials used are also presented in the chapter.

The test results and observations of both experimental series are presented in Chapter 4. The discussion and analysis of the test results and observations are also presented in the same chapter.

The numerical model geometry, material properties, loading, and boundary conditions are presented and discussed in Chapter 5. The concrete-FRP interface model of the debonding behaviour is also discussed in this chapter. The numerical model simulates the modified push-apart and pull-apart test methods and the output is compared to the experimental test results.

The parametric study is presented in Chapter 6. The main parameters affecting the bond behaviour between concrete and FRP sheets are investigated using the proposed numerical model. These parameters are the bond length, bond width, sheet stiffness, and the concrete strength. Charts showing the effect of each parameter are developed and analysis of the effect of each parameter on the bond behaviour is discussed.

Chapter 7 details an investigation of the comparison between different bond test methods using numerical models. The relationship between the results of each method is discussed and evaluated. Based on the analysis, two test methods are proposed as standard test methods for FRP sheets bonded to concrete based on the analysis.

Regression analysis based models predicting the effective bond length and the bond capacity of FRP sheets bonded to concrete are detailed in Chapter 8. Comparisons with other proposed models from the literature were performed using experimental test results from this study and from the literature. Based on the comparison, the regression analysis based model proposed in this study showed more accurate and reliable predictions than the models proposed in the literature.

A summary and the conclusions of the research conducted are presented and recommendations for changes to the FRP design codes and for future research are proposed in Chapter 9.

2. LITERATURE REVIEW

2.1 Introduction

This chapter presents an overview of FRP materials, the advantages and disadvantages of using the material, and the forms in which they are manufactured. The strengthening schemes for flexure and shear and the possible failure mechanisms are also presented. The parameters affecting the bond behaviour are discussed and the findings and conclusions of the previous studies are summarized. A review of the different conventional bond test methods used in different bond research is presented. Finally the most significant existing bond strength and FRP effective length models are presented in this chapter.

2.2 Fibre Reinforced Polymers (FRP)

FRP materials consist of fibres of high strength and high modulus of elasticity embedded in a matrix of polymeric material at distinct interfaces. Both fibres and matrix retain their physical and chemical identities and they also produce a combination of properties that cannot be achieved with either acting alone. In general, fibres are the principal load-carrying elements, providing the major contribution of strength and stiffness of the composite and most of its desirable properties. The surrounding matrix keeps the fibres in the desired location and orientation, acts as a load transfer medium, and protects the fibres from environmental damages (e.g. temperature, and humidity). The properties of the composite material depend largely on the properties of the fibres and matrix used, and the relative proportion in which each component is present (Drimoussis and Cheng, 1994).

Fibres may be oriented randomly within the matrix, in certain prescribed alignments, or unidirectionally. As all the attractive properties of the composite depend on the fibres, the greatest benefit is gained when it is loaded in the direction in which the fibres are oriented. When the load is applied at a different orientation, away from the fibres, the properties of the matrix begin to dominate. This effect can

be seen in Figure 2-1. Although shown in particular for a glass FRP (GFRP) material, this is typical of FRP's in general (Holloway and Leeming, 1999).

2.2.1 Types of Fibres

There are many types of fibres, some of which are not commonly used in civil engineering projects (e.g. polyethylene, boron, and ceramic) and some of which are commonly used because of their properties. These are glass, carbon, and aramid fibres.

Glass fibres are commonly used because there is more experience with them and because they are relatively less expensive than the carbon and aramid fibres. Glass fibres are available in several types according to the required application (e.g. E-glass used for electrical applications, C-glass for chemical applications). Some of the important properties of glass fibres are a low tensile modulus and high strength, a softening point of 800-1000°C, high insulating properties, sensitivity to alkaline environment, and a relatively low resistance to sustained loads and moisture. The fibres are coated with an agent to minimise abrasion damage but fibres can be easily damaged in handling.

Carbon fibres are gaining interest for use in structural applications despite their higher cost compared to glass fibres because some of their properties are superior to those of glass in some areas (e.g. durability in marine environments). Carbon fibres have two main types namely PAN-based carbon and Pitch-based carbon. PAN-based carbon is derived from acrylic nitrile and has a modulus of elasticity of the order 200 GPa and tensile strength of the order of 3000 MPa. Pitch-based carbon is derived from coal tar and has a modulus of elasticity of the order 50 GPa and tensile strength of the order of 700 MPa. Some of the important properties of carbon fibres are excellent fatigue resistance, high conductivity to heat and electricity, and excellent moisture and chemical resistance. Carbon fibres are also sensitive to galvanic corrosion and have an elastic modulus that is comparable to that of steel (Drimoussis and Cheng, 1994, and Tadros et al., 1998).

Aramid fibres are used in fewer applications than glass and carbon fibres. They have low tensile modulus and high strength and their electrical conductivity is low. Temperature and alkaline solutions increase creep strains and moisture has the effect of decreasing tensile properties. Figure 2-2 shows a typical comparison of responses of different fibre types compared to steel properties.

2.2.2 Types of Matrix

There are two main different types of resin matrix, namely polymer and metal. Polymer matrix is the one used in civil engineering applications, where it has two main types, the first is thermoset matrices (e.g. epoxy, polyester, and vinyl ester) and the other is thermoplastic matrices (e.g. polyether ether ketone, polyphenylene sulfide, and polysulfone). Thermoset matrices are most commonly used because of preferable properties such as high modulus and strength and superior characteristics under long-term loading. Thermoset matrices undergo irreversible chemical change when cured but are stable under high temperatures and aggressive environments.

On the other hand thermoplastic has undesirable properties such as its low-modulus and strength and it is also susceptible to softening at high temperatures. Due to its disadvantages, it is not permitted for tendons and primary reinforcement according to the CSA-S6 (1988).

2.2.3 Forms of FRP Materials

FRP materials used in structural engineering applications can be supplied as finished end products in a variety of pultruded structural shapes or in the form of bars, tendons, wire meshes, cables, plates, sheets or as micro fibres to be used as additives to concrete mixes. However, the properties of the composites will be different, depending on the size of the fibres and their orientation. Using longer fibres significantly increases both the strength and the modulus of elasticity. Continuous fibres are used as reinforcements when high performance and weight reduction is

needed and when thermal expansion is to be kept at very low levels (Donnet and Bansal, 1990).

External reinforcement of concrete structures with bonded FRP requires the use of either sheets or plates. Sheets are made of dry or pre-preg fibres to be fully impregnated with resin during installation. They are flexible in that they can easily follow the contour of a surface and bend at corners. Plates are fully cured material systems manufactured by pultrusion or other suitable techniques such as lay-up. The application technique is similar to steel plates. Plates, independently of their thickness, have their own rigidity. In the case of plate adhesion, the adhesive layer is perhaps thicker and more easily identifiable. Changing the thickness of the FRP plate significantly modifies the crack distribution and changes the failure mechanism (Arduini et al., 1996). In this study only FRP sheets are investigated.

2.2.4 Advantages of Using FRP

FRPs have high strength-to-weight and high modulus. Because of their strength and toughness they can be used in thin sections, leading to lightweight and easy handling and installation. FRPs are non-conductive, non-magnetic, and have excellent corrosion resistance, eliminating some of the disadvantages of using steel. They also have high fatigue resistance. FRPs have low relaxation creep, which leads to lower long-term deflections. They also have a longer useful life, which in turn gives a lower life cycle cost. FRPs are easy to form, where they can be bonded to curved or irregular surfaces. They can also be supplied in long lengths, thus reducing the need for lapping at joints. FRPs are light and easy to handle on a construction site so that there is no need for special equipment (Cheng, 1998, and Tadros et al., 1998).

2.2.5 Disadvantages and Limitations of using FRP

FRP materials have certain advantages, but they also have limitations, which must be circumvented, if they are to be used for best results. FRPs have higher first cost. But especially in bridge works, the cost savings due to labour savings can be substantial if the time required for retrofit and traffic disruption could be minimised.

FRPs have lower modulus of elasticity than steel, which means lower stiffness and higher deflection. FRPs have unknown long-term durability in construction, because these materials are relative newcomers and their history is short.

There is relative lack of experience in using FRPs in civil engineering projects. As owners, designers, and contractors become more familiar with this technology, it is envisioned that the number of applications will rapidly increase. Design codes and standards for the use of FRPs are unavailable, where many manufacturers produce their own proprietary products. In North America work is in progress towards producing FRP design codes. Draft documents are being circulated within technical committees and should be completed in the near future (Nanni, 1997).

FRPs have lack of apparent ductility and low fire resistance. Because the addition of FRPs having linear behaviour up to fracture eliminates the possibility of flexural tension softening, there is concern that beams reinforced in this manner would have inadequate ductility (Bonacci, 1996). Fires of the intensity that occur in buildings can destroy all plastics. Some burn readily and ought not to be employed in structural engineering; others are slow burning or self-extinguishing.

Any particular FRP material is likely to possess some but not all of both advantages and disadvantages. The designer must decide which properties are most important for a particular application and then choose the appropriate material.

2.3 Adhesive Used to Bond FRP Sheets to Concrete

The success of this strengthening technique is critically dependent on the performance of the epoxy used to bond the FRP plates/sheets to the concrete surface. Numerous types of epoxies with a wide range of mechanical properties are commercially available.

The adhesive must be compatible with both FRP plates/sheets and concrete. Researchers showed that rubber-toughened epoxies are particularly suited for this

application. The adhesive should have sufficient stiffness and strength to transfer the shear force between the concrete beam and the composite plate. The adhesive should be tough enough to prevent brittle bond failure caused by cracking of the concrete and have good resistance to salt and moisture and be usable under the prevailing environmental conditions (Saadatmanesh and Ehsani, 1991a, Ritchie, 1991, and Chajes et al., 1996).

Chajes, et al. (1996) studied the effect of the type of adhesive on the average bond strength. They concluded after studying four types of different adhesive that an "off-the-shelf" epoxy could be effectively used to bond composite material plates to concrete. They also pointed out that the use of ductile adhesives (i.e. those having a low stiffness and a large strain to failure) leads to less effective bond.

Swamy, et al. (1986) tested various lap shear specimens with steel plates having adhesive thickness ranging from 0.5 mm to 3.0 mm and found no variation in results due to adhesive layer thickness.

2.4 Strengthening of Reinforced Concrete Beams

FRP sheets and plates have been used to strengthen various types of Reinforced Concrete (RC) members. The effectiveness of the strengthening reinforcement, that is, the load carried by the FRP at the ultimate limit state, depends on its failure mechanism, which, in turn, depends on various factors (Triantafillou, 1998). The common FRP strengthening methods using bonded sheets and plates used to strengthen concrete girders in flexure and shear will be presented.

2.4.1 Flexural Strengthening of RC Beams

One or more layers of FRP sheets or plates are externally bonded to the tension surface of the RC beam in order to strengthen it in flexure, as shown in Figure 2-3. When FRP plates are used, special attention shall be given to the debonding and end peeling problems. Vertical wrapping is an effective way for anchoring the flexural

FRP sheet or plate. Taping at the end of the FRP sheets and the use of GFRP vertical wrapping could also be a solution (Cheng, 1998).

Tumialan et al. (1999) carried out an experimental investigation and concluded that strengthening of RC beams with externally bonded CFRP sheets was effective and lead to increases in flexural strengthening between 30% and 60%. Arduini and Nanni (1997a) and Cheng (1998) also stated that the load carrying capacity of RC beams increased and the deflection decreased at service loads due to flexural strengthening with FRP sheets as illustrated in Figure 2-4.

2.4.2 Shear Strengthening of RC Beams

A RC member must be designed to develop its full flexural strength to insure a ductile flexural failure mode under extreme load. Hence a beam must have safety margins against other types of failure modes that are more dangerous and less predictable than flexural failure. Shear failure or diagonal tension failure is a failure mode that has a catastrophic effect, should it occur. If a RC member deficient in shear strength is overloaded, shear failure may occur suddenly without advance warning of distress. Therefore, a RC member must have sufficient shear strength to insure ductile flexural failure.

FRP sheets are used to wrap concrete sections in the transverse direction in order to reinforce diagonal tension cracks in much the same way as steel stirrups. The most effective method of shear strengthening with FRP sheets is to wrap the entire cross section of the beam with FRP. Typically, this is not practical from a construction standpoint. The presence of monolithic slabs or other supported elements often prevents wrapping the sheet around the top of the section.

It is more difficult to add shear reinforcement to concrete beams, especially when the beams are not isolated but are instead part of a floor beam system. To best provide external shear reinforcement, it is desirable to encase the beam web with external reinforcement. This can be more easily accomplished using a flexible

material, such as a FRP sheet, than using a plate, since the sheet can conform to any arbitrary shape (Chajes et al., 1995).

Typical FRP configurations for shear strengthening of concrete beams are shown in Figure 2-5. The external reinforcement in the figure is in the form of bonded sheets extending into the compression zone (U-jacket), where bonding may be supplemented by mechanical fastening, as in Figure 2-5(b). Another possibility is that of Figure 2-5(d), where FRP sheets are wrapped around the web of the beam (Triantafillou, 1998). Horizontal anchor sheets can be used to prevent peeling at the top of the shear reinforcement. The load carrying capacity is increased due to shear strengthening as shown in Figure 2-6.

Shear strengthening reinforcement may be in the form of a continuous jacket or as spaced strips (discontinuous strapping). Discontinuous strapping, as shown in Figure 2-5, avoids trapping water inside the girder, allows for evaporation, is easier for inspection, and is effective in optimizing the amount of material used.

Because FRP is an anisotropic material with high strength in the direction of the fibres, the fibres may be oriented in such a way to best reinforce diagonal tension cracks. This is achieved by the use of inclined strips, Figure 2-5. However, vertically oriented plies are easier to install and may reduce the total length of the wrap. Cheng (1998) concluded that vertical and inclined shear strengthening yield almost similar increase in shear strength but stated that lower strain was observed in stirrups for the beams strengthened with inclined straps.

It has been found that the use of biaxial FRP reinforcement increases the overall performance of the system (Triantafillou, 1998). Biaxial FRP reinforcement is achieved by placing two unidirectional FRP plies in mutually perpendicular directions, as shown in Figure 2-5. The ply in the primary direction acts to provide most of the reinforcement. While the ply in the secondary direction limits shear crack openings and provides anchorage for the ply in the primary direction.

2.5 Possible Failure Mechanisms

The failure mechanisms observed and recorded in RC beams strengthened with FRP sheets could be categorised into two main groups depending on whether they were strengthened in flexure or in shear.

2.5.1 Failure Mechanisms for Beams Strengthened in Flexure

All failure modes show at first a linear-elastic behaviour followed by a crack in the mid-span region of the beam. Thereafter, a large non-linear phase is recorded with the development of numerous flexural cracks, in this phase, the strain in the FRP plate increased considerably, as well as the beam deflection. Changing the thickness of the FRP plate, the bonded length, or adding FRP shear reinforcement significantly modifies the crack distribution along the beam and changes the failure mechanism (Arduini et al., 1997a). In the following the failure mechanisms are discussed in detail.

FRP rupture in tension occurs when the FRP strain exceeds the ultimate value in the zone of maximum moment or at stress concentrations (e.g. corners or debonded areas). This occurs after large deflection of the member has taken place, which shows good structural performance (Figure 2-7a). From an economical point of view, the rupture of the FRP plate or sheet seems to be desirable because it means that all the resources of FRP are utilised. Appreciable strength gains for fracture type failures are only possible when the original beam is very lightly reinforced (Bonacci, 1996).

Concrete crushes when the concrete compressive strain exceeds its ultimate value in the cross-section of maximum moment as shown in Figure 2-7b. This occurs after a large deflection of the member, which is a better structural performance. Bonacci (1996) stated that specimens failing in flexural compression preserved considerably more of the deflection capacity of the conventionally reinforcement control beams than were the case for the other failure modes.

Peeling-off failure occurs due to failure at the concrete-adhesive interface, which is debonding between FRP and concrete. The bond between the sheet and the concrete may fracture in a sudden manner as the result of catastrophic propagation of a crack along the FRP-concrete interface. Possible reasons for the existences of such a crack are imperfections in the spreading of the adhesive, flexural cracking in the concrete, peeling-off of the plate when the concrete tensile face is not perfectly flat, or fatigue loads. This failure mechanism is facilitated by low ultimate strain values of the adhesive. As the adhesive fails in uniaxial tension in a given zone, there is no shear stress or normal stress transfer between the FRP and the concrete. At the ends of this zone, a high shear and normal stress transfer is needed to balance the force in the unbounded FRP plate (Triantafillou and Plevris, 1992). This failure mechanism is shown in Figure 2-7c.

Concrete cover delamination results from a combination of shear and normal tensile stress in the concrete in the plane of the longitudinal steel bars. This failure mechanism initiates at the ends of the FRP plate, results in the propagation of a horizontal crack, and causes separation of the concrete cover, as shown in Figure 2-7d. It is also brittle and occurs at load values lower than expected with conventional design equations. The occurrence of shear-tension indicates that it is no longer possible to increase the flexural capacity of the member by increasing the FRP thickness.

In the first two modes of failure, the ultimate strength of the structural member can be predicted easily by following conventional RC flexural theory. However, whenever the mode of failure is peeling-off or concrete cover delamination, the strengthened member is not able to reach its ultimate strength. From the point of view of design, it is important to recognize this premature type of failure and determine algorithms for its prediction. These failures are sudden, brittle and occur with no warning (Tumialan et al., 1999).

2.5.2 Failure Mechanisms for Beams Strengthened in Shear

Once shear forces develop inclined cracks in the concrete, high tensile stresses are developed in the portions of the FRP sheet that bridge these cracks. The tensile stresses in vertically oriented FRP sheets are a result of the vertical separation of rigid bodies of concrete on either side of the crack. These tensile stresses must be transferred to the concrete on each side of the crack by interfacial bond stresses. If this interfacial bond is compromised before rupture of the FRP sheet, a delamination failure occurs. The delamination failure could take the form of debonding at the concrete-adhesive interface or shearing of the concrete below the concrete-FRP sheets interface, as discussed in Section 2.5.1. The tensile fracture of the FRP sheet at a stress, which may be lower than the tensile strength of the FRP material, occur due to stress concentrations (e.g. at corners or debonded areas).

Whether delamination or fracture of the FRP sheet will occur first depends on the bond conditions, the available anchorage length and/or the type of anchorage at the FRP ends, the thickness of the laminates and others. In many cases, the actual failure mechanism is a combination of FRP delamination at certain areas and fracture at others. In general, as the FRP become stiffer and thicker, delamination dominates over tensile fracture (Triantafillou, 1998).

Debonding and concrete shearing underneath the FRP sheet failures are more difficult to characterize and analyse than the other potential modes. They depend on factors that are foreign to analyses of conventional nature such as mechanical preparation of the concrete surface before the application of the epoxy and the sensitivity to faulting motions along member cracks propagating to the tension face (Bonacci, 1996).

2.6 Conventional Bond Test Methods

There are several different test arrangements conventionally used for FRP bond research. The main categories of bond tests based on the type of load on the FRP sheets are direct tension, bending, and shear type tests.

2.6.1 Direct Tension Bond Tests

The direct tension type bond test shown in Figure 2-8 measures the normal bond stress between the FRP sheet and concrete. The FRP sheet is bonded to the surface of a concrete block. The block is secured in place and an apparatus that applies the load is bonded to the FRP sheet. The tensile load is applied perpendicular to the direction of the fibres through the bonded apparatus. The bond strength is measured by dividing the ultimate tensile load by the bond area. The bond area is usually square 40 × 40 mm, which is relatively small compared to the other test methods. The test results conducted by Horiguchi and Saeki (1997) show that the bond strength recorded using this test method is higher than both the bending and shear type specimens as shown in Figure 2-9. The corresponding type of application is rare and the stress condition is undesirable.

2.6.2 Bending Bond Tests

The bending type bond test shown in Figure 2-10 uses a simply supported RC beam specimen with FRP sheets bonded to the bottom tensile face. The beam has a rectangular or inverted T-shape cross-section. The beam is saw cut in the centre up to about half the depth from the tensile lower surface to simulate a crack at the centre of the beam. The specimen has either a notch or a hinge in the centre of the compression side as shown in Figure 2-10, in order to ease the bending of the specimen and to control the distribution of the internal forces (De Lorenzis et al., 2000). The FRP sheet is bonded to the lower tensile face of the beam. A four-point loading is usually adopted in this test method. As the load increases the concrete cracks at the saw cut location and both tensile and bending stresses are transferred to the FRP sheet.

2.6.3 Shear Bond Tests

The shear type test specimens better represent the bond in shear strengthening of RC members. The shear type bond tests are grouped in this study into three categories that are based on the method of load application. These categories are direct pull bond tests, indirect pull-apart tests, and indirect push-apart tests.

2.6.3.1 Direct Pull Bond Tests

The single-lap bond test set-up, shown in Figure 2-11, is a direct pull bond test. This method is one of the simple test methods used to calculate the bond strength between concrete and FRP sheets. It consists of a concrete block secured to the fixed head of a testing machine with one end of an FRP sheet bonded to one side and the other end gripped in the moving head of the testing machine. The load is applied directly to the FRP sheet when the moving head rises. This test requires special attention during bonding the FRP sheet and then aligning it in the testing machine. The width of the sheet is restricted to 25 mm due to grip problems.

From the test results of Chajes et al. (1996) using this test method it was indicated that the maximum interfacial bond stress would be 5.5 MPa. In this test arrangement the concrete block encounters compression while the FRP is in tension as shown in the free body diagram in Figure 2-12. Bizindavyi and Neale (1999) used the same test specimen but bonded the sheet at a distance away from the loaded edge to overcome the high compression at the loaded end of the concrete block.

2.6.3.2 Indirect Pull-Apart Tests

The specimen in this method consists of two concrete prisms with a steel rebar embedded in the centre of each prism. The prisms are aligned and the FRP sheets are bonded to two opposite sides of the prism. The specimen is placed in a testing machine with the machine heads gripping the rebar. As the head moves the force generated in the embedded bars is transferred to the FRP sheets through bond between the concrete and the FRP sheets, as shown in the free body diagram in Figure 2-13(b).

Maeda et al. (1997) indicated that the highest average bond stress calculated using this test method was 2.94 MPa. Bonding the sheets, and handling the specimen after bonding the sheets is problematic in this test arrangement due to the gap between the concrete prisms. The load in the FRP sheets, and in return the bonded area, is limited to the bond slip strength of the steel rebar.

2.6.3.3 Indirect Push-Apart Tests

The push-apart bond test, shown in Figure 2-14(a) only requires the use of a hydraulic jack to apply the load, which makes it suitable for field verifications in retrofit situations. It is clear from the free body diagram shown in Figure 2-14(b) that the concrete is in compression while the FRP is in tension, similar to that of the direct pull test. Special care is also required with aligning the concrete blocks during bonding the sheets and during the test set-up.

Several researchers used this type of specimen. The results from Drimoussis and Cheng (1994) and Alexander and Cheng (1997) showed a maximum average bond stress of 2.6 and 2.3 MPa respectively while Dolan et al. (1998) had a maximum of 3.6 MPa. The difference is attributed to the different material properties and bond lengths used in the studies.

There are many tests conducted using the previous conventional bond test methods and from the previous discussion it is clear that there is a need to assess the performance of these methods and to develop a rational and simplified standard test method. An attempt to relate the different types of tests in order to be able to use their results in developing design equations and guidelines based on a broad database of consistent results is also required.

2.7 Factors Affecting Bond Behaviour

Despite the diversity of reinforcing materials used, the different concrete compressive strengths investigated, and the different specimen geometry and loading employed, there is a rather general agreement on the main factors affecting the bond strength between FRP and concrete. These factors are the FRP bond length, bond width, stiffness, concrete tensile strength, and concrete surface preparation. Certain other factors have also been reported to have a significant effect on the bond behaviour such as the test method and the anchorage type and detail.

2.7.1 FRP Sheet Bond Length

The effect of the bond length of FRP sheets bonded to concrete on the bond behaviour has been the focus of study by several researchers. Drimoussis and Cheng (1994) tested push-apart specimens with bond lengths of 100 mm, 200 mm, and 300 mm. They observed that there was no significant change in the test results due to the increase in length from 200 mm to 300 mm.

Chajes et al. (1996) conducted a series of direct pull tests with FRP bond lengths ranging from 50 to 200 mm. They concluded that there exists a development length for a joint beyond which no further increase in failure load can be achieved (i.e. effective length, L_e). They also concluded that the ultimate capacity (P_u) is directly proportionate to the bond length (L) but with the effective length as a limit. The relationship is given by

$$P_u = RL \quad L < L_e \quad (2-1a)$$

$$P_u = RL_e \quad L \geq L_e \quad (2-1b)$$

in which R is the average bond resistance defined as:

$$R = \frac{F_1 - F_2}{\Delta L} \quad (2-1c)$$

Here F_1 and F_2 are the forces in the composite material plate at gauges 1 and 2, and ΔL is the distance between gauges 1 and 2. Chajes et al. (1996) also stated that

additional experimental and analytical research is needed and that the plate width effect needs to be investigated.

Alexander and Cheng (1997) studied the effect of the bond length on the bond behaviour using a series of sixteen push-apart tests. The bond lengths investigated ranged from 50 mm to 175 mm. They proposed a bond stress vs. bond length relationship in which the effective bond length is 110 mm.

Brosens and van Gemert (1997) performed direct pull tests with a constant bond width of 80 mm but with bond lengths ranging between 150 mm and 250 mm. They concluded that an increase in the bond length increased the failure load, but stated that when the bond length exceeds a critical length, the fracture load remains constant. They stated that the value of the effective length could be determined experimentally and that in their case the value was larger than 275 mm. They also concluded that the influence of the bond length decreases at longer lengths.

Another study by Maeda et al. (1997) was conducted on the bond mechanism of CFRP sheets bonded to concrete using pull-apart tests. They concluded that bond lengths above 100 mm did not change the ultimate load, implying the existence of an effective bond length of 100 mm. They also stated that the effective bond length decreases as the FRP sheet stiffness increases.

Horiguchi and Saeki (1997) studied pull-apart specimens with CFRP bond length of 40, 100, and 200 mm and with a fixed bond width of 75 mm. They concluded that the effective bond length was 60 mm. Täljsten (1997) carried out direct pull tests on steel and CFRP bonded plates and came to the same conclusion of the existence of an effective bond length.

From the above it is clear that there is a general agreement on the existence of an effective bond length above which no increase in the failure load is achieved. The value of the effective bond length proposed varies significantly from one study to the

other, ranging from 60 mm to over 275 mm. The variation is mainly due to the different configurations, material properties, and test methods used. A detailed study on the parameters affecting the effective length is required.

2.7.2 FRP Sheet Bond Width

Brosens and Van Gemert (1999) developed a bond strength model that included the effect of the FRP bond width. The width effect was introduced through a coefficient that includes the ratio between the FRP sheet width to the concrete specimen width. They also concluded through pull-apart tests with CFRP sheet widths of 80 mm and 120 mm and various numbers of plies that the anchorage length (effective length) is nearly independent of the sheet width.

Ueda et al. (1999) studied the bond width effect using a series of pull-apart bond tests. The width of the CFRP sheets ranged from 10 mm to 200 mm. FRP sheets with bond widths less than 40 mm failed by sheet breakage. They concluded that the FRP sheets with narrower width indicated greater bond strength than sheets with wider width. They also observed that the failure zone is wider than the width of the FRP sheet.

De Lorenzis et al. (2000) studied the effect of the width of CFRP sheets on the bond behaviour using bending tests. The widths of the sheets studied were 50 mm and 100 mm. The findings showed that doubling the width doubled the failure load, which suggests that the width did not influence the average bond strength.

Again the limited number of studies and the discrepancies between them are apparent, which shows the need to study the effect of the bond width on the bond behaviour.

2.7.3 FRP Sheet Stiffness

Maeda et al. (1997) studied the effect of the number of layers of FRP sheets on the bond mechanism using pull-apart tests. They concluded that the ultimate load increases as the FRP sheet stiffness increases. They also stated that the effective bond length decreases as the sheet stiffness increases.

Ueda et al. (1999) concluded in their research on CFRP sheets using different test methods that the greater the stiffness of the sheets the greater the bond strength and the less the strain gradient in the sheets.

De Lorenzis et al. (2000) studied the effect of the number of CFRP plies using bending tests. They concluded that the failure load increases with the increase of the number of plies but the proportion is not linear, where doubling the plies increases the failure load by only 50%.

Nakaba et al. (2001) concluded in their experimental investigation on pull-apart tests that the maximum load increases as the stiffness of the FRP sheet increases. They also stated that the FRP stiffness influences the bond strength and the shape of the stress distributions.

2.7.4 Concrete Strength

Swamy et al. (1986) tested a series of double-lap shear tests (pull-apart tests) with steel adherents bonded to concrete. They tested samples with concrete compressive strengths ranging from 24 to 70 MPa and found that the average bond strength at failure varied almost linearly from 2.15 to 3.3 MPa.

Chajes et al. (1996) conducted a series of direct pull tests with compressive strengths ranging from 24 to 45 MPa. They concluded that if the failure mode is governed by shearing of the concrete below the glue line, the ultimate bond strength is

proportional to the square root of the concrete compressive strength. They also recommended that more tests be done before a final relationship can be proposed.

Horiguchi and Saeki (1997) studied the effect of the concrete quality on the bond behaviour of CFRP sheets using three different bond test methods, namely the shear test (pull-apart test), the bending test, and the tensile test. They concluded that the bond strength increases as the concrete compressive strength increases. The effect was most significant for the tensile test and least for the pull-apart test. They also concluded that the value of the concrete compressive strength (f'_c) influences the failure mechanism. Failure occurred in the concrete when $f'_c < 25.3$ MPa and delamination at the adhesive interface (debonding) occurred when f'_c was high.

Nakaba et al. (2001) and Kobayashi et al. (2001) concluded that the maximum local bond stress increases as the concrete compressive strength increases. Both tests used pull-apart bond tests in their investigations. De Lorenzis et al. (2000) on the other hand, who used beam specimens observed no evidence that f'_c had an effect on the bond strength. They referred this observation to the failure mode, which was at the concrete-epoxy interface.

2.7.5 Concrete Surface Preparation

Chajes et al. (1996) studied the effect of the surface preparation on the average bond strength using direct pull tests. They concluded that concrete surface preparation could influence the bond strength.

Yoshizawa et al. (1996) conducted a study using pull-apart tests on the effect of the type of concrete surface preparation on the bond of CFRP sheets. They concluded that the surface preparation by using water jet doubled the capacity of the specimen as compared to sandblasting.

De Lorenzis et al. (2000) stated that the performance of the bending specimen with roughened surface was much better than that of the specimen with sandblasted

surface. They concluded that the surface preparation of the concrete could significantly affect the average bond strength but also stated that further study is required to quantify the influence of the surface preparation on the bond performance.

2.7.6 Type of Test Conducted

Several researchers have indicated the effect of the type of bond test method conducted on the test results. Chajes et al. (1996) indicated the need to conduct additional experimental and analytical research to study the effect of the type of test conducted (direct pull test versus pull-apart test).

Horiguchi and Saeki (1997) studied the effect of the test method conducted on the bond of CFRP sheets. Three different types of tests were conducted; namely, shear tests (pull-apart tests), flexural tests, and direct tensile tests. They concluded that the test method had a significant effect on the bond, where the tensile test produced the highest average bond strength followed by the bending test. The lowest average bond strength was found in the shear tests, as shown in Figure 2-9.

2.7.7 Anchorage Details

Because of premature failure due to debonding of FRP sheets from the concrete surface, it is often very difficult to develop the full strength of the composite material. Thus, many investigations have been conducted to determine required development lengths and the effect of end anchorage on the behaviour of FRP sheets bonded to concrete.

Examination of the various premature failure modes in concrete leads to the conclusion that premature failure usually initiates at the end of the plate in flexural strengthening and in the region of diagonal shear cracks in shear strengthening. The reason for the premature failure in flexure strengthening is the stress concentration created by termination of the plate. This implies that proper detailing of the plate end

and additional plate anchorage techniques should be used. A wide variety of plate termination details and end-anchorage techniques have been studied in the literature.

By contrast the reason for premature failure in the shear strengthening case is the existence of shear cracks and insufficient FRP sheet bond development length.

A number of studies reported using special anchorage details for FRP sheet flexure strengthening, consisting of anchor bolts, U-shaped straps near the cut-off, or staggered cut-offs of multiple-layered plates. In addition to these particular details, there were studies on the variation in the distance between the end support and the edge of the FRP plate. The capacity increase of strengthened beams and the conventionally reinforced control beams showed little sensitivity to either the plate gap near the support or to the use of special anchorage details. About half of the cases with special anchorage details still failed by debonding (Bonacci, 1996).

Sharif et al. (1994) found that anchor bolts successfully eliminated plate separation for FRP but that premature failure was still observed as longitudinal cracks develop in the concrete adjacent to the FRP plate, causing separation of the concrete cover below the longitudinal steel. Roberts and Haji-Kazemi (1989) concluded that the use of anchor bolts should not be expected to reduce significantly the magnitude of the normal forces and increase the strength of the plated beams.

By using glued angle plates or transverse FRP wraps, the plating material can be effectively anchored to the tensile face of the beam. The effectiveness of this technique has been commented on by Arduini et al. (1995) who found that a great deal of ductility could be observed until plate rupture or shear failure of the wrap or angle plates. Erki and Heffernan (1995) found that the failure mode of a CFRP plated beam could be changed from premature plate debonding to tensile failure of the sheet at mid span by adding a CFRP wrap around the sides and bottom of the beam in the anchorage zones.

Ali and Oehlers (1997) studied the effect of bonding side plates on the resistance of plated beams to peeling in the presence of longitudinal cracks. Experimental results indicated that side plates provided additional shear reinforcement and increased the sheet resistance to peeling due to cracking in the order of 100 %.

The use of one-piece FRP I-shaped sheets has been investigated by Sharif et al. (1994). In a comparison of anchor bolts, side plates, and I-shaped sheets as anchoring techniques for FRP sheets, the I-shaped sheets provided superior results. Experimental data indicated that I-shaped sheets could change beam behaviour from brittle to ductile and allow the plated member to achieve the full composite strength.

Because FRP sheets are much thinner than steel plates of equivalent capacity the peeling effect at the end of the sheets is highly reduced and the likelihood of a need for end fixing is reduced (Hollaway and Leeming, 1999). Depending on the sheet/plate location and concrete cross section the choice of anchorage technique will be different. Because research in this area is limited, the only way to be certain that a particular anchorage technique will work in practice is to conduct laboratory tests. This will ensure a safe and effective solution. However, research indicates that FRP side wraps for FRP plating should be used wherever possible.

Sato et al. (1997a) studied several anchoring methods for CFRP sheets used for shear strengthening. Figure 2-15 shows the anchorage methods investigated. They recommended using longer anchoring bolts that penetrate the entire beam width. They also concluded that sheets with mechanical anchorage were more effective compared to those without them. They qualitatively demonstrated the shear strength improvement due to the mechanical anchors but recommended further study on the quantitative assessment of the anchorage efficiency.

Mechanical anchors made of steel, although effective in the laboratory, are not very practical for field application due to drawbacks such as stress concentration and, in the case of bolting, discontinuity of the FRP at drilling locations. In some cases bolting or jacketing cannot be carried out because of possible damage to the

reinforcing or prestressing bars or due to insufficient space around the beam. In the case of CFRP, there is also a likelihood of galvanic corrosion because of steel-carbon fibre contact, which is also a concern.

2.8 Bond Strength Models

In section 2.6 failure modes were presented and discussed. An enormous amount of research effort has focused on determination of the types, causes, and prevention of premature failure modes. Various attempts have been made to characterize the behaviour of these failure mechanisms so that a rational design approach can be formulated.

Different researchers have proposed several bond strength models. The models can be classified into three categories: empirical models based on regression of test data, fracture mechanics based models, and design models that use simplified assumptions. A review of the significant proposed models is presented below.

2.8.1 Empirical Models

Sato et al. (1996) stated that Tanaka (1996) carried out an experimental series on push-apart test specimens and presented a simple expression for the average bond stress

$$\tau_b = 6.13 - 0.92 \ln L \text{ (MPa)} \quad (2-2)$$

in which L is the bond length in mm. The ultimate bond capacity of the joint is given by multiplying τ_b by the width b_p and length L of the bond area. This model does not take into consideration the effective bond length.

Alexander and Cheng (1997) studied the effect of the bond length on the bond behaviour using a series of push-apart tests. They proposed a bond stress model in which:

$$\tau_b = \begin{cases} 2.3 & L \leq 60 \text{ mm} \\ 3.86 - 0.026L & 60 \text{ mm} < L < L_e \\ 1.0 & L \geq L_e \end{cases} \quad (2-3)$$

Here τ_b is the average bond strength in MPa, L is the bond length in mm, and L_e is the effective bond length taken as 110 mm.

Hiroiyuki and Wu (1997) conducted a set of pull-apart tests on CFRP sheets. Based on the test results, they proposed the following empirical equation that predicts the average bond stress at failure, τ_b , in terms of the bond length, L (cm).

$$\tau_b = 5.88L^{-0.669} \text{ (MPa)} \quad (2-4)$$

The ultimate load was obtained by multiplying τ_b by the bond area $b_p L$. Again, this model does not take the effective bond length into consideration.

The model adopted in the CSA S806-02 (2002) and ISIS Canada Design Manual (2001) for predicting the average bond strength at failure, τ_b , is that proposed by Maeda et al. (1997). The proposal was based on the experimental results obtained from pull-apart test specimens using CFRP sheets.

$$\tau_b = 110.2 \times 10^{-6} E_p t_p \text{ (MPa)} \quad (2-5)$$

where t_p (mm) and E_p (MPa) are the FRP sheet thickness and modulus of elasticity, respectively. The ultimate load was obtained by multiplying τ_b by the effective bond area $L_e b_p$. The following equation in terms of E_p (MPa) and t_p (mm) give the effective length, L_e in mm.

$$L_e = \frac{25350}{(t_p \cdot E_p)^{0.58}} \quad (2-6)$$

Bizindavyi and Neale (1999) tested a series of direct pull tests on both CFRP and GFRP sheets with 25 mm bond width. They proposed an exponential equation based on curve fitting of the experimental results. The equation took the form:

$$\tau_b = A \cdot \exp(-\psi \cdot L) \quad (2-7)$$

where τ_b and L are given in MPa and mm respectively and A and ψ are coefficients obtained from curve fitting the test results. The coefficients were shown to be

different for CFRP sheets and GFRP sheets and also different for one ply and two plies of FRP.

Ueda et al. (1999) carried out a series of tests and proposed an equation to predict the maximum local bond stress. The equation was derived based on force equilibrium and the observed distribution of the strain in the FRP sheets. The equation took the form:

$$\tau_b = 0.19t_p E_p \leq 7.3 \text{ MPa} \quad (2-8)$$

where t_p and E_p are the sheet thickness in mm and the modulus of elasticity in MPa respectively. Only the sheet stiffness was taken into consideration with a τ_b limit value of 7.3 MPa, which is based on a maximum effective stiffness of 38.4 GPa.mm.

2.8.2 Fracture Mechanics Based Models

Chen and Teng (2001) reported that Holzenkämpfer (1994) investigated the bond strength between steel plates and concrete using non-linear fracture mechanics (NLFM). The bond capacity, P_u , is calculated as:

$$P_u = \begin{cases} 0.78b_p \sqrt{2G_f E_p t_p} & \text{if } L \geq L_e \\ 0.78b_p \sqrt{2G_f E_p t_p} \frac{L}{L_e} \left(2 - \frac{L}{L_e}\right) & \text{if } L < L_e \end{cases} \quad (\text{kN}) \quad (2-9a)$$

where the effective length L_e and the fracture energy G_f are given by

$$L_e = \sqrt{\frac{E_p t_p}{4f_{ct}}} \quad (\text{mm}) \quad (2-9b)$$

$$G_f = c_f k_g^2 f_{ct} \quad (\text{N.mm/mm}^2) \quad (2-9c)$$

$$k_g = \sqrt{1.125 \frac{2 - b_p/b_c}{1 + b_p/400}} \quad (2-9d)$$

Here f_{ct} is the tensile strength of concrete; c_f is a constant determined in a linear regression analysis using pull-apart tests and k_g is a geometrical factor related to the width of the bonded plate b_p and the width of the concrete member b_c .

Täljsten (1994) investigated the bond strength between concrete and both steel and CFRP plates using NLFM analysis.

$$P_u = \sqrt{\frac{2E_p t_p G_f}{1 + \alpha_T}} b_p \quad (2-10a)$$

where

$$\alpha_T = \frac{E_p t_p}{E_c t_c} \quad (2.10b)$$

in which E_p and E_c are the modulus of elasticity in MPa of the FRP and concrete, respectively, t_p and t_c are the thickness in mm of the FRP and concrete, respectively, and G_f is the fracture energy in N·mm/mm². The fracture energy needs to be calculated from the measured values of the load, deformation, and bond shear stress.

Neubauer and Rostásy (1999) conducted a series of pull-apart tests on CFRP sheets bonded to concrete. They concluded that the fracture energy could be calculated using:

$$G_f = k_p c_f f_{ct} \quad (2-11)$$

in which f_{ct} is the tensile strength of concrete, and the factor c_f contains all the secondary effects and was taken as 0.202 mm, which is an average value from 70 specimens. The factor $k_p > 1.0$ considers the influence of the plate width relative to the width of the concrete member and usually does not exceed 1.3. They also proposed a modified form of Holzenkämpfer's (1994) model, so that it applies to both steel and CFRP. The model takes the form:

$$P_u = \begin{cases} 0.64k_p b_p \sqrt{E_p t_p f_{ct}} & \text{if } L \geq L_e \\ 0.64k_p b_p \sqrt{E_p t_p f_{ct}} \frac{L}{L_e} \left(2 - \frac{L}{L_e}\right) & \text{if } L < L_e \end{cases} \quad (2-12a)$$

$$L_e = \sqrt{\frac{E_p t_p}{2f_{ct}}} \quad (2-12b)$$

Because of the complexity of the fracture mechanics based models they are not used as design rules. Other researchers proposed simplified models to be used in design as shown in the following subsection.

2.8.3 Design Proposed Models

By assuming a rectangular shear stress distribution across the full bond length, Van Gemert (1980) proposed an expression for the ultimate load of a bonded FRP sheet joint:

$$P_u = 0.5wLf_{ct} \quad (2-13)$$

in which w and L are the FRP bond width and length, and f_{ct} is the concrete tensile strength. The equation implies that a sufficiently long bonded length can carry any given load, which contradicts the well-established fact that any additional bond length beyond the effective bond length cannot increase the ultimate load.

Chaalal et al. (1998) assumed that the bond behaves as a Mohr-Coulomb material. For shear strengthening, they assumed that the maximum shear stress is twice the average stress and the maximum shear stress does not exceed the Mohr-Coulomb strength equation given by Varastehpour and Hamelin (1996). This gives:

$$\tau_b = \frac{2.7}{1 + k_1 \tan 33^\circ} \quad (2-14a)$$

where

$$k_1 = t_p^4 \sqrt{\frac{k_a}{4E_p I_p}} \quad (2-14b)$$

$$k_a = E_a \frac{b_a}{t_a} \quad (2-14c)$$

where b_a , t_a , and E_a are the width, thickness, and Young's modulus of the adhesive, respectively; and I_p is the moment of inertia of the FRP plate. This proposal also does not take the effective bond length into consideration.

Khalifa et al. (1998) proposed a modification of the model proposed by Maeda et al. 1997 and included the effect of the concrete strength. The tensile strength is assumed proportional to $(f'_c)^{2/3}$, where f'_c is normalized relative to the concrete strength of 42 MPa in Maeda et al.(1997) tests.

$$\tau_b = 110.2 \times 10^{-6} \left(\frac{f'_c}{42} \right)^{2/3} E_p t_p \quad (2-15)$$

The effective bond length is calculated using Equation (2.5)

Chen and Teng (2001) based on existing fracture mechanics analysis and experimental observations proposed the following bond capacity model:

$$P_u = 0.427 k_p k_L \sqrt{f'_c} b_p L_e \quad (2-16a)$$

$$L_e = \sqrt{\frac{E_p t_p}{\sqrt{f'_c}}} \quad (2-16b)$$

$$k = \begin{cases} 1 & \text{if } L \geq L_e \\ \sin \frac{\pi L}{2L_e} & \text{if } L < L_e \end{cases} \quad (2-16c)$$

$$k_p = \sqrt{\frac{2 - b_p / b_c}{1 + b_p / b_c}} \quad (2-16d)$$

where k_p and k are the width ratio factor and the length factor respectively.

Chen and Teng (2001) also compared the performance of the empirical and design models with experimental results. They concluded that the models that do not take the effective length into consideration significantly underestimate the bond strength and lead to very large scatter. They also stated that the models by Khalifa et al. (1998) and Neubauer and Rostásy (1997) showed reasonable performance.

2.9 Summary

A review of the literature indicates that a considerable research effort has been directed towards the use of FRP sheets for structural strengthening and rehabilitation. The technique of FRP plating is widely recognised within the research community and is gaining acceptance in the construction industry with hundreds of field applications worldwide. However, rational design approaches for the use of FRP materials in construction need to be formulated.

There is limited information on the anchorage of FRPs to concrete or on the most important design factors to ensure a quality bond, such that the full capacity of the composite can be developed. A lack of understanding of the true effect of the parameters controlling the bond behaviour was seen from the discussions presented and from the wide discrepancy in critical values observed.

Reviewing the different conventional bond test methods used in different bond research pointed out the need to develop a rational standard test method for FRP sheets bonded to concrete. Developing a relationship between the results of these models will also help in developing a consistent database.

Although to date a considerable amount of research has been devoted to the bond capacity of FRP sheets and plates to concrete, there is no commonly accepted model predicting the failure load and the effective bond length (Chen and Teng, 2001). The available empirical models are all based on the bond length or the stiffness of the FRP sheet. On the other hand fracture mechanics models that include various variables are not used in design due to their complexity.

The following chapter describes in detail the experimental program conducted in this research in order to investigate the effect of different parameters on the bond behaviour between FRP sheets and concrete.

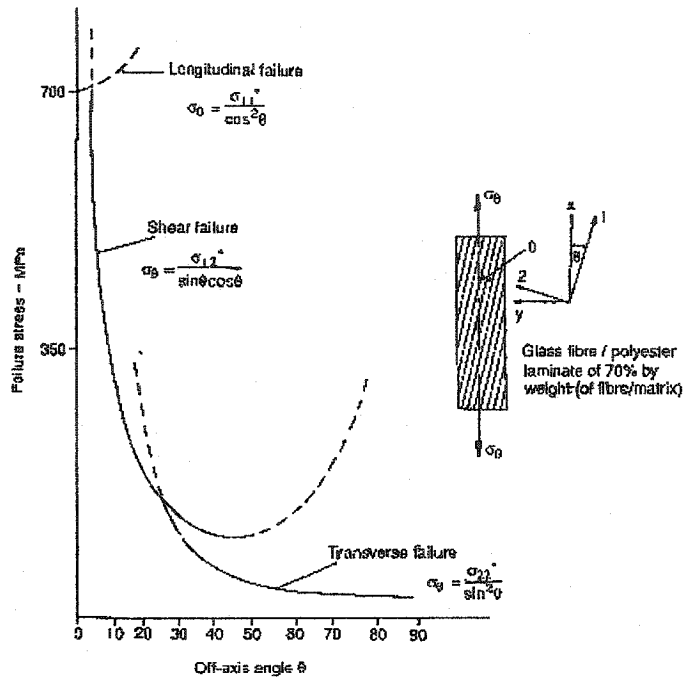


Figure 2-1 Typical failure stress of unidirectional GFRP with respect to axis orientation (Holloway and Leeming, 1999)

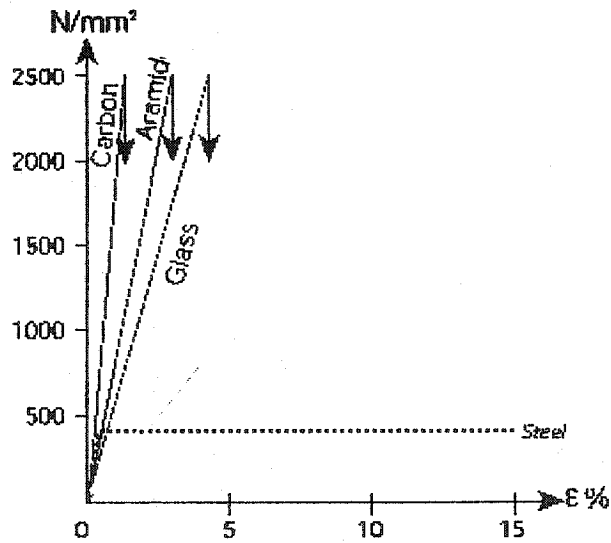


Figure 2-2 Typical stress vs. strain relationship for different types of fibres

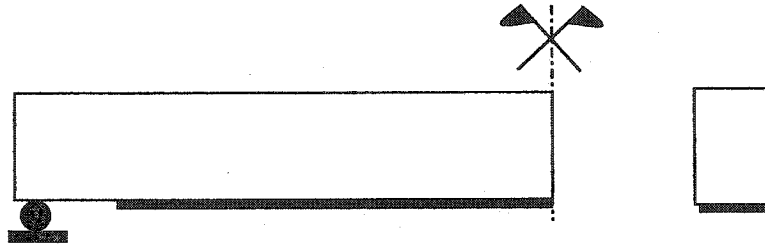


Figure 2-3 Flexure strengthening of RC beams (Cheng, 1998)

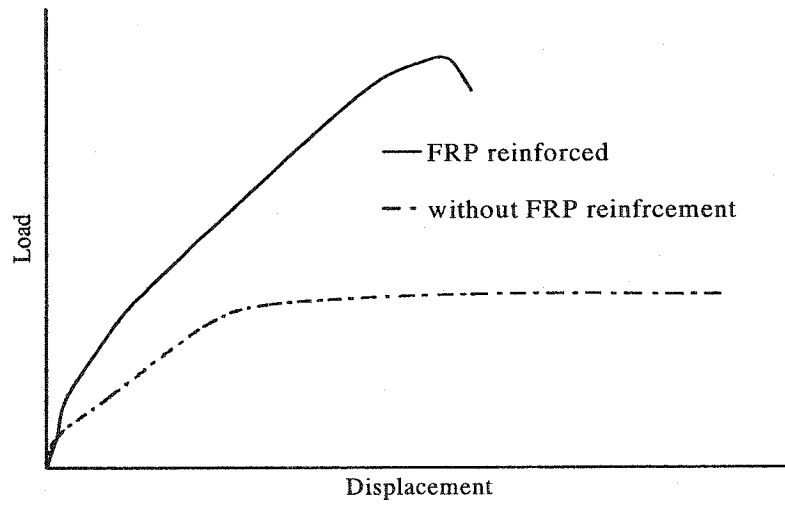


Figure 2-4 Load vs. deflection relationship for beams with and without FRP flexural reinforcement (Cheng, 1998)

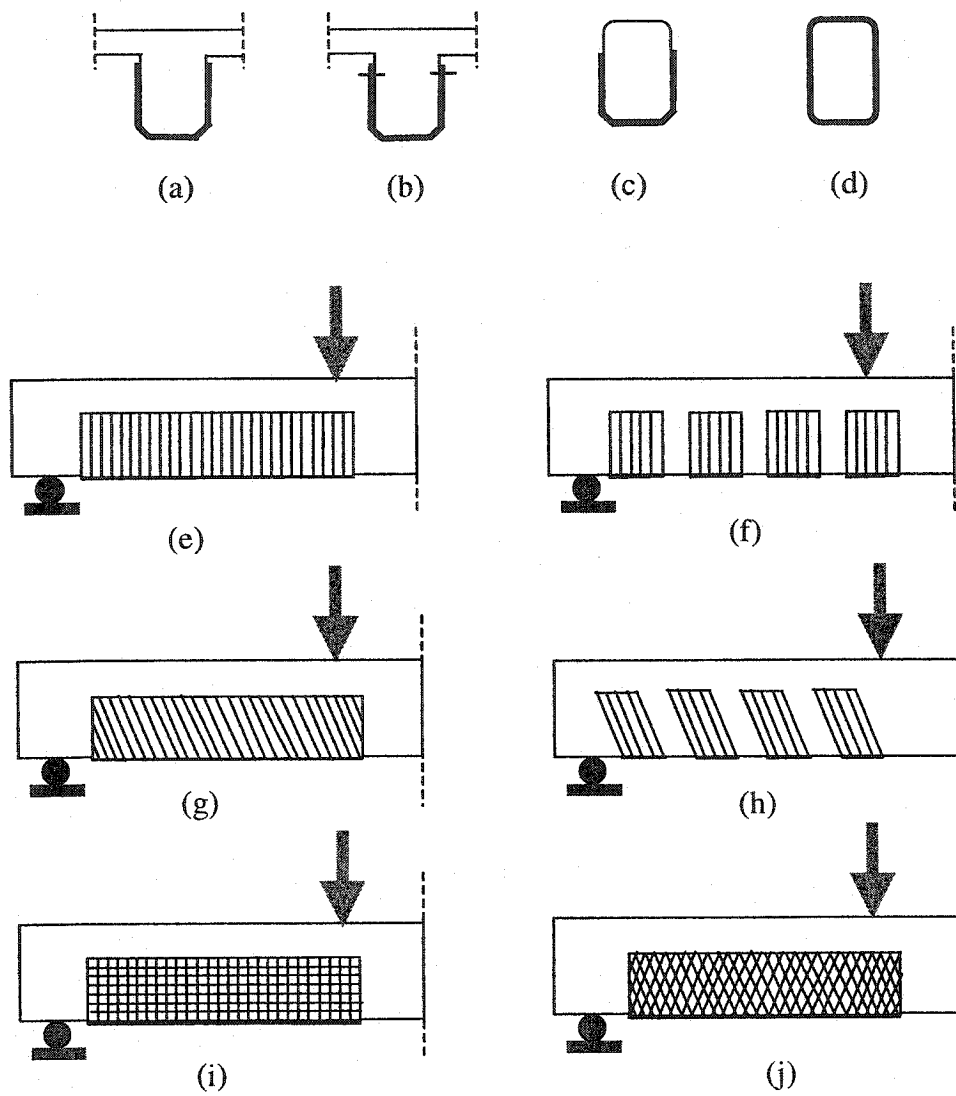


Figure 2-5 Shear strengthened RC beams (Cheng, 1998)

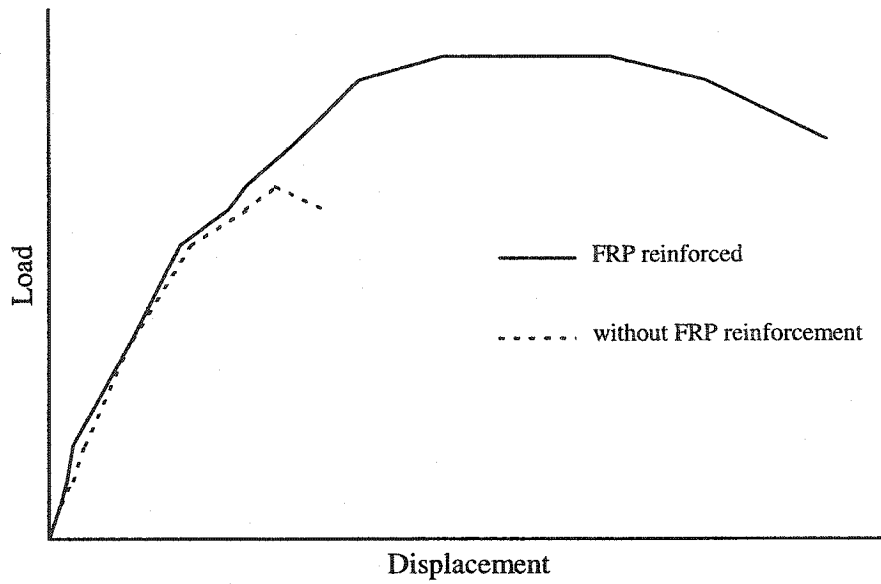


Figure 2-6 Load vs. deflection relationship for beams with and without FRP shear reinforcement (Cheng, 1998)

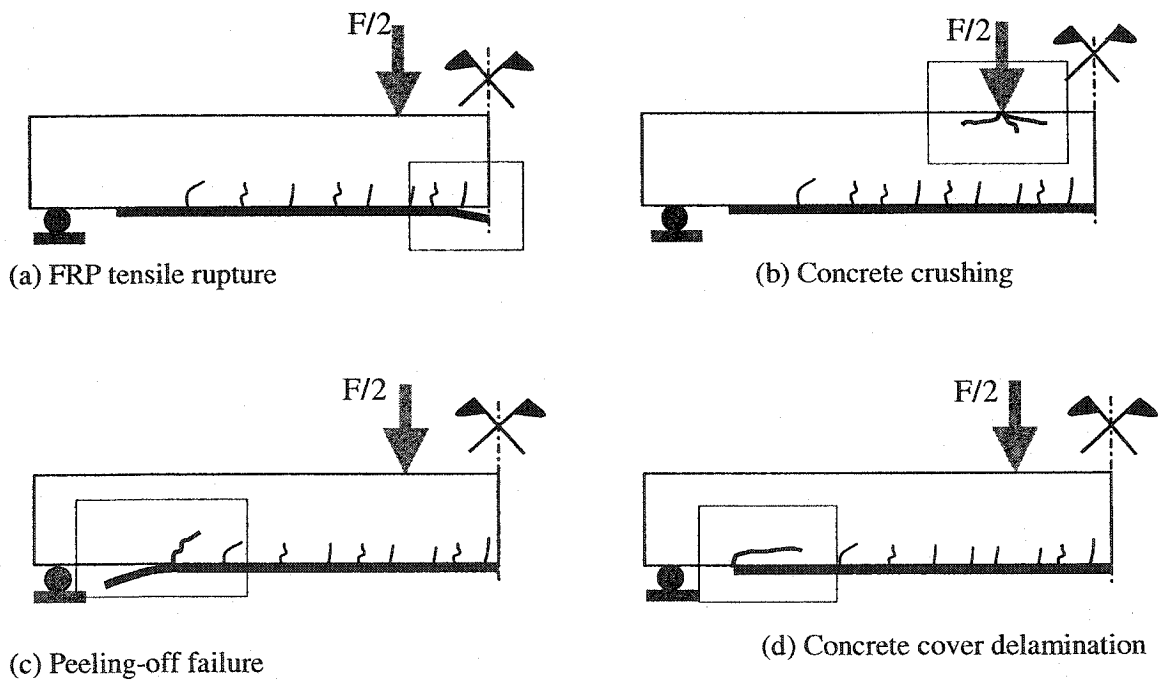


Figure 2-7 Possible failure mechanisms of RC beams strengthened in flexure (Arduini and Nanni, 1996)

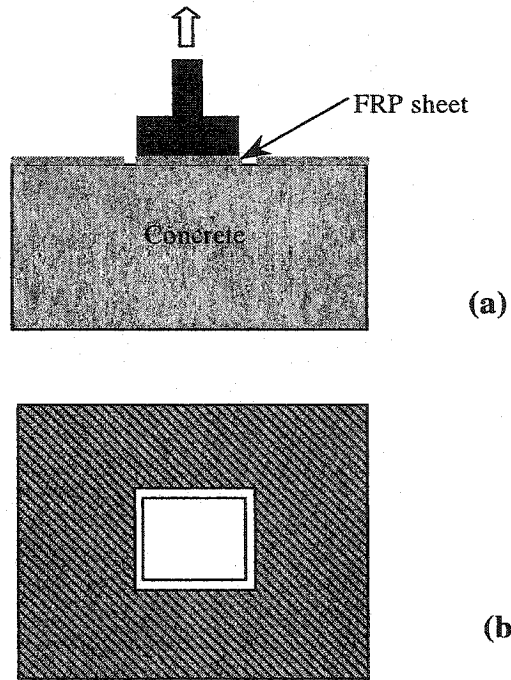


Figure 2-8 Direct tension bond test (a) elevation (b) plan view

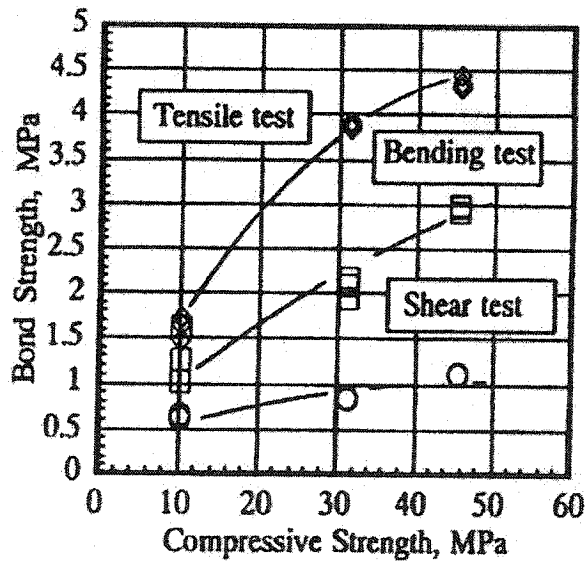


Figure 2-9 Bond strength-compressive strength (Horiguchi and Saeki, 1997)

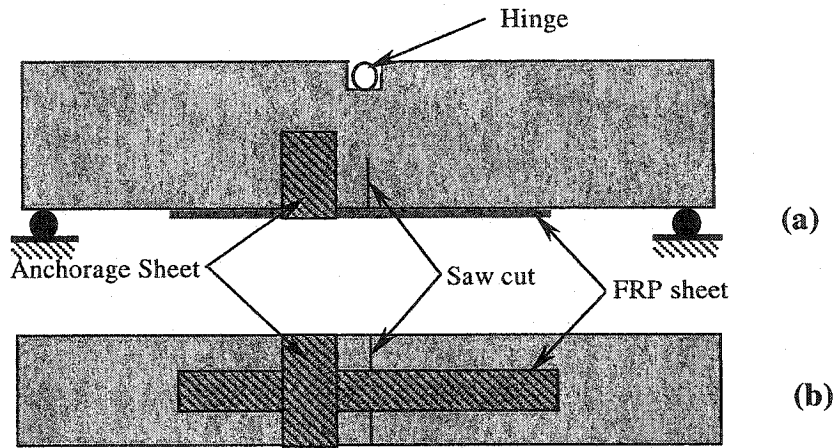


Figure 2-10 Bending bond test (a) elevation (b) bottom plan view

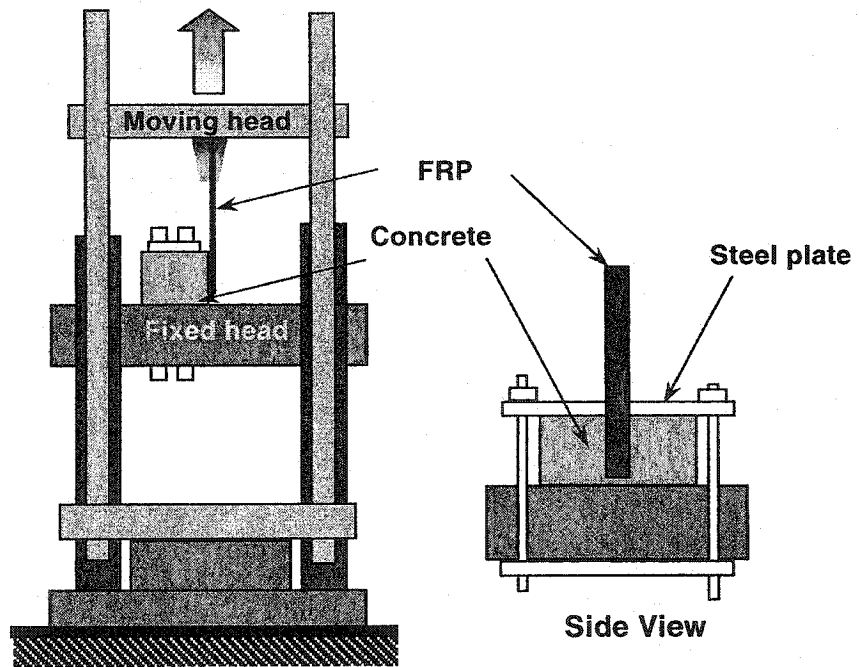


Figure 2-11 Direct pull-apart bond test set-up (Chajes et al., 1996)

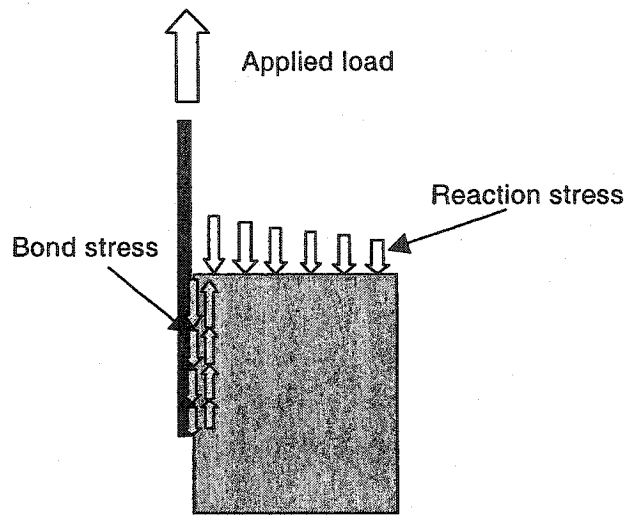


Figure 2-12 Direct pull-apart bond test specimen free body diagram

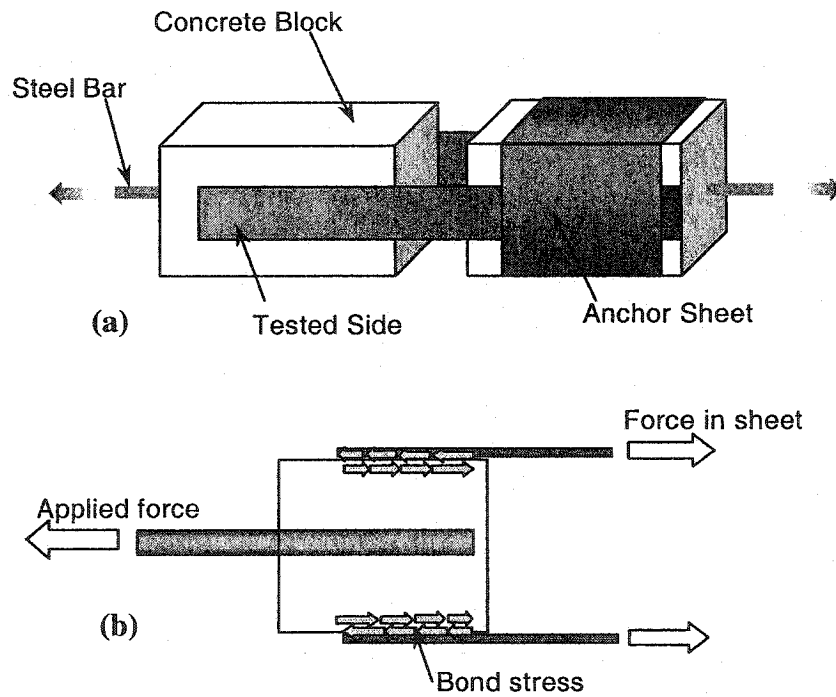


Figure 2-13 Pull-apart bond test (a) set-up (b) free body diagram, plan view

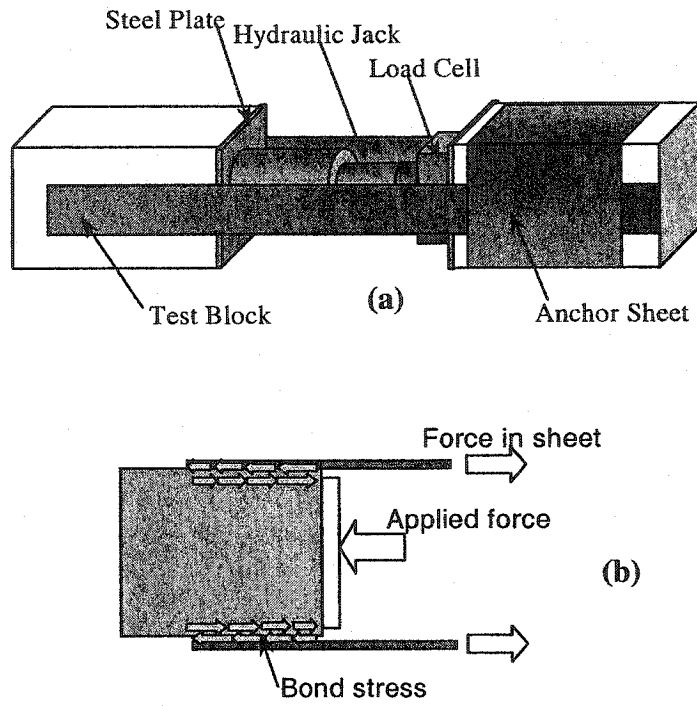


Figure 2-14 Push-apart bond test (a) set-up (b) free body diagram

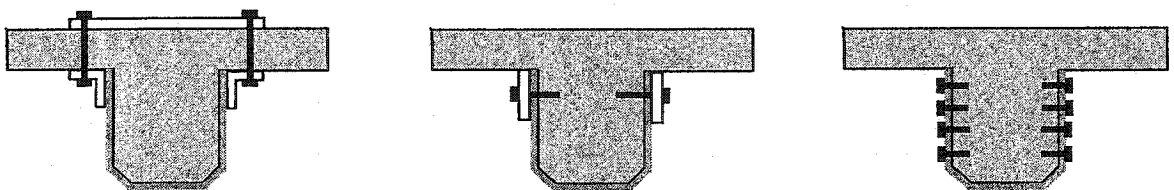


Figure 2-15 Anchoring methods for shear strengthening (Sato et al., 1997a)

3 EXPERIMENTAL PROGRAM

3.1 Introduction

The primary objective of the experimental program was to investigate in detail the parameters controlling the bond length and strain distribution for FRP sheets bonded to concrete. The experimental program consists of two test series. Each test series was conducted using a different bond test method. The first series (S-series) used a proposed modified push-apart test and the second series (P-series) used a pull-apart test. A detailed description of each test specimen, the test set-up, instrumentation, and the property of the materials used are presented. The variables studied in each series are also discussed and presented in this chapter.

3.2 Modified Push-Apart Test

A series of five modified push-apart test specimens were carried out in order to assess the new test method and to study the effect of the FRP sheet dimensions on the bond behaviour. The specimen is a modification to the conventional push-apart type specimen presented in Section 2.8.1. All the specimens in the series had the same concrete shape and dimensions. The variables in this series were the FRP sheet bond length and width.

3.2.1 Specimen Description

Each specimen was a rectangular concrete block with a rectangular empty core in the centre, as shown in the isometric view in Figure 3-1. The empty core was obtained by securing styrofoam to the form base, as shown in Figure 3-2. The styrofoam had the required core dimension and was removed after casting the concrete. The concrete dimensions were chosen to prevent the crushing of the concrete in compression at the load location and also to minimize the deformation of the concrete arms at high loads. Metal sheets were placed along the width of the specimen arms in their centre to force the crack to form in the centre of the specimen arms. A rigid steel plate was fixed to the inner face of the specimen to form a flat surface for applying the load. The steel

reinforcement was detailed in such a way to prevent the failure of the inner corner of the specimens. Figure 3-3 shows the details and dimensions of the specimen, the reinforcement, as well as the loading arrangement.

The arrangement of the CFRP sheets bonded to the arms of the specimen eliminates the compression field in the concrete within the test region, on which the sheets are bonded, thus closely simulating a crack in a beam. One side of the CFRP sheets has an anchor sheet bonded along the width to force the failure to be on the other (tested) side. This was done in order to reduce the amount of instrumentation on the sheets

3.2.2 Test Set-up and Instrumentation

Each specimen was laid on a flat smooth steel surface on which it was free to slide. Steel plates 20 mm thick were placed vertically and secured with plaster to the inner face of the specimen as shown in Figure 3-3. A 220 kN capacity hydraulic jack placed in the centre of the hollow core applied the load in stroke control with a rate of 0.05 mm/min. The jack was controlled by an MTS controller system. A 220 kN capacity load cell located between the hydraulic jack and the steel plate measured the applied load. An LVDT inside the hydraulic jack was used to measure the displacement at the centre of the specimen and was also used in regulating the stroke applied by the jack. LVDTs' were also used to measure the displacement at the faces of the specimen. The change in displacement between the centre and the face of the specimen allows an estimate of the deflection of the concrete arms to which the sheets are applied. Figure 3-4 shows the modified push-apart test set-up and instrumentation.

Strain gauges with 5 mm gauge length were applied to the face of the CFRP sheets on the tested side at various locations in order to measure the strain distribution along the length and width of the CFRP sheets. Figure 3-5 shows the location of the strain gauges on the CFRP sheet for each tested specimen. The bond length and width of the CFRP sheets are also shown in the Figure.

3.2.3 Variables Studied

Besides implementing the new test method, several variables were investigated in this test series. Specimen S2, S3, and S5 all had the same bond widths of 150 mm but different bond lengths of 50, 100, and 150 mm, respectively, in order to study the bond length effect on the bond behaviour. The lengths were chosen based on previous studies in the literature (Drimoussis and Cheng, 1994, Chajes et al., 1996, Maeda et al., 1997, and Horiguchi and Saeki, 1997), which showed the effective bond length to range between 60 and 110 mm.

Specimens S4 and S5 had the same bond length of 150 mm but different bond widths of 100 and 150 mm, respectively, in order to study the bond width effect on the bond behaviour. Another specimen with a width of 50 mm was prepared for testing but the specimen was damaged in a laboratory accident. The CFRP width values were taken based on strip widths typically used in practical beam repairs (Deniaud and Cheng, 2000). The second series of tests investigated bond widths of 25, 50, 100, and 150 mm as will be discussed later.

Specimen S1, S3, and S4 all had the same CFRP sheet bond area of $15,000 \text{ mm}^2$ but each had a different L/w ratio in order to study the FRP sheet L/w ratio effect on the bond behaviour. Table 3-1 lists the variables for the modified push-apart test specimens.

3.3 Pull-Apart Test

A series of 26 pull-apart test specimens were carried out in order to assess the test method, compare the results with the modified push-apart test, and to investigate the anchorage requirements for the FRP sheets. The test specimen is a slightly modified from the specimen used in the pull-apart test method discussed in Section 2.6.3.2. All specimens in the series had the same concrete dimensions.

3.3.1 Specimen Description

Each specimen was a concrete prism with two embedded concentric steel bars and metal sheets placed at mid height, to act as crack initiators when the load is applied. An overview of the steel forms, and reinforcement is shown in Figure 3-6 and Figure 3-7(a). Specimens studying the anchor sheet effect had anchor sheets on both sides of the tested sheet. These specimens had spiral reinforcement confining the steel bars, as shown in Figure 3-6(b), which were added in order to reduce the possibility of any bond-slip of the rebars that apply the load to the concrete. The steel bars were 25 mm diameter and each 500 mm long with half their length inside the concrete prism. The bars were secured in place by passing each bar through an opening in the side form and placing it inside a 28.5 mm diameter and 30 mm long pipe bonded to the metal sheet in the centre of the form. The steel bars alignment configuration is illustrated in Figure 3-7(b). Figure 3-8 shows the specimen dimensions and details of the FRP sheets for the different bond configurations.

3.3.2 Test Set-up and Instrumentation

Each specimen was placed vertically in an MTS 1000 testing machine. The specimen top and bottom bars were secured in the upper and lower head of the MTS machine, respectively, using hydraulic grips. The test was conducted in stroke control with a rate of 0.05 mm/min. A data acquisition system recorded the strains, the applied load, and the displacement. The load-displacement response was plotted on a computer screen during the test. Figure 3-9 shows the pull-apart test set-up and instrumentation.

The strain gauges were applied to study the strain distribution along the length and width of the sheets and to compare the results with previous results from the modified push-apart tests. Strain gauges with 5 mm gauge length were applied to the face of the CFRP sheets on the tested side of specimens P9 through P13 at various locations, as shown in Figure 3-11.

3.3.3 Variables Studied

This test series had several objectives including studying the same variables as the S-series in order to verify the results and compare the test methods. Another objective was to investigate an experimental procedure to estimate the effective bond length. Then finally an investigation into the effect of anchor FRP sheets on the behaviour of FRP sheet bonded to concrete.

Specimens P1 through P8 were used to investigate an experimental procedure to determine the effective bond length. The FRP sheet width was taken as 100 mm in all eight specimens and the sheet bond length was taken equal to kL_{ca} , where k is the length factor, ranging from 0.6 to 2.0 with increments of 0.2. The anticipated effective length, L_{ca} , was estimated using an equation proposed by Maeda et al (1997):

$$\tau_b = 110.2 \times 10^{-6} E_p t_p \text{ (MPa)} \quad (3-1)$$

in which t_p and E_p are the FRP thickness in mm and modulus of elasticity in MPa, respectively. The thickness of the laminated CFRP sheet, t_f , was assumed 0.51 mm, and the modulus of elasticity, E_f , was assumed as 45,000 MPa in the equation. The value of L_{ca} based on the previously stated values was calculated to be 75 mm. The number of specimens was chosen in order to have enough results to accurately identify the effective bond length. The bond length values, kL_{ca} , were chosen in order to capture the behaviour within a sufficient range.

Specimens P9, P10, and P11 with the same bond width of 150 mm and with bond lengths of 50, 100, and 150 mm, respectively, were used to study the bond length effect. Specimens P12, P13, P8, and P11 had the same bond length of 150 mm and bond widths 25, 50, 100, and 150 mm, respectively, and were used to study the sheet width effect on the bond behaviour. The pull-apart specimens P9 through P13 had the same FRP sheet bond length and width as the specimens in the S-series. The effect of the test method used was investigated by comparing the results of specimens P9 through P13 with the results from the modified push-apart specimens S1 through S5 as will be shown in Chapter 4.

Although the use of externally bonded FRP composites has been implemented in many strengthening projects, there has always been a concern for the end anchorage. This is particularly important when the length of the FRP system is restricted and the bonded length beyond a critical section is not sufficient to achieve the ultimate strength of the FRP reinforcement. There has been research on the use of different anchorage methods for both flexure and shear strengthening as presented in Section 2.7.7. The literature shows the importance of the external anchorage on preventing plate peeling. Externally bonded anchor sheets are preferred over mechanical anchorages that add significantly to both project cost and complexity (Spadea et al., 1998) in addition to the drawbacks discussed in Section 2.7.7 of using anchors made of steel.

The effect of bonded FRP anchorage sheets was investigated using specimens P14 through P26, which studied some of the CFRP sheet anchor requirements. The effect of the distance of the anchor from the crack, a , was studied using specimens P14 through P17, which had their anchors above the tested sheet, and P21 through P24, which had their anchors below the tested sheet. The effect of the anchor extension beyond the tested sheet, b , was studied using specimens P17 through P20, which had anchors above the test sheet, and P24 through P26, which had the anchors below the test sheet. The sheets and anchors configurations studied are illustrated in Figure 3-8. Four specimens were used to verify the results of certain specimens in the series. The variables for each specimen are also detailed in Table 3-4.

Figure 3-10 shows the practical simulation of the distances “ a ” and “ b ” illustrated on a concrete girder strengthened in flexure and shear using FRP sheets. The distance “ a ” represents the distance from the anchor sheet to the crack and “ b ” represents half the spacing between the anchor sheets.

3.4 Material Properties

3.4.1 Concrete

Gravel with a nominal maximum size of 10 mm was used for coarse aggregate. The fine aggregate used was coarse sand. Both the gravel and the sand were dry, of

uniform characteristics, and free from injurious materials. Type 50 cement was used in the concrete mix. Clean tap drinking water free from impurities was used in the concrete mix and in the curing of the specimens.

Most research done in the literature used concrete with compressive strengths in the range of 45 MPa (Alexander and Cheng, 1997, Maeda et al., 1997, Brosens and Van Gemert, 1997, Udea et al., 1999, and Bizindavy and Neale, 1999). Because a comparison with the research results from the literature was planned, the concrete mix was designed to have a compressive strength of 45 MPa and is shown in Table 3-5 and Table 3-6 from the push-apart tests and the pull-apart tests, respectively. The concrete was mixed using a 0.3 m³ capacity concrete mixer. Three compression cylinders and two split cylinders were taken from each batch of concrete. The specimens along with the cylinders were cured with wet cloth for two days and then left in normal room temperature for 28 days. The average concrete compressive strength was 50.2 MPa and 47.1 MPa for the modified push-apart tests and pull-apart tests, respectively. The tensile strength was taken as 0.65 of the strength resulting from the split cylinder tests (Collins and Mitchell, 1987), which was calculated using the following equation:

$$f_{sp} = \frac{2P}{\pi Ld} \quad (3-2)$$

in which P is the crushing load, L is the length of the cylinder, and d is the diameter of the cylinder. The average tensile strength of the concrete was 2.6 MPa and 2.3 MPa for the modified push-apart tests and pull-apart tests, respectively. The results of the concrete compression tests and the split cylinder tests conducted in accordance with CSA/CAN Standard A23.2 (1994) are shown in Table 3-2 and Table 3-3 for the modified push-apart tests and pull-apart tests, respectively.

3.4.2 CFRP Sheets

The CFRP sheets used in these tests were Replark type 20 single layered unidirectional tapes supplied by Mitsubishi Canada Ltd. Coupon tests were carried out in accordance with ASTM Standard D 3039/D 3039M (1995) to determine the material properties of the CFRP sheets. The average result from five 300 mm long and 25 mm

wide specimens was used. The applied load and the strains in the sheet were monitored and recorded for the duration of the tests. Strain gauges were applied in the direction of the fibres and in the direction perpendicular to the fibres in order to plot the stress-strain curve for the sheet and hence determine the modulus of Elasticity of the sheet and also to measure the lateral Poisson's ratio. Although the sheets are unidirectional, ASTM procedure advises that Poisson's ratio be measured. The value of the modulus of elasticity and Poisson's ratio will be used in the numerical model that will be discussed in detail in Chapter 5. The ultimate stress, Poisson's ratio, and modulus of elasticity of the manufactures specifications and the coupon tests are shown Table 3-7. The thickness of the tested CFRP sheet was 0.38 mm for both test series.

3.4.3 Epoxy

The primer and resin used were both a two-component, high-modulus, and high-strength epoxies in which the two components are mixed at a 2:1 ratio by weight. The putty used was a two-component epoxy mixed at a 1:1 ratio by weight. Mitsubishi Canada Ltd supplied the primer, resin, and putty. The modulus of Elasticity (E), Poisson's ratio (ν), and the ultimate tensile strength (f_{ct}) of the materials obtained from the manufactures specifications, is listed in Table 3-7.

3.4.4 Steel

High-grade 10M rebars (Figure 3-3) were used in the modified push-apart tests to prevent any corner failure of the concrete specimen. 4 mm diameter plain steel bar stirrups were also used to separate the top and bottom 10M reinforcement. 25M deformed steel bars were used for the rebar in the pull-apart specimens. The stress in the bars was predicted to be much lower than the typical yield strength of these bars. The expected extension of the rebars under load was also negligible.

3.5 Surface Preparation and Bonding the FRP Sheets

The sheets were bonded to the concrete according to the manufacturer's recommendations and procedures. After grinding the concrete surface with a stone

wheel, the surface was cleaned and an epoxy primer applied to it in order to create a smooth flat bond surface. The primer was applied to concrete with a roller in the amount of 0.25 kg/m^2 . The same procedure was used for both test series.

In the P-series it was noticed that there were small voids in the surface. A layer of putty was applied after 24 hours, when the primer layer was no longer sticky, to fill the voids in the surface.

The resin was applied after 24 hours with a roller in the amount of 0.3 kg/m^2 after which the CFRP was bonded. The sheets were bonded in position within 10 minutes of applying the resin coating using a roller. Rolling continued until sheets were fully impregnated with resin. A plastic roller was used to smooth out the CFRP sheet surface. A resin topcoat in the amount of 0.2 kg/m^2 was then applied after 30 minutes to the entire sheet. The specimens were left for 24 hours to dry after which the specimens were left to cure in room temperature for a week until tested.

Table 3-1 Modified push-apart test variables

Specimen	L (mm)	w (mm)	L/w	f'_c (MPa)
S1	75	200	0.38	51.1
S2	50	150	0.33	50.4
S3	100	150	0.67	51.3
S4	150	100	1.50	50.4
S5	150	150	1.00	51.1

Table 3-2 Modified push-apart concrete compression and split cylinder test results

Specimen	f'_c (MPa)	d (mm)	L (mm)	P (kN)	$(f_{sp})_{av}$ (MPa)
S1, S3	51.3	152.5	305.0	326.0	4.1
S5	51.1	152.7	305.0	310.0	4.3
S2, S4	50.4	152.4	305.0	284.0	4.1

Table 3-3 Pull-apart test concrete compression and tensile split cylinder test results

Specimen	$(f'_c)_{av}$ (MPa)	d (mm)	L (mm)	P (kN)	f_{sp} (MPa)	$(f_{sp})_{av}$ (MPa)
P1- P10	46.9	151.8	305	247.3	3.4	3.25
		152.1	304	225.2	3.1	
P11- P20	47.3	151.7	305	283.4	3.9	3.75
		152.4	305	262.8	3.6	
P21- P30	46.4	151.3	305	275.4	3.8	3.55
		151.9	304.5	239.8	3.3	

Table 3-4 Pull-apart test variables

Specimen	L (mm)	w (mm)	a (mm)	b (mm)	f'_c (MPa)	Remarks
P1	45	100	---	---	46.9	Estimating the effective bond length (No anchor sheets)
P2	60	100	---	---	46.9	
P3	75	100	25	50	46.9	
P4	90	100	---	---	46.9	
P5	105	100	---	---	46.9	
P6	120	100	---	---	46.9	
P7	135	100	---	---	46.9	
P8	150	100	---	---	46.9	
P9	50	150	25	25	46.9	Length effect (Anchor sheet at one end)
P10	100	150	25	25	46.9	
P11	150	150	25	25	47.3	
P12	150	25	25	75	47.3	Width effect, including P11 (Anchor sheet at one end)
P13	150	50	25	75	47.3	
P14	100	50	0	75	47.3	Anchor sheets at both ends and above the tested sheet
P15	100	50	25	75	47.3	
P16	100	50	50	75	47.3	
P17	100	50	75	75	47.3	
P18	100	50	25	50	47.3	
P19	100	50	25	25	47.3	
P20	100	50	---	---	47.3	
P21	100	50	0	75	46.4	
P22	100	50	25	75	46.4	
P23	100	50	50	75	46.4	
P24	100	50	75	75	46.4	
P25	100	50	25	50	46.4	
P26	100	50	25	25	46.4	

Table 3-5 Push-apart test concrete mix for 1.0 m³

water/cement	Water (kg)	Cement (kg)	Sand (kg)	Gravel (kg)
0.57	200	350	700	1055

Table 3-6 Pull-apart test concrete mix for 1.0 m³

water/cement	Water (kg)	Cement (kg)	Sand (kg)	Gravel (kg)
0.54	240	442	921	790

Table 3-7 Material properties

	E (GPa)	ν	f_{ct} (MPa)	Remarks
Concrete	32.1**	0.15	2.6	Push-apart test
	30.8**	0.15	2.3	Pull-apart test
CFRP	230	0.26	3400	Manufactures specifications *
	45	0.26	422	Coupon tests
Adhesive	2.8	0.35	42	Manufactures specifications*

* Based on fibre strength

** Based on 45% secant modulus

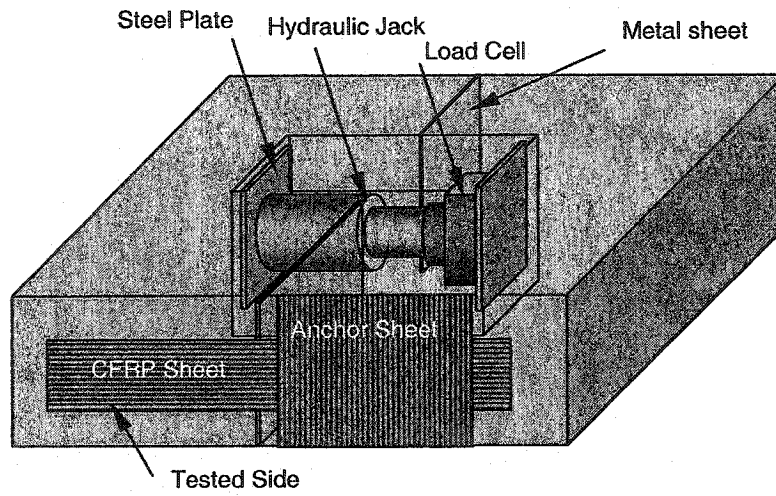


Figure 3-1 Orthographic of the modified push-apart test

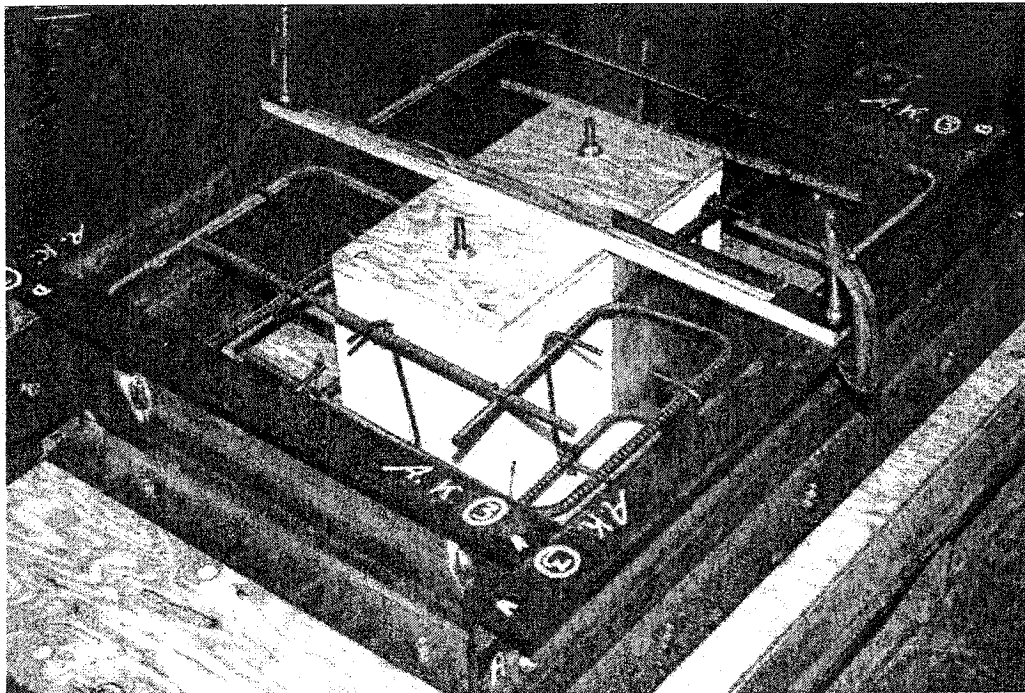


Figure 3-2 Modified push-apart test steel form and cage details

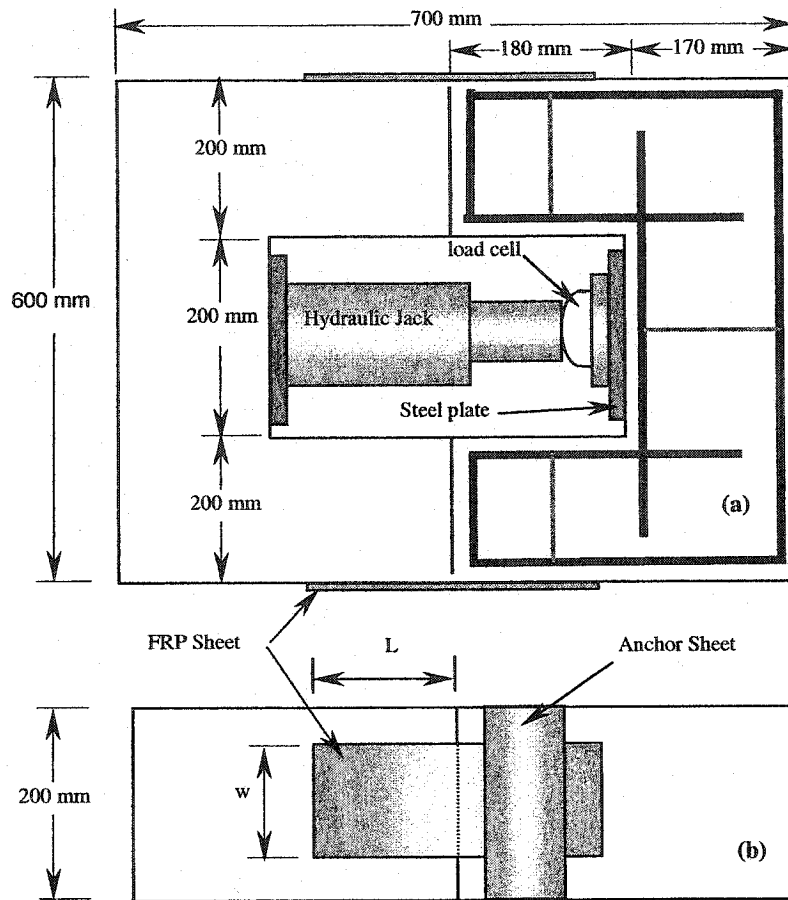


Figure 3-3 Modified push-apart test (a) plan view (b) side view

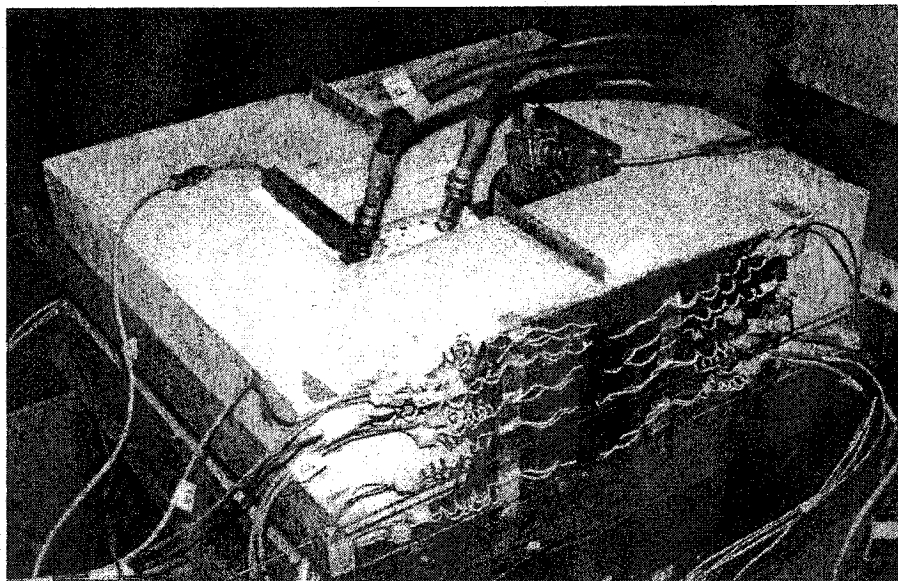


Figure 3-4 Modified push-apart test set-up and instrumentation

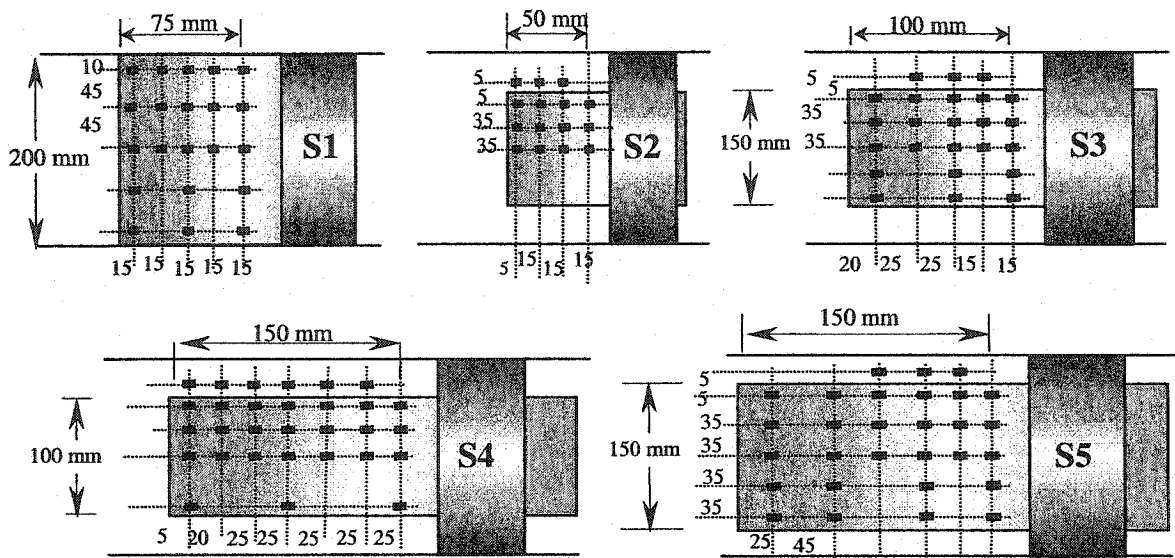


Figure 3-5 S-series strain gauge locations on CFRP sheets and concrete

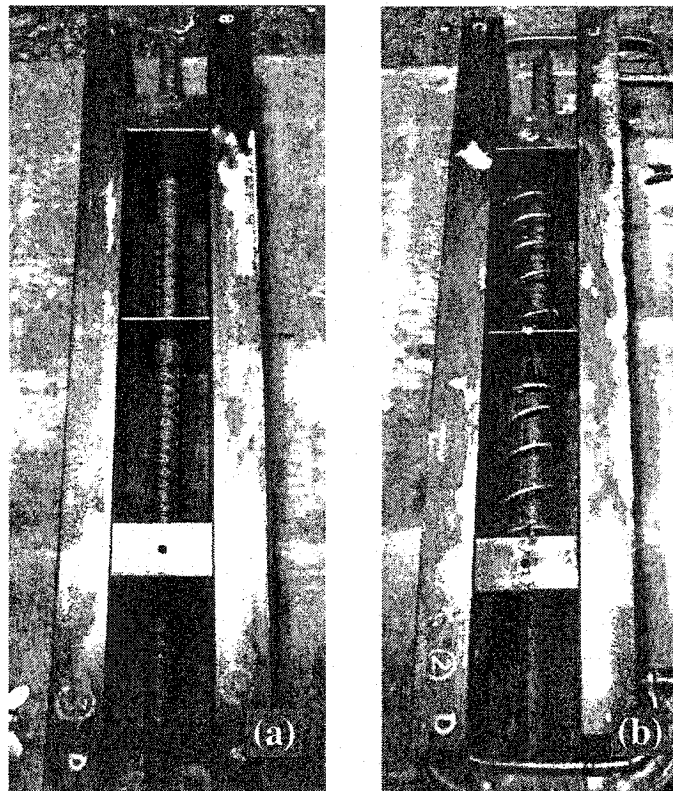


Figure 3-6 Pull-apart specimen forms and reinforcement (a) without spiral (b) with spiral

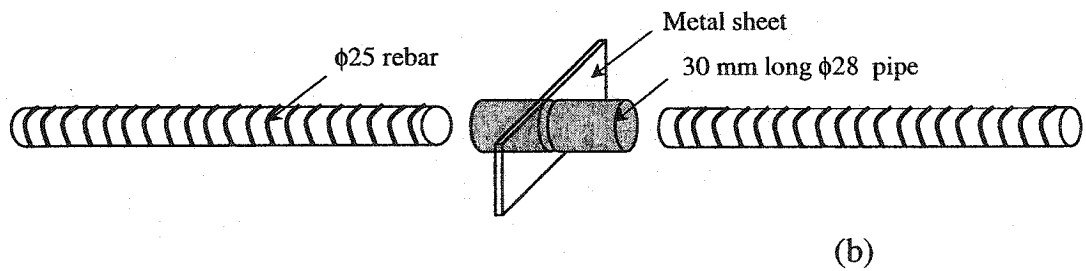
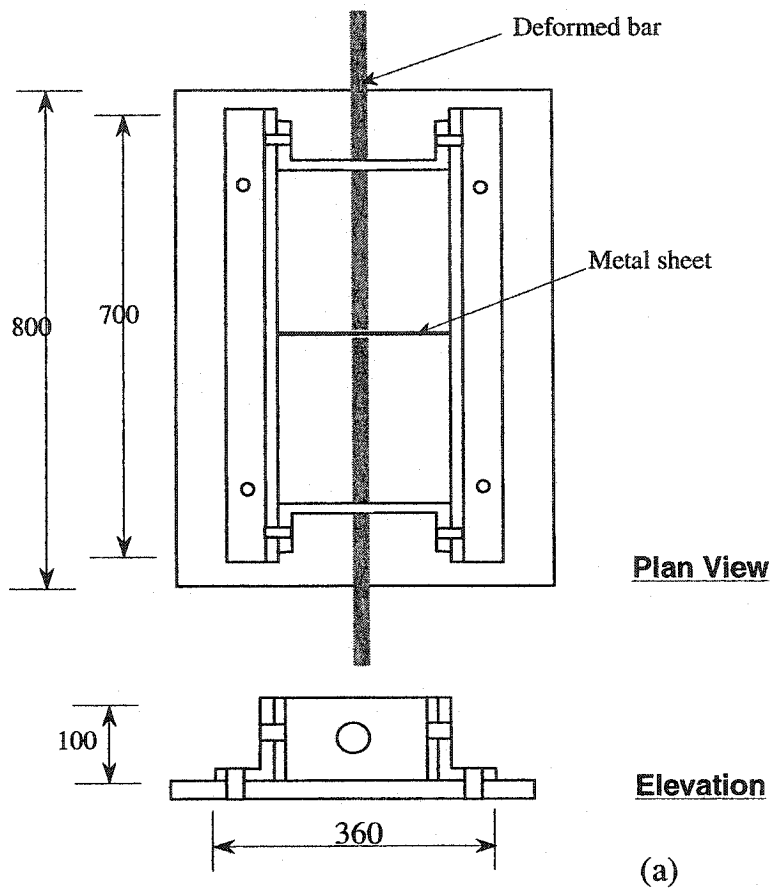


Figure 3-7 Pull-apart specimen (a) Steel form (b) bars alignment arrangement

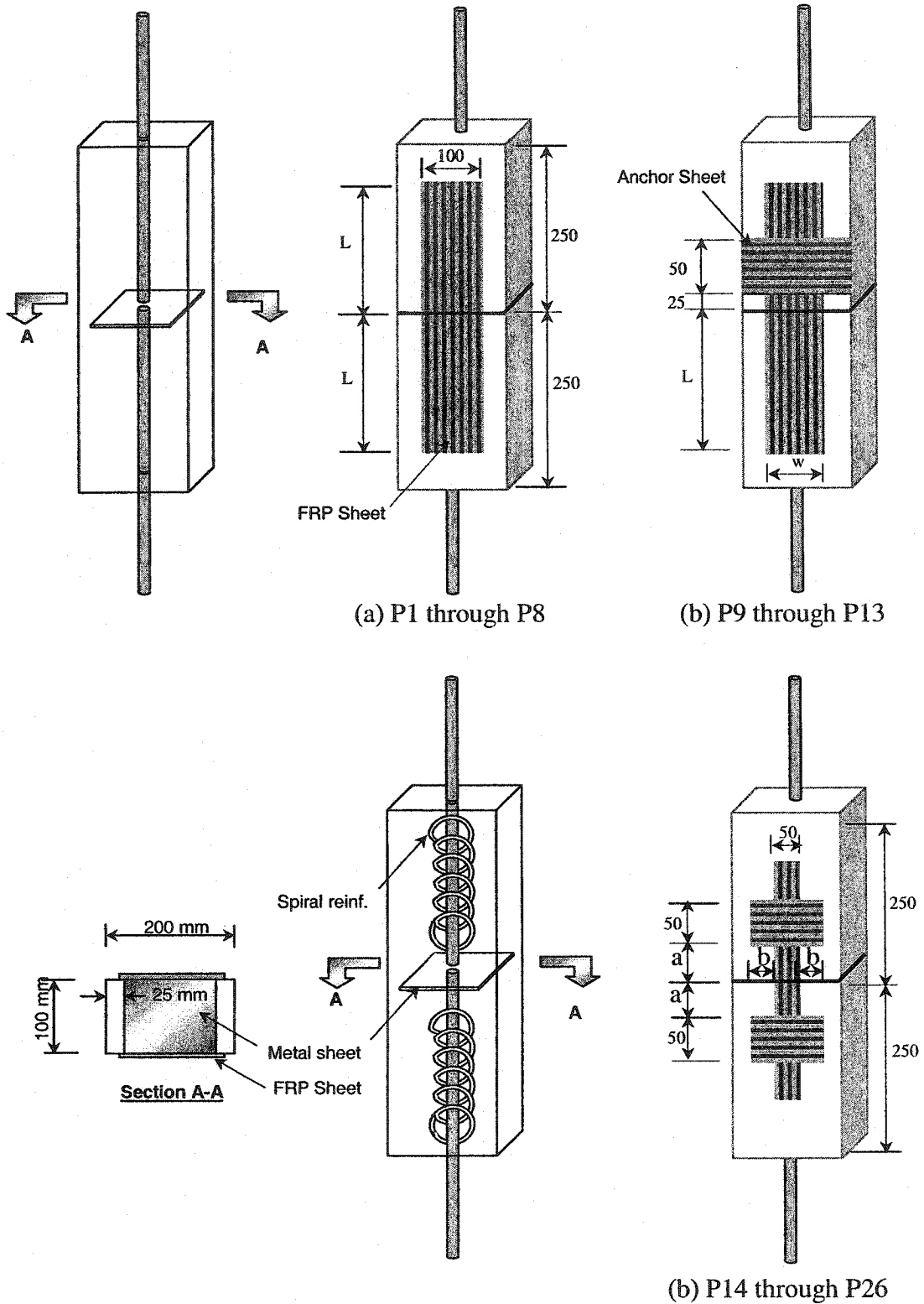


Figure 3-8 Pull-apart specimen dimensions, details, and sheet and anchor configurations

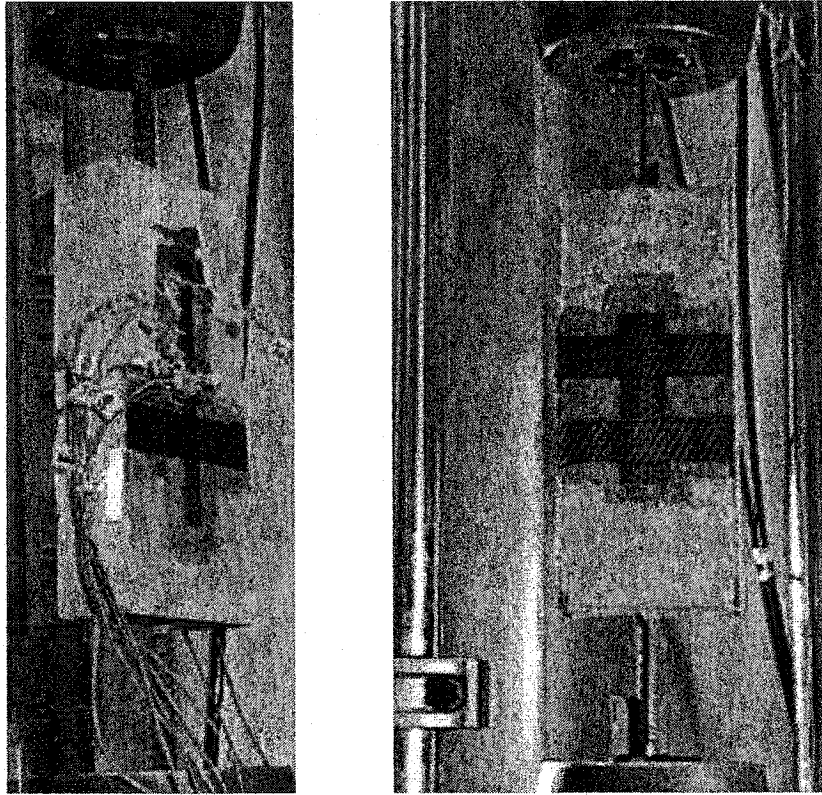


Figure 3-9 Pull-apart test set-up and instrumentation

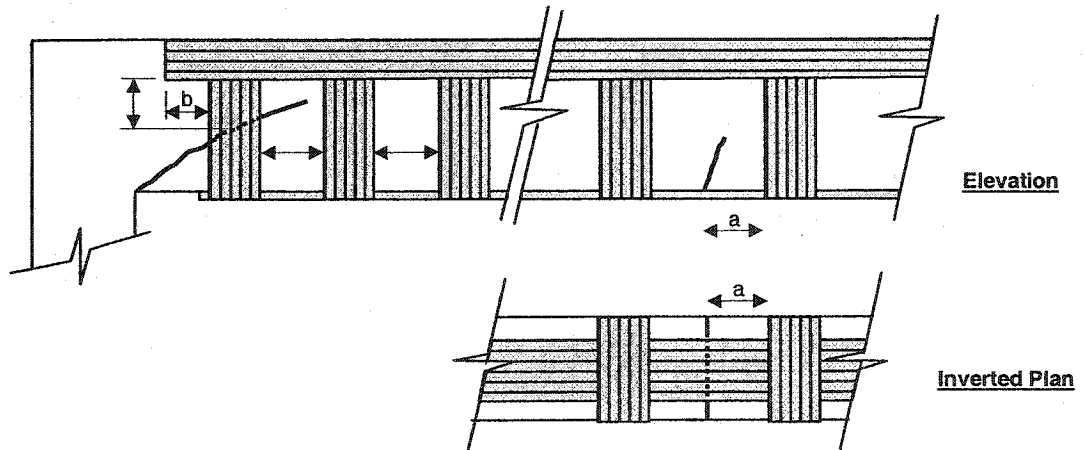


Figure 3-10 Concrete girder strengthened in flexure and shear with FRP sheets

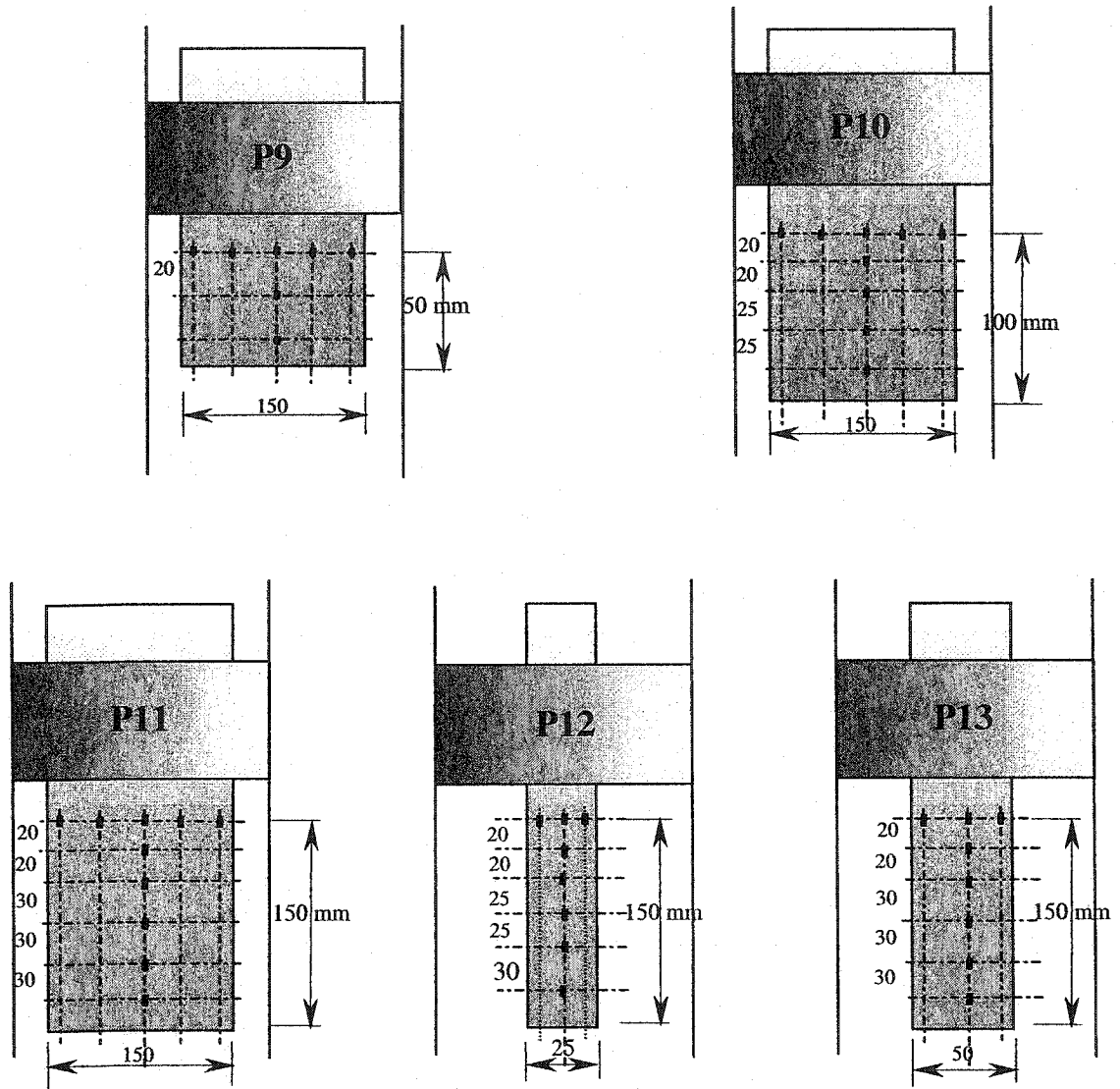


Figure 3-11 Strain gauge locations and sheet dimensions for specimens P9 to P13

4 TEST RESULTS, OBSERVATIONS, AND DISCUSSION

4.1 Introduction and Overview

Two series of concrete specimens bonded with CFRP sheets were tested in the University of Alberta structural laboratory. The first series, S-series, employed a modified push-apart procedure and the second series, P-series, employed a pull-apart procedure. Specimen description, instrumentation, variables and the material properties for each test series were discussed in detail in Chapter 3. This chapter presents and discusses the test results and the observed behaviour of the specimens in both series.

Besides implementing the modified push-apart test method, specimens S2, S3, and S5 in the S-series investigated the CFRP bond length effect (L), specimens S4 and S5 investigated the bond width effect (w), and finally specimens S1, S3, and S4 investigated the length to width, L/w , ratio effect on the bond behaviour.

The P-series, which employed a pull-apart procedure, consisted of 26 specimens. Specimens P1 through P8 in the P-series implemented a procedure to determine the effective bond length. Specimens P9 through P11 studied the bond length effect while specimens P8, P11, P12, and P13 investigated the bond width effect on the bond behaviour. Specimens P9 through P13 had the same variables as specimens S1 through S5 in order to study the effect of the test method on the results.

The effect of anchor sheets on the bond behaviour included specimens P14 through P26. The specimens had different anchor configurations designed to study the anchor location when having the anchor sheet bonded above or below the tested sheet. The effect of the distance of the anchor sheet from the crack "a" and the effect of the anchor sheet extension beyond the tested sheet "b" on the bond behaviour were also studied.

4.2 Failure Mechanism

4.2.1 Modified Push-Apart Test Failure Mechanism

As described in detail in Chapter 3, the load was applied to all specimens in the S-series with a 220 kN capacity hydraulic jack. The load was applied monotonically in stroke control until failure and the load together with the displacements and strains were read directly from a data acquisition system.

Specimen S2 had a unidirectional CFRP sheet bond length of 50 mm on each side of the crack. An anchor sheet was applied to one side of the tested sheet. The sheet in S2 was mistakenly cut in the wrong direction causing the fibres to be in the direction of the crack instead of perpendicular to the crack. This caused the sheet to fail as soon as the concrete cracked. The expression “joint” used here refers to the assembly of concrete, adhesive, and FRP sheet. The specimen was then clamped and CFRP sheets bonded above the initial fractured sheets. The specimen in this case became a pre-cracked specimen and the CFRP sheet became bi-directional.

All specimens failed by debonding type failure, with a portion of the concrete shearing near the crack, and forming a wedge of concrete bonded to the FRP sheet. The metal sheet placed in the specimen arm to initiate the crack was at a distance averaging 18 mm from the bond face of the concrete. This caused a stress concentration in the concrete at this neck area, which caused the formation of the concrete wedge. Bizindavyi and Neale (1999) reported a similar three-dimensional mode of failure in the direct pull concrete block occurred at the loaded end. The crack propagation and the formation of the failure surface are shown in Figure 4-1. As the load increases, micro cracks appear, which then propagate to form shear cracks. The failure surface close to the crack was inclined at an angle ϕ in all the specimens, as shown in Figure 4-2. The angle ϕ ranged between 34° and 41.6° , and averaged 38° as shown in Table 4-1. This initial failure zone formed close to the failure load and this area of concrete stayed bonded to the CFRP sheet after failure occurred, as shown in Figure 4-3b. As a specimen reaches the failure load, the failure zone propagates parallel to the concrete surface rapidly with no increase in

load, and the amount of concrete bonded to the remaining portion of the sheet is an irregular thin layer as shown in Figure 4-3b.

Table 4-1 lists the initial failure zone dimensions for all specimens. The initial failure length is almost the same in all specimens ($c \approx 38$ mm) except for specimen S1, which had a CFRP sheet covering the full specimen width ($c = 61$ mm). This variance in behaviour points out the need to study the effect of the FRP sheet width relative to the specimen width on the failure mechanism and the behaviour of the joint in general. The average bond strength τ_b listed in Table 4-1 was calculated by

$$\tau_b = \frac{P_u}{2L \cdot w} \quad (4.1)$$

in which, P_u is the measured ultimate load in the load cell, and L and w are the CFRP sheet length and width, respectively, in the test zone.

4.2.2 Pull-Apart Test Failure Mechanism

As described in detail in Chapter 3, the specimens of the P-series were placed in a MTS universal-testing machine in a vertical position. The load was applied monotonically in stroke control until failure and the load together with the displacements and strains were read directly from a data acquisition system. Specimens P1 through P13 are a subset of specimens with variable bond length and width. Specimens P14 through P26, which had anchor sheets on both sides of the tested sheet but constant bond length and width, are considered a different subset.

The results from specimens P6 and P20 were inconsistent with the results from all other specimens in the series. The reason for the relatively high load capacity in these specimens was unknown but could be due to better concrete surface condition that limited the use of putty. These specimens were, therefore, discarded from the analysis.

Failure started in all the specimens in the first subset, P1-P13, with the concrete cracking at the metal sheet location (the crack initiator location), then shear cracks

appeared and gradually increased in length until the CFRP sheet debonded. Debonding started at the crack location and progressed towards the free end of the sheet. Ultimate load occurred when the sheet was totally debonded in a sudden zip type failure. The crack in the centre of all the specimens opened at one face only until failure, as shown in Figure 4-4. The face that had the crack opening was eventually the face that had the bond failure.

The amount of concrete attached to the sheet at the crack location after failure ranged from a very thin layer to a chunk 20 mm wide and inclined 42° at the crack location. A typical post failure mode for specimens P1 through P13, except for specimen P3, is shown in Figure 4-5. The distance of the metal sheet from the concrete surface to which the CFRP sheets were bonded (d_1) averaged 18.8 mm in the S-series and was nil in the P-series. The distance d_1 affected the amount of concrete attached to the CFRP sheet after failure. The S-series type failure simulates a failure at which the crack is developed after bonding the CFRP sheets while the P-series simulates a failure at which the CFRP sheets are bonded to a pre-cracked concrete surface.

4.2.3 Anchor Sheets

Specimen P3 had an anchor sheet placed 90° to the load direction at one end of the tested sheet, partially covering the test sheet and partly bonded to the concrete beyond the test sheet end. The specimen failed at the anchored side of the sheet, which was 70 mm in length compared to an unanchored side of 80 mm. As the load increased, the anchor was torn at the location where the tested sheet ends, as shown in Figure 4-6. This caused the effective width of the anchor to be 50 mm. This failure mode showed that an extra 10 mm in length was stronger than having a 50 mm wide anchor perpendicular to the sheet. Further investigation to verify this observation is required.

The second subset specimens P14 through P26 that were intended to study the anchor sheet effect on the bond behaviour exhibited uniformly the same failure mechanism. Failure started with the concrete cracking at the metal sheet location. Shear cracks then appeared and gradually increased and widened. Debonding started in

the tested sheet at the crack location then propagated towards the end of the sheet. Anchor debonding started over the area in contact with the tested sheet and occurred simultaneously as the tested sheet debonded. As the centre crack widened, the anchor appeared to stretch towards the crack location, as shown in Figure 4-7. The debonding in the anchor then propagated towards one of its edges at about 20% of the ultimate load.

The location of the anchor sheet being above or below the tested sheet did not show any change in the failure mode. For example Figure 4-8 shows the failure modes of specimen P15 with anchor sheet above the tested sheet and P22 with anchor sheet below the tested sheet. The anchor sheet in specimens P17 and P24 was torn at the location where the tested sheet ends, as shown in Figure 4-9. In this case the tested sheet debonded from the concrete. The effective width of the anchor corresponded to the part of the anchor directly above or below the sheet for specimens P14 through P19 and P21 through P26, respectively.

It is concluded from the previous discussion that the width of the perpendicular anchor sheet that is not directly above or below the tested sheet is ineffective. It is also observed that placing the anchor sheet above or below the test sheet makes no difference to the failure mechanism.

4.3 Load Transfer Process

Strain gauges were applied to the CFRP sheet surface along the length and across the width of the sheet in the modified push-apart tests and five of the pull-apart tests, as detailed in section 3.2.2 and section 3.3.2, respectively. The strain gauges were applied in order to study the load transfer process along the bond length and across the bond width of the CFRP sheet, which would provide a better understanding of the bond behaviour between FRP sheets and concrete.

4.3.1 Load Transfer Along the CFRP Sheet Length

Figure 4-10 through Figure 4-14 show the average strain distributions at the centre of the CFRP sheets along the length at different load levels for specimens S1 through S5,

respectively. The figures show that as the load increase the strain values increase across an increasing portion of the bond length, indicating that more bond area resists the load as it increases.

The strain distributions along the length of specimens P9 through P13 are shown in Figure 4-15 through Figure 4-19, respectively. The strain distribution along the length shows a change in trend as the load increases. The strain distribution is concave at lower loads then transforms into a convex shape as the load reaches 70% of the ultimate load. All specimens of the P-series showed this trend except for specimen P9, which did not have enough strain gauges to show it. The same observation was made in the S-series. The change in the strain distribution trend with a large increase in the strain values is similar to a snap-through behaviour and indicates debonding of the CFRP sheet. This observation reflects on the comparison between the strain distributions of different specimens, where the strain distribution shape and hence values at various locations will depend on the load level at which the comparative strain distributions are at.

The term transfer length is defined as the distance from the crack location to the point where the strain is negligibly small. Because of the limited number of strain readings along the CFRP sheet length, the transfer lengths were reasonably estimated from Figure 4-10 through Figure 4-19. Figure 4-20 shows the load vs. the estimated transfer length for specimens S2, S3, and S5 with the same CFRP sheet bond width of 150 mm. The figure shows that the transfer length increases as the load increases. The increase in the transfer length at the lower load levels was almost constant but the rate then increased rapidly at the higher loads for specimens with bond lengths above the effective length, as seen by the steeper slopes for S3 and S5 in Figure 4-20. The same behaviour occurred in the P-series as shown in Figure 4-21, which shows the load vs. the transfer length for specimens P9, P10, and P11 having the same bond width of 150 mm. This behaviour, the transfer length rate increasing as the load increases, indicates an increase in the CFRP sheet debonding rate, which leads to the zip action type failure.

Bizindavyi and Neale (1999) stated that there exists an initial transfer length that is constant for all load levels lower than the initial cracking load. They stated that the initial cracking load ranged from 55 % to 68% of the ultimate tensile capacity of the FRP sheets depending on the number of plies. This statement could not be verified either from their published test results or the test results published in this research considering the limited number of strain readings along the CFRP sheet length.

In order to investigate the load transfer mechanism along the length in detail, the average bond strength in the centre of the CFRP sheet along the bond length for specimen S5 is shown in Figure 4-22 as a function of the relative load level, which is the current load divided by the ultimate load (F/F_{max}). The average bond stress (τ_b) was calculated by

$$\tau_b = \frac{E_p t_p (g_i - g_j)}{\Delta L_{i-j}} \quad (4.2)$$

in which g_i and g_j are the strain values at points i and j , respectively, ΔL_{i-j} is the distance between i and j , and E_p and t_p are the modulus of elasticity and thickness of the CFRP sheet, respectively. A schematic sketch and derivation of equation (4.2) are shown in Figure 4-23. The distances between the strain gauges for S5, shown in Figure 3-5, were divided into segments. The segment numbering and location along the CFRP sheet length are indicated in the legend of Figure 4-22. Line (1) in the figure identifies the location where τ_b in segment 2 increases as τ_b in segment 1 decreases. Line (2) and (3) also show the same behaviour for segments 3 and 2, and 4 and 3, respectively. The decrease in τ_b in a region corresponds to debonding taking place and the build-up of τ_b in the adjacent region indicates that the load is transferring to that region. The same behaviour was observed for the P-series as shown in Figure 4-24. This figure shows the average bond strength distribution plotted against the relative load level for segments along the CFRP sheet bond length of specimen P10.

The negative strain gradient that appears within 30 mm from the crack at 65% of the ultimate load (see Figure 4-22) is attributed to the concrete active crack zone shifting relative to the strain gauge location as the load increases. Similar behaviour was

observed in all S-series specimens. P-series specimens did not show such behaviour because there was no flexural shear crack zone in these specimens.

From the previous discussion it is concluded that the load is transferred from the crack location towards the free end of the CFRP sheet and that the bonded area of the sheet resisting the load increases as the load increases. Debonding takes place as the bond strength is exceeded in the bonded area resisting the load. The bonded area then shifts away from the crack and moves towards the free end of the sheet, which marks the debonding propagation. The rate of debonding increases as the ultimate load is approached. This behaviour causes the zip action that is observed in these kinds of tests, but more importantly it indicates that an “effective bond length” that does not necessarily start at the crack is perhaps best used to estimate the bond strength.

4.3.2 Load Transfer Across the CFRP Sheet Width

Figure 4-25 through Figure 4-29 show the strain distribution across the CFRP sheet width at the crack location for specimens S1 through S5, respectively. The figures show that the strain distribution along the sheet width did not have a defined trend as a whole, where the strain values at the edge were always higher compared to those at the centre of the sheet while the strain values half way between the centre and the edge of the sheet fluctuated relative to that at the centre. At the crack location, the increase in the average strain value at the edge of the sheet over that at the centre of the sheet at ultimate load ranged from 9.3% in S1 to 134% in S2 and averaged 58% for all five specimens. The total average value of the difference between the edge and centre strain was 39%, excluding S2, which had a CFRP sheet with fibres parallel to the crack bonded below the tested sheet.

Figure 4-26 shows the strain distributions at different load levels along half the width of the CFRP sheet in specimen S2 at distances 0, 15, 30, and 45 mm from the crack location. The figure shows that the edge strain was consistently higher than the centre strain throughout the sheet length and at all load levels.

The strain distributions along the width of specimens P9 through P13 are shown in Figure 4-30 through Figure 4-34, respectively. As in the S-series, the strain distribution along the width of the sheet did not have a defined trend as a whole but the strain value at the edge of the sheet was consistently larger than that in the centre of the sheet for all specimens. At the crack location, the increase in the average strain value at the edge of the sheet compared to that at the centre of the sheet at the ultimate load ranged from 8% in P13 to 48.6% in P11 and averaged 31% for all five specimens.

It is not simple to back calculate the stress distribution from the strain values for a number of reasons. The shear lag effect complicates the picture and may interfere with accuracy of the strain gauges located near the edges of the sheet. Debonding may not occur evenly across the sheet width. But the trend is nonetheless true as will be shown later using numerical analysis.

Figure 4-35 shows the CFRP sheet width plotted against the strain difference between the edge and the centre of the sheet at the crack location at different load levels. The figure was developed using the results from specimens S4, S5, P11, P12, and P13 that had the same bond length of 150 mm. Least squares prediction lines were developed using the built in option in MS EXCEL (1999) program for load levels of 50%, 70%, and 100% of the ultimate load. The least squares prediction lines show that the difference in strain between the edge and centre of the CFRP sheet increases as the width of the sheet increases. This behaviour is further studied with the 3D numerical model detailed in Chapter 6.

Figure 4-36 shows the strain distributions at both the sheet centre and at the edge along the length at various load levels in specimen S4. The shaded areas in the figure show that the difference between the strain values at the edge of the sheet and its centre increases as the load increases. The difference is also greater near the crack than away from the crack location.

Figure 4-37 and Figure 4-38 show the average bond stress (τ_b) distributions across the CFRP sheet width at the crack location for specimens S1 and S4, respectively.

Specimens S1 and S4 had different FRP sheet lengths and widths and were chosen as examples to illustrate a behaviour. The charts legends show the distance from the CFRP sheet centre. Equation (4-2) was used to calculate the values of τ_b in the charts. The figures show that τ_b distribution in the CFRP sheets develops after the concrete specimen cracks. This occurred at around 20% of the ultimate load for all specimens except for S2, which was pre-cracked. The τ_b distribution in specimen S2 started as soon as the load was applied as shown in Figure 4-39. Closer to the crack, the magnitude of τ_b at the edge of the sheet is higher than that at the centre in all specimens. The τ_b distributions show several trend changes as indicated by the vertical dash lines, where the sudden change in the trend indicates debonding.

Figure 4-40 and Figure 4-41 show the average bond stress (τ_b) distributions across the CFRP sheet width at the crack location for specimens P10 and P11, respectively. Specimens P10 and P11 had different bond widths and were chosen as an example to illustrate a behaviour. Equation (4-2) was also used to calculate the values of τ_b in those charts. The figures show that τ_b distribution in the CFRP sheets develops as soon as the load is applied, which is similar to the behaviour of specimen S2 that was pre-cracked. The crack initiator metal sheet placed in the P-series specimens causes the concrete specimen to perform as pre-cracked. The figures also show that there are trend changes in the τ_b diagram at the locations shown by vertical dashed lines. The sudden drop in the τ_b diagram indicates debonding of the sheet, where the test was in stroke control.

From the previous discussion it is concluded that the strain values at the edge of the CFRP sheet were higher than those at the centre throughout the sheet length and at all load levels. The difference in strain increases as the load increases and as the distance from the crack decreases. The difference between the strain values at the edge and those at the centre of the sheet was 35% on average at ultimate load at the crack location. The difference also appeared to increase as the sheet width increases.

4.4 Bond Length

4.4.1 General Discussion

The modified push-apart specimens S2, S3, and S5 had the same bond width of 150 mm, but had bond lengths of 50, 100, 150 mm, respectively. Figure 4-42 shows the load response plotted against the deflection for these specimens. It was observed from the curves that the specimens had the same trend except for specimen S2, which was pre-cracked and showed a slightly softer behaviour. The ultimate capacity also increased with increasing the bond length but to a certain limit. This is apparent from specimens S3 and S5 with bond lengths of 100 mm and 150 mm, respectively, where there was no significant change in the ultimate capacity with the increase in bond length. It is concluded that the bonded length beyond a certain distance from the crack causes no increase in the ultimate capacity of the joint. This distance is referred to as the effective bond length. This conclusion is similar to the findings of other researchers in the literature (Drimoussis and Cheng, 1994, Chajes et al., 1996, Alexander and Cheng, 1997, Brosens and Van Germert, 1997, Maeda et al., 1997, Horiguchi and Saeki, 1997, Täljsten, 1997).

For a given configuration (sheet width, stiffness, surface conditions, etc.), ultimate strength develops over this effective length, and then debonding propagates through the rest of the sheet without a limit. The value of the effective length depends on many variables of which the most significant, according to the literature, are the sheet stiffness and the concrete tensile strength (Holzenkämpfer, 1994, Neubauer and Rostásy, 1997, Chen and Teng, 2001). It appears from Figure 4-42 that the value of the effective bond length in the S-series with $w = 150$ mm is between 50 mm and 100 mm. Taking the effective bond length of 100 mm for specimens S4 and S5 resulted in τ_b equal to 2.13 MPa and 1.79 MPa, respectively. The difference in τ_b between S3 and S5 having bond lengths of 100 and 150 mm, respectively was 5% and the overall average τ_b value was 2.06 MPa. The overall average τ_b for conventional push-apart tests studied by Drimoussis and Cheng (1994), and Alexander and Cheng (1997) were 2.6 and 2.3 MPa, respectively. The difference in the τ_b values is due to the different concrete strengths, CFRP stiffness, and test specimens configurations used.

Figure 4-43 shows the load-displacement responses for the P-series specimens P9, P10, and P11 with bond lengths of 50, 100, and 150 mm, respectively. The specimens had the same CFRP sheet bond width of 150 mm. The curves show the same trend but with P10 and P11 having higher ultimate capacity than P9. There is no significant change in the ultimate load when increasing the bond length from 100 mm to 150 mm, which is similar to the findings from the S-series.

Figure 4-44 shows the strain distribution in the centre of the CFRP sheet along the bond length for specimens S2, S3, and S5 at 20 kN. There was no significant difference between the strain distribution of specimens S3 and S5. This indicates that the strain distribution and magnitude does not change on increasing the bond length beyond the effective bond length. However, the strain values at the crack location were higher for specimen S2 with a smaller bond length. This indicates that specimens S3 and S5 with larger bond lengths had better stress distributions.

Specimens P9, P10, and P11 had the same variables as those in S2, S3, and S5. Figure 4-45 shows the strain distribution in the centre of the CFRP sheet along the bond length at 20 kN for these specimens. The figure shows that the P-series had the same behaviour as the S-series but with different strain values.

4.4.2 Effective Length Evaluation

Conclusions from the literature and the current research showed the importance of evaluating the effective bond length in order to assess the average bond strength that is used in strengthening and design calculations. An experimental procedure, explained in section 3.3.3, was proposed to estimate the effective bond length for FRP sheets bonded to concrete. The procedure is also adopted in Annex J in the CSA-S806-02 (2002). Specimens P1 through P8 investigated the validity of the proposed procedure.

The load response plotted against the deflection for specimens P1 through P8, with the exception of P6 as discussed in section 4.2.2, are shown in Figure 4-46. The curves show the same trend but with different ultimate loads and displacement values. Specimen P7 showed a slightly softer behaviour and a reduced ultimate load due to the

existence of air voids under the CFRP sheets that created discontinuity in the glue joint and weakened the bond strength by reducing the area of adhesive. Figure 4-46 shows that the maximum displacement increases as the bond length increases, which maybe interpreted as an increase in ductility of the joint as the bond length increases.

The ultimate loads achieved are plotted against the bond lengths for specimens P1 through P8 in Figure 4-47. A moving average trend line was added using a built-in option in program MS EXCEL (2000) and a linear approximation was plotted manually. The linearized moving average trend line is bilinear with an inclined segment and a horizontal segment. The intersection of the segments indicates the location of the effective bond length, which is estimated to be 80 mm. This value is close to the 75 mm estimated value used in the selection of the tested bond lengths (Equation 3-1).

Based on the previous discussion, refinements to the proposed procedure to determine the value of the FRP sheet effective bond length are recommended. Due to the relatively high variability in bond related test results, taking the average of two tests for each bond length is proposed. Together with the expected ultimate load trend of previous and following bond lengths, any exceptional test result can be neglected and therefore safeguard for unexpected results. The FRP sheet bond lengths should be taken as kL_{ea} , where L_{ea} is the estimated bond length value obtained from equation (8-11), as discussed in Chapter 8. The length factor, k , is proposed to range from 0.6 to 1.6 with increments of 0.2 in order to optimize the number of specimens tested. Twelve specimens would be tested with two specimens for each variable in order to evaluate the effective bond length.

4.5 Bond Width

The load vs. displacement responses for specimens S4 and S5 with bond widths of 100 and 150 mm, respectively and with equal bond lengths of 150 mm are shown in Figure 4-48. The figure shows that increasing the bond width in specimen S5 by 50% over that of specimen S4 (from 100 mm to 150 mm) increased the ultimate load by 25.31%. This resulted in the average bond strength decreasing as the sheet width increased. This conclusion is similar to that of Ueda et al. (1999), which was discussed in

section 2.7.2. Their explanation was that the failure zone was wider than the width of the FRP sheet. This was also observed in the S-series but was only evident for the initial failure zone, which is the distance from the crack to the end of the chunk of concrete attached to the CFRP sheet (Figure 4-1d).

The initial failure zone was different in each test series as discussed in section 4.2.2. Increasing the width of P11 by 50% over that of P8 (from 100 to 150 mm), which is similar to that in the S-series, increased the ultimate load by 52.6%. This resulted in no significant change in the average bond strength as the bond width increased. This conclusion is different than that from the S-series and is similar to the findings of Brosens and Van Gemert (1999) and De Lorenzis et al. (2000) also discussed in section 2.7.2. Figure 4-48 also shows that the stiffness of the joint increased as the bond width increased.

Figure 4-49 shows the load-displacement response for specimens P12, P13, P8, and P11 with bond widths of 25, 50, 100, and 150 mm, respectively and having the same bond length of 150 mm. The figure shows that the overall stiffness of the joint increased as the CFRP sheet width increased, which is similar to the findings in the S-series. Figure 4-50 shows the CFRP sheet bond width vs. ultimate load for the same specimens. The figure shows that the ultimate load increases as the bond width increases. The figure also shows the sheet bond width plotted against the average bond strength. The average bond strength in the figure was calculated from equation (4-1). The diagram shows that increasing the bond width decreases the average bond strength to a certain limit at which the bond strength stabilizes with the increase in the bond width. This indicates the existence of an effective bond width beyond which no increase in the average bond strength is obtained. This effect has been studied in the parametric study that is detailed in Chapter 6.

The strain distributions in the centre of the CFRP sheets along the bond length of specimens S4 and S5 at different load levels are shown in Figure 4-51. The chart shows that at the same load of 20 kN, the strain distribution in S4, with smaller bond width, had higher values than those in S5 and also had a larger transfer length. Changing the

load level (P/P_u) from 0.75 to 0.94 did not significantly change the transfer length of S4. By comparing the strain distributions for both specimens at P/P_u of 0.75 and 0.94 it is seen that the strain values and transfer lengths decreases as the sheet width increases. The difference between the strain values in each specimen also decreases at higher load levels.

Figure 4-52 shows the strain distributions in the centre of the CFRP sheets along the bond length of specimens P11, P12, and P13 with the same bond length of 150 mm. At the same load of 10 kN, specimen P12 with bond width, w , of 25 mm had higher strain values than P13 with w of 50 mm. At the same load level of 0.5, specimens P11 and P13 had no significant difference in the strain values. Specimens P11, P12, and P13 also had no significant difference at the same load level of 70% of the ultimate load.

The S-series shows that the average bond stress decreases as the bond width increases. The majority of research results in the literature are based on narrow sheet widths, mostly 25 mm (Chajes et al., 1996 and Bizindavyi and Neale, 1999). This results in the average bond stress in these research results to be higher compared to the sheets used in strengthening actual structures, which tend to be much wider than 25 mm. The previous discussion shows the need to investigate the effect of the bond width on the value of the effective length and the average bond strength. The width effect was investigated in this research through conducting a parametric study using numerical models. The numerical models and the parametric study are detailed and discussed in Chapters 5 and 6, respectively.

4.6 Test Method

The test methods considered here are the modified push-apart test method and the pull-apart test method. Both are indirect test methods. The effect of the test method will be discussed by comparing the results of the S-series and the P-series specimens that had similar variables.

Both test methods exhibited similar failure modes except that unlike the P-series, it was not clear which side would fail in the S-series. The amount of concrete that stayed bonded to the CFRP sheet after failure was different in each test method due to the difference in the crack initiator (metal sheet) distance from the concrete face to which the CFRP sheets were bonded. This caused the S-series to behave as an uncracked strengthened member while the P-series behaved as a pre-cracked strengthened member.

The load-displacement relationships for specimens in the two test methods with similar bond widths of 150 mm are shown in Figure 4-53. The load-displacement behaviour in the two methods were essentially the same but with different magnitudes.

The strain distributions along the length of the sheet from both the P-series and the S-series at different load levels are shown in Figure 4-54 through Figure 4-56. Although the strain gauge locations were different, there was no significant difference between the strain distributions in the two methods when the load levels were both above or both below 70% of the ultimate load level. When the load level in one method was above 70% the ultimate load while the other method was below that level, there appeared to be a difference in the strain distribution, as shown in Figure 4-54 at 20 kN and Figure 4-55 at 30 kN.

The test method effect was studied in detail in Chapter 7 using numerical models. Four test methods were investigated and compared. These test methods are the modified push-apart test, the pull-apart test, the direct pull test, and the push-apart test. The numerical models used are described and the results from the various test methods analysed and compared.

4.7 L/w Ratio

Specimens S1, S3, and S4 had the same bond area but different values of the ratio of bond length to bond width, L/w , in order to study its effect on the bond strength. Figure 4-57 shows the load-displacement behaviour for these specimens at mid span. From the curves it is apparent that as the L/w ratio decreases, the stiffness of the sheet

increases. The stiffness of the sheet is directly related to the sheet width rather than the bond area, where increasing the width by 50% (from 100 mm to 150 mm), and 33.3% (from 150 mm to 200 mm) increases the stiffness by 57.6%, and 26.9%, respectively.

Figure 4-57 also shows that S4 had a lower ultimate load than S1 and S3, which showed no significant difference in their ultimate loads. The low ultimate load in S4 is as result of the lower bond width of 100 mm compared to 150 and 200 mm in S1 and S3, respectively. A bond length of 150 mm, which is higher than the effective length, does not add to the ultimate load.

The strain distributions along the length of the CFRP sheets for the same specimens are shown in Figure 4-58. At a load, P , of 40 kN the strain values and the transfer lengths increase as the ratio L/w increases. The difference between the strain values and transfer length of specimens S3 and S4 are significantly more than those between specimens S1 and S3. The reason is attributed to the difference in load level, P/P_u , and the difference in strain trend associated with it as discussed in section 4.3.1 and not as a result of the different L/w ratio. It was also observed that there is no significant difference between the transfer lengths at P/P_u of 0.71.

From the previous discussion it is concluded that the individual effects of the CFRP sheet bond length and bond width are the governing factors in the behaviour rather than the L/w ratio.

4.8 Anchor Sheet Configuration

The effect of FRP anchor sheet configurations on the bond behaviour of FRP sheets was studied in an attempt towards developing FRP reinforcement schemes that could avoid premature delamination failures. Thirteen P-series specimens were tested with different anchor sheet configurations, designed to study the effect of locating the anchor sheet above or below the tested sheet on the bond behaviour. The effect of the distance of the anchor from the crack "a" and the effect of the anchor sheet extension beyond the tested sheet "b" were also studied. The distances a and b are illustrated in Figure 3-8. Specimen P20 was discarded as discussed in section 4.2.2 and specimen P26 was

repeated for verification of results and the average values from both tests were considered.

4.8.1 Anchor Sheet Location Relative to the Tested Sheet

The effect of locating unidirectional CFRP anchor sheets above or below the tested CFRP sheet on the bond behaviour was investigated by comparing the results of six pairs of specimens with the same anchor configurations and dimensions except for the location of the anchor sheets relative to the tested sheet. Specimens P14 through P19 had the anchor sheets bonded above the tested sheet while specimens P21 through P26 had them bonded below the tested sheet.

The load-displacement responses of all specimens are shown in Figure 4-59 through Figure 4-64. The load was applied through stroke control. A sudden drop in the load-displacement curves indicates a crack opening. The drop in the load value at 0.5 mm displacement in Figure 4-59 was due to the sudden opening of the centre crack in the opposite unopened cracked face of the specimen. The descending branch in the curves indicates that a sheet was debonding, including the portion of the anchor sheet in line with the tested sheet. The sudden drop in the load at failure occurred when the sheet was totally debonded in a sudden zip action.

Comparison of the load vs. displacement responses in Figure 4-59 through Figure 4-64 indicates no significant difference in the load and displacement values in the case of specimens P15 and P22. Specimen P17 with the anchor sheet above the tested sheet achieved 11% higher load capacity but with 12.6% less displacement values relative to specimen P24, which had the anchor sheet below the tested sheet. In the last four pairs of specimens P14/P21, P16/P23, P18/P25, and P19/P26 the anchor below the sheet achieves between 10.9% and 25% higher load values and between 29.9% and 46.4% higher displacement values. The anchor sheet located below the tested sheet was, therefore, observed to show better or equivalent response compared to anchor sheets located above the tested sheet.

4.8.2 Anchor Distance from Crack

The load-displacement responses for specimens studying the anchor distance from the crack “a” for anchor sheets above the tested sheet and those below the tested sheet are shown in Figure 4-65 and Figure 4-66, respectively. When the anchor sheet was above the tested sheet, the distance “a” did not appear to affect the load capacity or the ductility of the joint except when the anchor sheet was at the crack face ($a = 0$). The average load capacity was slightly higher in the case of an anchor sheet below the tested sheet. This is illustrated in the ultimate load-distance “a” relationships shown in Figure 4-67. When the anchor sheet was at the crack face ($a = 0$) both anchor locations showed an increase in the load capacity and ductility of the joint.

4.8.3 Anchor Extension Beyond Tested Sheet

The load-displacement responses for specimens studying the extension of the perpendicular anchor sheets beyond the tested sheet “b” for anchor sheets above the tested sheet and those below the tested sheet are shown in Figure 4-68 and Figure 4-69, respectively. There was no significant difference in the ultimate load when the anchor sheet was above the tested sheet while the displacement did not have a defined trend. In the case of an anchor sheet below the tested sheet, neither the ultimate load nor the displacement had a defined trend. The ultimate load trend is illustrated in Figure 4-70, which shows the ultimate load plotted against the distance “b” for the specimens in Figure 4-68 and Figure 4-69.

From the previous discussion it is concluded that unidirectional CFRP anchor sheet located below the tested CFRP sheet showed better or equivalent overall bond behaviour compared to anchor sheets located above the tested sheet. The anchor distance from the crack “a” did not appear to affect the load capacity or the ductility of the joint, except when the anchor sheet was at the crack face ($a = 0$) where an increase in the load capacity and ductility of the joint occurred. The extension of the perpendicular anchor sheets beyond the tested sheet “b” does not appear to have a direct relation with the ultimate load or the ductility of the joint.

Table 4-1 Push-apart bond test specimens' details and results

Test #	L (mm)	w (mm)	L/w	d ₁ (mm)	d ₂ (mm)	c (mm)	φ	f' _c (MPa)	P _u (kN)	τ _b (MPa)
S1	75	200	0.38	20	45	61	36.4	51.1	54.81	1.83
S2	50	150	0.33	16	27	40	34.0	50.4	39.85	2.66
S3	100	150	0.67	17	32	36	41.6	51.3	56.40	1.88
S4	150	100	1.50	15	33	40	39.5	50.4	42.71	1.42
S5	150	150	1.00	26	30	38	38.3	51.1	53.52	1.19

Table 4-2 Pull-apart bond test specimen's details and results

Test #	L (mm)	w (mm)	a (mm)	b (mm)	f' _c (MPa)	P _u (kN)	τ _b (MPa)	Remarks
P1	45	100	---	---	46.9	20.06	2.22	
P2	60	100	---	---	46.9	22.55	1.88	
P3	75	100	25	50	46.9	23.27	1.55	
P4	90	100	---	---	46.9	23.04	1.28	
P5	105	100	---	---	46.9	24.30	1.16	Effective length (No anchor sheet)
P6	120	100	---	---	46.9	33.60	1.40	
P7	135	100	---	---	46.9	22.14	0.82	
P8	150	100	---	---	46.9	24.90	0.83	
P9	50	150	25	25	46.9	28.78	1.92	Length effect (Anchor sheet at one end)
P10	100	150	25	25	46.9	40.49	1.35	
P11	150	150	25	25	47.3	38.1	1.69	
P12	150	25	25	75	47.3	9.88	1.32	Width effect, including P11 (Anchor sheet at one end)
P13	150	50	25	75	47.3	13.93	0.93	
P14	100	50	0	75	47.3	18.77	1.88	
P15	100	50	25	75	47.3	15.55	1.56	
P16	100	50	50	75	47.3	15.96	0.94	Anchor at both ends Anchor sheets above
P17	100	50	75	75	47.3	16.19	1.62	
P18	100	50	25	50	47.3	15.49	1.55	
P19	100	50	25	25	47.3	15.19	1.52	
P20	100	50	---	---	47.3	31.48	3.15	
P21	100	50	0	75	46.4	20.33	2.03	
P22	100	50	25	75	46.4	15.08	1.51	
P23	100	50	50	75	46.4	18.26	1.83	Anchor at both ends Anchor sheet below
P24	100	50	75	75	46.4	15.61	1.56	
P25	100	50	25	50	46.4	19.17	1.92	
P26	100	50	25	25	46.4	18.09	1.81	

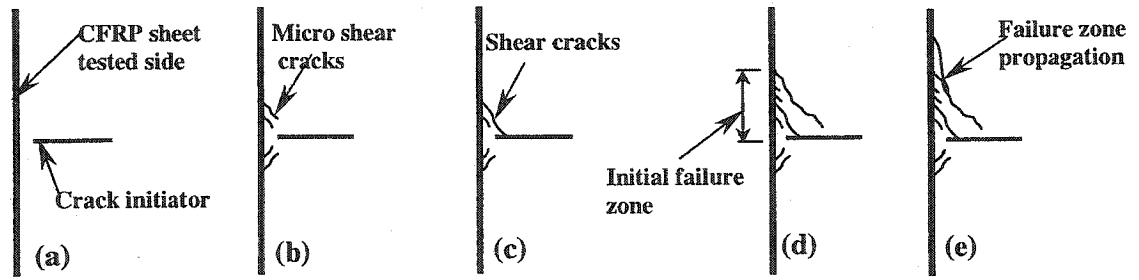


Figure 4-1 Crack propagation and failure zone formation sketch

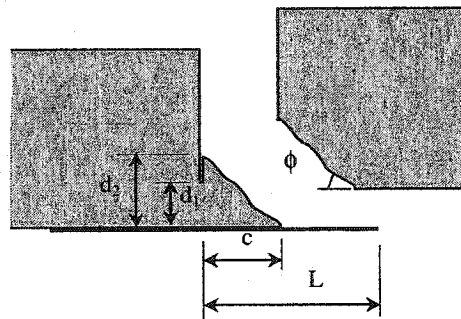


Figure 4-2 Schematic sketch of the failure zone plan view in the push-apart tests

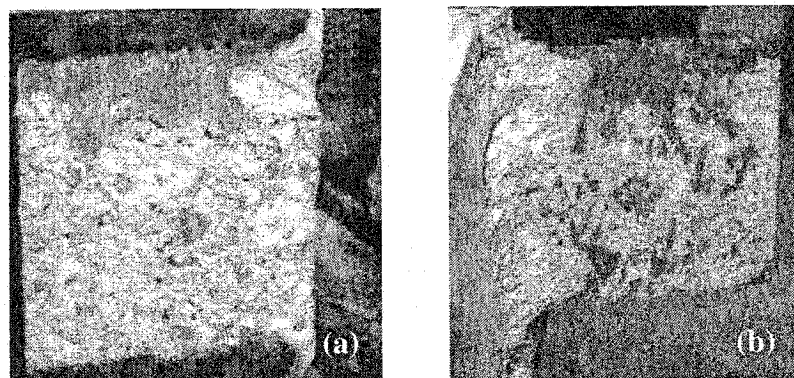


Figure 4-3 Push-apart failure surface (a) concrete (b) CFRP sheet

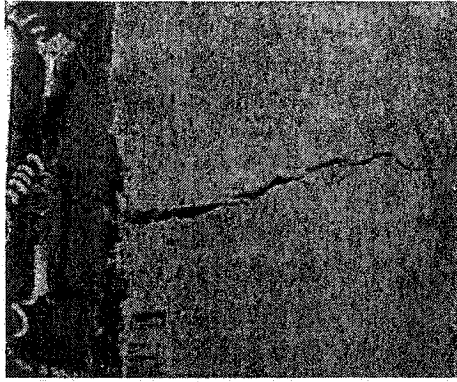


Figure 4-4 Side view of a pull-apart specimen showing crack opening

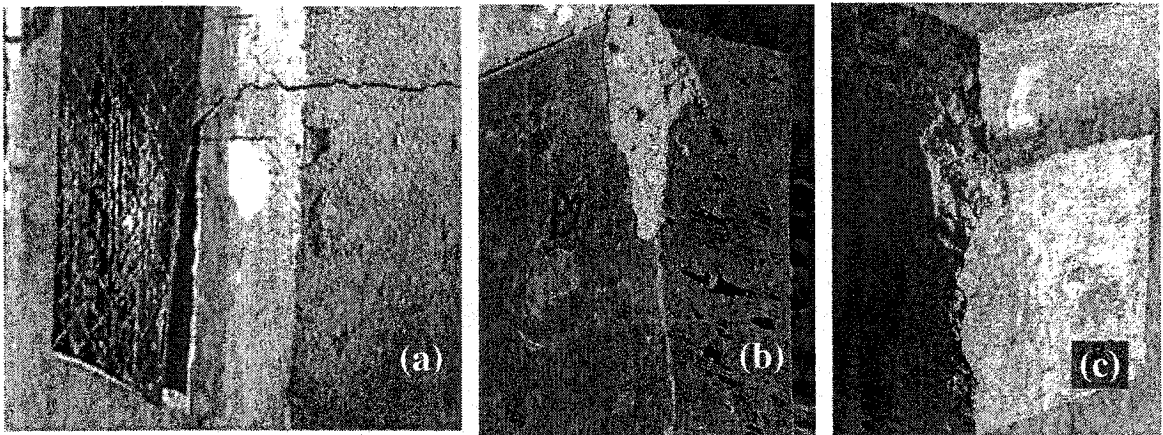


Figure 4-5 Typical failure mode for specimens P1 through P13, except for specimen P3 (a) side view (b) CFRP sheet surface (c) concrete surface

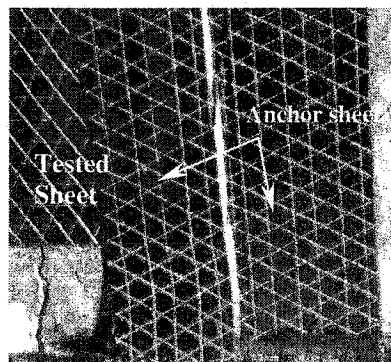


Figure 4-6 Specimen P3 failure mode

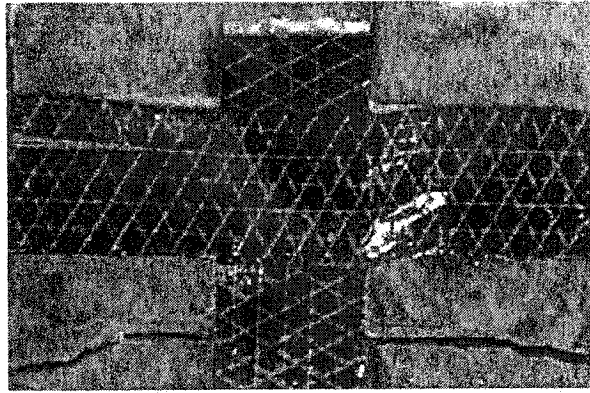


Figure 4-7 Specimen P15 failure mode

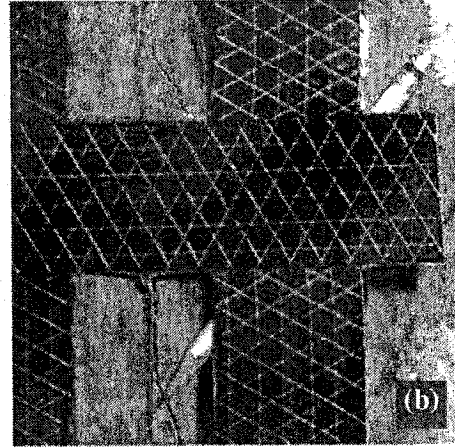
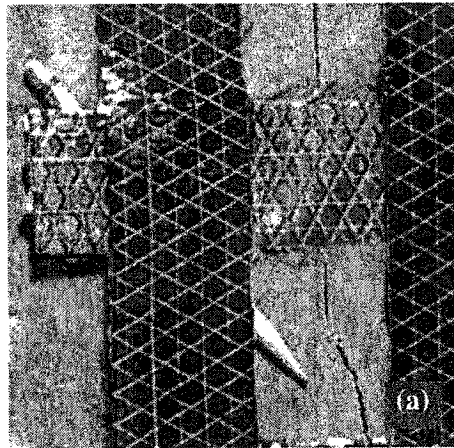


Figure 4-8 Typical failure for specimens with anchor (a) above sheet (b) below sheet

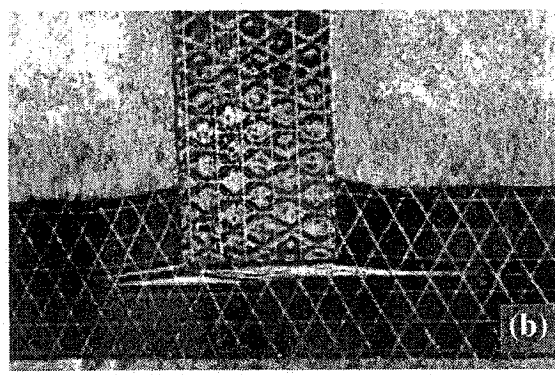
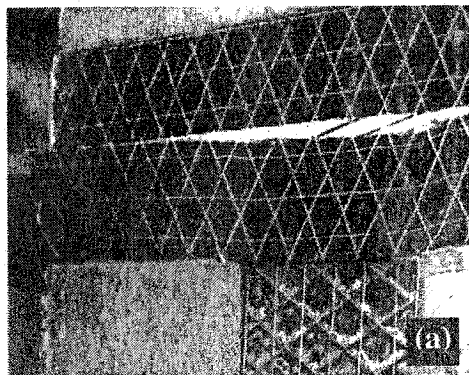


Figure 4-9 Failure mode (a) Specimen P17 (b) Specimen P24

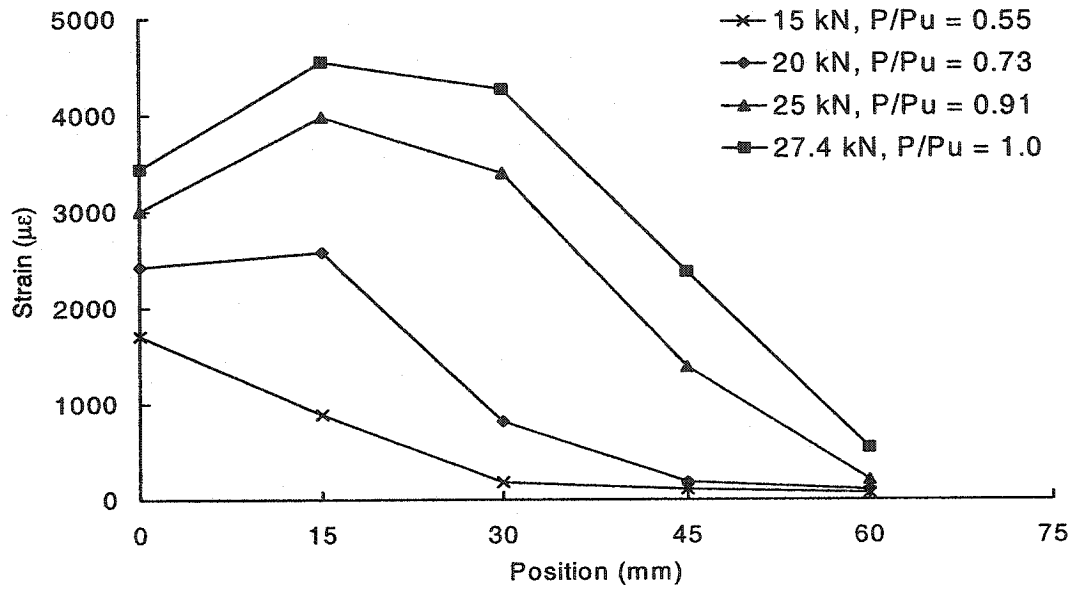


Figure 4-10 Average strain distributions for specimen S1

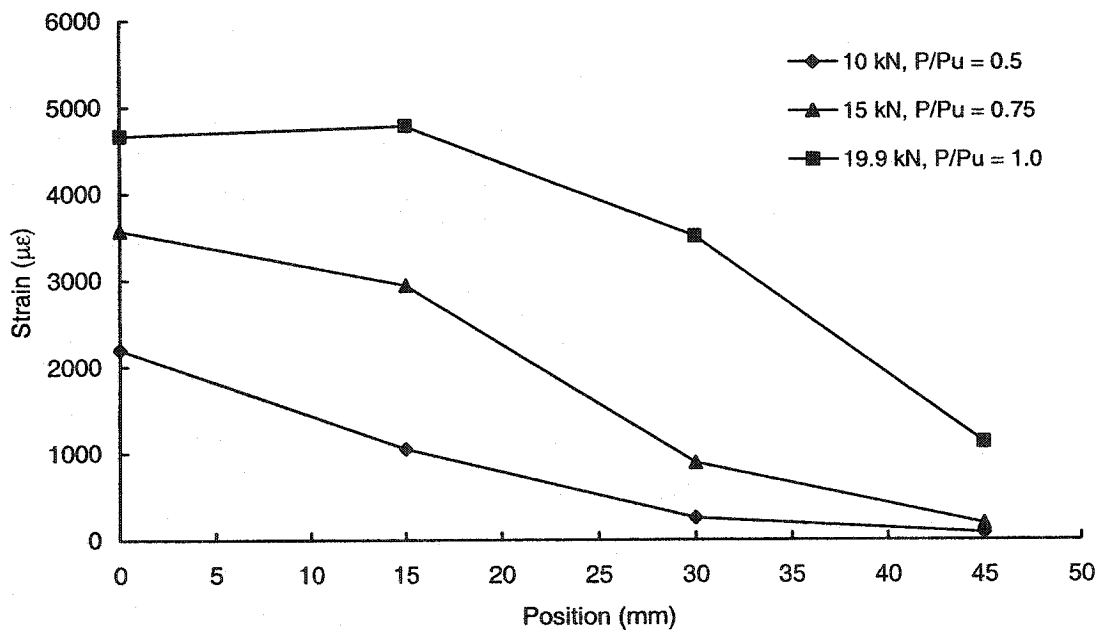


Figure 4-11 Average strain distributions for Specimen S2

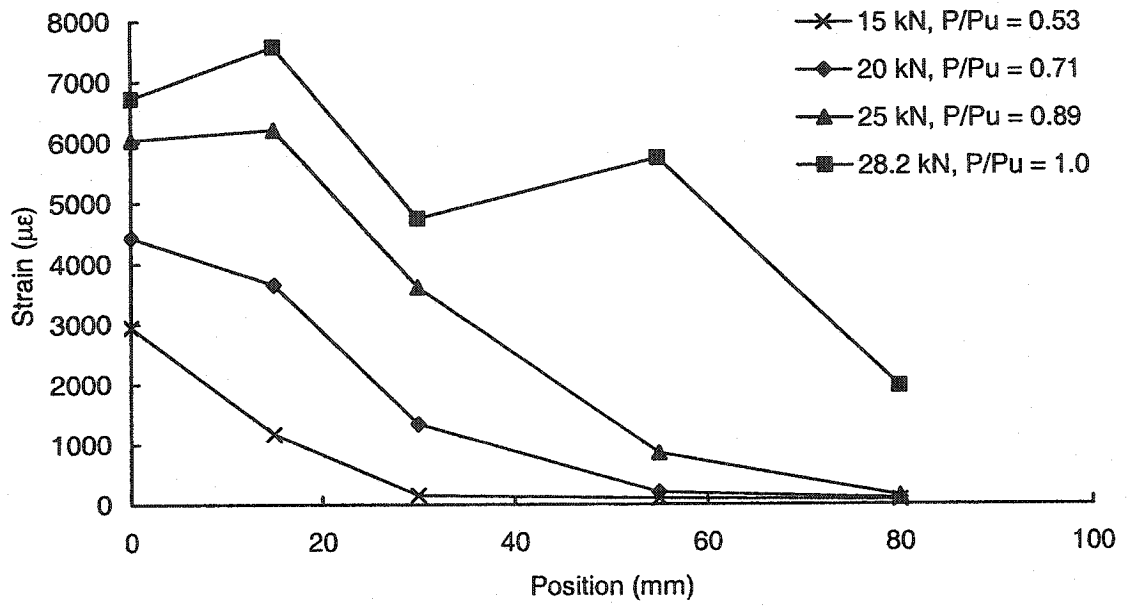


Figure 4-12 Average strain distributions for Specimen S3

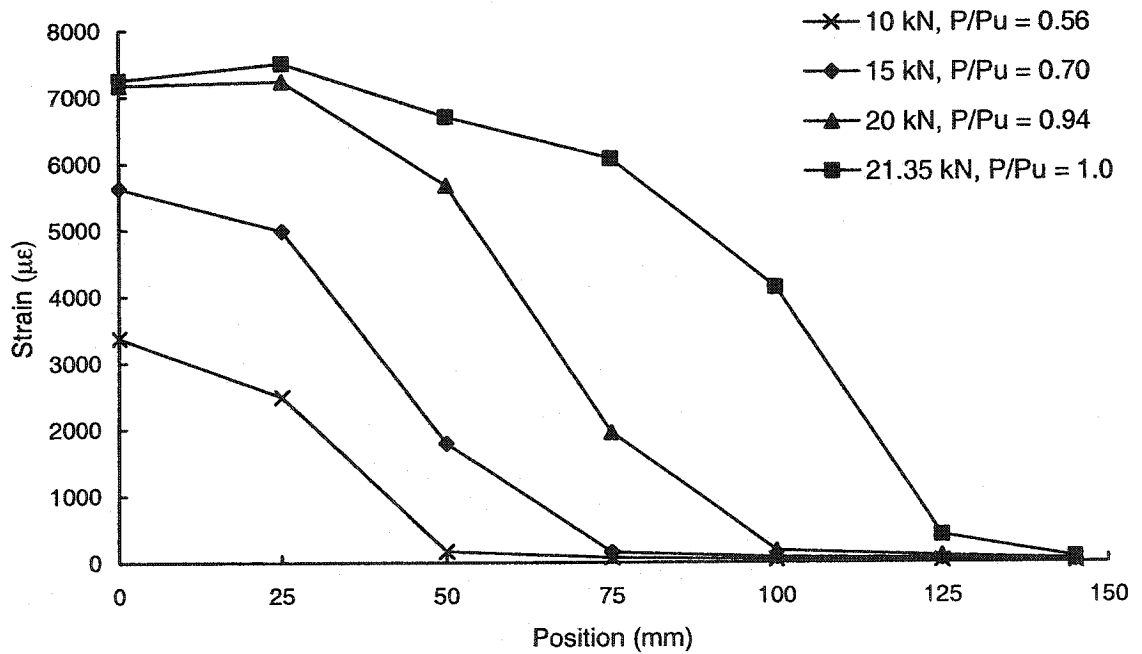


Figure 4-13 Average strain distributions for Specimen S4

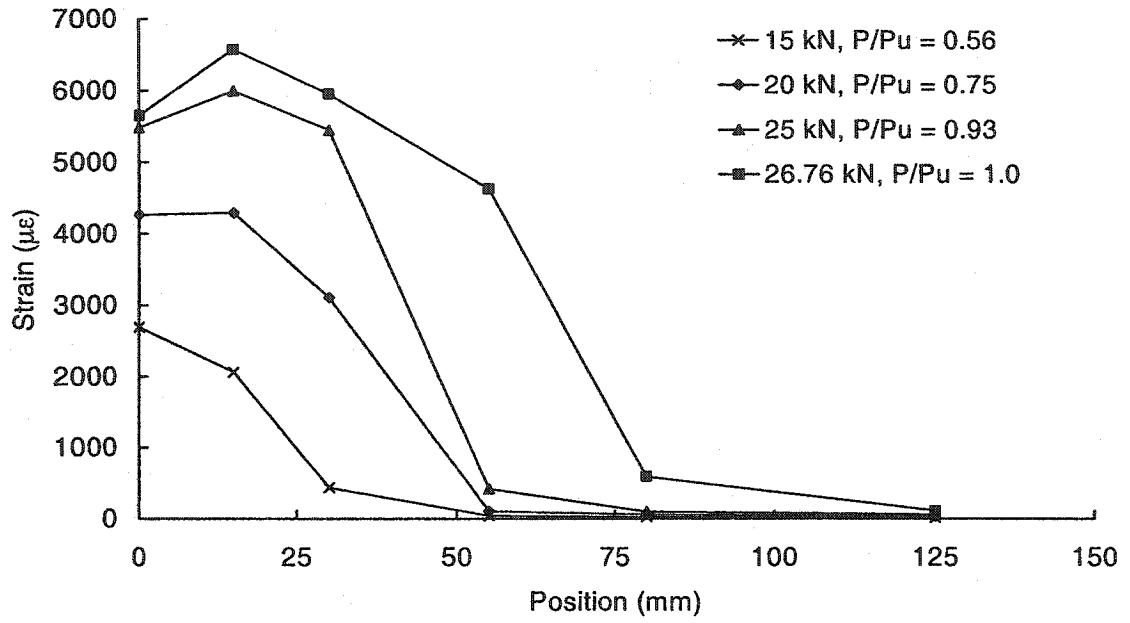


Figure 4-14 Average strain distributions for Specimen S5

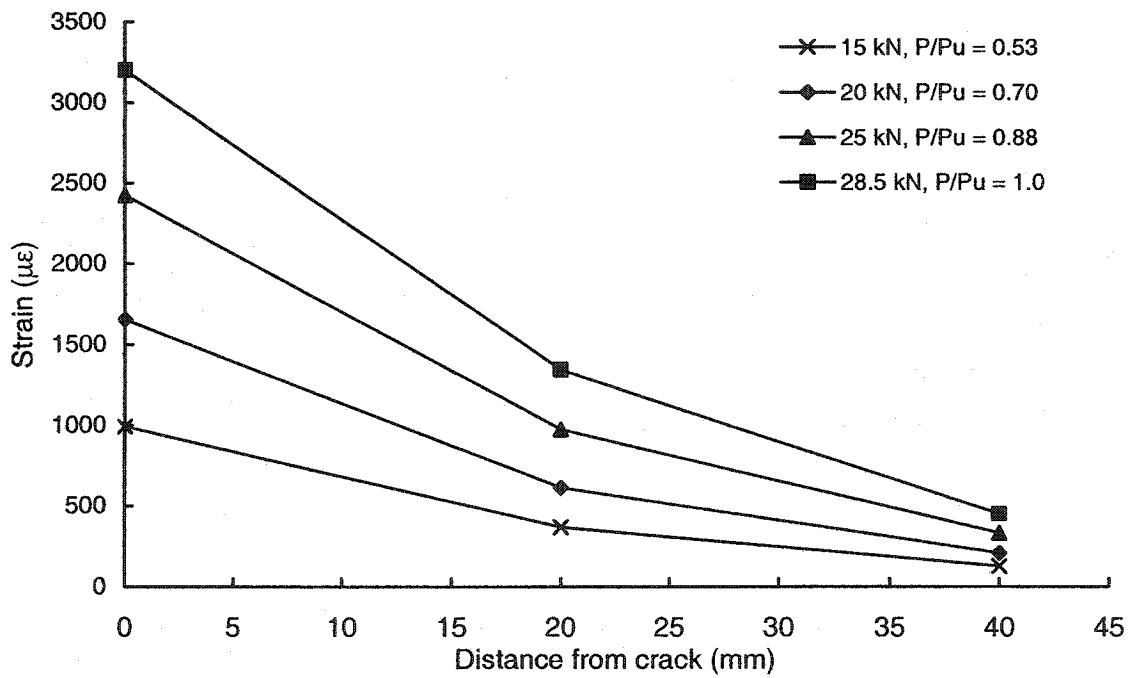


Figure 4-15 Strain distributions at centre of sheet for specimen P9

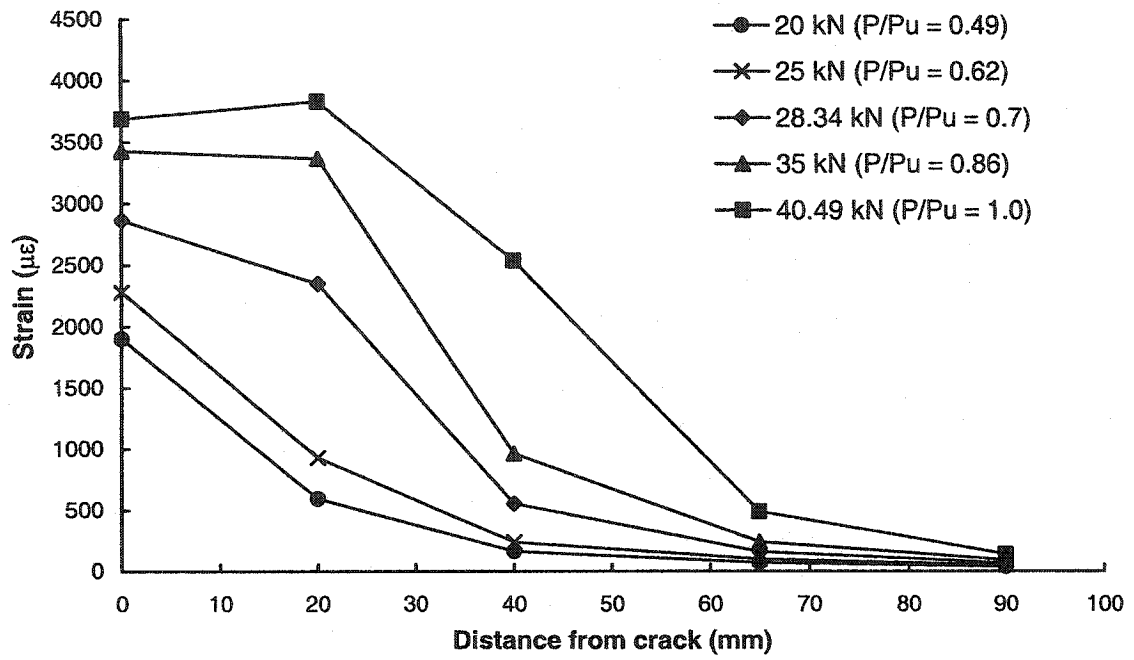


Figure 4-16 Strain distribution at centre of sheet for specimen P10

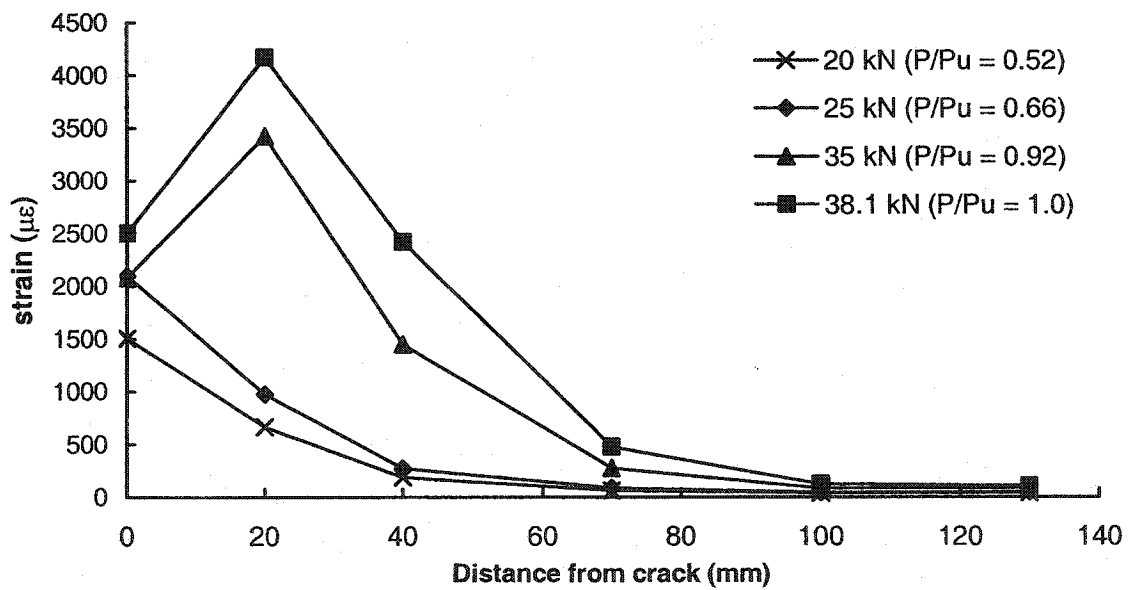


Figure 4-17 Strain distributions at centre of sheet for specimen P11

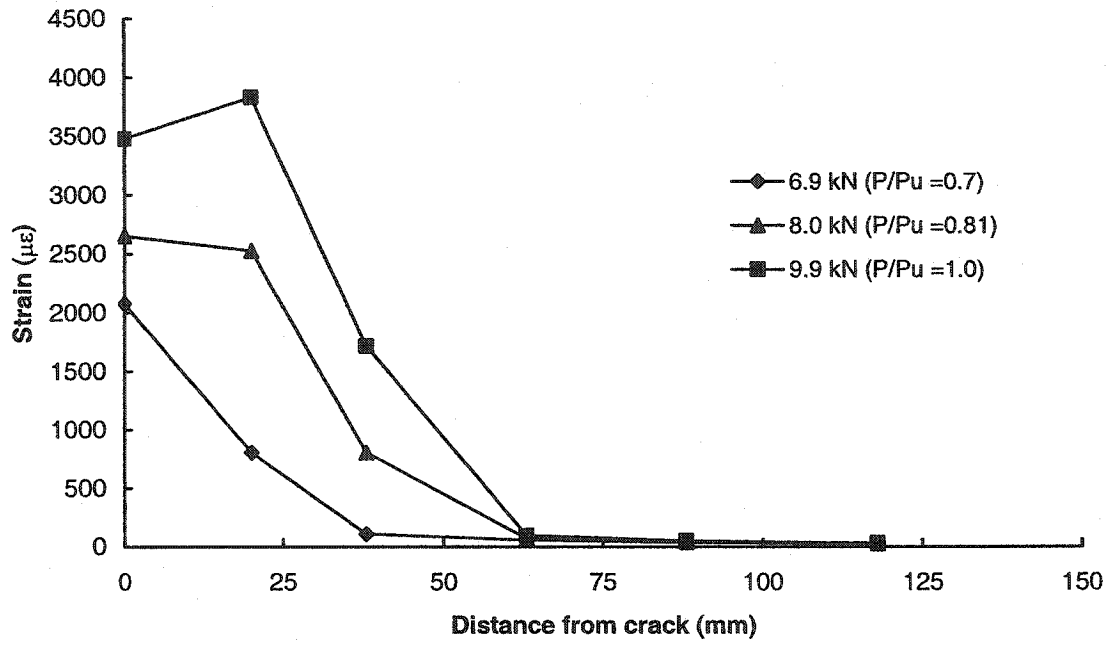


Figure 4-18 Strain distributions at centre of sheet for specimen P12

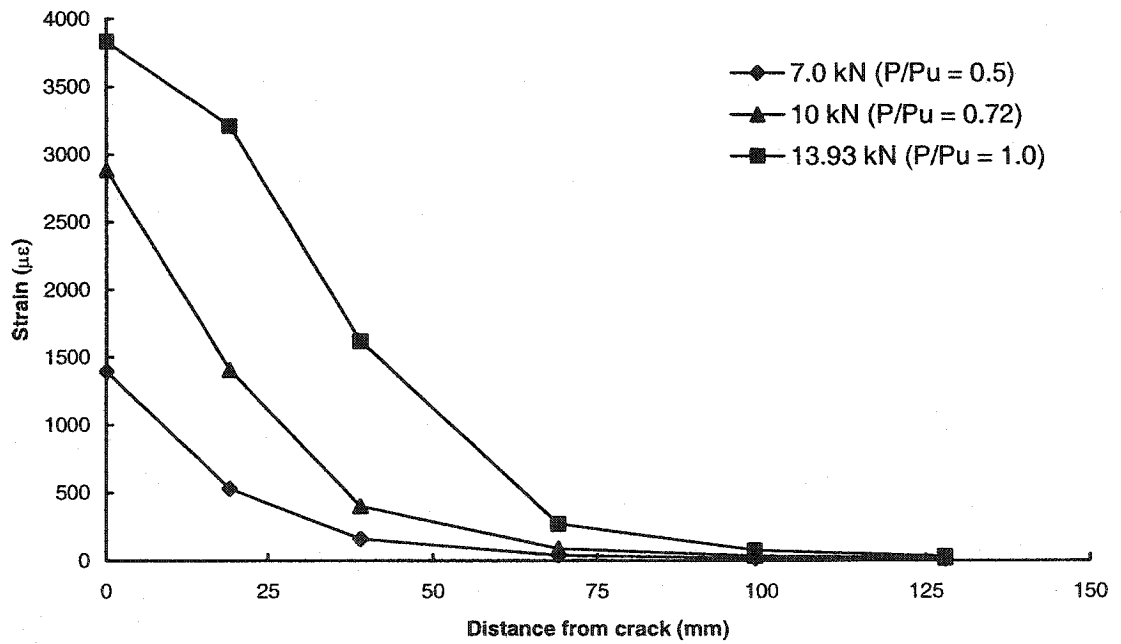


Figure 4-19 Strain distributions at centre of sheet for specimen P13

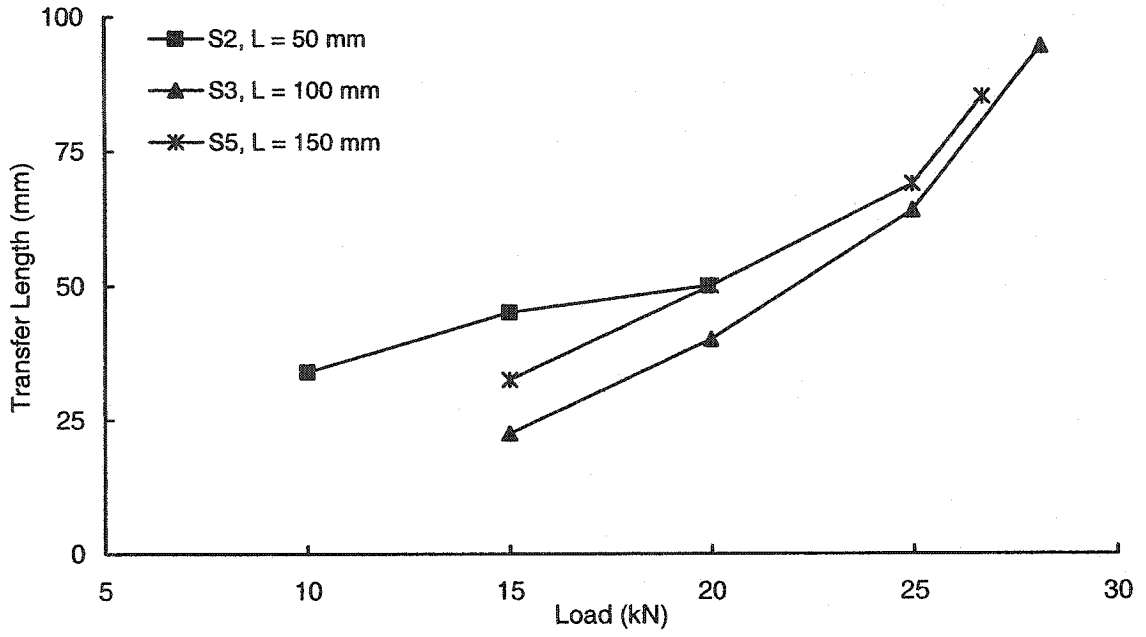


Figure 4-20 Load vs. transfer length for S-series specimens with $w = 150$ mm

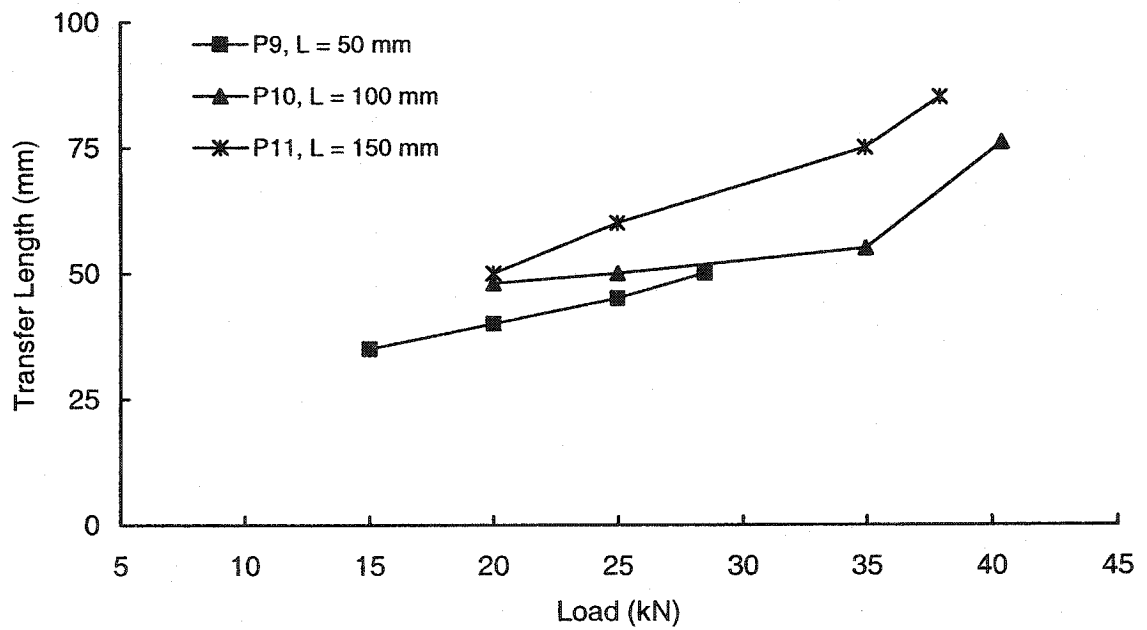


Figure 4-21 Load vs. transfer length for P-series specimens with $w = 150$ mm

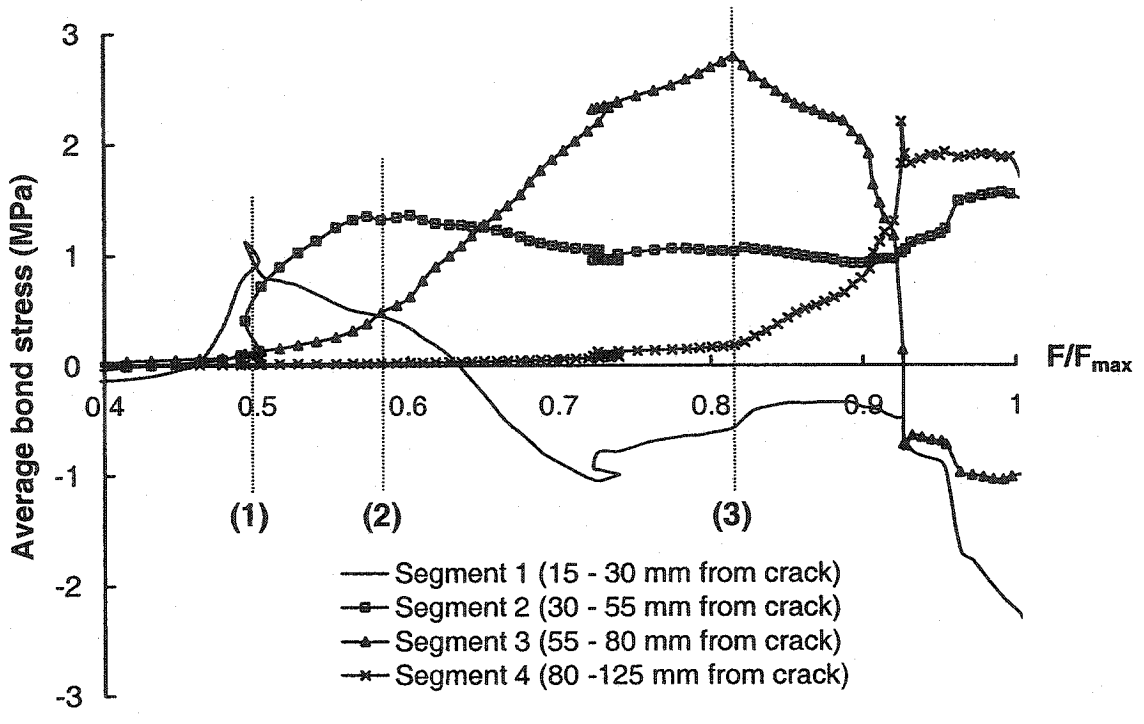


Figure 4-22 Average bond stress in sheet centre vs. relative load for specimen S5

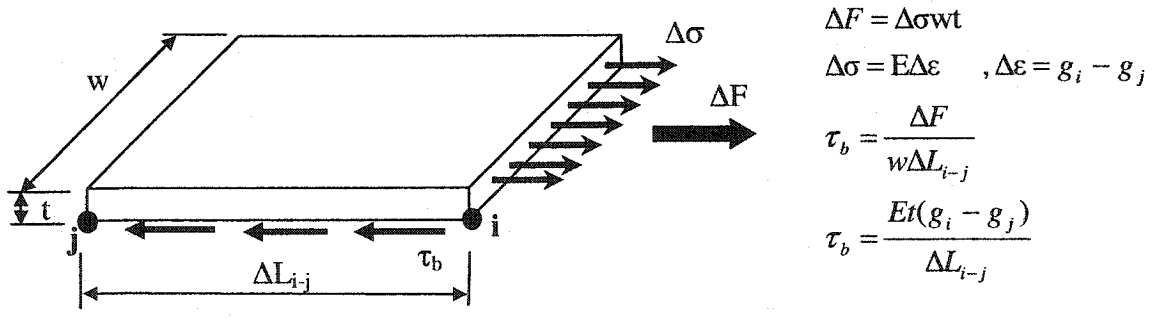


Figure 4-23 Schematic sketch of deriving incremental average bond stress

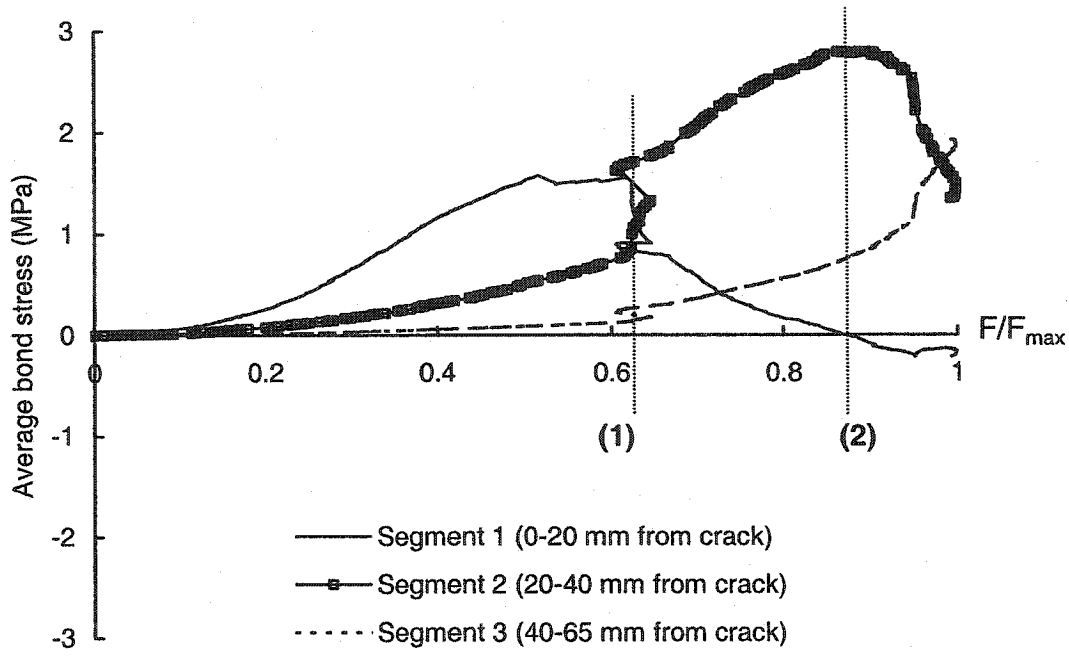


Figure 4-24 Average bond stress in sheet centre vs. relative load for specimen P10

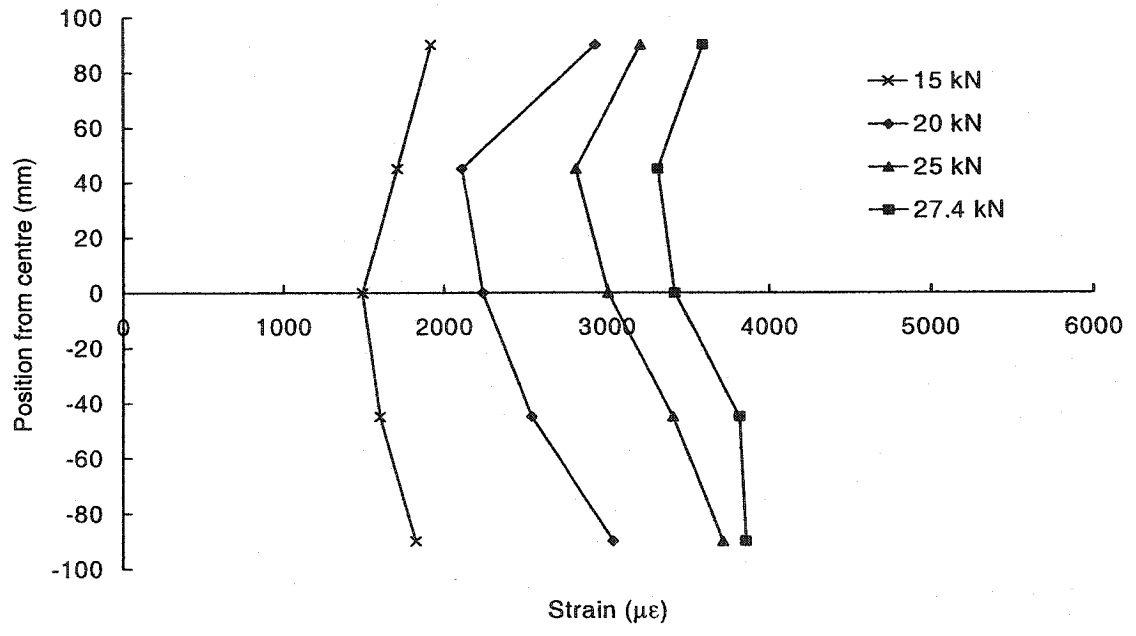


Figure 4-25 Strain distributions along the sheet width of S1 at crack location

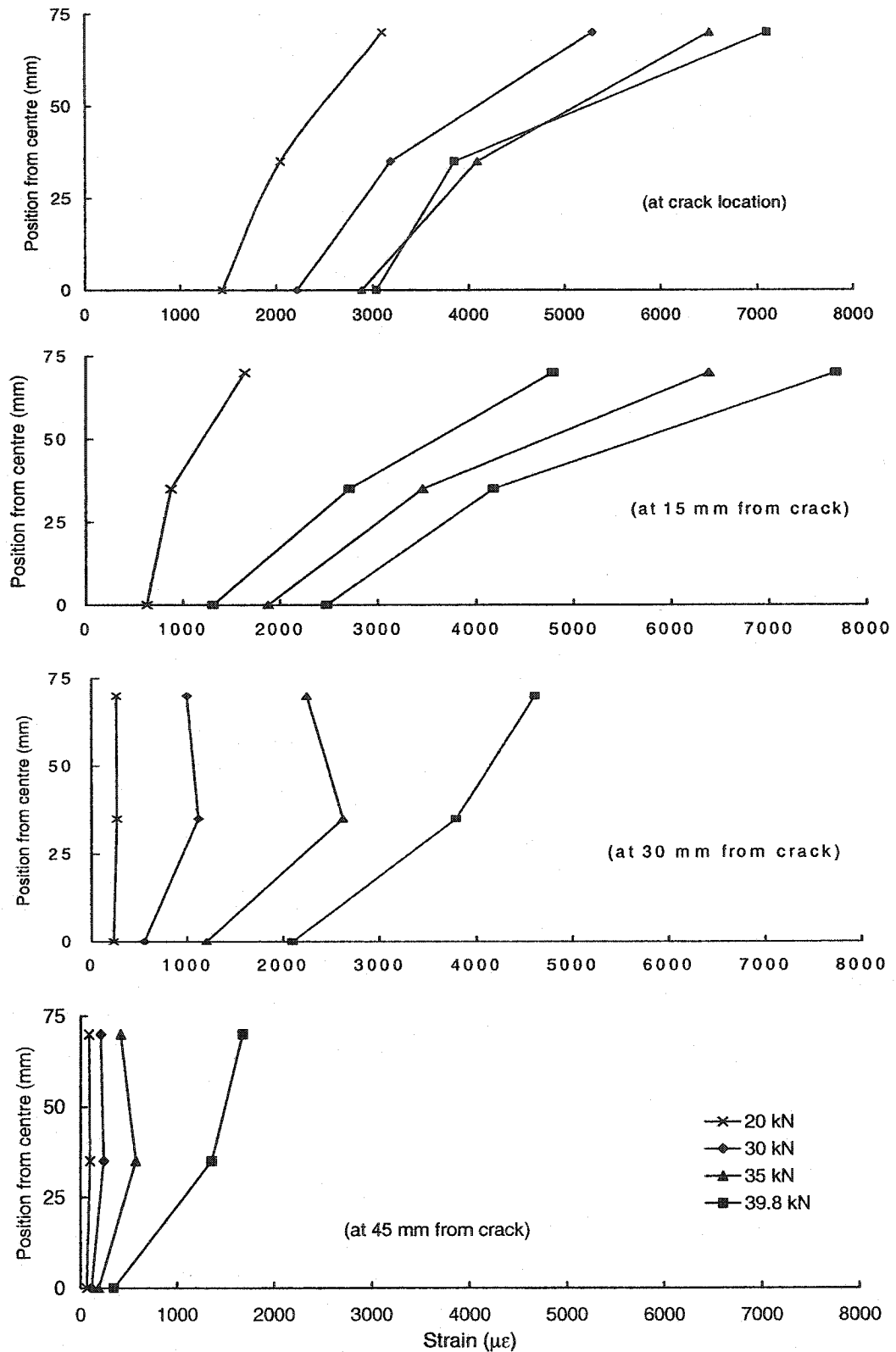


Figure 4-26 Strain distributions along half the sheet width of S2 at 0, 15, 30, and 45 mm from the crack location

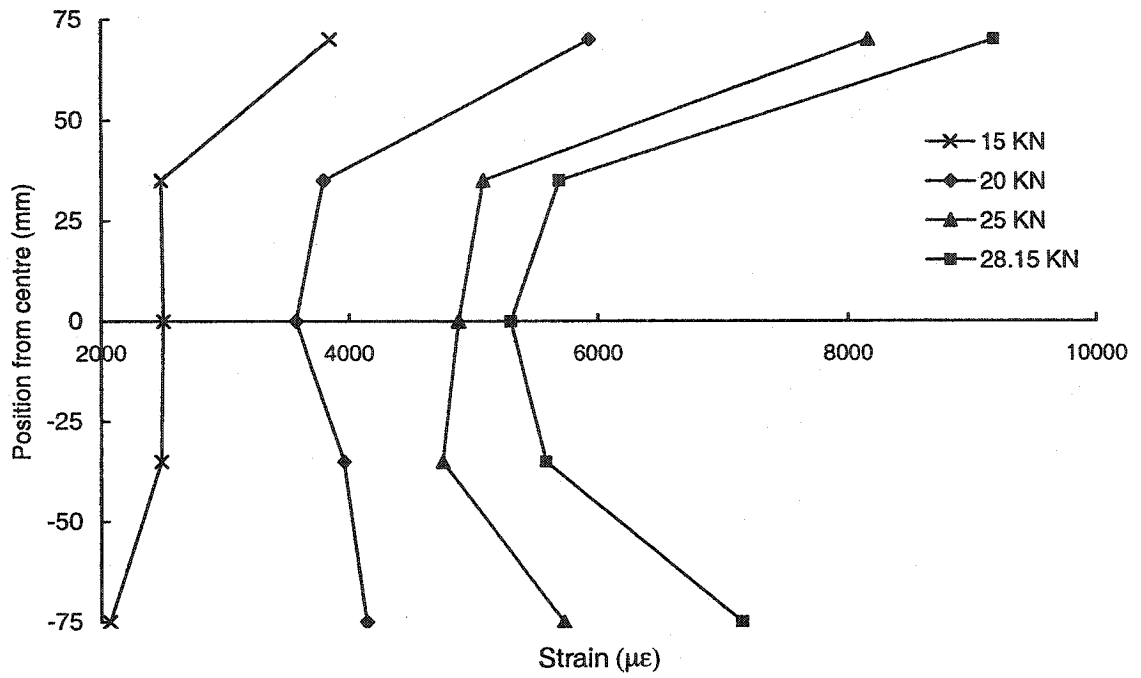


Figure 4-27 Strain distributions along the sheet width of S3 at crack location

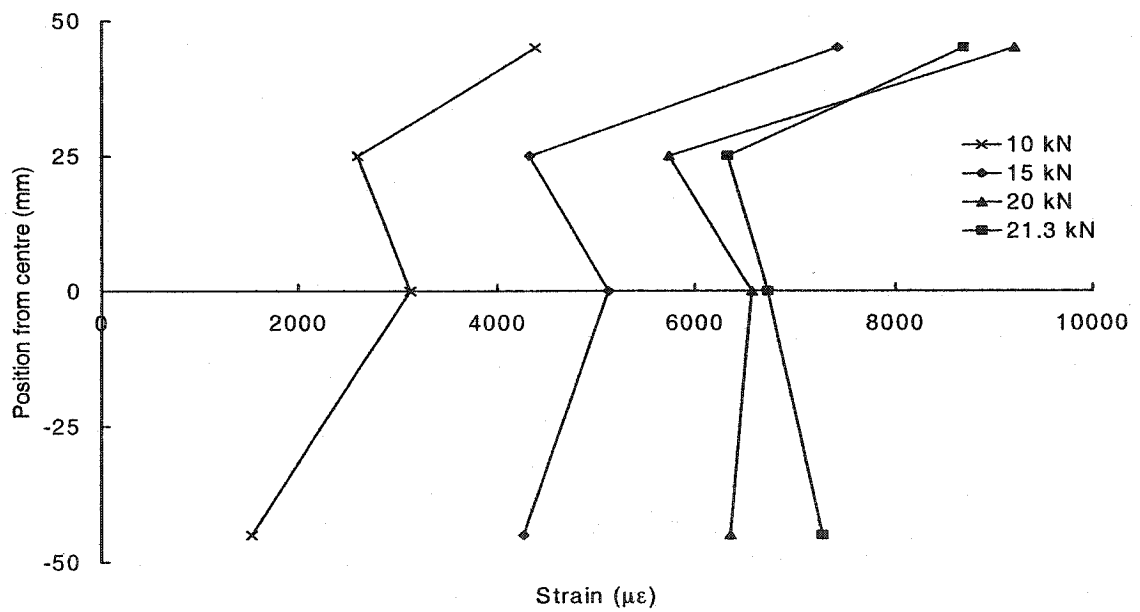


Figure 4-28 Strain distributions along the sheet width of S4 at crack location

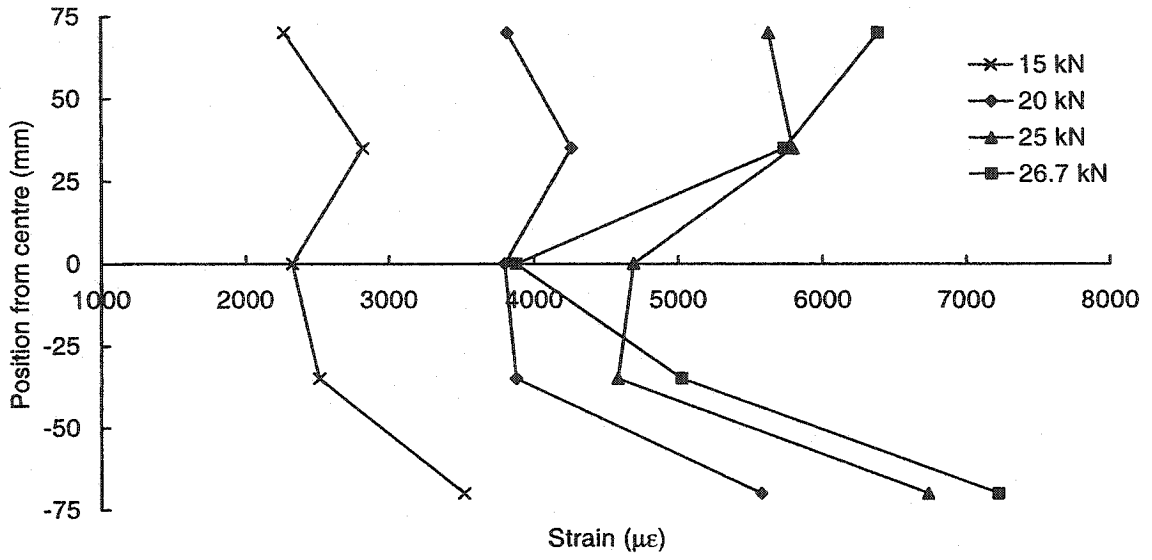


Figure 4-29 Strain distributions along the sheet width of S5 at crack location

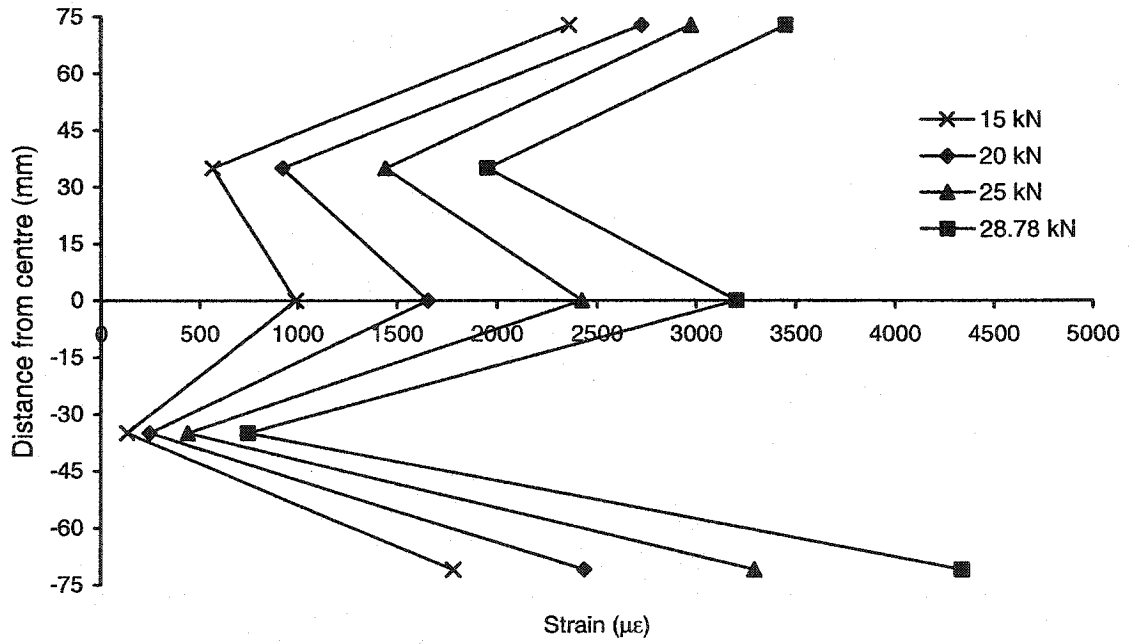


Figure 4-30 Strain distributions across the width of P9 at crack location

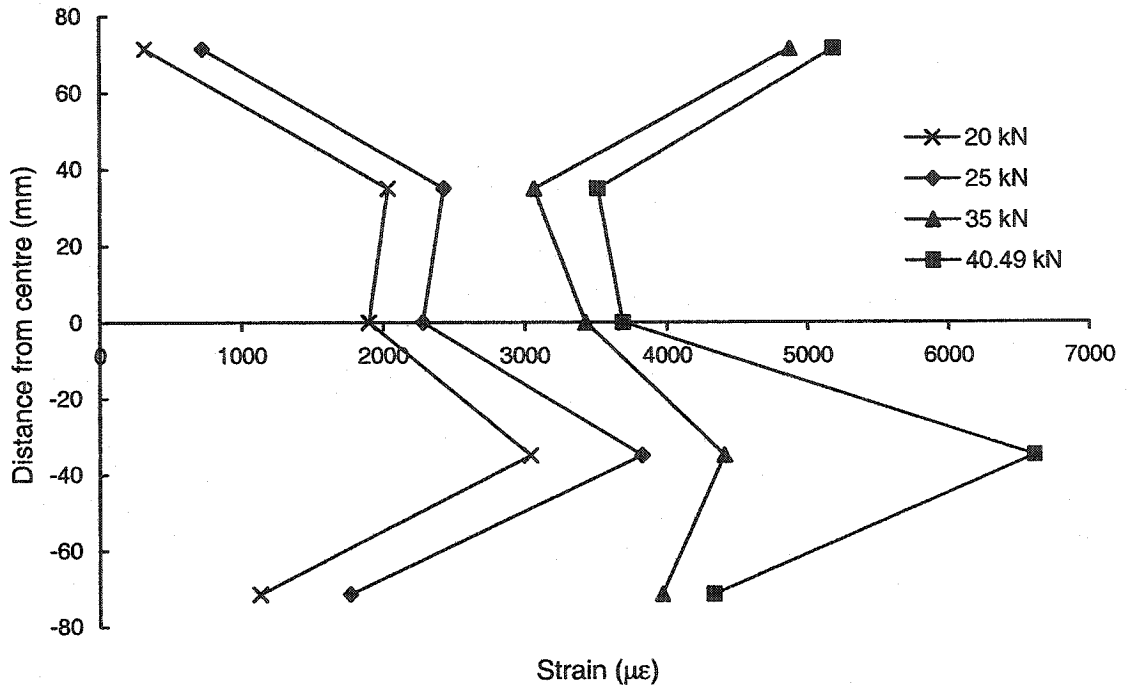


Figure 4-31 Strain distribution across the width of P10 at crack location

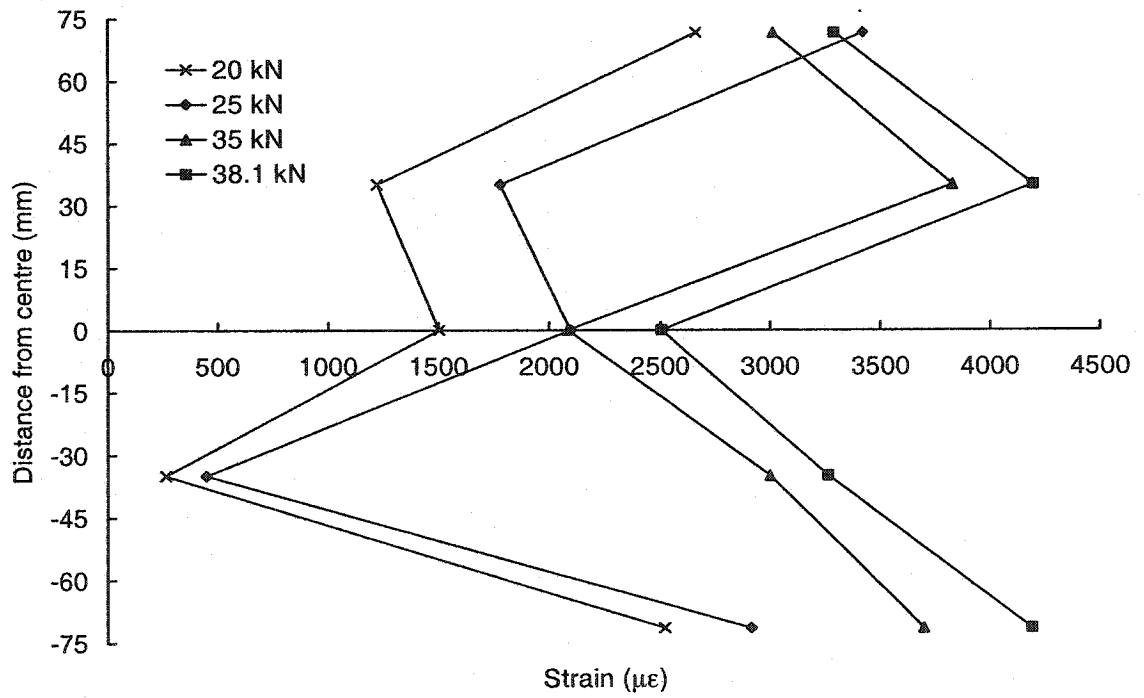


Figure 4-32 Strain distributions across the width of P11 at crack location

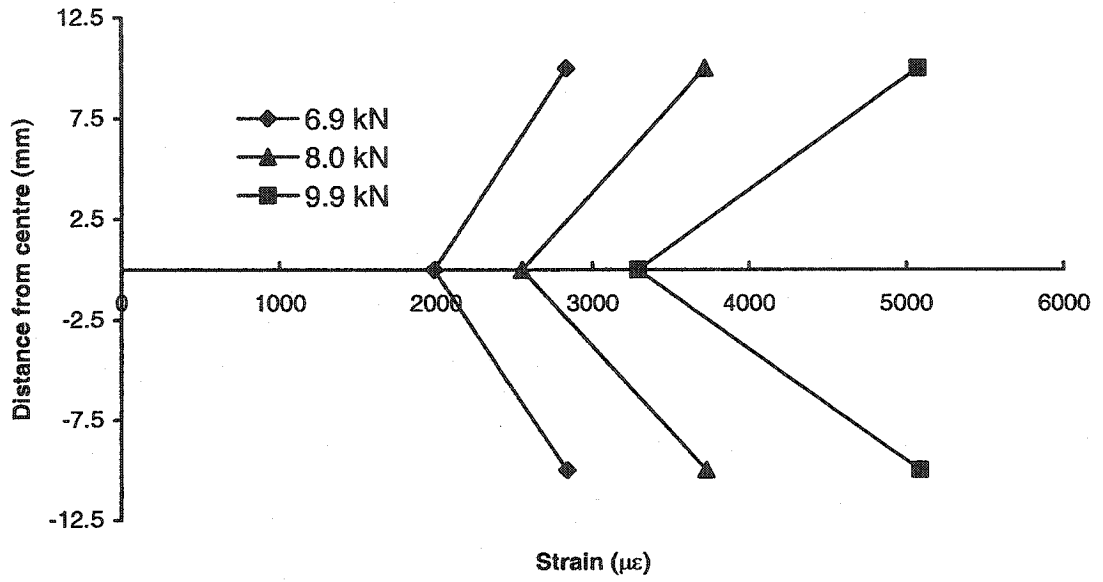


Figure 4-33 Strain distributions across the width of P12 at crack location

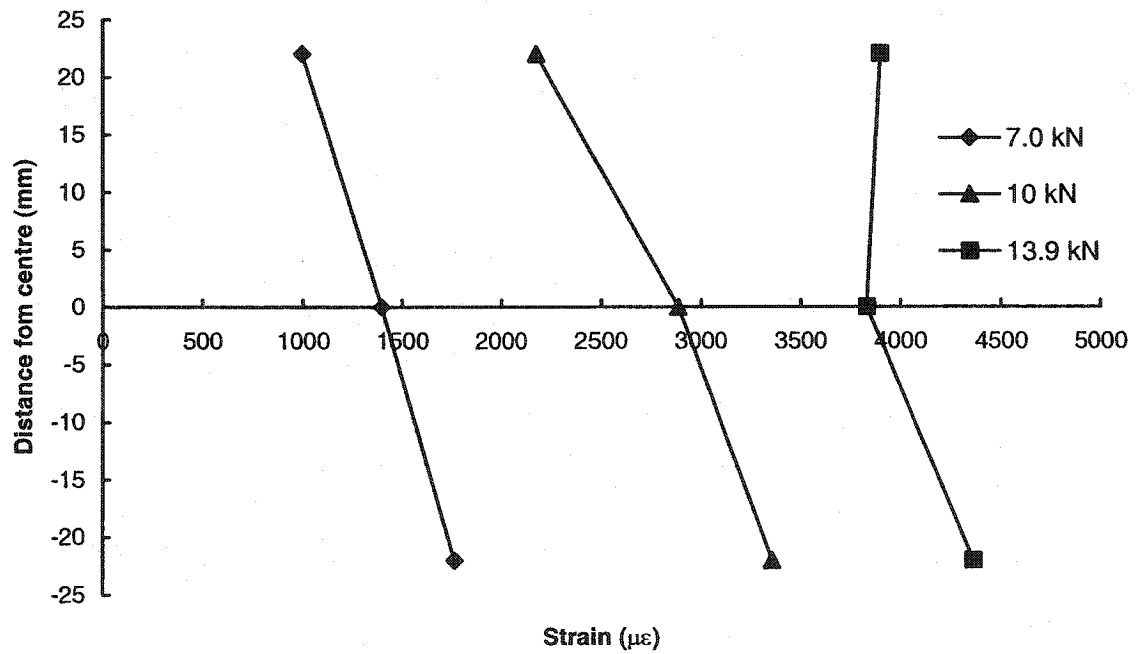


Figure 4-34 Strain distributions across the width of P13 at crack location

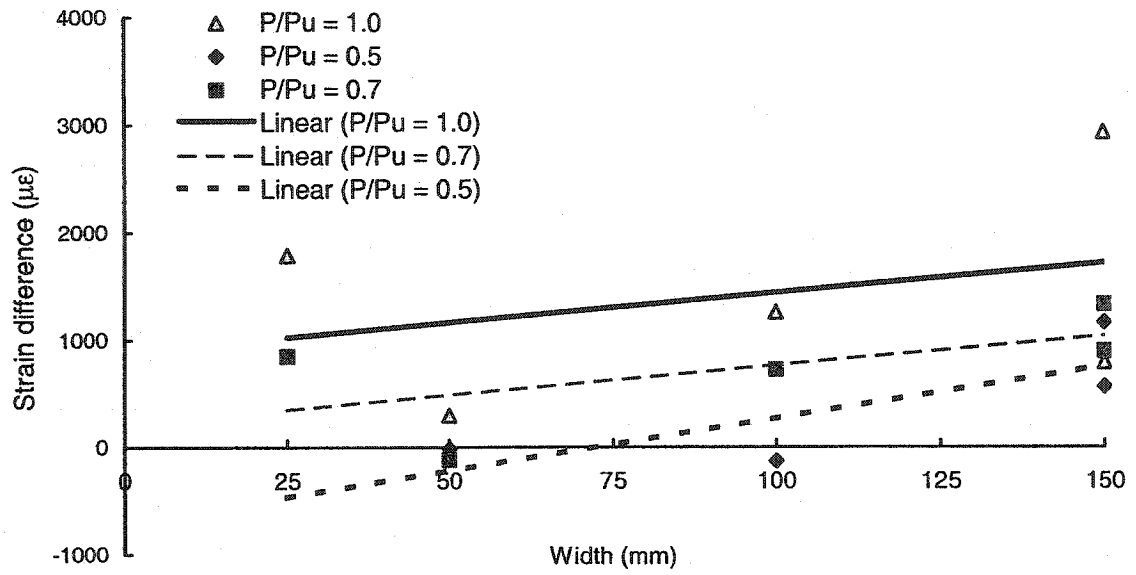


Figure 4-35 CFRP sheet width vs. strain difference between the edge and centre of the sheet at the crack location

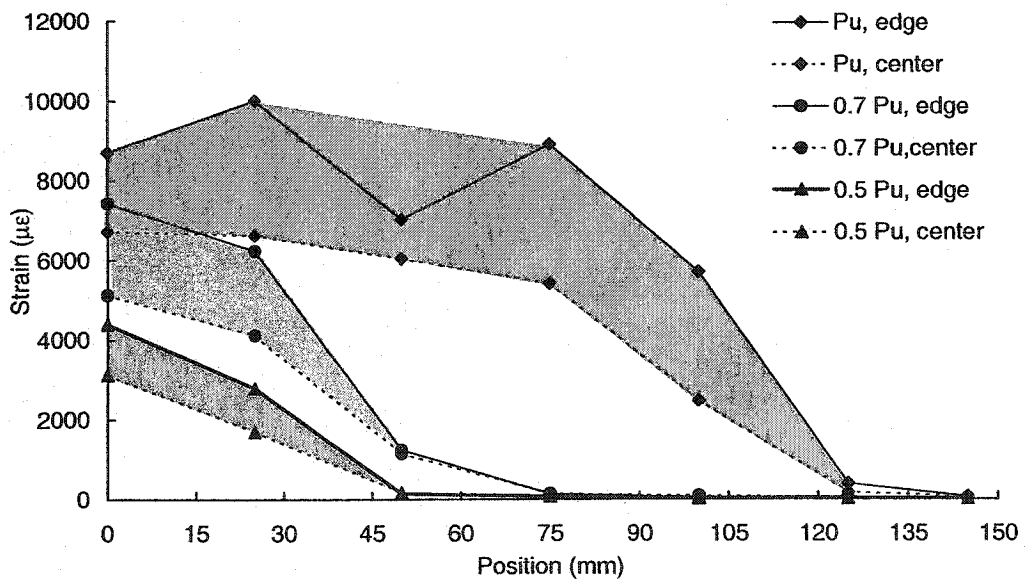


Figure 4-36 Strain distributions in the sheet centre and edge along its length at various load levels in S4

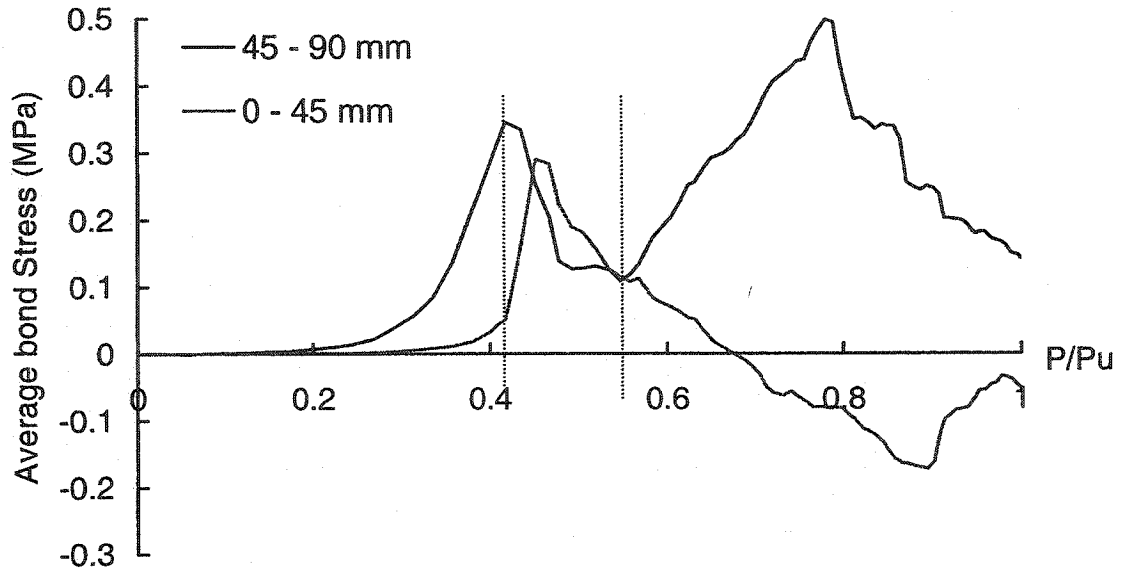


Figure 4-37 Average bond stresses along the sheet width vs. normalized load level, specimen S1

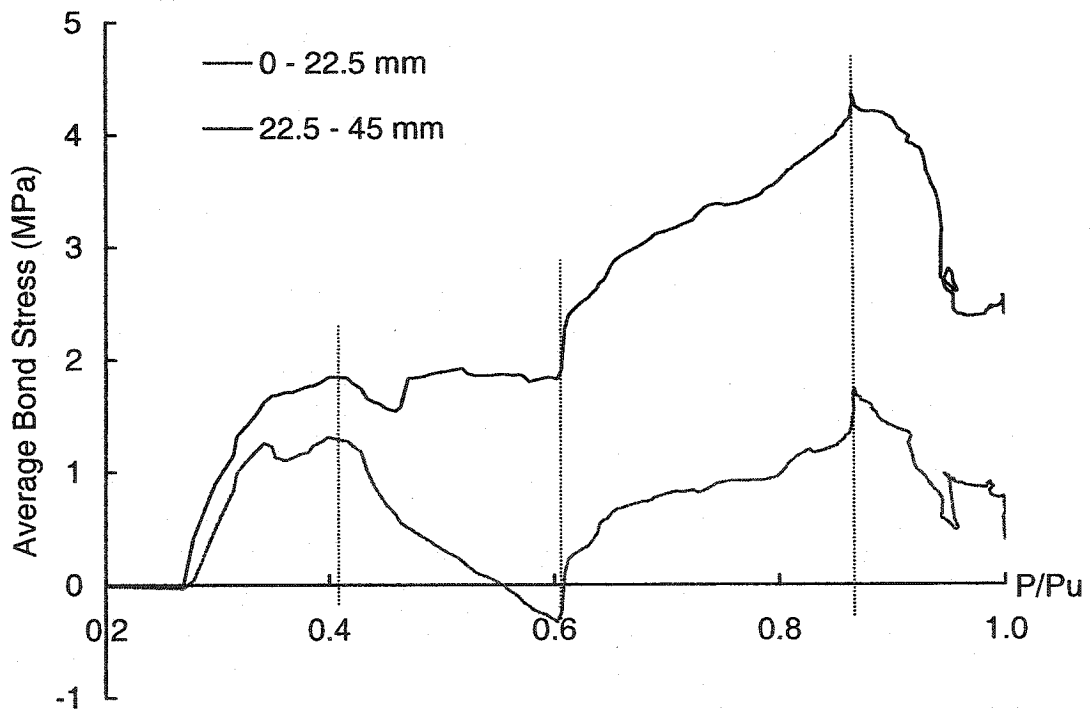


Figure 4-38 Average bond stresses across the sheet width vs. normalized load level, specimen S4

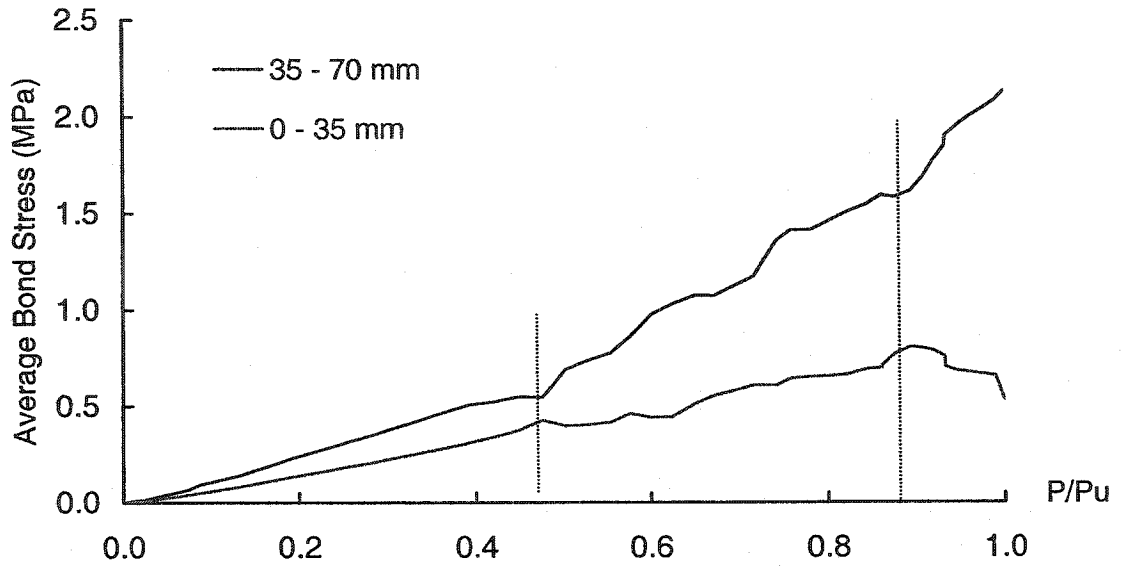


Figure 4-39 Average bond stresses across the sheet width vs. normalized load level, specimen S2

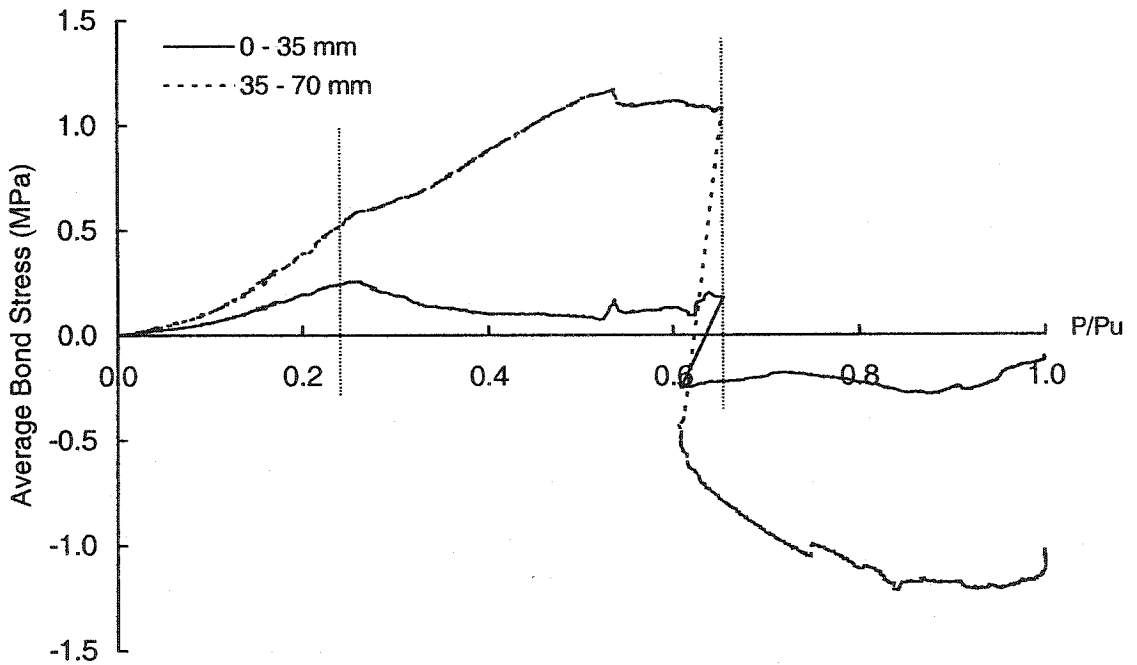


Figure 4-40 Average bond stresses across the sheet width vs. normalized load levels, specimen P10

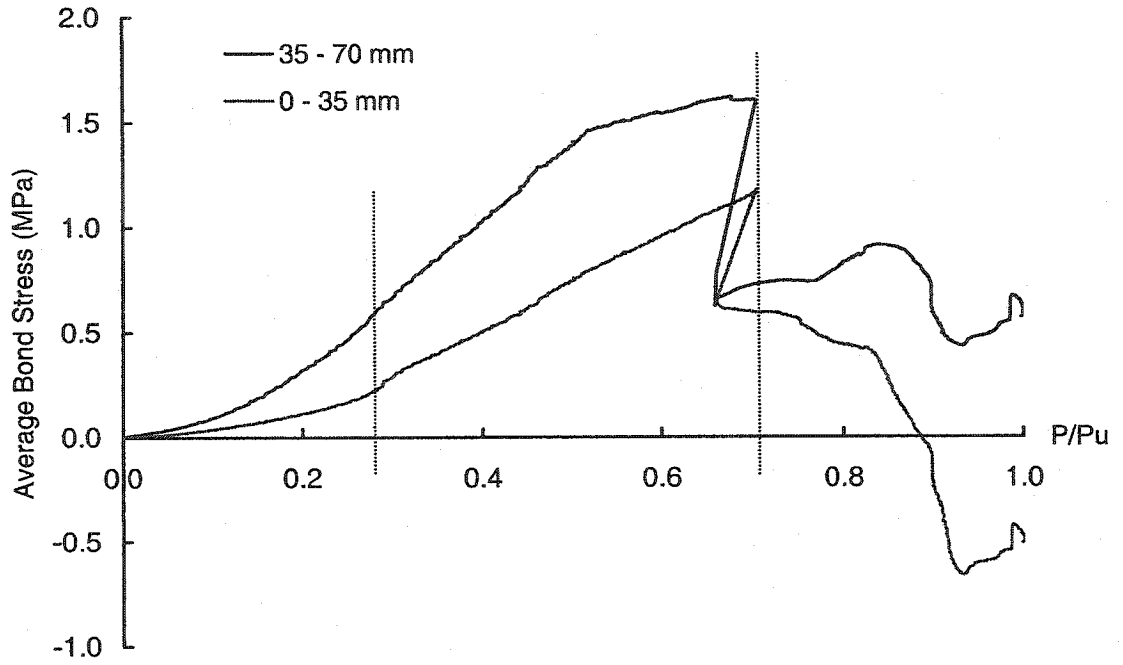


Figure 4-41 Average bond stresses across the sheet width vs. normalized load level, specimen P11

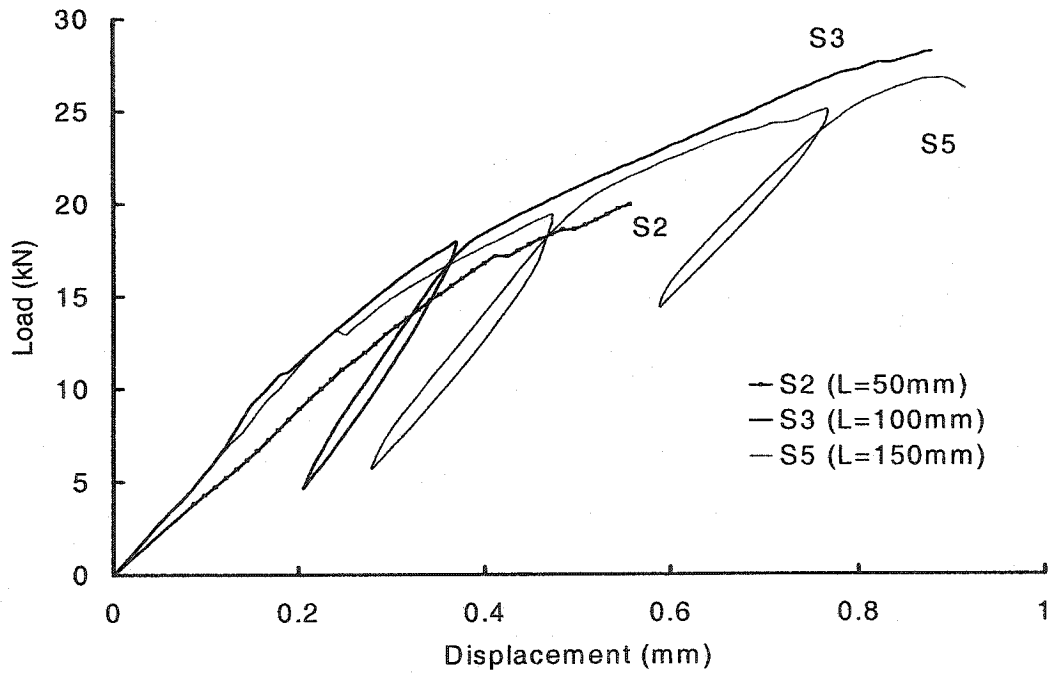


Figure 4-42 Response curves for specimens with $w = 150$ mm

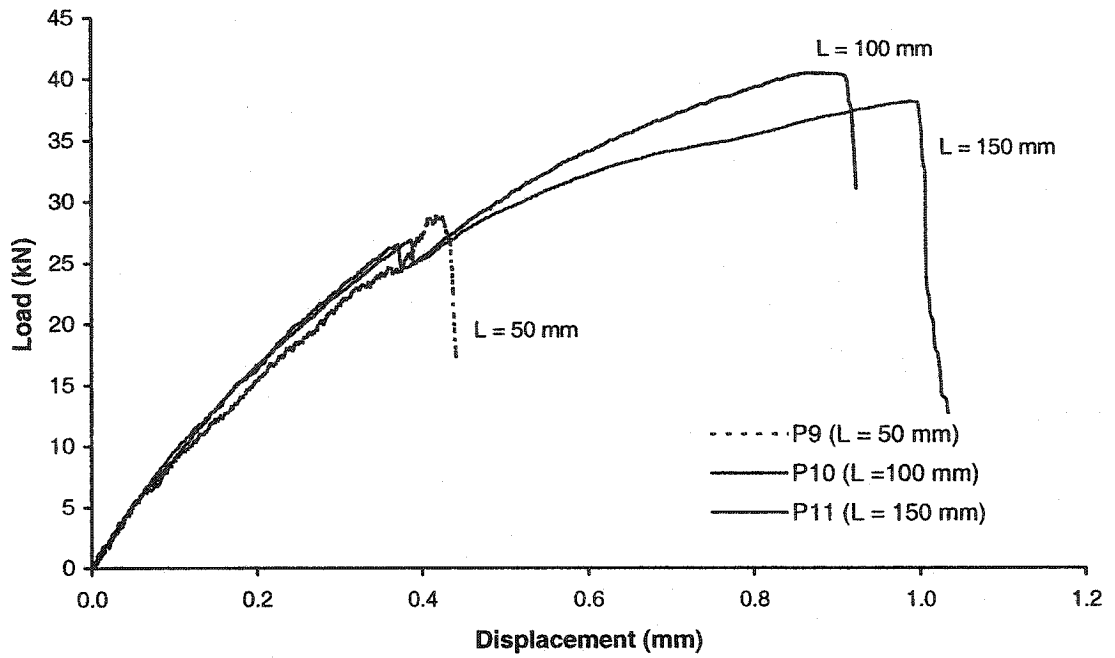


Figure 4-43 Response for specimens with $w = 150$ mm

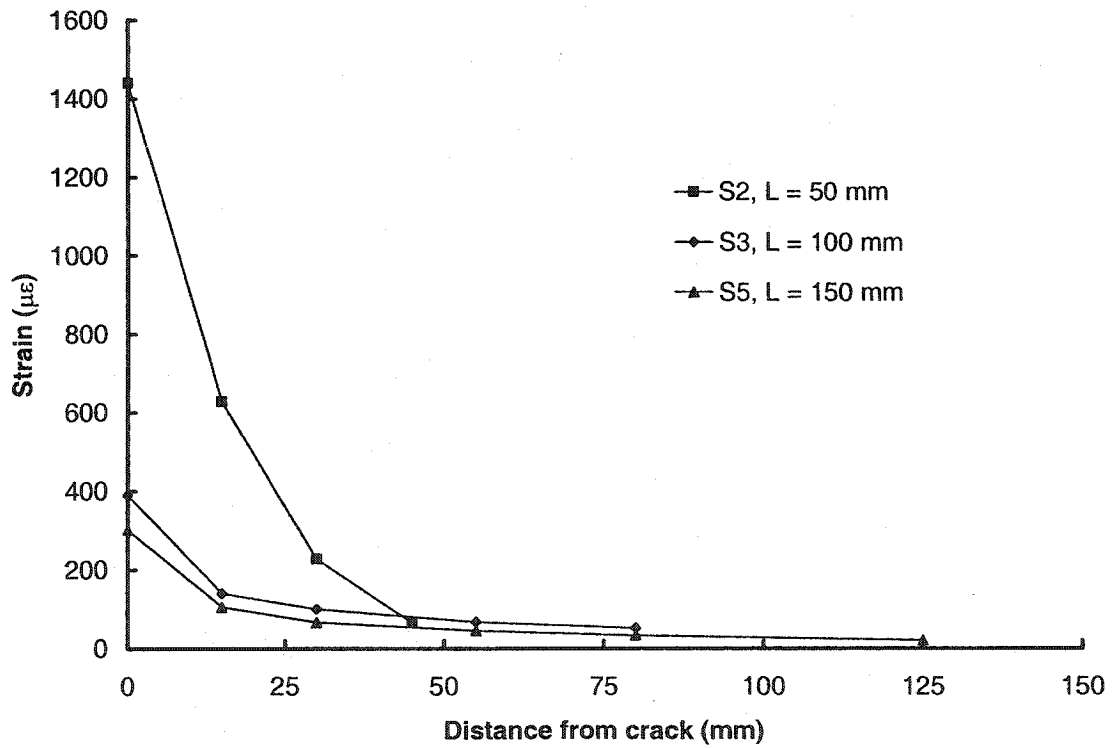


Figure 4-44 Strain distributions along the sheet centre at 20 kN, $w = 150$ mm

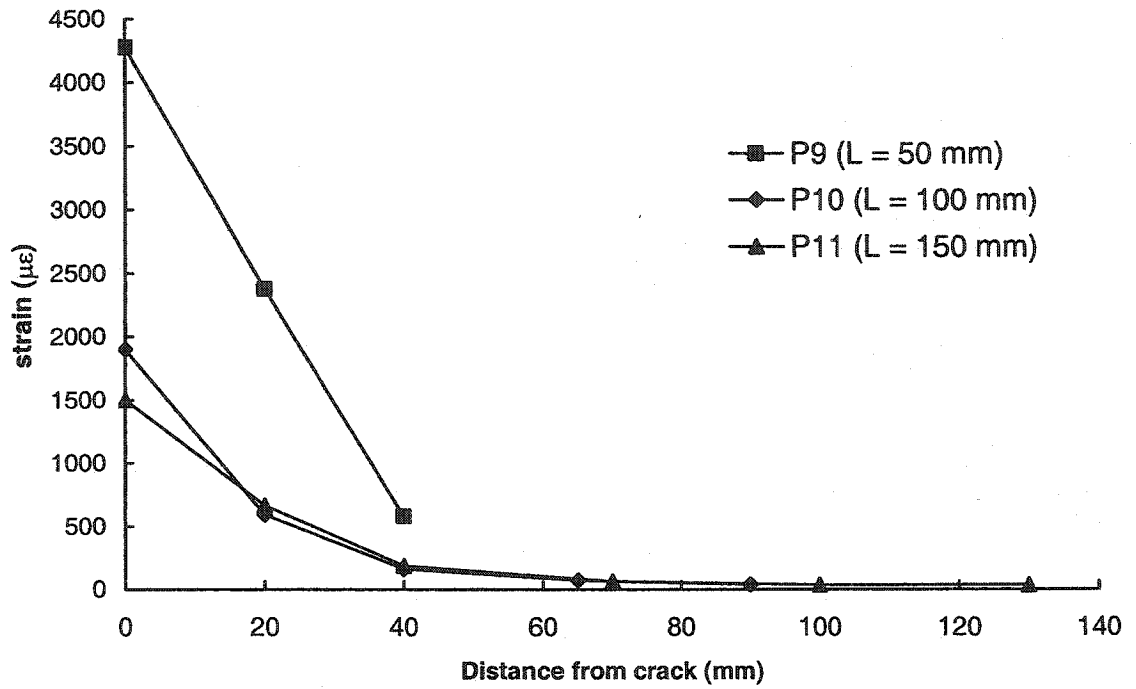


Figure 4-45 Strain distributions along the sheet centre at 20 kN, w = 150 mm

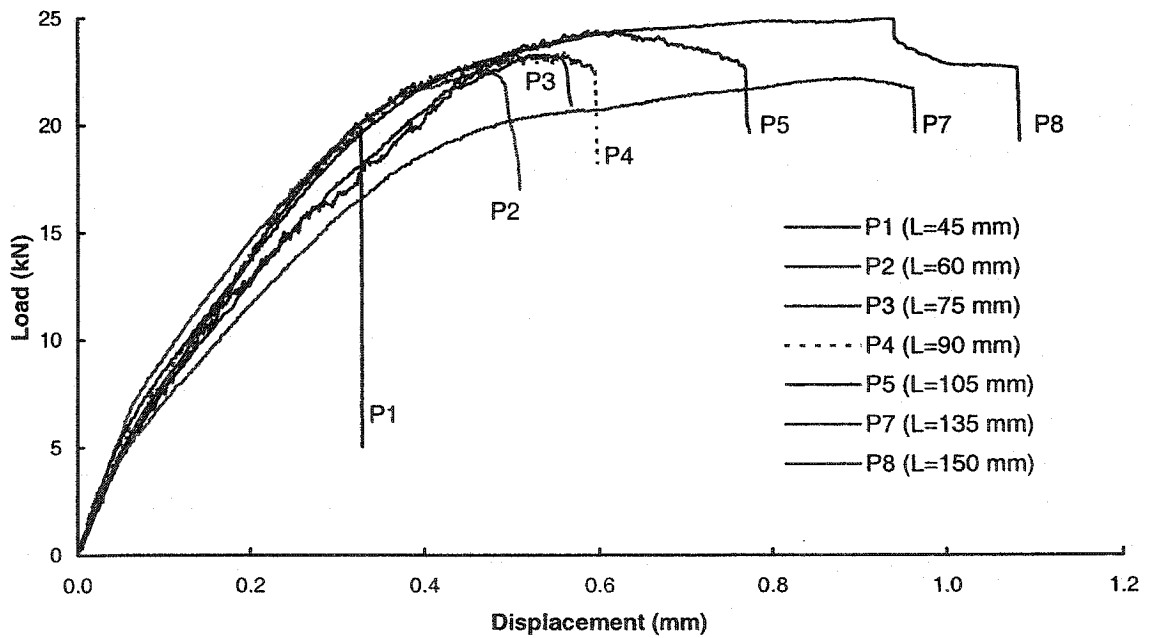


Figure 4-46 Response of specimens with the same sheet width, w = 100 mm

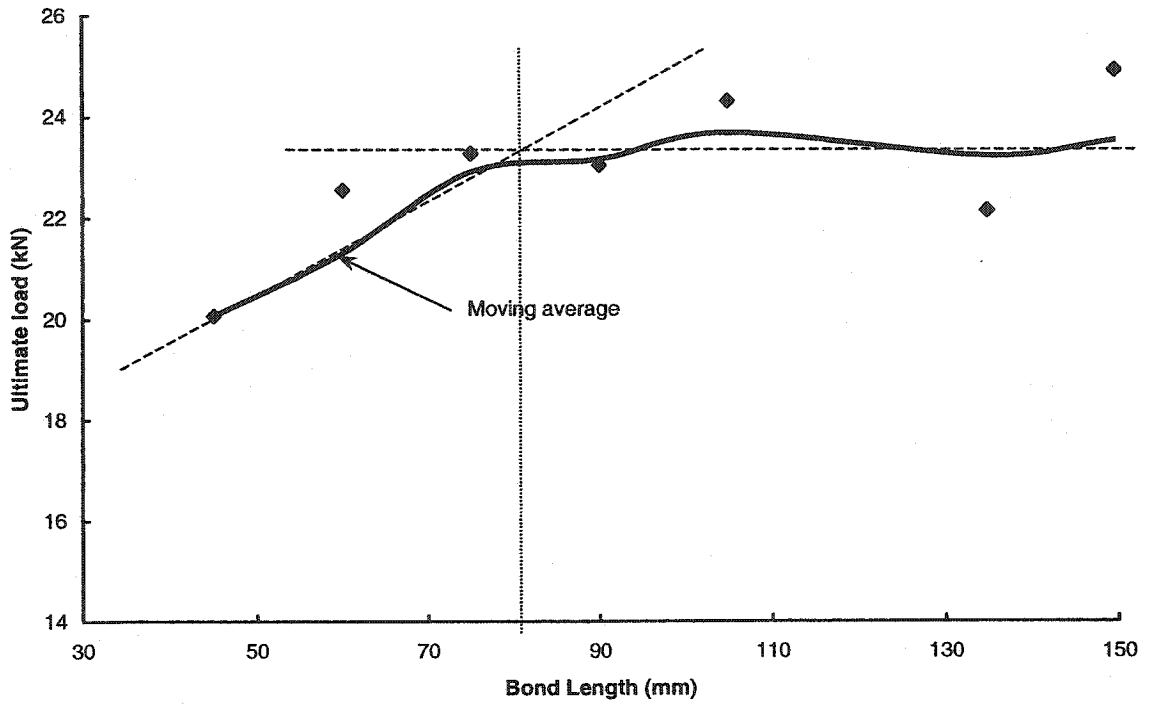


Figure 4-47 Load vs. bond length for specimens with $w = 100$ mm

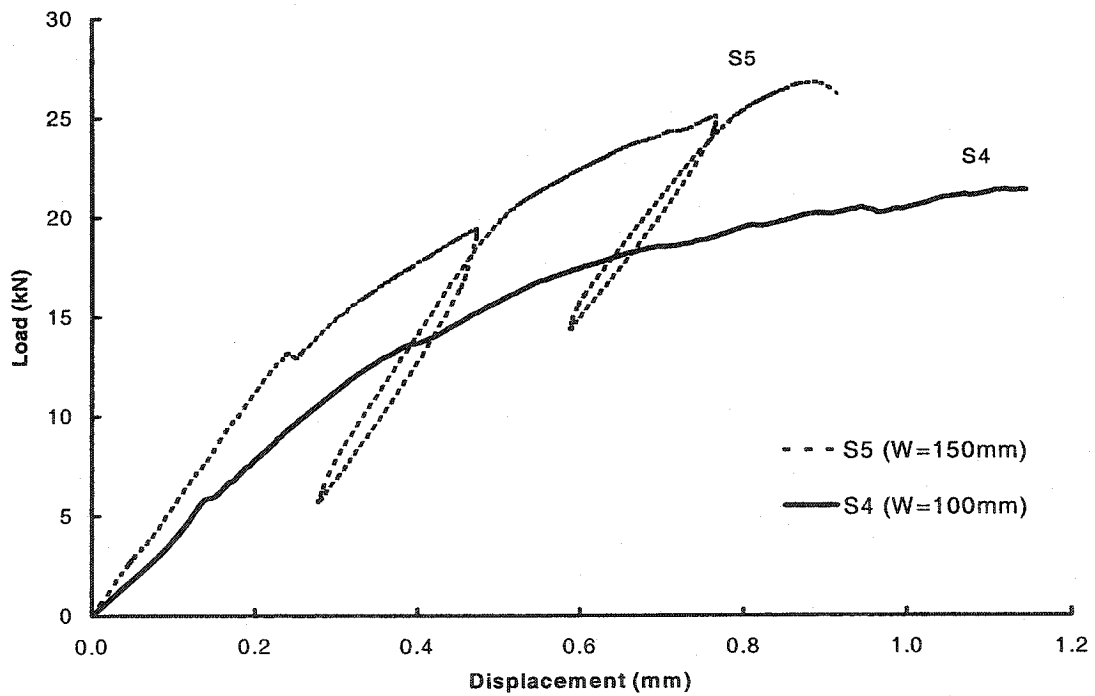


Figure 4-48 Response of specimens with $L = 150$ mm

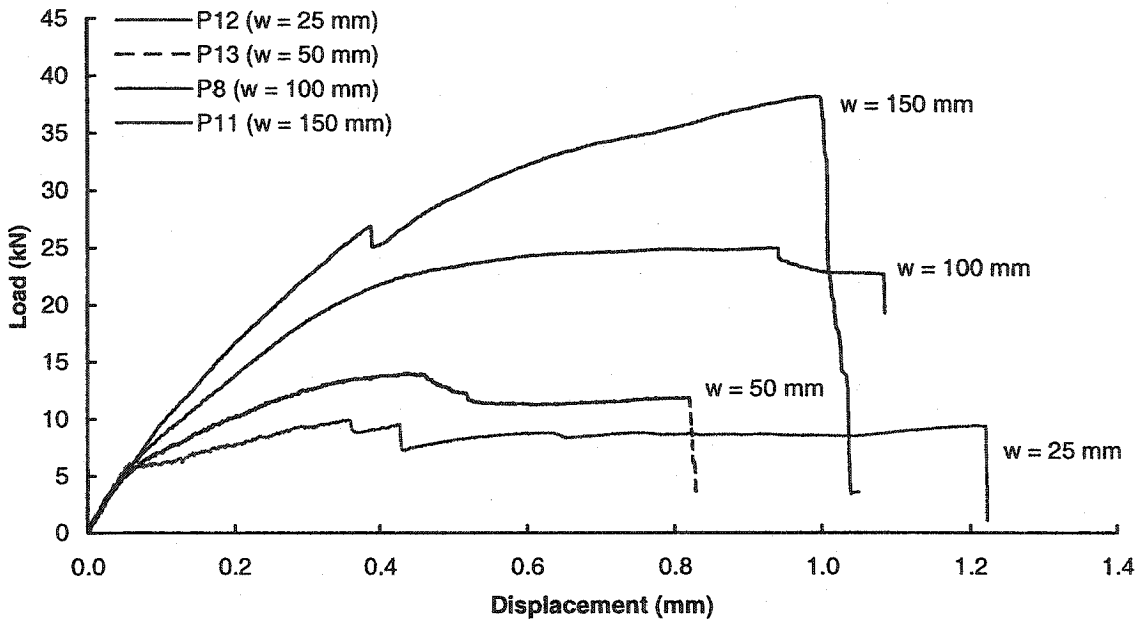


Figure 4-49 Response of specimens with $L = 150$ mm

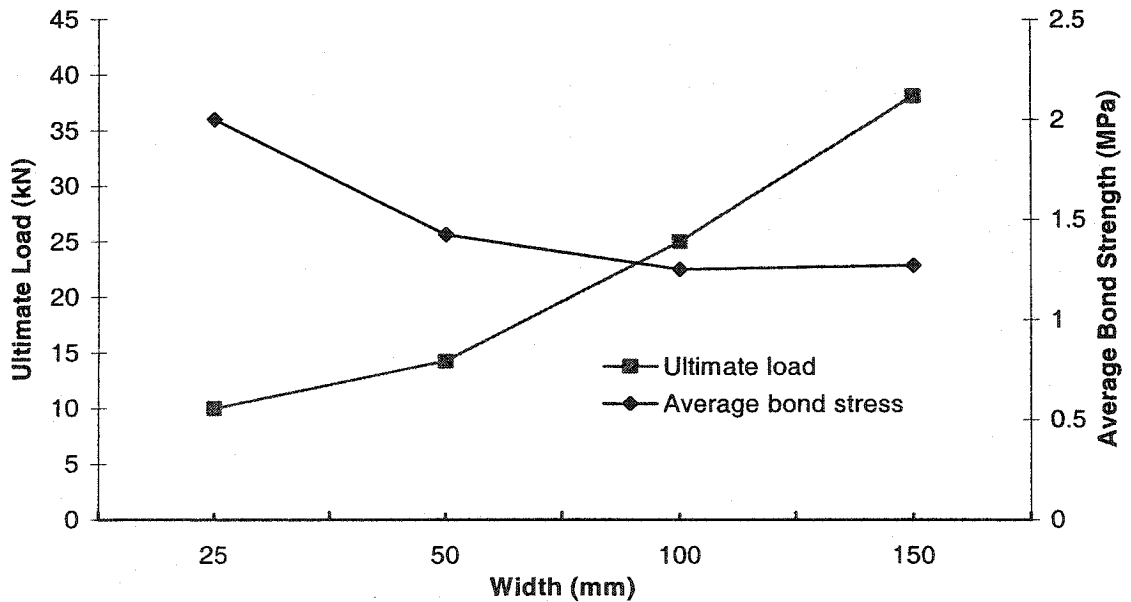


Figure 4-50 Width and average bond strength for P-series specimens, $L = 150$ mm

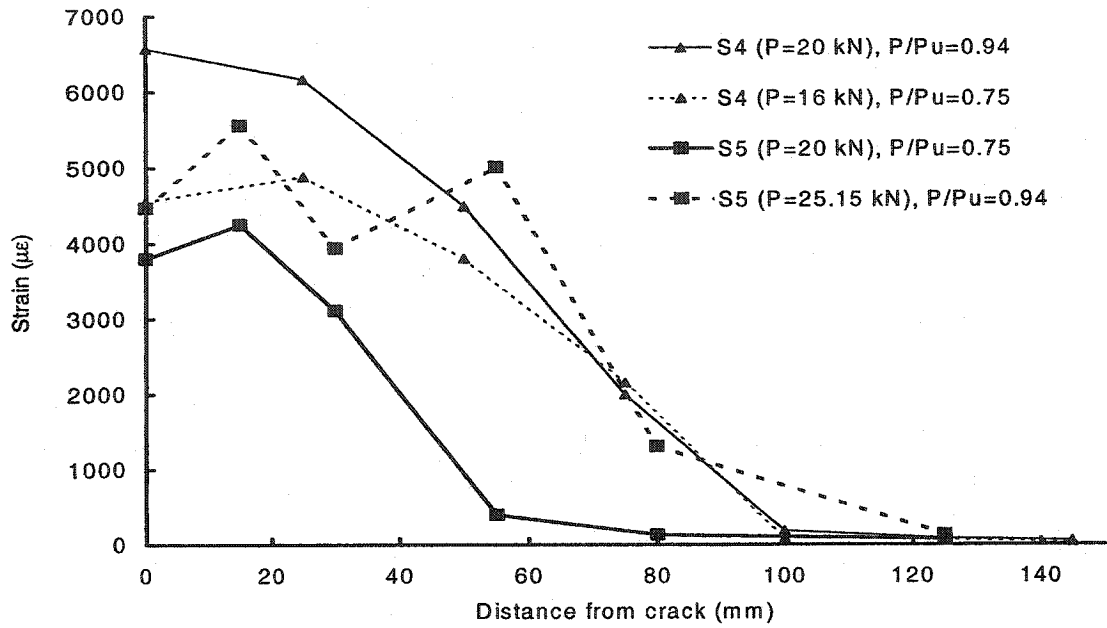


Figure 4-51 Strain distributions along centre of the sheet for S-series, L = 150 mm

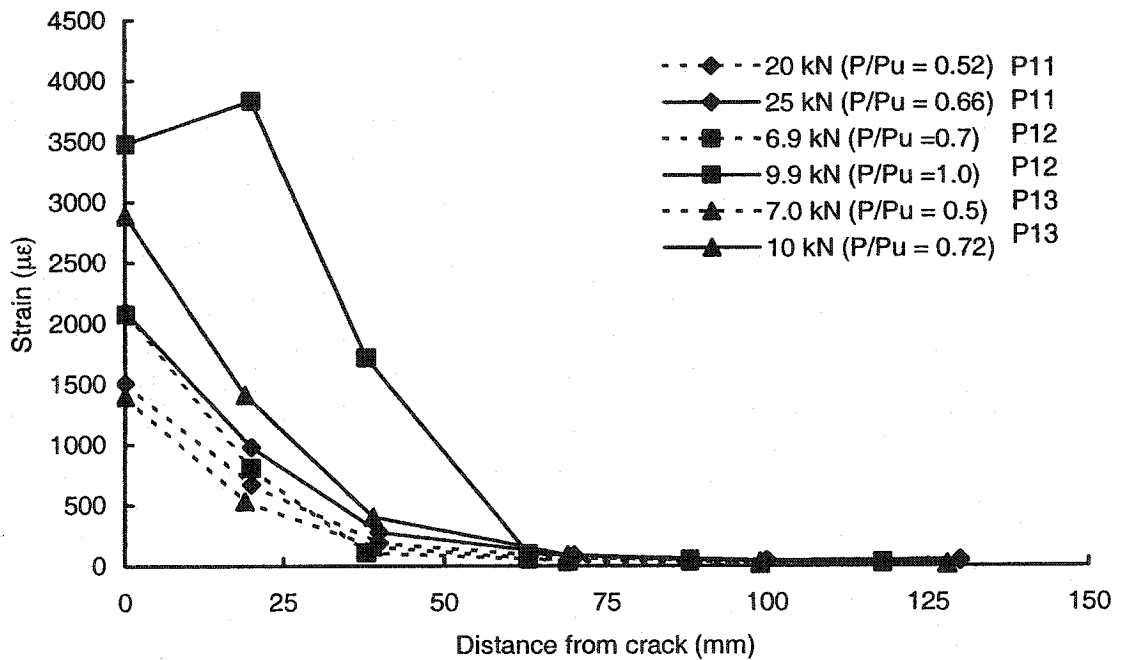


Figure 4-52 Strain distributions along centre of the sheet for P-series, L = 150 mm

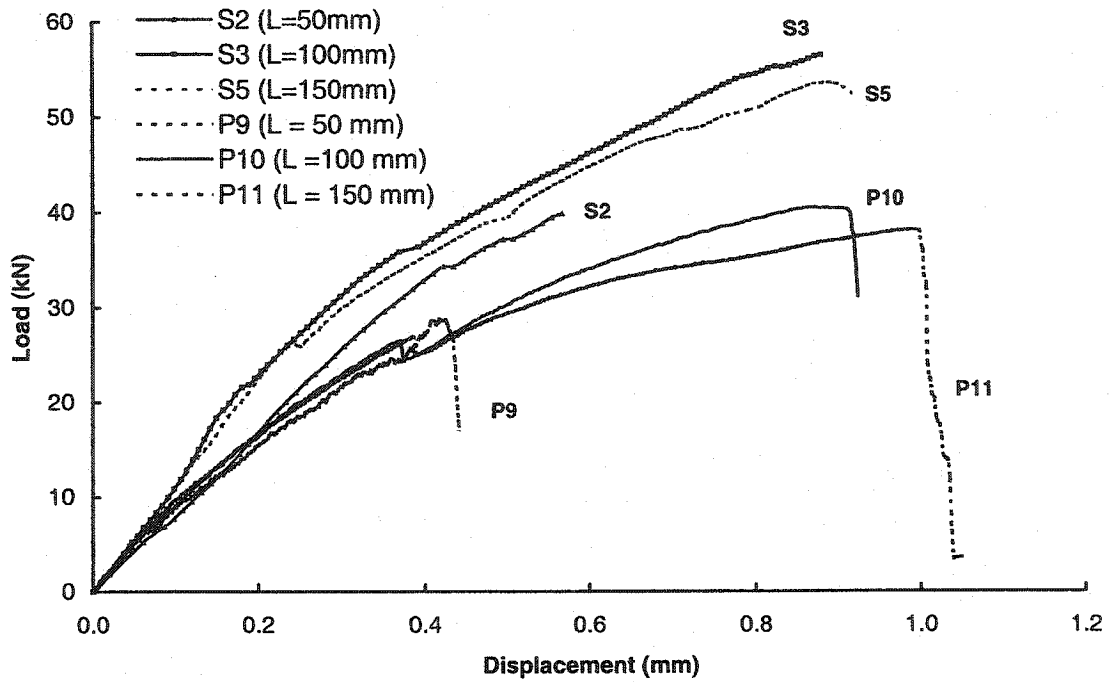


Figure 4-53 Response comparison for specimens with $w = 150$ mm

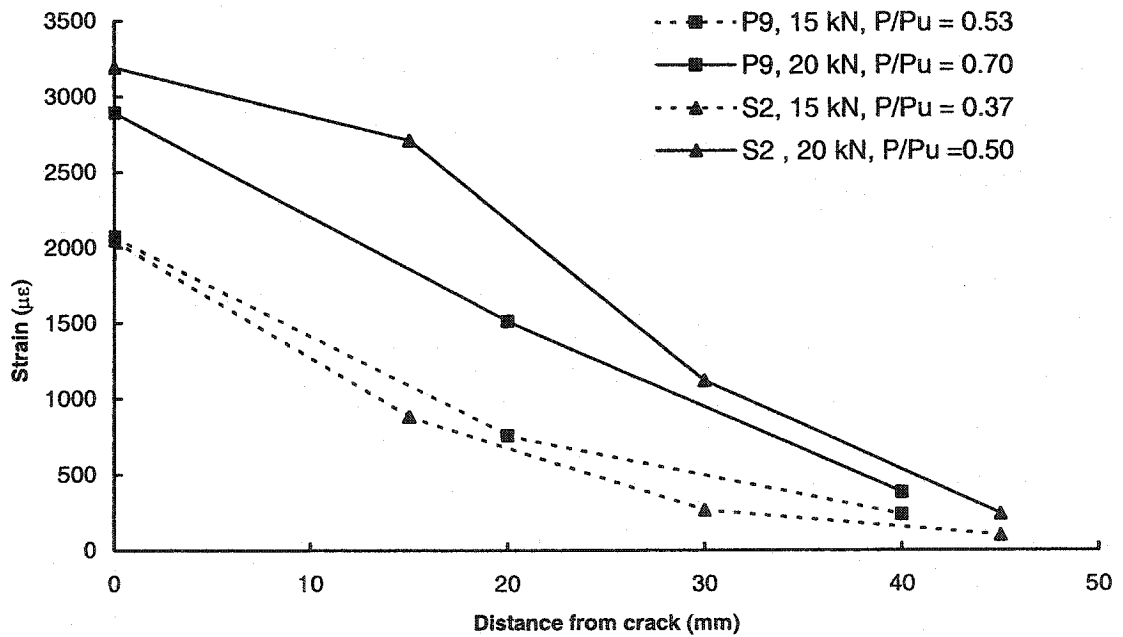


Figure 4-54 Strain distributions at centre of sheet for specimens P9 and S2

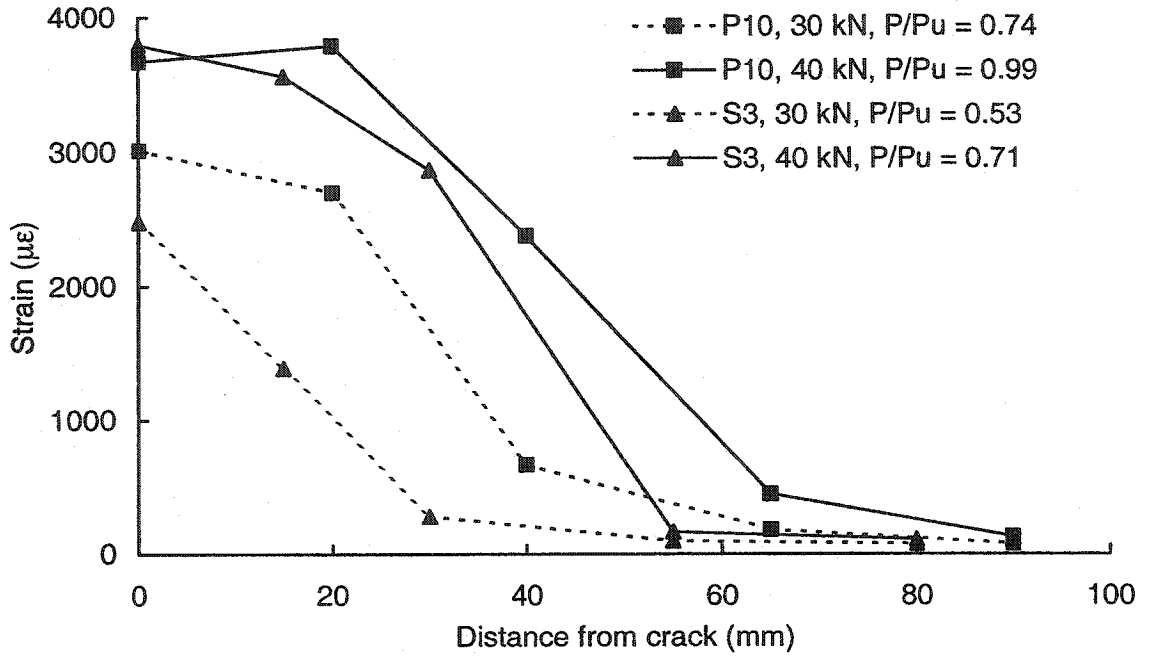


Figure 4-55 Strain distributions at centre of sheet for specimens P10 and S3

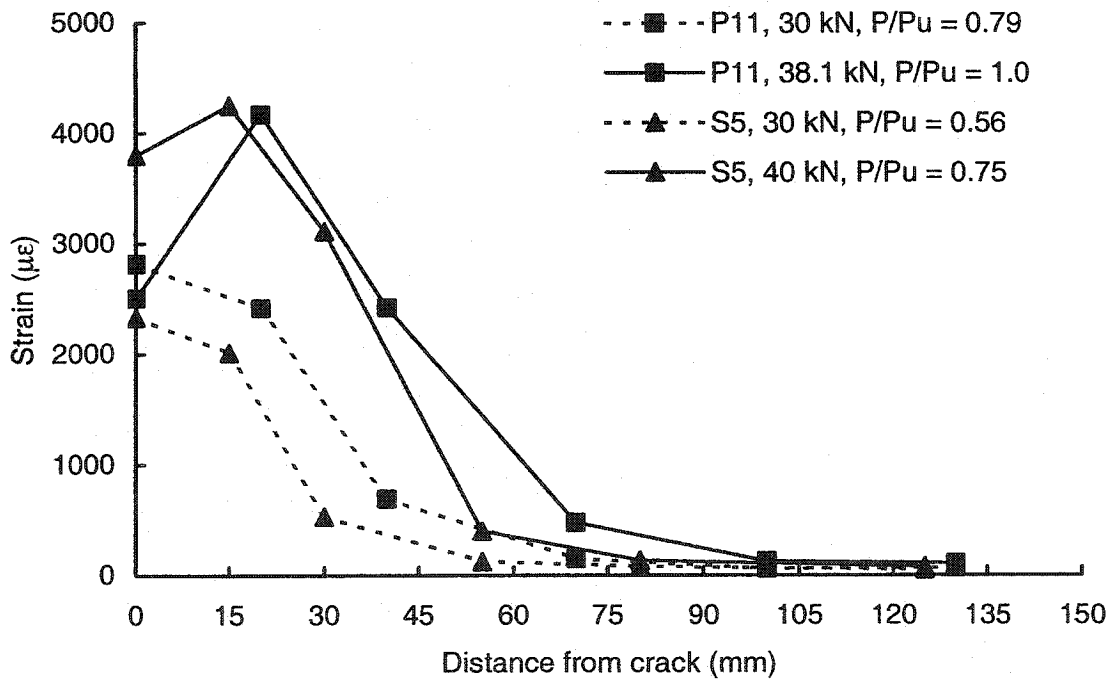


Figure 4-56 Strain distributions at centre of sheet for specimens P11 and S5

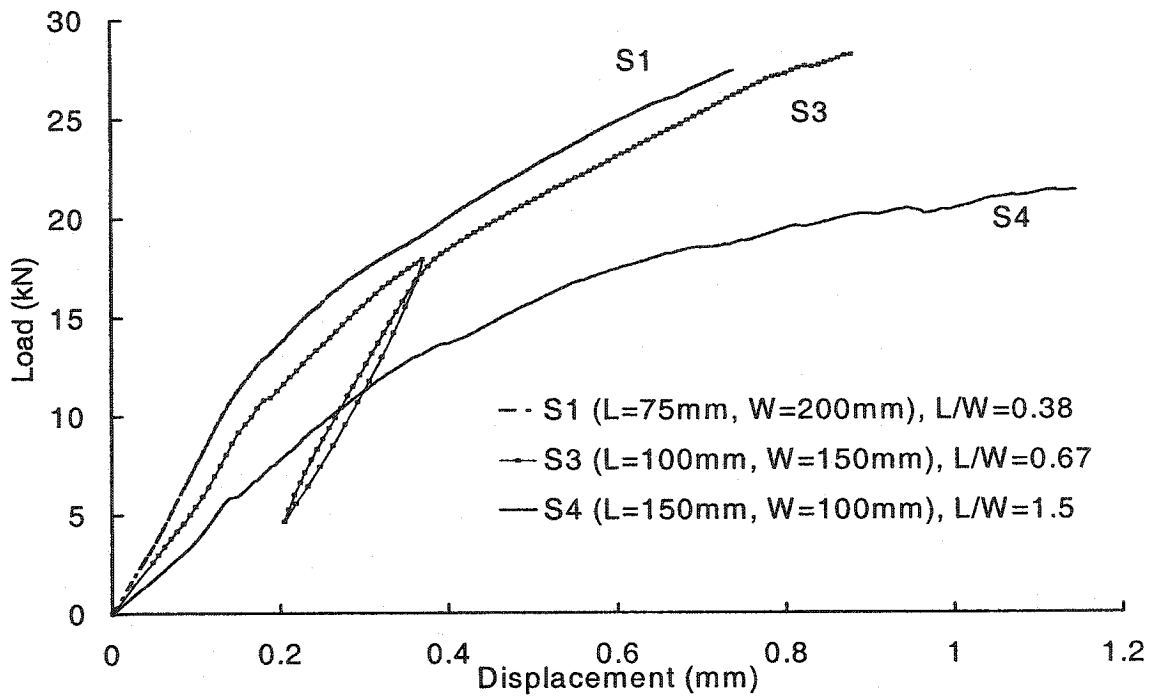


Figure 4-57 Response for specimens with the same bond area

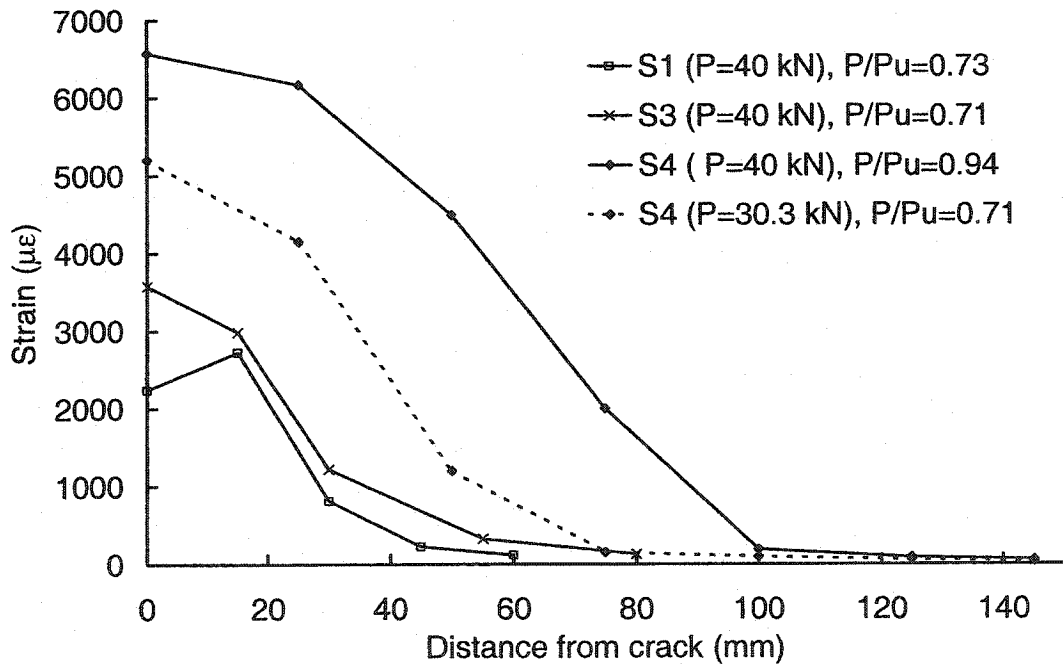


Figure 4-58 Strain distributions along the sheet centre, same bond area

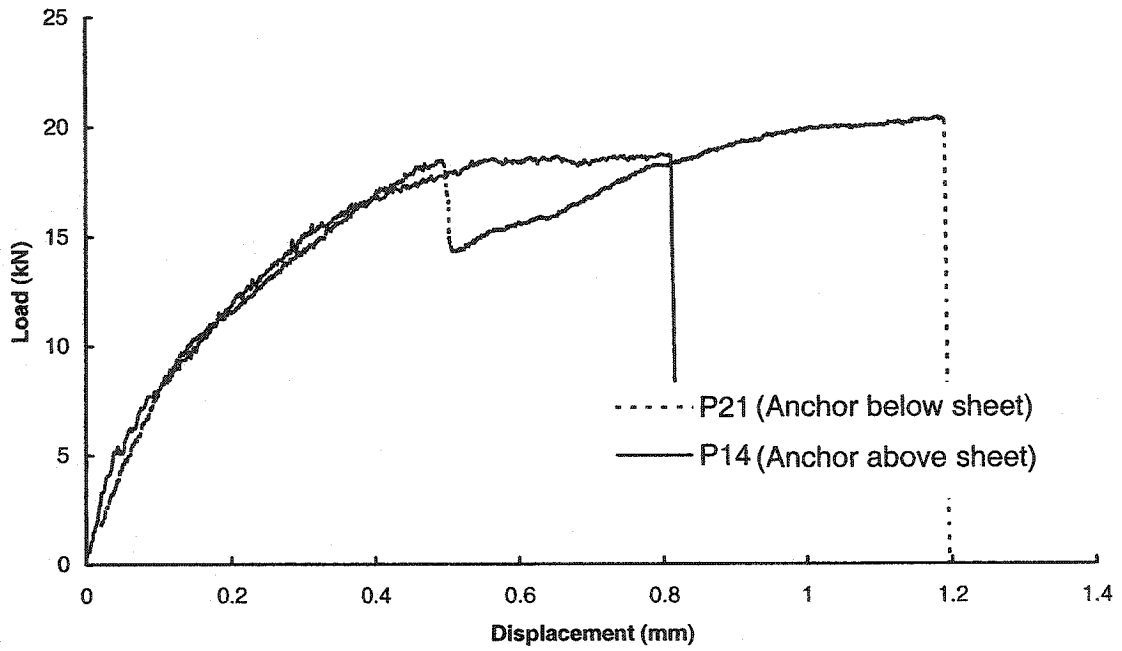


Figure 4-59 Response of specimens with $a = 0$ and $b = 75$ mm

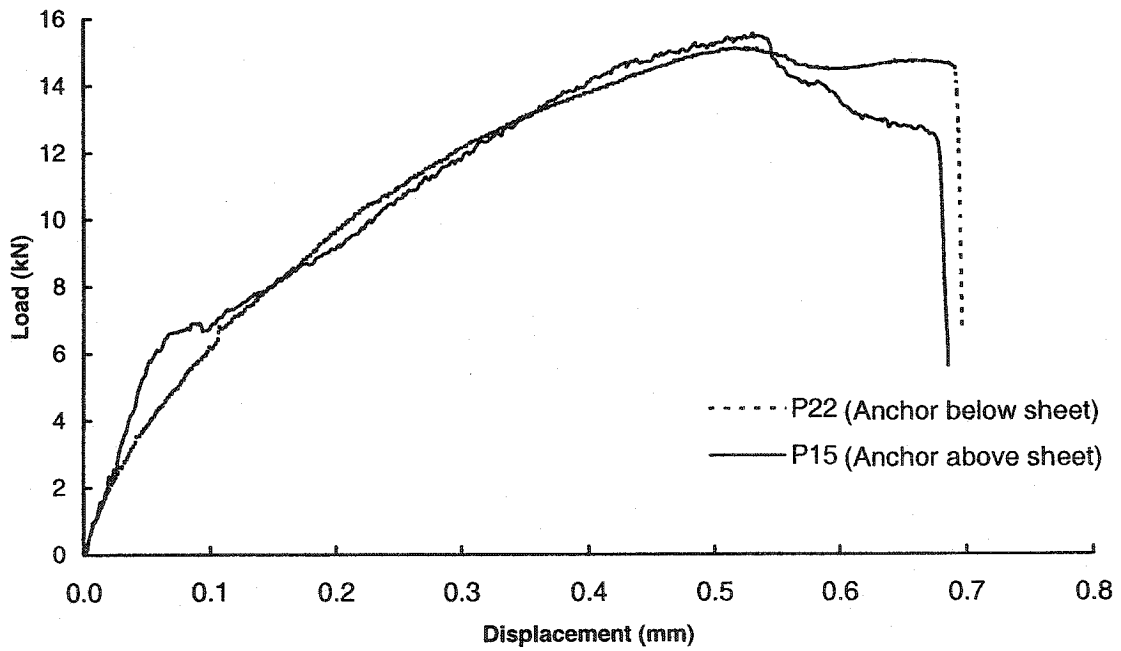


Figure 4-60 Response of specimens with $a = 25$ mm and $b = 75$ mm

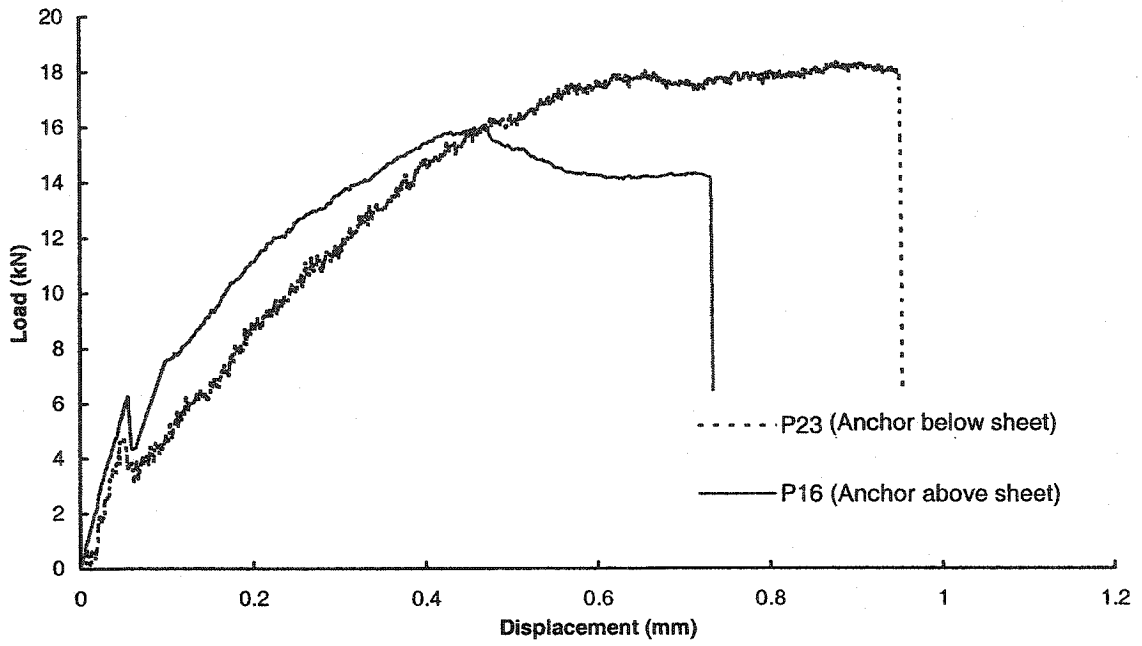


Figure 4-61 Response of specimens with $a = 50$ mm and $b=75$ mm

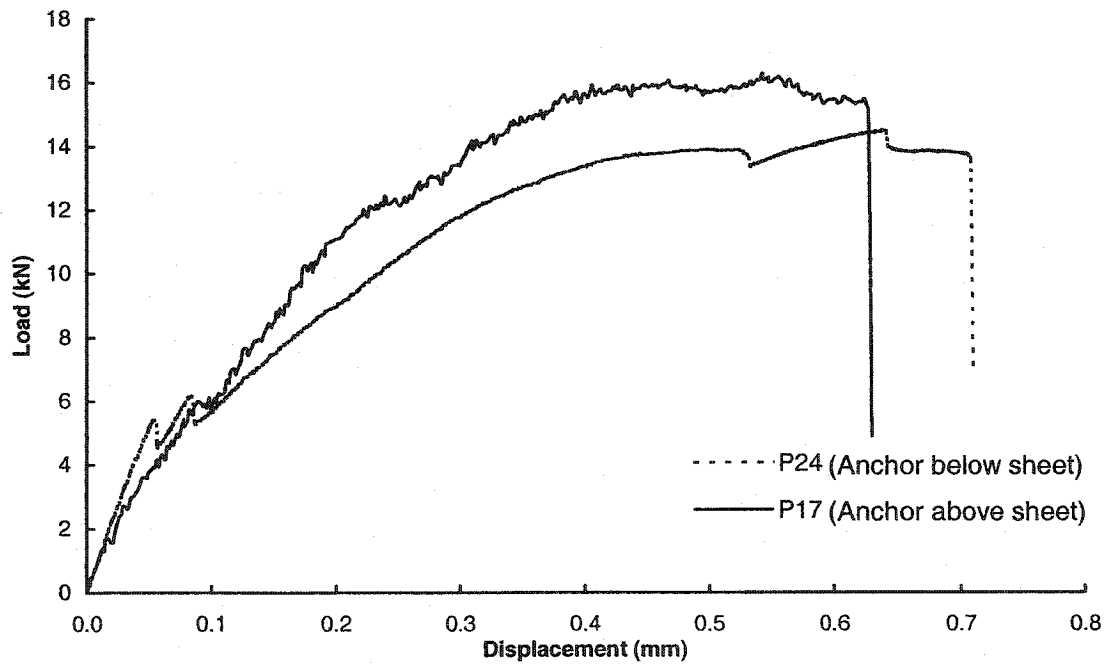


Figure 4-62 Response of specimens with $a =75$ mm, $b=75$ mm

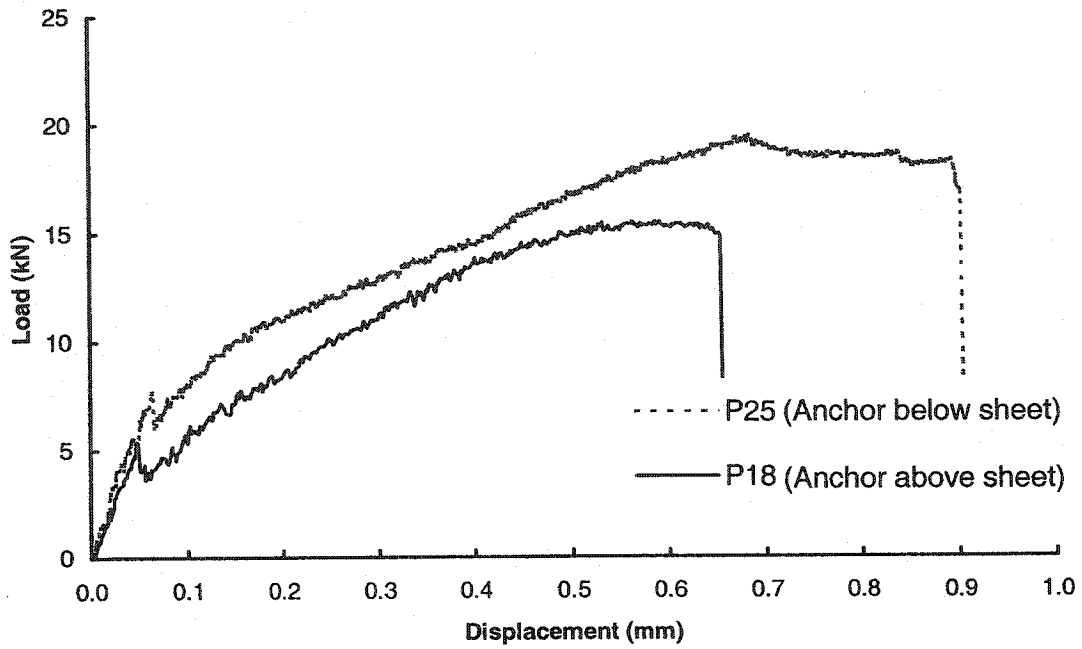


Figure 4-63 Response of specimens with $a = 25$ mm, $b = 50$ mm

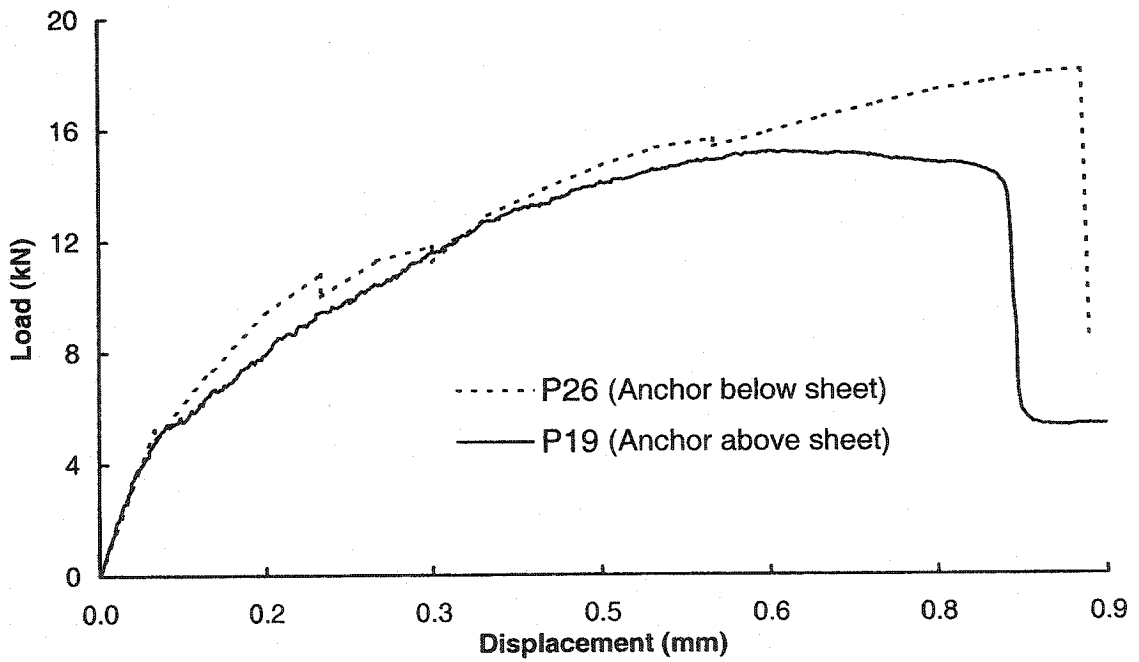


Figure 4-64 Response of specimens with $a = 25$ mm, $b = 25$ mm

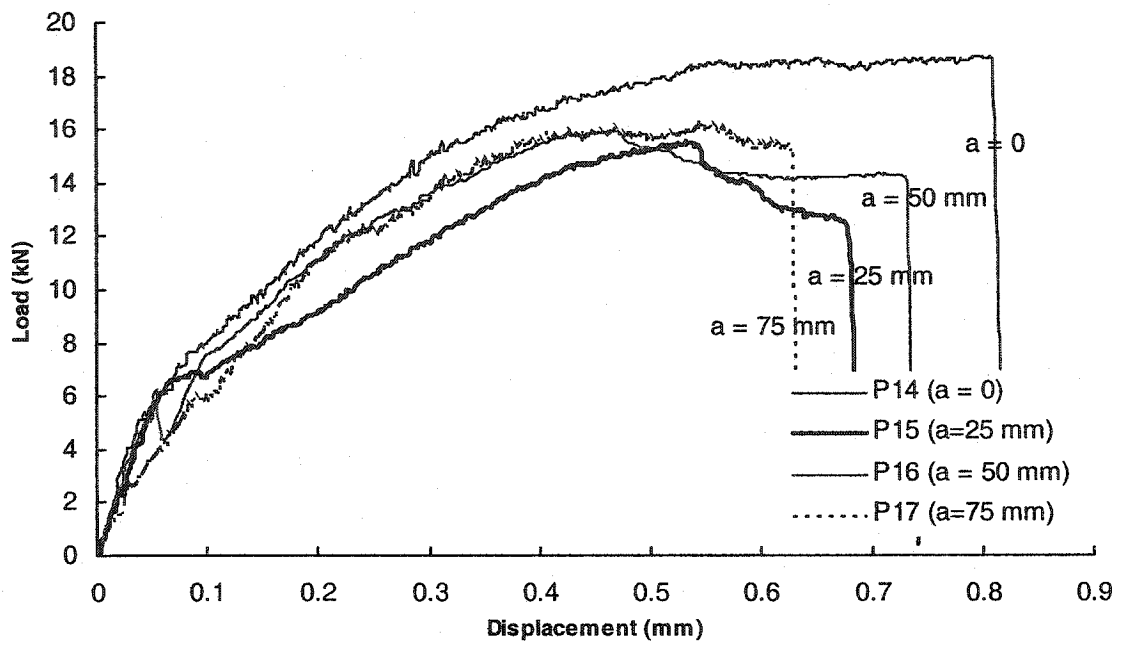


Figure 4-65 Effect of distance from crack “a”, anchor above and $b = 75 \text{ mm}$

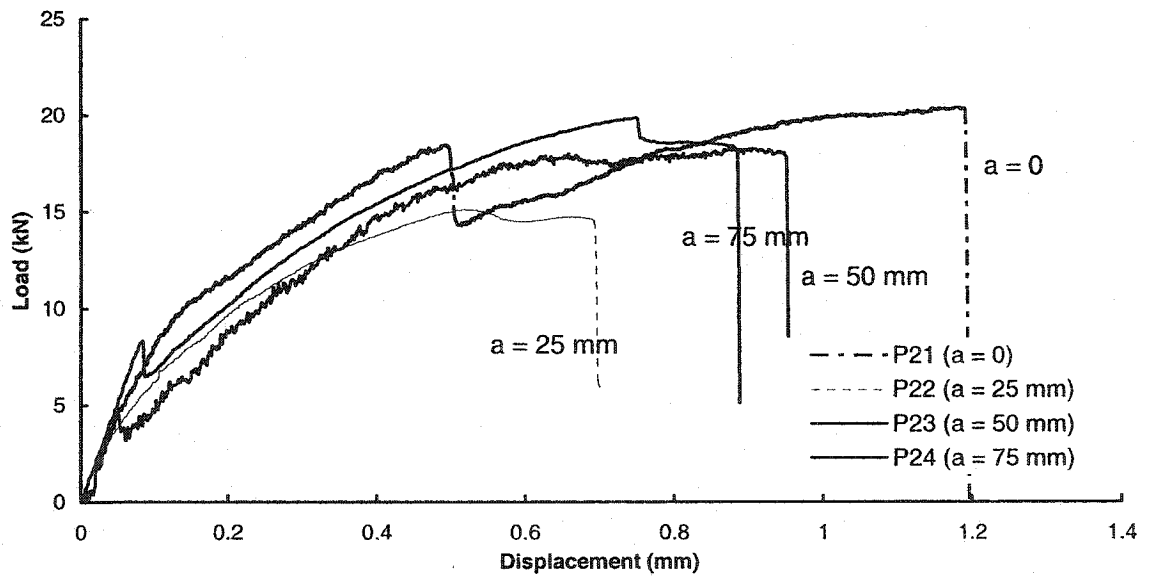


Figure 4-66 Effect of distance from crack “a”, anchor below sheet and $b = 75 \text{ mm}$

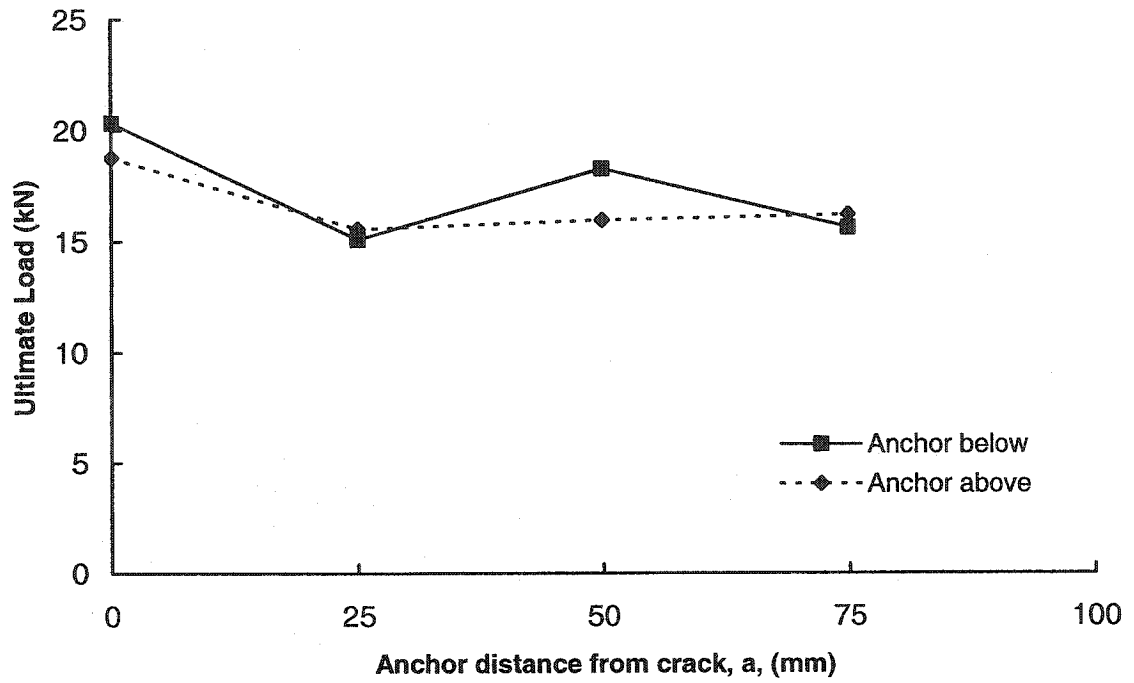


Figure 4-67 Anchor distance from crack for specimens with $b = 75$ mm

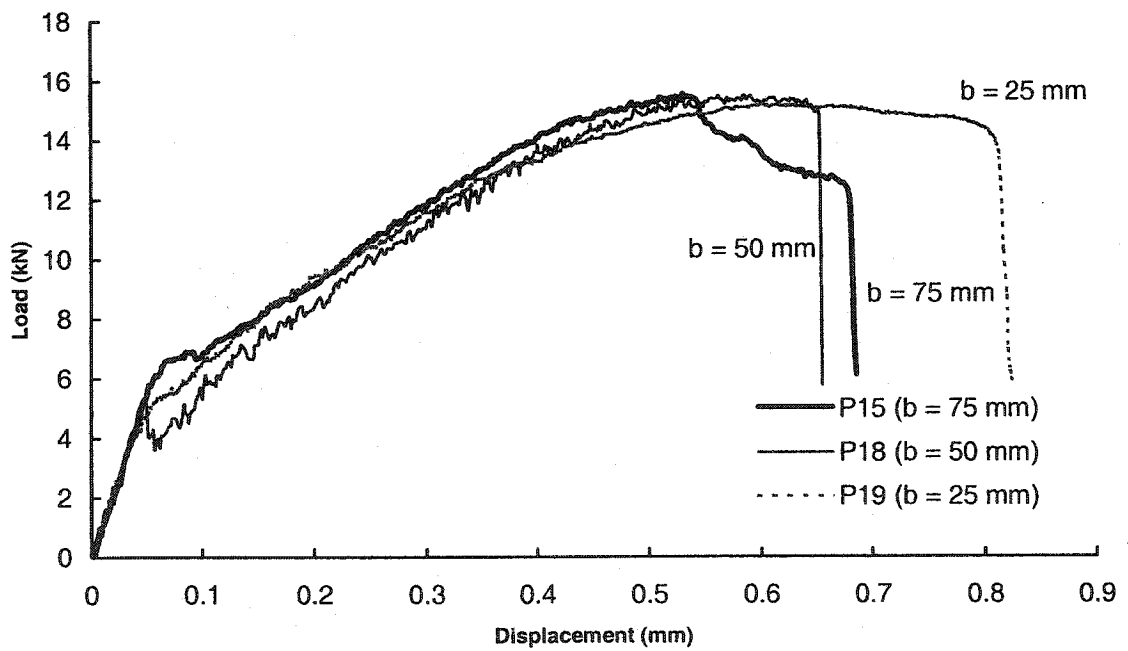


Figure 4-68 Effect of anchor extension beyond sheet "b" when the anchor is above the sheet and $a = 25$ mm

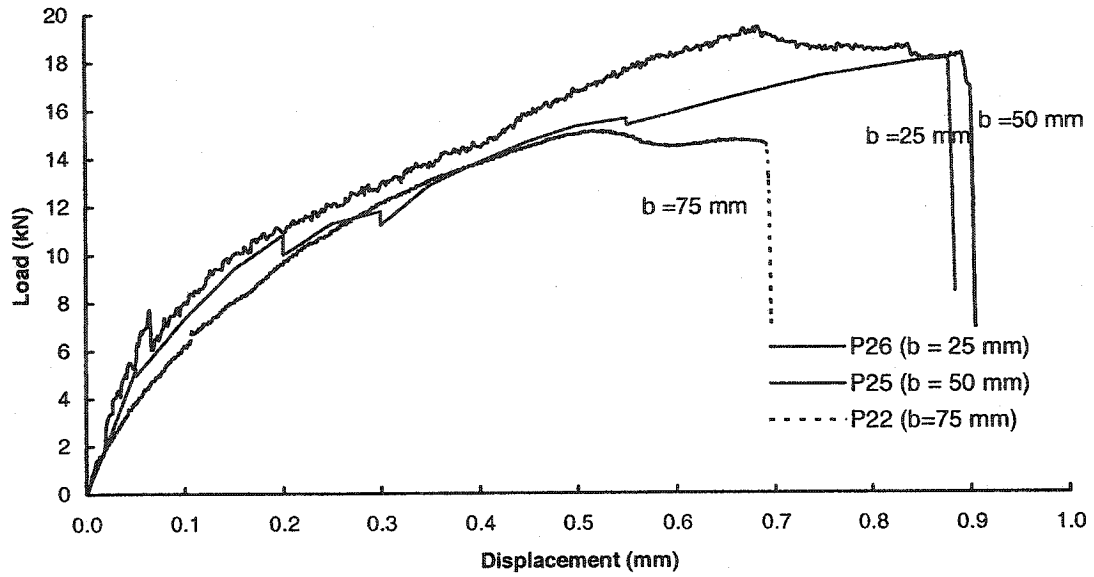


Figure 4-69 Effect of anchor extension beyond sheet “b” when the anchor is below the sheet and a = 25 mm

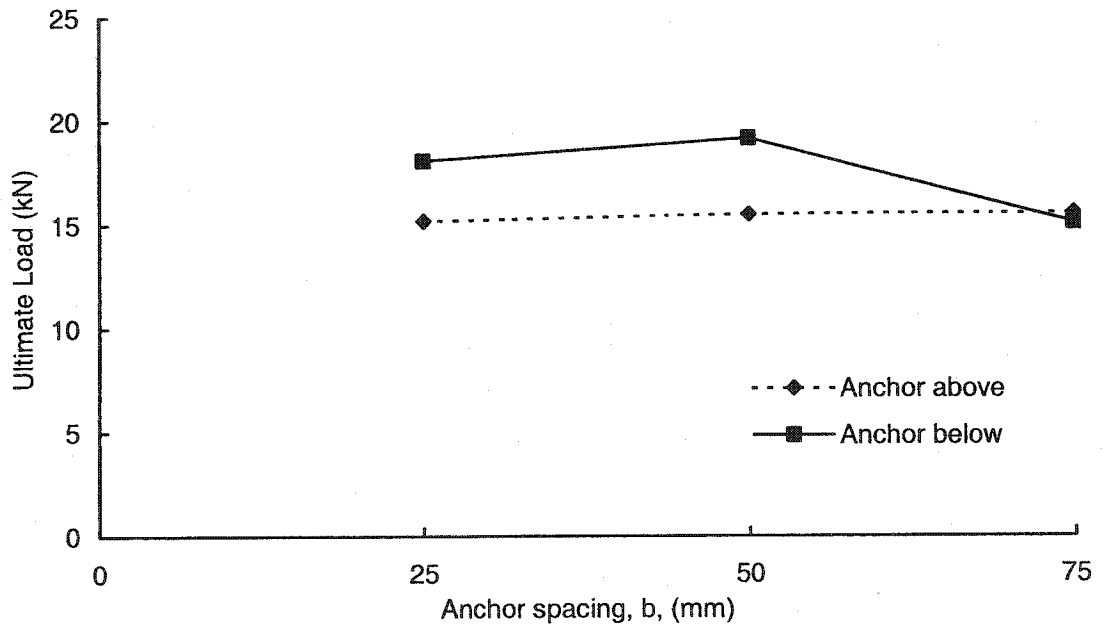


Figure 4-70 Anchor spacing for specimens with a = 25 mm

5. NUMERICAL MODELS

5.1. Introduction and Overview

Chapters 3 and 4 described in detail the parameters tested experimentally in this research. These parameters covered a limited range of variability. In order to extend the range, a number of finite element models were developed. In this chapter these models are verified against the test results, and are used in the following chapters to produce additional data for the development of design charts and guidelines.

Two types of models were developed: using the commercial finite element program ABAQUS (1998) two-dimensional (2D) and three-dimensional (3D) models. Two 2D non-linear finite element models were developed, one each to simulate the modified push-apart test and the pull-apart test; both were previously tested experimentally and detailed in Chapter 3. As mentioned above, 3D non-linear finite element models were also developed in order to study the strain distribution across the width of the CFRP sheets, which could not be performed using the 2D models. The numerical models were developed with the objective to conduct a parametric study on the main parameters affecting the bond behaviour between FRP sheets and concrete. The effect of the type of test conducted on the test results was also investigated using the numerical models. To confirm the validity of the models, the output was compared to the experimental results from the test series detailed in Chapters 3 and 4. All the models are detailed and discussed in this chapter together with a comparison between the numerical output and experimental results.

The formulation of the problem in all cases was based on small displacements and infinitesimal strains. Material nonlinearities were accounted for as well as debonding in the form of interface surfaces, where possible. The analysis was conducted incrementally with equilibrium established in every increment iteratively.

5.2. Geometric Modeling

5.2.1. 2D Models

Only one half of each specimen in both the modified push-apart test and the pull-apart test was modeled making use of symmetry along the line of action of the loads, which is shown as axis of symmetry 1 in Figure 5-1 and Figure 5-2. There was no symmetry along axis of symmetry 2 in both tests because of the existence of an anchor sheet on one side of the tested sheet, which was placed in order to ensure the failure of the other unanchored side. The effect of the anchor sheet was taken into consideration in the model as will be explained later. The geometry and mesh dimensions of the modified push-apart test model and half the pull-apart test model are illustrated in Figure 5-3 and Figure 5-4.

The concrete mesh was built from 10×10 mm four-node plane stress elements with reduced integration (ABAQUS element CPS4R). The 10×10 mm dimension was the minimum mesh size, considering the maximum aggregate size used in the specimens. Reduced integration was used in order to soften the behaviour of the model because numerical solutions using four node elements are generally stiffer than observed in the experiments (Bathe, 1996). First order quadrilateral elements with reduced-integration were also chosen based on recommendations of ABAQUS/Standard (1998) for their use in problems involving contact or large distortions.

The CFRP sheet mesh was built of 0.38×10 mm CPS4R elements, where the thickness of the sheet was 0.38 mm and the 10 mm side was taken similar to the concrete mesh dimension to facilitate the formation of the initially bonded condition. Four-node plane stress elements were also used here similar to the concrete elements for compatibility at the contact nodes. Node to node correspondence was established with the adjacent elements at the concrete surface. Contact and debonding are modelled at that interface.

The steel rebars in the modified push-apart model were modeled using one-dimensional strain compatible threads that can be defined singly or embedded in oriented surfaces. These elements are superposed on the mesh of plain concrete elements and are used with a standard metal J2 plasticity material constitutive relation.

On the other hand, the steel rebars in the pull-apart test were modeled using 10 mm long truss elements. The rebars were 400 mm long with 250 mm of their length embedded in the concrete specimen. Since half of the specimen was modeled along the rebar axis, only half the bar cross-section area was specified.

The 20 mm thick steel plate used to uniformly distribute the load to the inner face of the modified push-apart specimen was modeled with a mesh composed of 10×20 mm CPS4R elements. The elements dimensions were taken to match the concrete elements. Figure 5-3 and Figure 5-4 show the geometry and mesh of the 2D modified push-apart and half the pull apart models, respectively.

5.2.2. 3D Models

Due to symmetry in geometry and loading, one eighth of both the modified push-apart specimen and the pull-apart specimen were modeled along the planes of symmetry 1, 2 and 3 shown in Figure 5-5a and Figure 5-6a. This reduced significantly the size of the models and in return reduced the computational time. The portion that was modeled is shown in Figure 5-5b and Figure 5-6b for a typical modified push-apart specimen and a typical pull-apart specimen, respectively.

Concrete was modelled with a fine mesh at the bonded CFRP sheet locations in the modified push-apart model in order to obtain more accurate results at the stress concentration zones. A coarse mesh was used at locations away from the stress concentrations in order to reduce the mesh size and in turn the computational time. The fine mesh in the modified push-apart model was built from 10×10×10 mm eight-node cube elements with reduced integration (C3D8R), where the cube size was limited by the

maximum aggregate size of 10 mm used in the specimens. The pull-apart model had a concrete mesh built from 10×10×10 mm C3D8R; the model was relatively small.

The mesh for the CFRP sheet was built from 10×10 mm four-node shell elements with reduced integration. The 10×10 mm dimensions were taken similar to the corresponding concrete element mesh dimension at the face to facilitate bonding the corresponding nodes together for compatibility at the contact surface. The thickness of the shell elements was 0.38 mm, which is the CFRP sheet thickness in the experimental tests.

The steel rebars in the modified push-apart model were simulated using one dimensional strain compatible threads, similar to those used in the 2D model. The steel rebar in the 3D pull-apart model was modeled using 10×10×10 mm C3D8R elements, where the use of line elements caused local failure and distortion of the concrete elements at the loaded embedded rebar to concrete location. Since one eighth of the specimen was modeled along the rebar axis, only one column of elements was specified for the rebar. The rebar elements were continuous inside the concrete mesh and were assumed to have perfect bond with the concrete.

The steel plate used to load the specimen in the modified push-apart model was modeled with a mesh of 10×20×30 mm C3D8R elements. The 10×30 mm dimensions were taken similar to the opposing concrete element face dimension for compatibility at their interface and the 20 mm side was the thickness of the steel plate.

Figure 5-7a and Figure 5-8 show the geometry and mesh of the 3D modified push-apart and pull apart models, respectively.

5.3. Boundary Conditions and Loading

The modified push-apart tests were self-contained with the load applied with a hydraulic jack placed in the core of the concrete specimen. The specimen is placed on a

flat steel surface with the hydraulic jack placed on steel saddles in a horizontal position. On the other hand, the push-apart tests were placed vertically in a universal testing machine with the load applied to the specimen through the rebars. Symmetry was utilized in order to simplify the models and to reduce computational time. The proper boundary conditions at the axis and planes of symmetry for the 2D and 3D models, respectively, were applied and are illustrated and explained in the following subsections.

5.3.1. Boundary Conditions and Loading of 2D Models

One half of the modified push-apart and pull-apart specimens was modeled making use of the symmetry along the line of action of the load, which is axis of symmetry 1 in Figure 5-1 and Figure 5-2. Rollers were taken along axis of symmetry 1 in the figures, where the movement was allowed in the direction of the load and was restrained in the perpendicular direction. The boundary conditions for the modified push-apart and pull-apart 2D models are shown in Figure 5-3 and Figure 5-4, respectively.

The load was applied quasi-statically to the models in a displacement control mode, which is similar to that employed in the experimental tests. Displacement control was implemented in the model as a roller support that moves with specified increments of displacement. The load location was at the centre of the steel bearing plates in the modified push-apart model, where the hydraulic jack applied the load to both ends. On the other hand, the load location for the pull-apart model was at the end of one of the steel bars while the other end had a hinge preventing movement and rotation in all directions, which simulates the machine grip in the experimental tests. An initial displacement of 0.01 mm was applied with increments of 0.01 mm for a total displacement of 1.0 mm, which was taken higher than the maximum displacement in the experimental tests.

5.3.2. Boundary Conditions and Loading of 3D Models

As mentioned in Section 5.2.2, one eighth of both the modified push-apart specimen and the pull-apart specimen were modeled in the 3D models due to symmetry along the planes of symmetry 1, 2, and 3, shown in Figure 5-5a and Figure 5-6. Rollers were placed along planes of symmetry 1, and 2. The rollers allowed the movement of the

joints in the direction parallel to the planes of symmetry but restrained their movement in the perpendicular direction due to symmetry in geometry and loading. Rollers were also placed at the FRP sheet intersection with the plane of symmetry 3. The boundary conditions for the modified push-apart and pull-apart 3D models are shown in Figure 5-7b and Figure 5-8, respectively.

The end of the steel rebar was fixed in order to simulate the test machine grips on the bar ends. The load was applied quasi-statically to the models in displacement control similar to the 2D model except that the analysis procedure was different as will be discussed in Section 5.6.

5.4. Material Properties

The material properties in the models were taken similar to those obtained from the experimental test program, while properties that were unavailable from the tests were reasonably assumed. The materials used in the experimental tests were concrete, CFRP, adhesive, and steel. The modeling of each material property in the numerical model is discussed in detail in the following subsections.

5.4.1. Concrete

The constitutive theory implemented in the ABAQUS concrete material model was used and is fairly simple. When the principal stress components are predominantly compressive, the response of the concrete is modeled with an elastic-plastic constitutive theory, using a simple form of yield surface. In that case, associated flow is assumed and isotropic hardening values are used. In tension, however, cracking in the concrete is assumed to occur when the stresses reach a failure surface, called the “crack detection surface” shown in Figure 5-9, which shows the concrete failure surface in plane stress.

The shape of the concrete failure surface is defined through several parameters, which depend on the concrete material properties. These parameters are the ratio of the ultimate biaxial compressive stress to the uniaxial compressive ultimate stress, which was taken as 1.16, and the absolute value of the ratio of uniaxial tensile stress at cracking to the ultimate uniaxial compressive strength, assumed to be 0.053. The ratios of the

magnitude of the principal component of plastic strain at ultimate stress in biaxial compression and at cracking to the tensile cracking stress under uniaxial were taken to be 1.28 and 0.333, respectively. These are all default values generally accepted by researchers and recommended by ABAQUS (1998) except for the uniaxial tensile to compressive stress ratio, which was taken to match the experimental tests.

A linear elastic portion and a nonlinear plastic portion defined the concrete behaviour in compression. The linear elastic portion of the concrete behaviour was defined by Young's modulus (E_c) and Poisson's ratio (ν_c). The value of E_c was calculated in accordance with the CSA Standard A23.3-94, (1995) recommended 45% secant modulus:

$$E_c = 4500 \sqrt{f_c'} \quad (5-1)$$

in which f_c' is the uniaxial concrete compressive strength. The value of ν_c was taken as 0.15, which is a typical concrete value. The concrete was assumed to have isotropic behaviour in the elastic range.

The properties of the concrete in compression outside the elastic range were defined through the input of the absolute value of the compressive yield stress (f_{cy}), the compressive strength (f_c'), and the absolute value of the plastic strain (ϵ_{cp}), which corresponds to elastic unloading from f_c' . The value of f_c' was taken similar to the experimental tests, which were 51 MPa and 47 MPa in the modified push-apart and the pull-apart test, respectively, and the plastic strain was taken as 0.0013 in both models. The concrete behaviour beyond f_{cy} produces some unrecoverable (inelastic) straining and the response of the material softens. An ultimate stress (f_c') is reached after which the material softens until it can no longer carry any stress. The failure stress is defined by the failure surface described previously.

The concrete model in ABAQUS is a smeared crack model in the sense that it does not track individual micro cracks, rather state variables are calculated independently at each integration point of the model, and are assumed to represent the behaviour of the

material in the region in a gross manner. The presence of cracks then enters into these calculations by the manner in which the cracks affect the stress and material stiffness associated with an integration point.

The modeling of the concrete-rebar interaction and the energy release during cracking are critical to the response in the post cracking range in tension. This effect is introduced in the model using an option in ABAQUS that models the associated concrete-rebar interaction as a gradual loss of strength in reinforced concrete beyond the cracking strain, known in the literature as tension stiffening, or alternatively the energy release as cracking propagates across the volume represented by a material point, known in the literature as tension softening (Chen, 1982).

Introducing the tension stiffening effect is intended to model the fact that concrete cracks discretely, so that between the cracks the rebar strains are much lower than at the cracks. This behaviour is dependent on the ratio of reinforcement volume to concrete volume. In ABAQUS this effect is not well defined. In any case, proper tension stiffening behaviour representation is an issue in micro behaviour. In our case, this is not an issue, because cracking at the interface of concrete and FRP sheet is away from the rebar, and tension softening is more important. Tension softening in the post-cracking regime was defined by defining the displacement, u_o , at which a linear loss of stiffness after cracking, caused by the full development of a crack process zone, gives zero stress. Properly the value of u_o should yield energy of fracture per unit area typical of the particular concrete under consideration. For our concrete and mesh size, the value of u_o was equivalent to ten times the value of displacement at cracking, u_{ct} , and was calculated as shown in Figure 5-10. This is a limiting value for standard concrete behaviour and gives a reasonable match to experimentally measured responses. The plain concrete uniaxial behaviour in both the compression and tension regions is shown in Figure 5-11.

5.4.2. CFRP

The CFRP in both models was in the form of sheets bonded to the concrete surface. The CFRP sheets used have a linear-elastic stress-strain relationship ending with brittle failure. The CFRP sheets material was defined as orthotropic with a strong direction in

the direction of the fibres. The general stress-strain behaviour for the CFRP material is shown in Figure 5-12a. The cross direction strength is governed by the matrix strength. In our tests, which were unidirectional, this was not an issue.

The CFRP sheet orthotropic elasticity in plane stress is defined by the values of the modulus of elasticity in the main and secondary direction in the plane of the sheet (E_1 , E_2), the shear modulus (G_{12} , G_{13} , and G_{23}), and Poisson's ratio (ν_{12}). The model used is valid for small elastic strains and must satisfy the conditions of Drucker Stability (ABAQUS/Standard, 1998). The values of E_1 and ν_{12} , were taken as 50000 MPa and 0.26, respectively, which match the manufactures specified properties. The values of E_2 , G_{12} , G_{13} , and G_{23} were taken as 2000, 4000, 4000, and 4000 MPa, respectively, which are taken from the literature (ABAQUS/Standard, 1998) to represent matrix properties.

Plane stress orthotropic failure measures were used in the model. The measures are indications of material failure, normally used for FRP materials (ABAQUS/Standard, 1998). The input data for the stress-based failure theories used in ABAQUS are the tensile and compressive stress limits in both the main and secondary direction of the CFRP sheet and the maximum shear stress in its plane. Only the tensile strength in the main direction is important and it was taken to be 3400 MPa similar to the manufacturer specified properties.

5.4.3. Adhesive

In an earlier stage of the work (not shown here) a parametric study was carried out to determine the effect of the elastic properties of the adhesive layer between the CFRP sheet and concrete on the behaviour, and whether the thickness of this layer could be ignored in the model. No significant change in the strain distributions in the CFRP sheet or in the load-displacement response was observed when the adhesive layer thickness was disregarded. The debonding behaviour in the model was unchanged with and without the adhesive layer. This finding was in agreement with previous conclusions by Fashole-Luke (1999). Consequently, it was decided not to model the thickness of the adhesive layer in the analysis. Details of the CFRP-concrete interface modelling are discussed in Section 5.5.

5.4.4. Steel

The steel used in the specimens was in the form of bars and plates. The specific modelling in each case was discussed above. The material model used was an elasto-plastic model for the rebar and linear elastic for the bearing plate. The elastic behaviour for both materials was governed by the modulus of elasticity (E_s) and Poisson's ratio (ν_s). The values of E_s and ν_s were taken as 220000 MPa and 0.3, respectively. Beyond the elastic range the rebar behaviour was modeled by defining the yield strength (f_{sy}), ultimate strength (f_{su}), and the plastic strain at ultimate strength (ϵ_{sp}). The values of f_{sy} and f_{su} for the rebars were taken as the manufacturers specifications as 425 MPa and 645 MPa, respectively, while those for the steel plate were taken as 350 MPa, 500 MPa, respectively. A typical value for ϵ_{sp} was taken as 0.096 for both the steel rebar and plate. The stress-strain behaviour for the steel taken in the models is shown in Figure 5-12b.

5.5. Concrete-CFRP Sheet Interface

The CFRP sheet was modeled as initially bonded to the concrete surface in the 2D models then debonded at the interface joints when the interface stresses reached a defined critical limit. The crack location was predefined at the specimen centre line of symmetry. Introducing the debonding of the CFRP sheet from the concrete surface was essential in modeling the failure mechanism. The CFRP sheet and concrete interface modeling in the 2D models is explained below.

The nodes of the shell elements that model the CFRP sheets defined a surface, while the corresponding nodes on the concrete face defined another surface. In order to identify the initially bonded condition of the CFRP sheet to the concrete, the nodes on the contact surfaces of both the CFRP sheet and the concrete elements were constrained such that, initially, the displacements of each corresponding pair of nodes were identical. As the width of the CFRP sheet was less than that of the concrete specimen, the widths of the contact surfaces were taken equal to the sheet bonded width.

The ABAQUS contact surface model assumes one surface is a master surface (in this case the concrete surface) and the other is a slave surface (CFRP sheet surface). Critical interface shear (τ) and normal stresses (σ) are at the contact interface nodes. Debonding of the slave surface from the master surface occur at the initially bonded interface nodes when the value of a critical interface stress criterion (f) reaches 1.0 within a certain tolerance “ η ”, default value of 0.1, such that

$$1-\eta \leq f \leq 1+\eta \quad (5-2)$$

in which “ f ” is defined by:

$$f = \sqrt{\left(\frac{\sigma_n}{\sigma_f}\right)^2 + \left(\frac{\tau_n}{\tau_f}\right)^2} \quad (5-3)$$

Here σ_n and τ_n denote observed normal and shear stresses carried across the interface, and σ_f and τ_f are limiting failure values. The adhesive normal and shear strengths, σ_f and τ_f , were taken from reported values in the literature as 6.0 and 3.5 MPa, respectively.

In order to activate the debonding between the FRP sheet and concrete surfaces, ABAQUS requires that the first node in the bonded surfaces be initially debonded to initiate the debonding mechanism. Therefore, in test specimen locations where an anchor sheet was placed, this node was not debonded to force failure in the unanchored side. Figure 5-13b shows magnification of the CFRP sheet debonding from the concrete in the 2D modified push-apart model. It was observed in the experimental tests that a chunk of concrete stayed bonded to the FRP sheet after the debonding failure of the specimen, as detailed in Section 4.2.1. This was not simulated in the tested part of the sheet due to the unbonding of the first node in the bonded surfaces. The strain in the load direction contour of the modified push-apart model at failure shown in Figure 5-14, shows that large strain values occur at the concrete loaded corner, which indicate the eventual failure of that portion of the concrete.

The debonding option in ABAQUS is also limited to 2D models. Since the 3D simulation was intended to investigate the strain distribution FRP sheet width and the sheet width to concrete width ratio effect, it was felt that debonding is not an issue, and the surface nodes in the 3D model were fully constrained.

5.6. Analysis Procedures

A nonlinear finite element analysis procedure was used to determine the response of the model. The solution is found in ABAQUS by specifying the loading as a function of time and incrementing time to obtain the nonlinear response. Therefore, by breaking the simulation into a number of time increments, an approximate equilibrium configuration is found at the end of each time increment.

The first increment size was assumed to be 0.1% of a limiting step of 1.0, which was chosen after several initial trials with higher increments that caused the program to stall. Subsequently, automatic control of the increment size was such that the increment size changes as the program develops the response in the step. This approach is more efficient than using a user defined increment size, where the user cannot predict the response ahead of time. The program determines if convergence is likely in a reasonable number of iterations by comparing consecutive values of the maximum achieved force residuals following every iteration. If subsequent iterations show the solution to be closer to equilibrium and convergence is likely, the program continues with the iteration process with the current increment size. If convergence is not likely, the program chooses a smaller increment size but up to a minimum specified value in order to prevent excessive computation in cases where a limit load approaches or some modeling error grows causing the solution to stall. At the end of each increment the structure is in approximate equilibrium and the results are recorded.

To avoid premature cutbacks of the time increment and stalling of the program because of the high nonlinearity in the system, the analysis was defined as discontinuous. This had the effect of increasing the default number of equilibrium iterations after which a logarithmic rate of convergence check is made. The iteration number at which check of

the logarithmic rate of convergence begins also increased as a result of defining the analysis as discontinuous.

Reinforced concrete solutions involve regimes where the load-displacement response is unstable because of excessive cracking. Since considerable nonlinearity was expected in the response, the modified RIKS solution strategy was used in the 3D model with automatic incrementation. The RIKS procedure uses the load magnitude as an additional unknown together with the displacements and uses 1% extrapolation of the strain increment. The 2D model did not use RIKS method, where the method does not work with problems involving debonding (loss of contact), as was the case in the 2D model. Modified Newton's iterations were used to solve the nonlinear equilibrium equations in all models.

5.7. Verification

The numerical models were verified by comparing their output with the experimental results that were discussed in detail in Chapter 4. The comparisons between the experimental results and the model output were performed on the overall load-deflection behaviour of the specimens and the strain distribution in the CFRP sheets at different load levels along the sheet length.

In order to find the overall load-displacement behaviour of the specimen, the reaction and displacement at the applied moving roller at all time increments were recorded throughout the analysis. The values were then plotted and compared to the corresponding experimental plots. As the program ABAQUS plots the strain distribution at a specified load increment, the strain distribution at the required load level was obtained by first determining the displacement at the required load from the load-displacement response. The strain distribution was then plotted along the specified nodes at the load increment corresponding to that specific displacement level.

5.7.1. 2D Model Verification

As mentioned before, Figure 5-13a shows the modified push-apart model mesh in a deformed configuration with a magnification factor of 30 and Figure 5-13b shows the CFRP sheet in the model debonding from the concrete with a magnification factor of 100. The figures show that the model behaves similarly to the experimental tests, where the CFRP sheet separates from the concrete surface as the critical interface stresses are reached. Similar results were obtained from the pull-apart model, as shown in Figure 5-15. The similarity in behaviour between the model and the experimental tests shows that the debonding type failure can be simulated using numerical models.

The overall behaviour comparison between the 2D modified push-apart numerical model output and the experimental results shows good agreement in the overall load-displacement behaviour as shown in Figure 5-16 through Figure 5-20 for specimens S1 through S5. These figures describe the total load plotted against the displacement between the loading points. The figures also show consistently higher strength predicted by the numerical model varying from 3.5% to 17.2%. This higher strength could be attributed to the variability in the adhesive-concrete interface strength.

The pull-apart model had the same trend as the experimental results, as shown in the load-deflection curves in Figure 5-21 through Figure 5-25 for specimens P9 through P13, respectively. These figures describe the total load plotted against the displacement at the loading point. The difference in values is attributed to the fact that the numerical model represents the perfect case with no eccentricity and the assumption that the load is transferred equally between the two bonded faces of the specimen.

A comparison is also made between the average strain distribution along the CFRP sheet length observed from the modified push-apart experimental results and that from the model at different load values. The comparison shows good agreement as shown in Figure 5-26 through Figure 5-30 for specimens S1 through S5. The introduction of the debonding effect allows modelling of the increase in the transfer length of the strain

distribution. The increasing transfer length in the strain distribution indicates the debonding of the sheet from the concrete as the load increases.

The strain distribution from the experimental tests and the numerical model along the FRP sheet length for specimens P9 through P13 are shown in Figure 5-31 through Figure 5-35. The experimental strain distribution for the pull-apart tests was measured at the centre of the sheet. The 2D model, however, represents the average strain across the width, which causes the model to predict higher strain values. With these taken into consideration, the strain distribution in the 2D pull-apart model is adequate for the overall trends.

5.7.2. 3D Model Verification

The 3D models were developed to study the strain distribution across the CFRP sheet width, which the 2D models could not investigate. The models were verified by comparing the strain distributions across the CFRP sheet width with the corresponding strain distributions from the experimental tests. The strain distributions from the experimental tests were taken as the average values from both bonded FRP sheets. As the debonding effect was not introduced in the 3D models, the load-deflection behaviour was affected and the model had a stiffer response at higher loads compared to the experimental response. This is shown in Figure 5-36 through Figure 5-39 for the modified push-apart model and in Figure 5-40 through Figure 5-44 for the pull-apart model. Therefore, the loads at which the strain distribution comparison is made are limited to lower load levels.

The model and experimental strain distributions across the CFRP sheets at different load levels at the crack location for specimens S1 through S5 are shown in Figure 5-45 through Figure 5-49, respectively, while those for P9 through P13 are shown in Figure 5-50 through Figure 5-54, respectively. Only one side of the experimental tests in the P-series specimens had strain gages across the sheet width. This could explain the big difference between the model and experimental strain of P12, which failed on the side with no instrumentation across the sheet width. The numerical model represented the

perfect case with no material irregularity or eccentricity in loading. The differences in the strain values between the models and the experimental tests were also attributed to the smaller CFRP sheet width used in the models due to the chosen mesh size. The specimens effected were S2, S3, and S5 in the S-series and all P-series, P9 through P13, where the 25, 50, and 150 mm widths were taken narrower in the models by 5, 10, and 10 mm, respectively. The model prediction of the strain distribution across the width and the relative strain distribution at different loads is seen as adequate to perform an investigation on the factors affecting the strain distribution across the FRP sheet width.

From the previous discussions, the good agreement of the numerical simulation with the experimental results in the 2D model and the trend agreement of the 3D model prove that it is possible to predict the load-displacement behaviour, the debonding type failure, and the strain distribution along the length as well as across the width of FRP sheets bonded to concrete using numerical models. This lends credibility to performing a study on various parameters and their effect on the bond behaviour of FRP sheets bonded externally to concrete surfaces using the proposed numerical models. It was decided that the modified push-apart model be used for the parametric study, where it showed better simulation with the corresponding experimental tests that had more strain readings than the pull-apart tests. The parametric study is detailed in the following chapter.

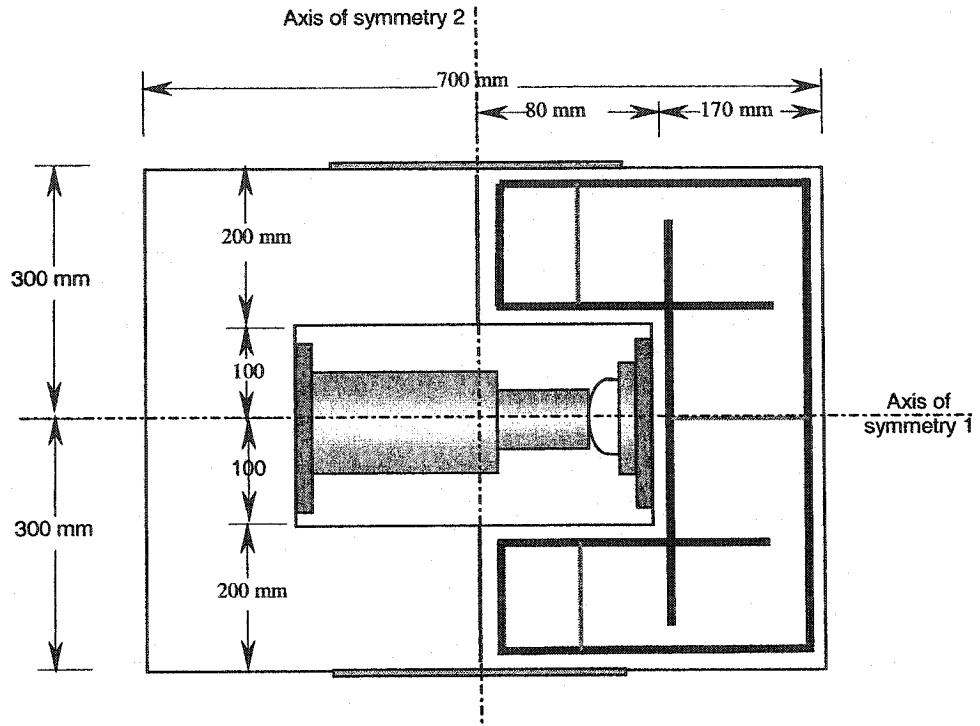


Figure 5-1 Modified push-apart specimen plan view and symmetry lines

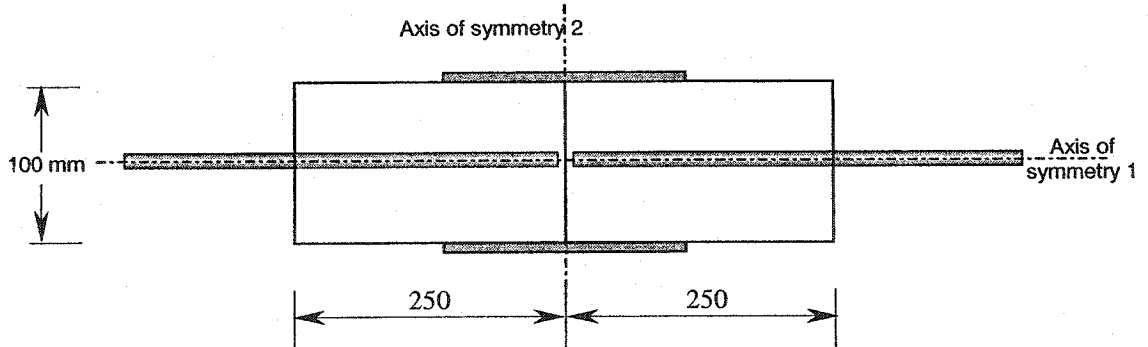


Figure 5-2 Pull-apart specimen elevation and symmetry lines

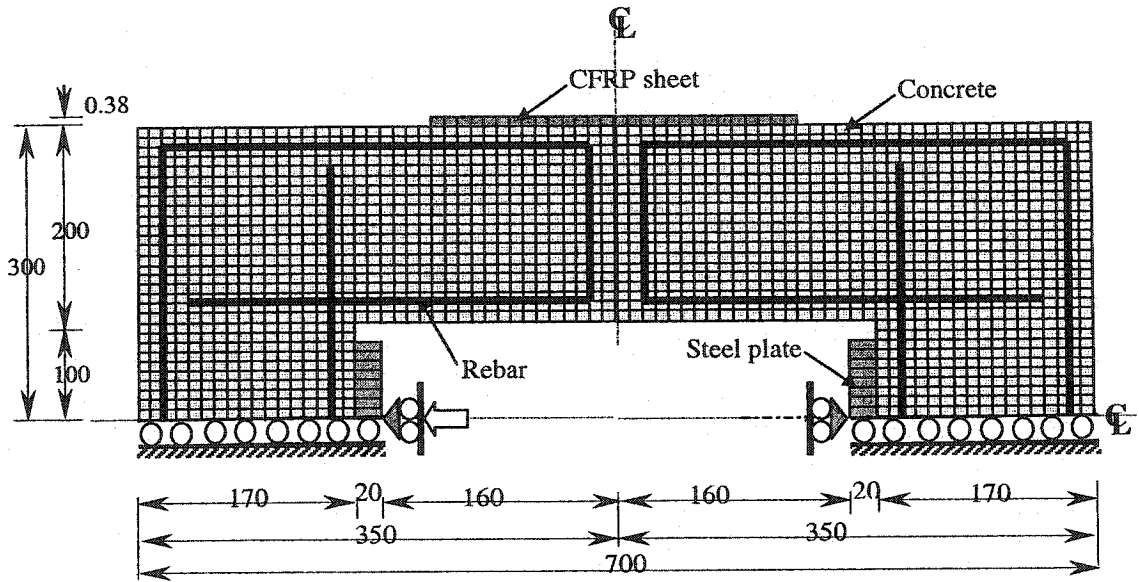


Figure 5-3 2D modified push-apart model mesh, loading, and boundary conditions

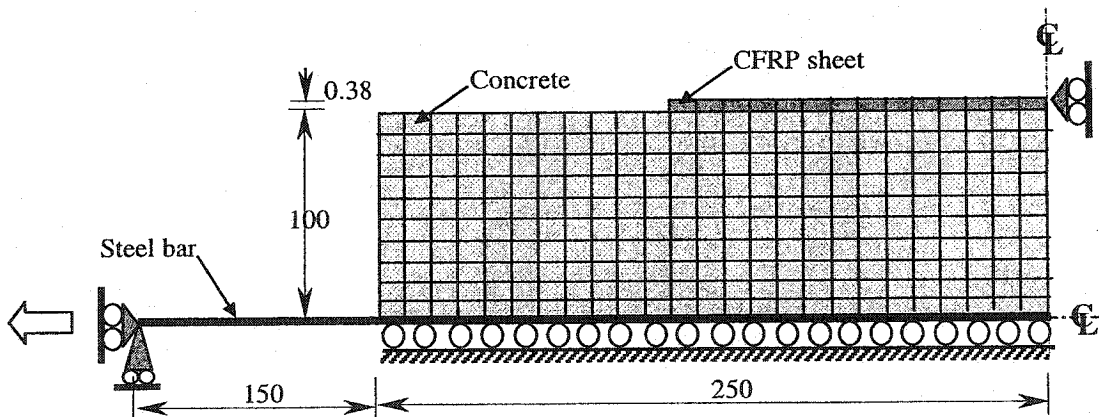


Figure 5-4 Half the 2D pull-apart model mesh, loading, and boundary conditions

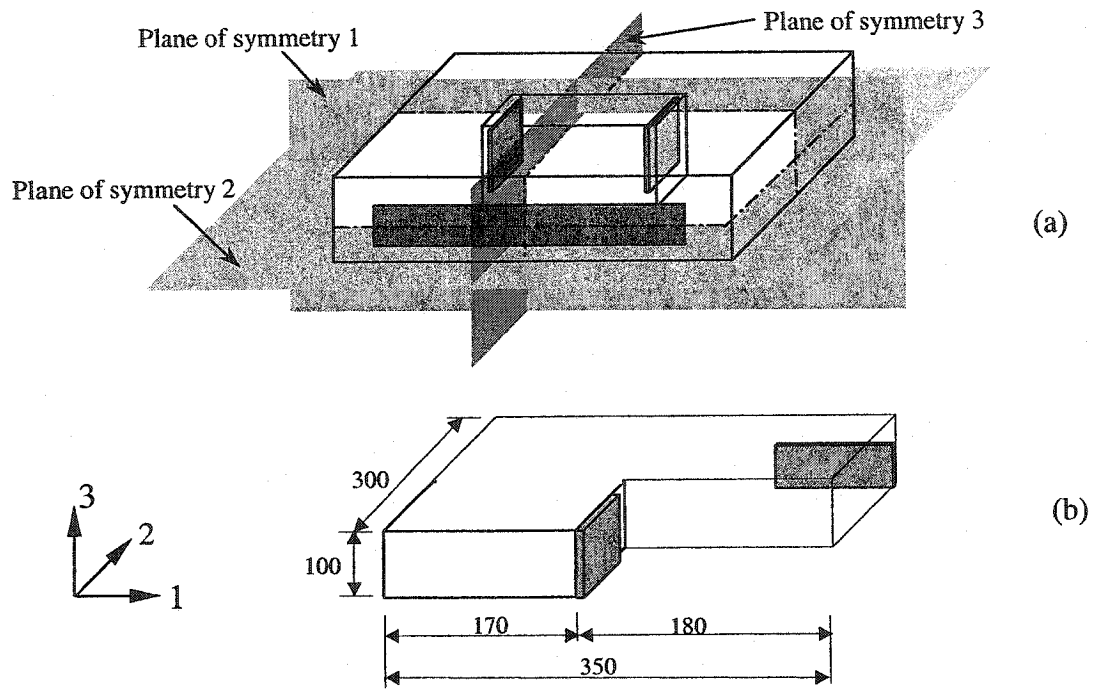


Figure 5-5 Modified push-apart specimen (a) planes of symmetry (b) modeled part

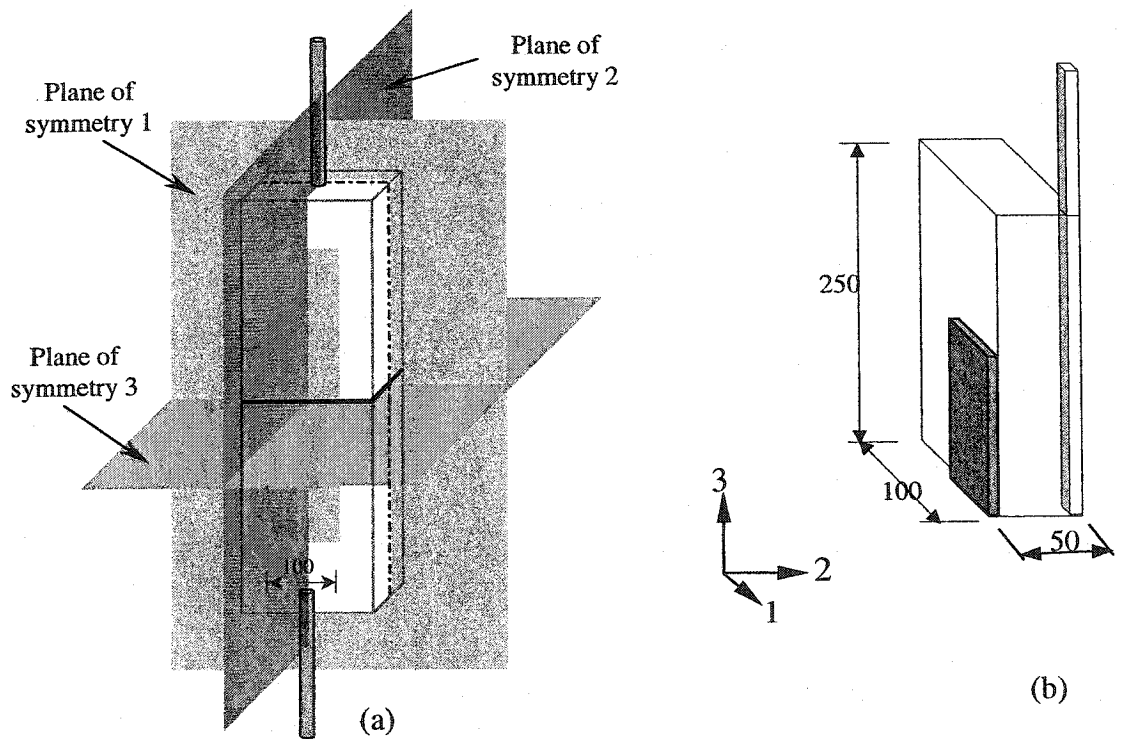
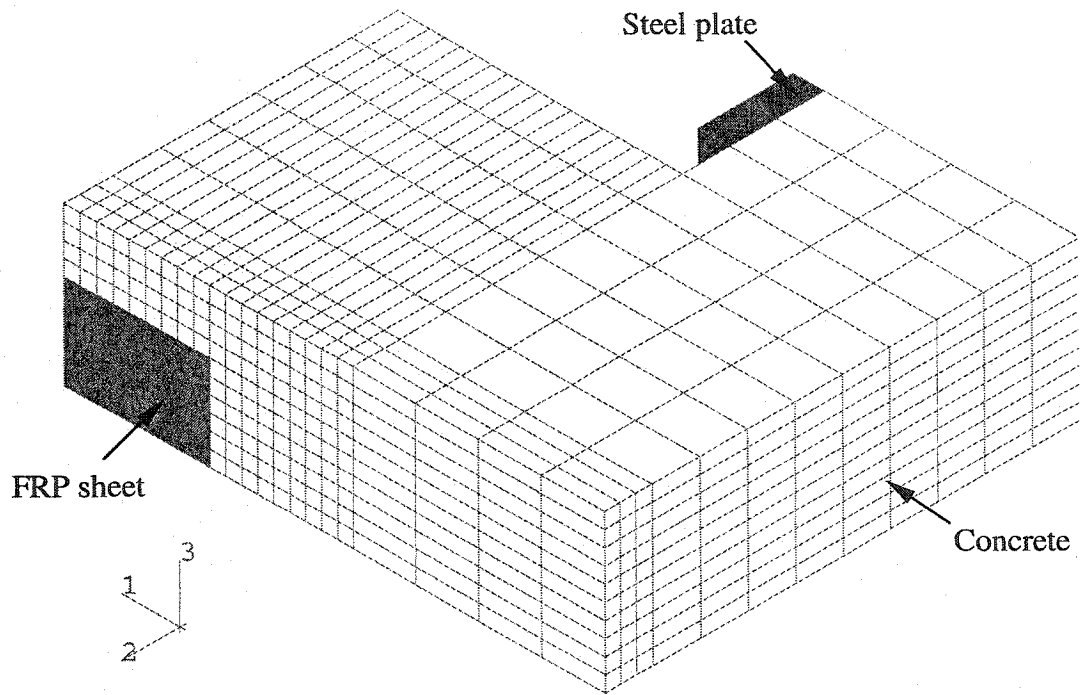
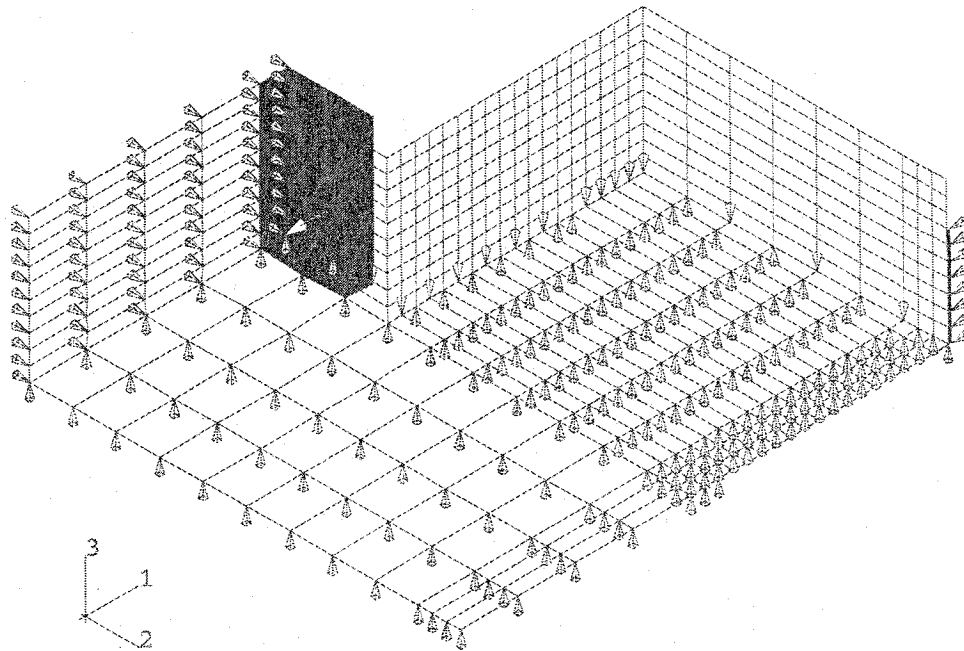


Figure 5-6 Pull-apart specimen (a) planes of symmetry (b) modeled part



(a) Geometry and mesh



(b) Loading and boundary conditions

Figure 5-7 Modified push-apart 3D model

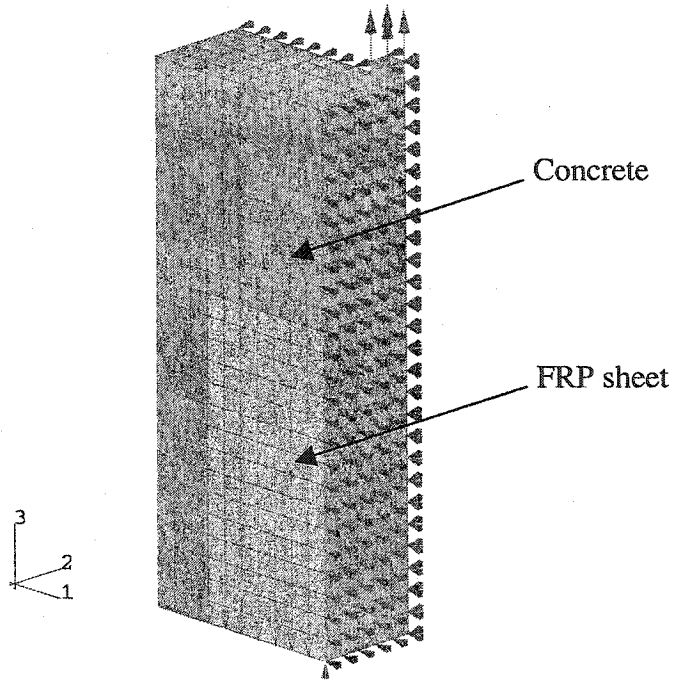


Figure 5-8 Pull-apart test mesh, loading, and boundary conditions

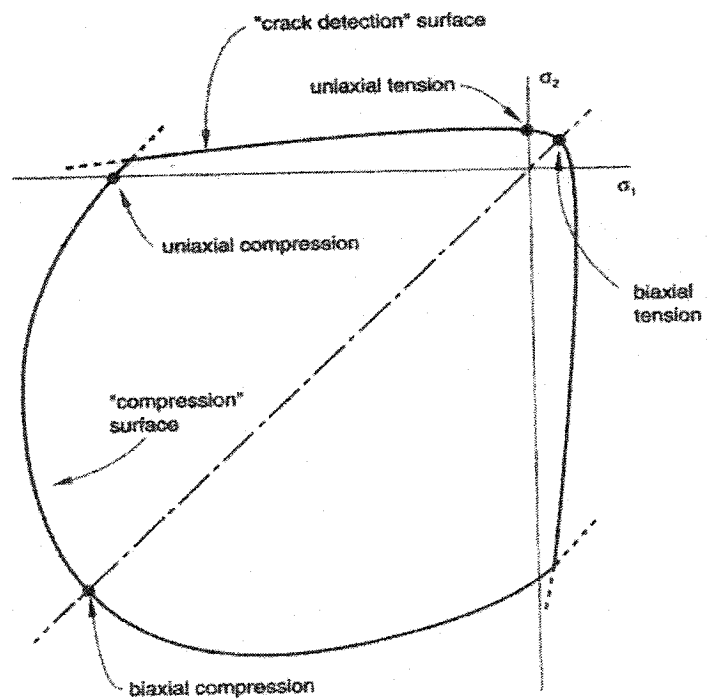


Figure 5-9 Concrete yield and failure surfaces in plain stress (ABAQUS, 1998)

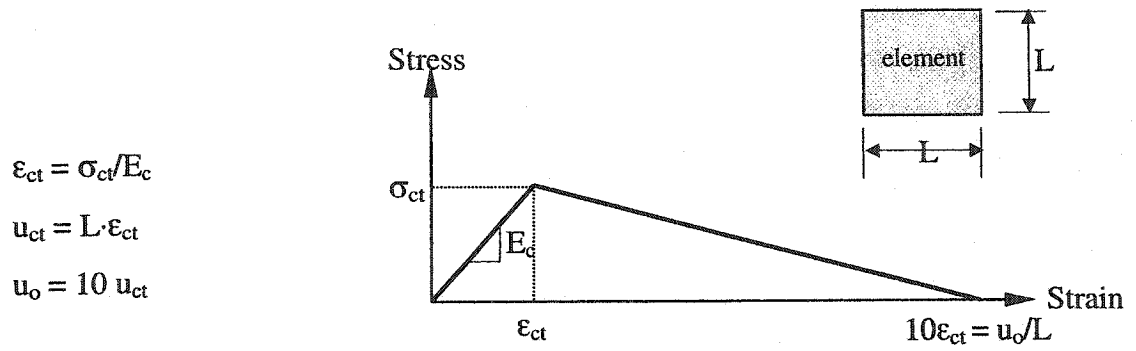


Figure 5-10 Calculation of the displacement at which a linear loss of strength after cracking gives zero stress

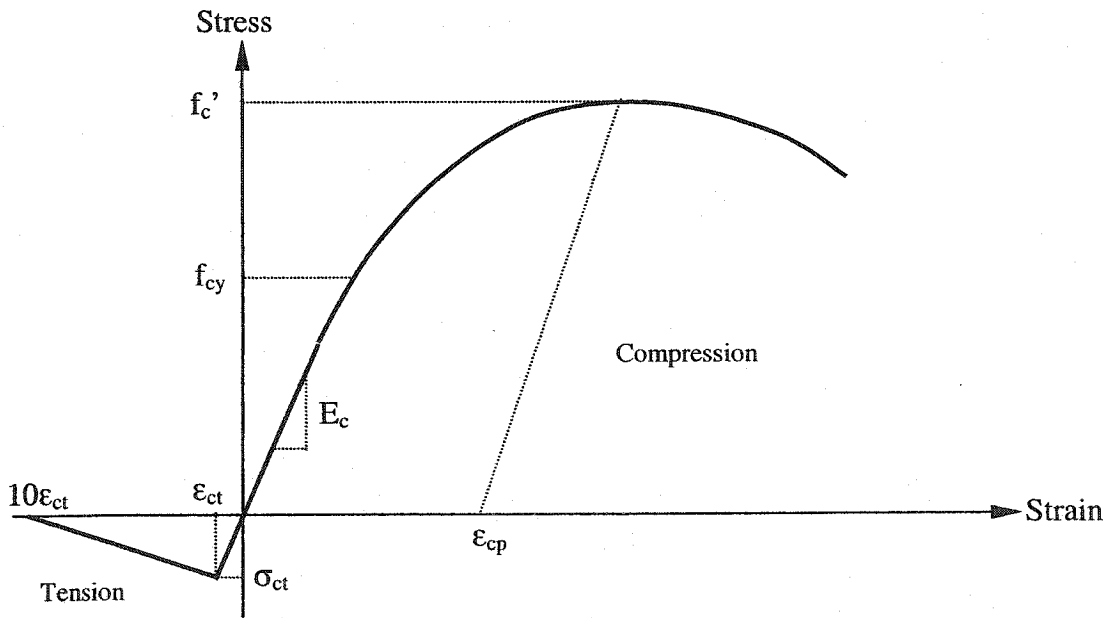


Figure 5-11 Uniaxial behaviour of plain concrete (ABAQUS, 1998)

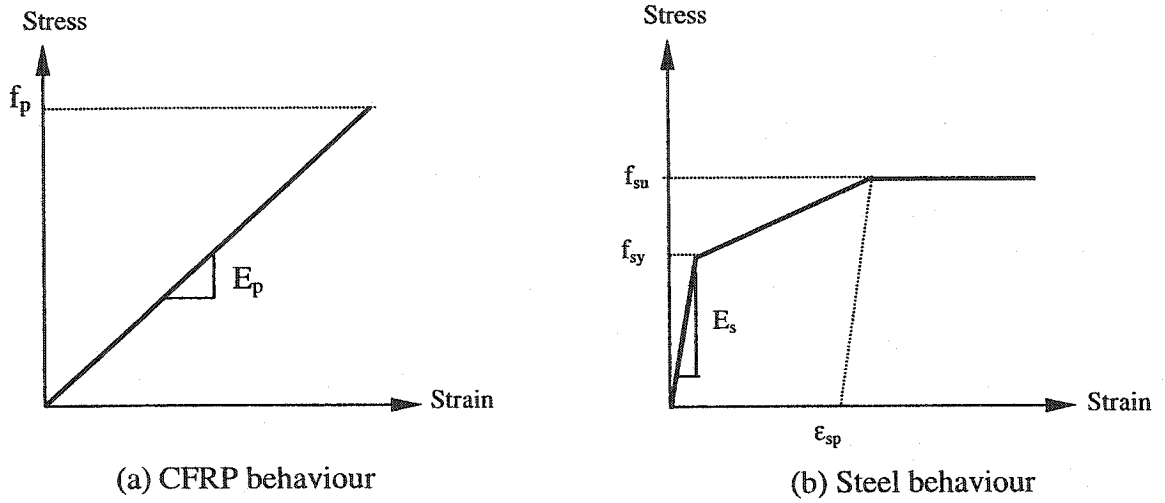


Figure 5-12 Stress-strain behaviour for CFRP and steel

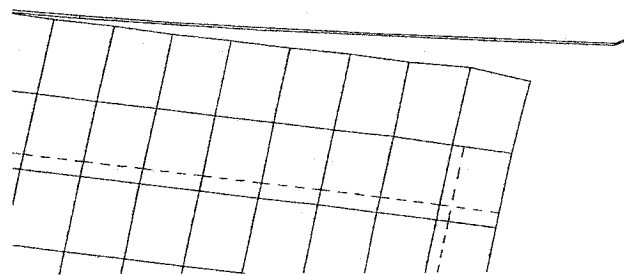
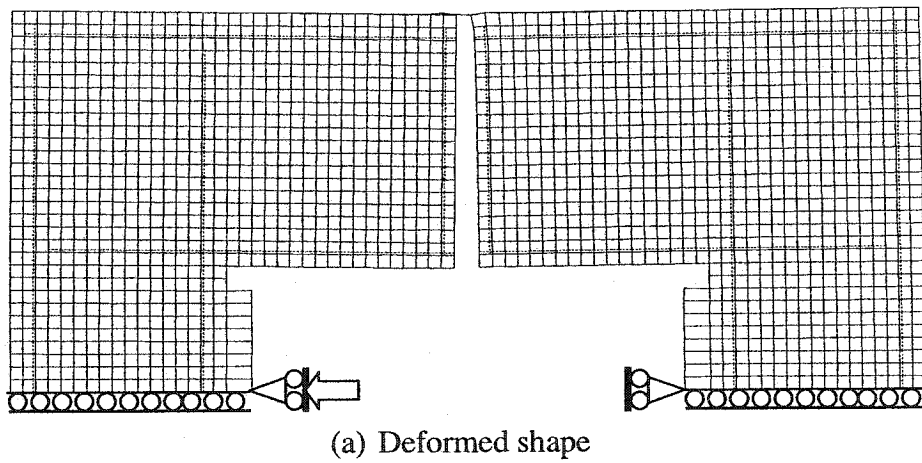


Figure 5-13 2D modified push-apart model

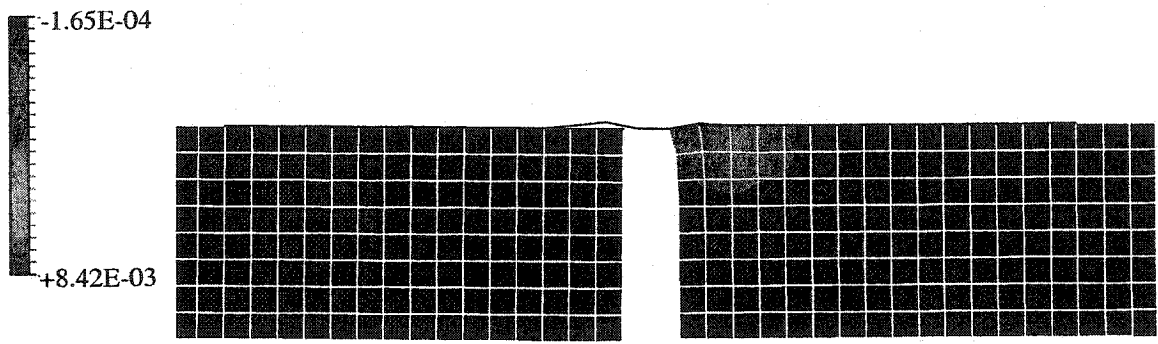


Figure 5-14 Strain contour in load direction for modified push-apart model

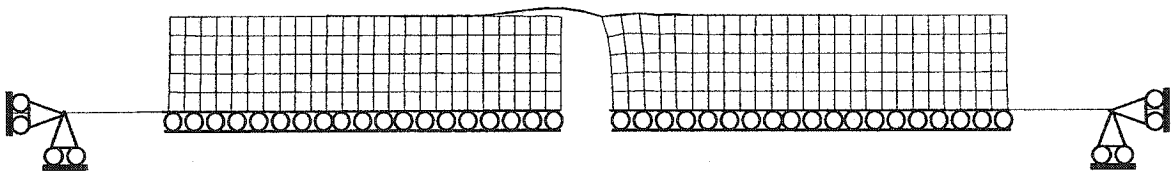


Figure 5-15 2D pull-apart mesh, boundary conditions, and deformed shape

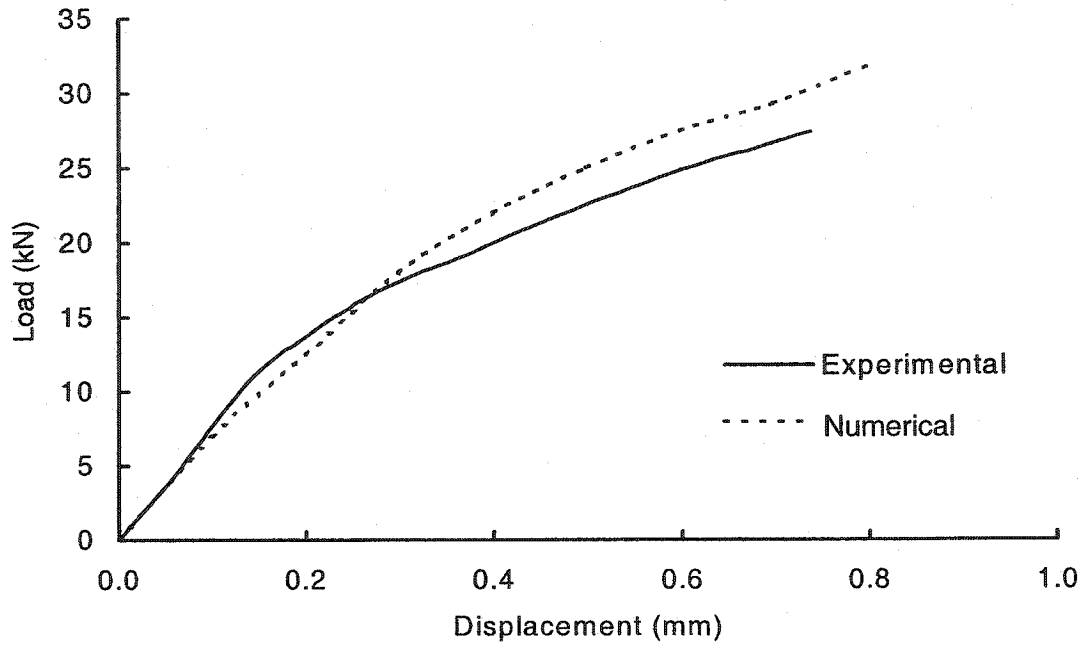


Figure 5-16 Load-displacement curves experimental and 2D model of S1

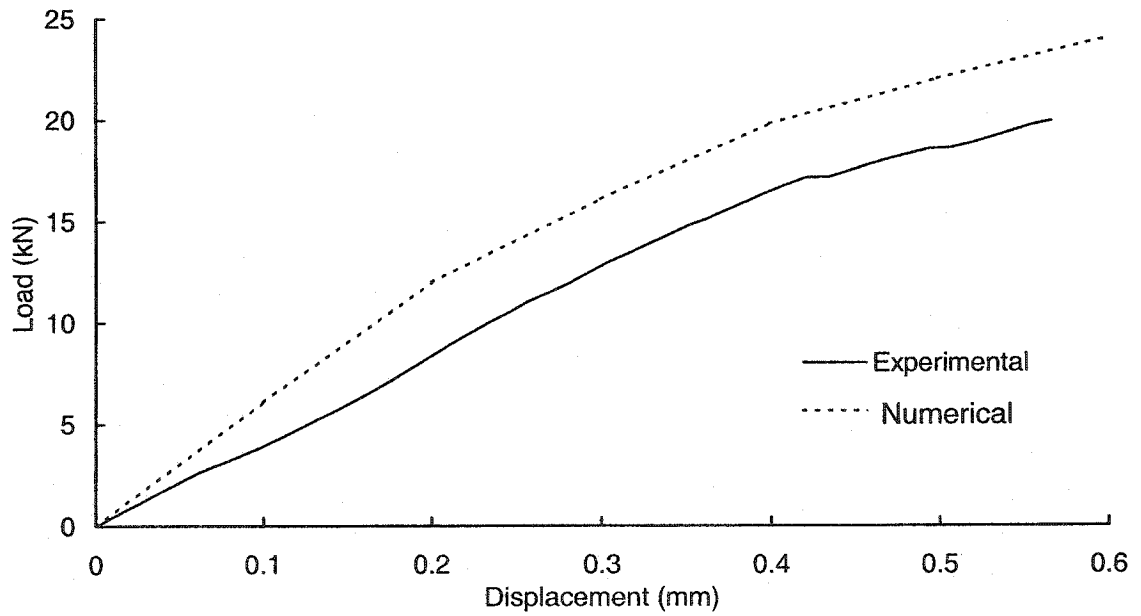


Figure 5-17 Load-displacement experimental and 2D model of S2

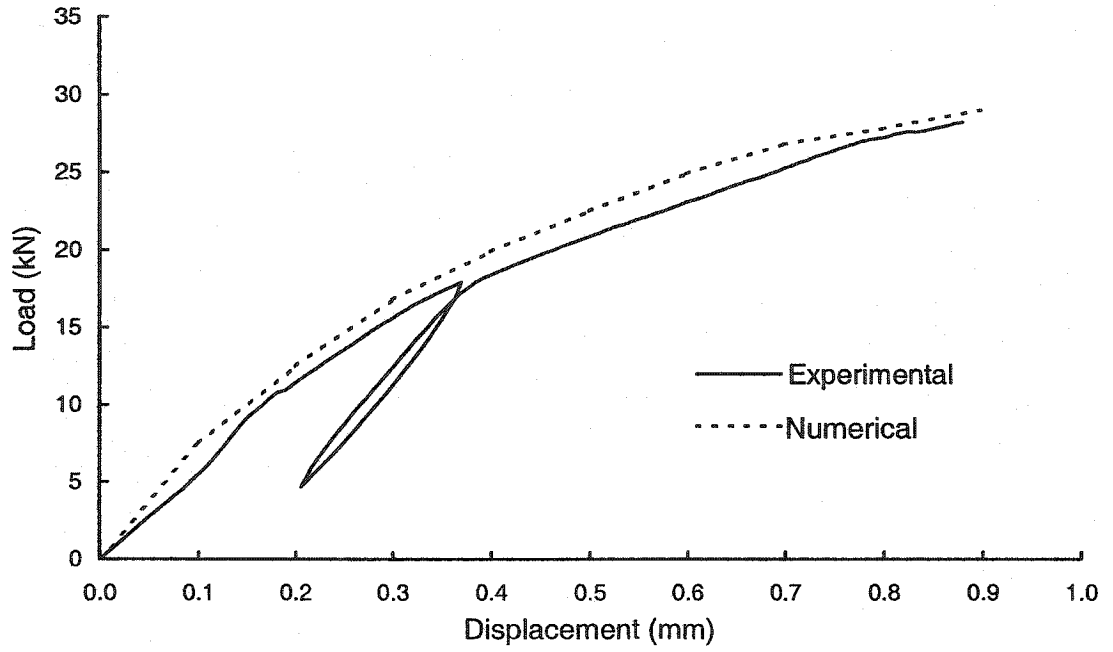


Figure 5-18 Load-displacement experimental and 2D model of S3

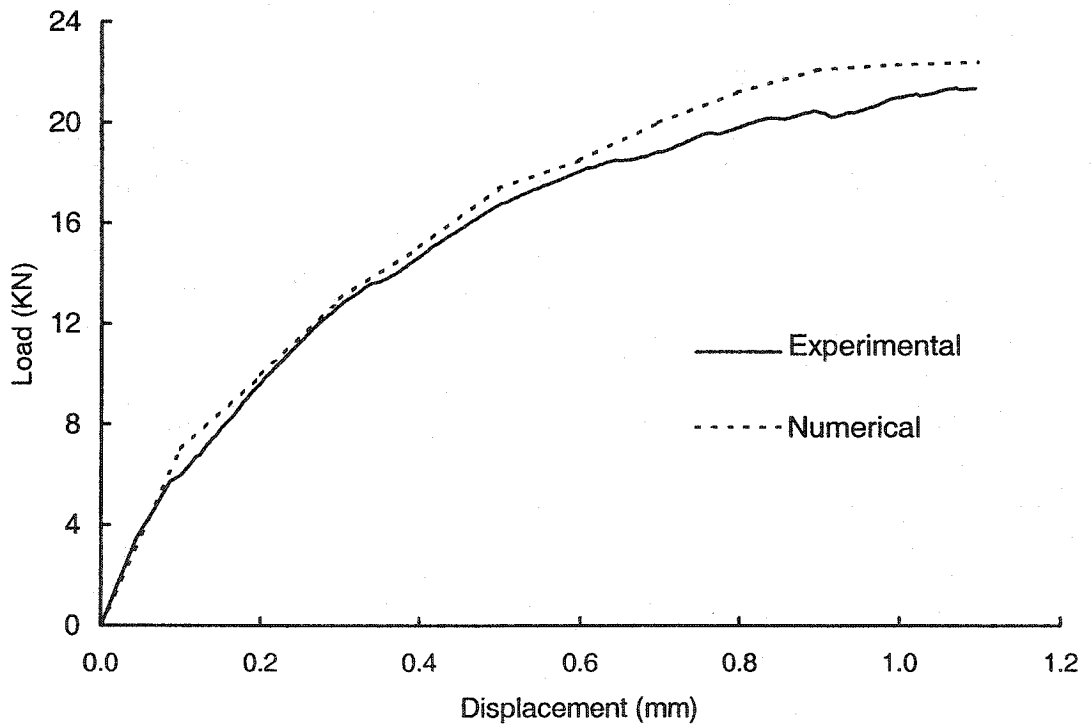


Figure 5-19 Load-displacement experimental and 2D model of S4

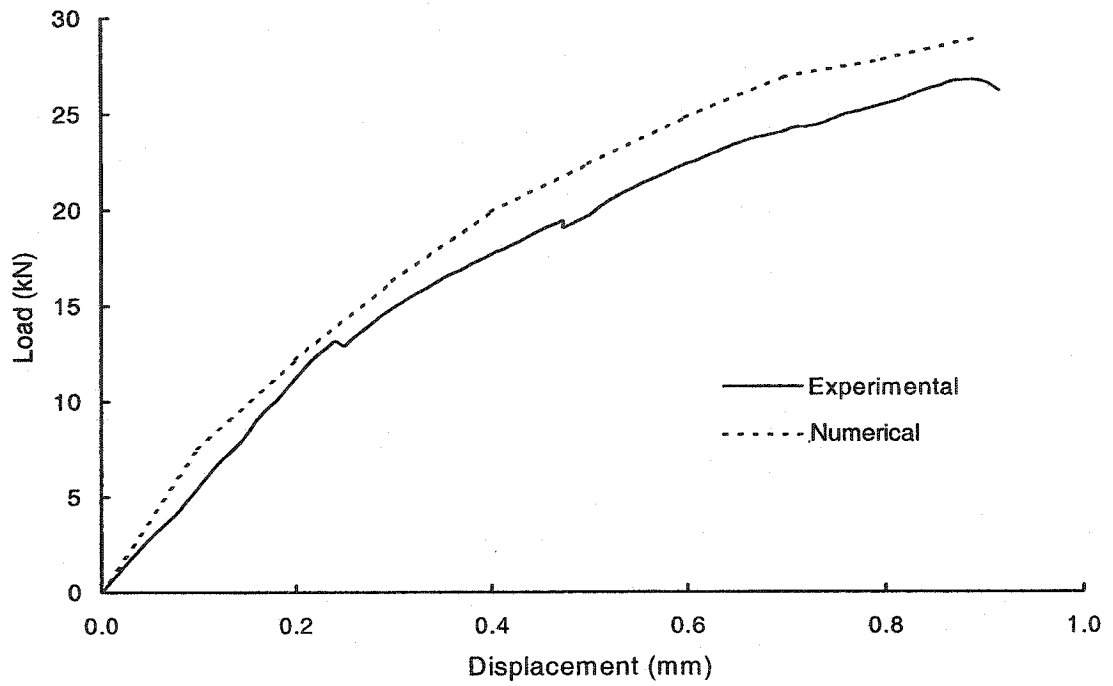


Figure 5-20 Load-displacement experimental and 2D model of S5

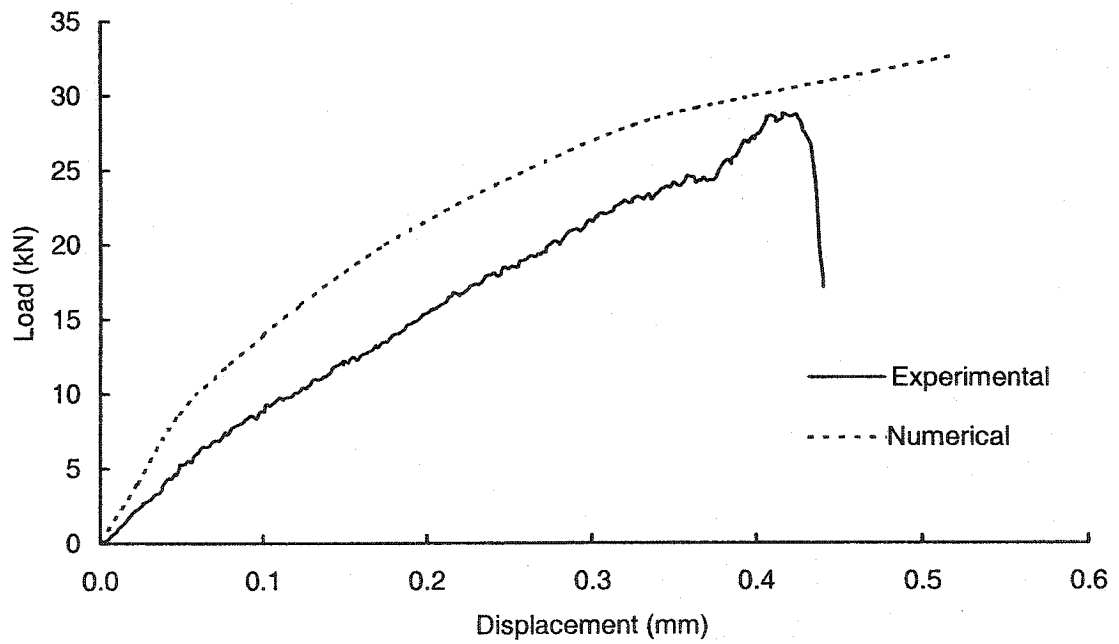


Figure 5-21 Load-displacement for experimental and 2D model of P9

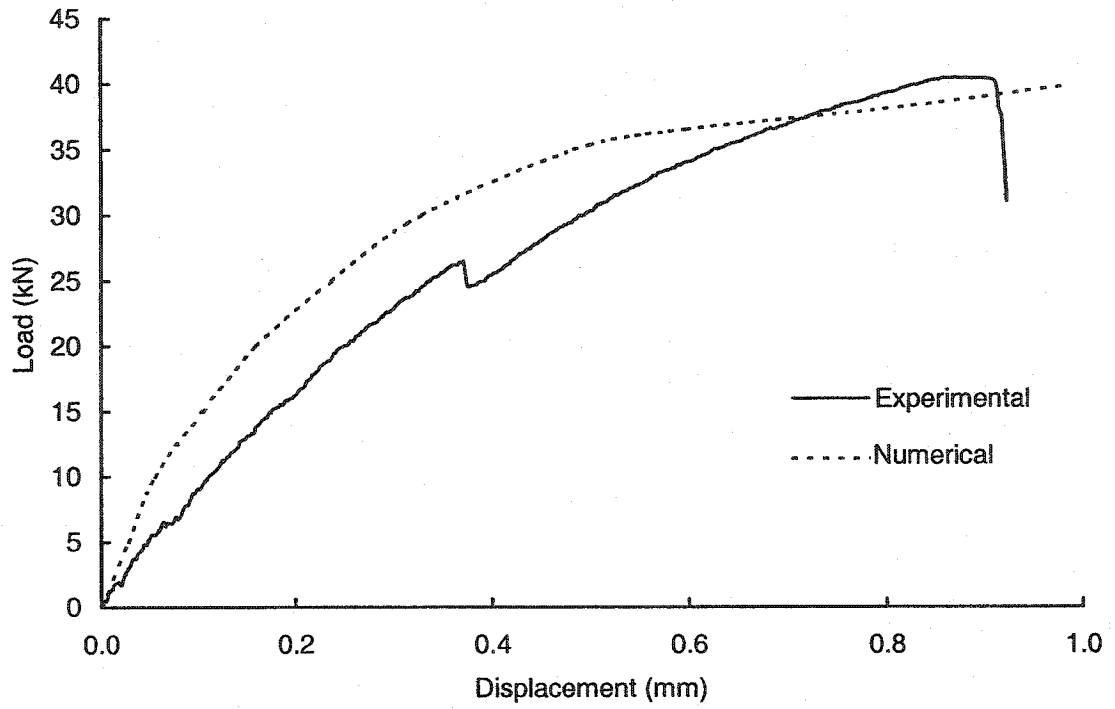


Figure 5-22 Load-displacement for experimental and 2D model of P10

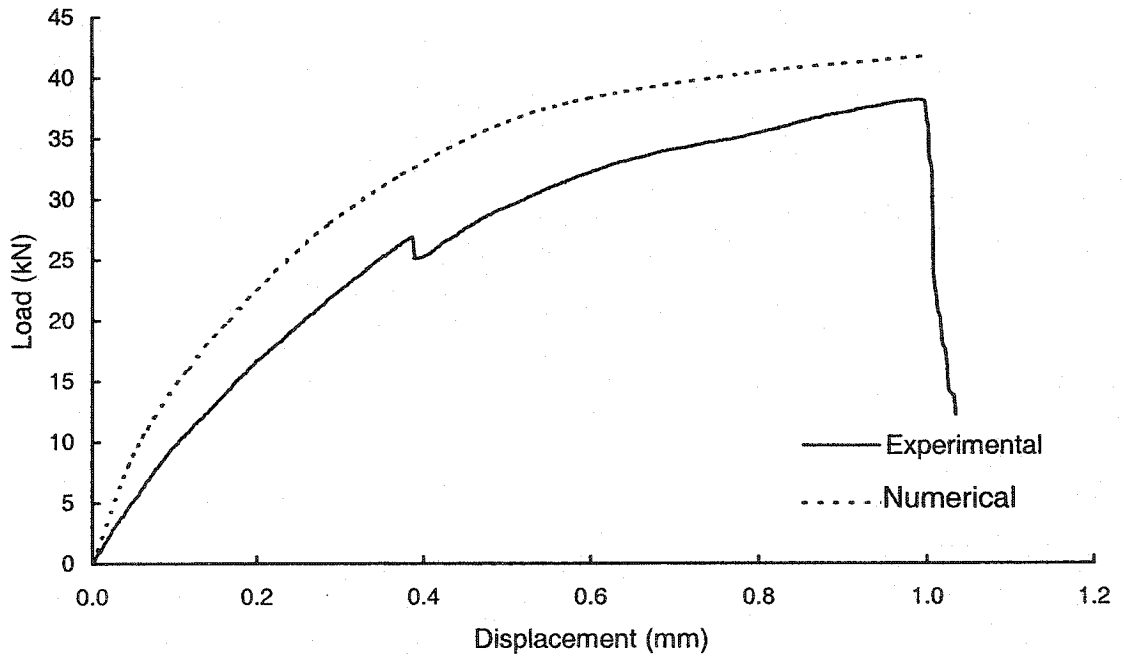


Figure 5-23 Load-displacement for experimental and 2D model of P11

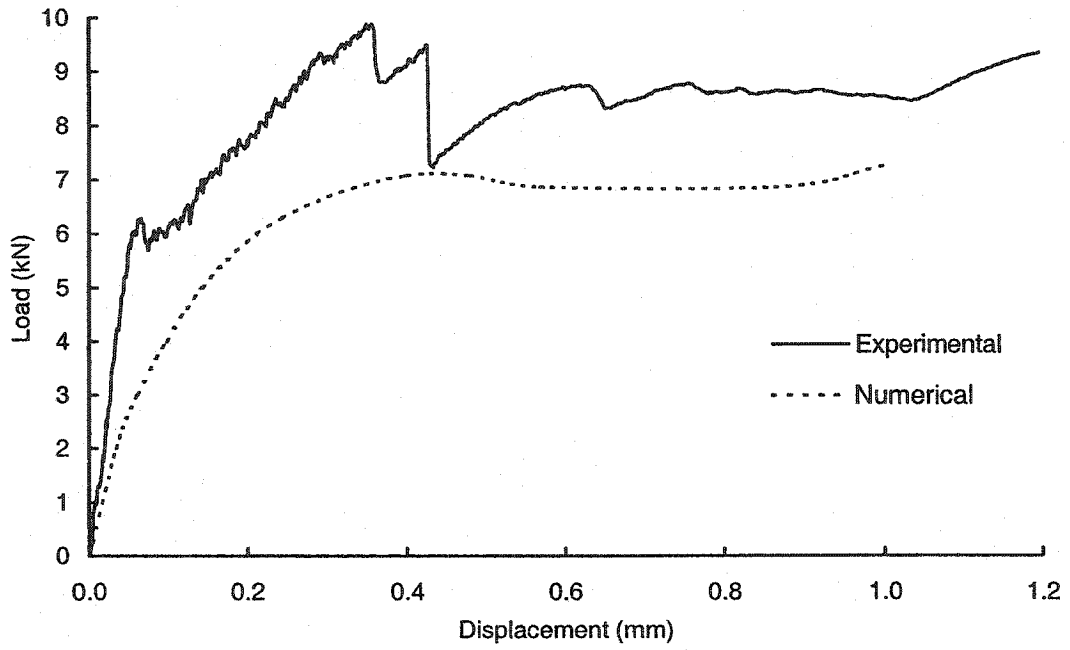


Figure 5-24 Load-displacement for experimental and 2D model of P12

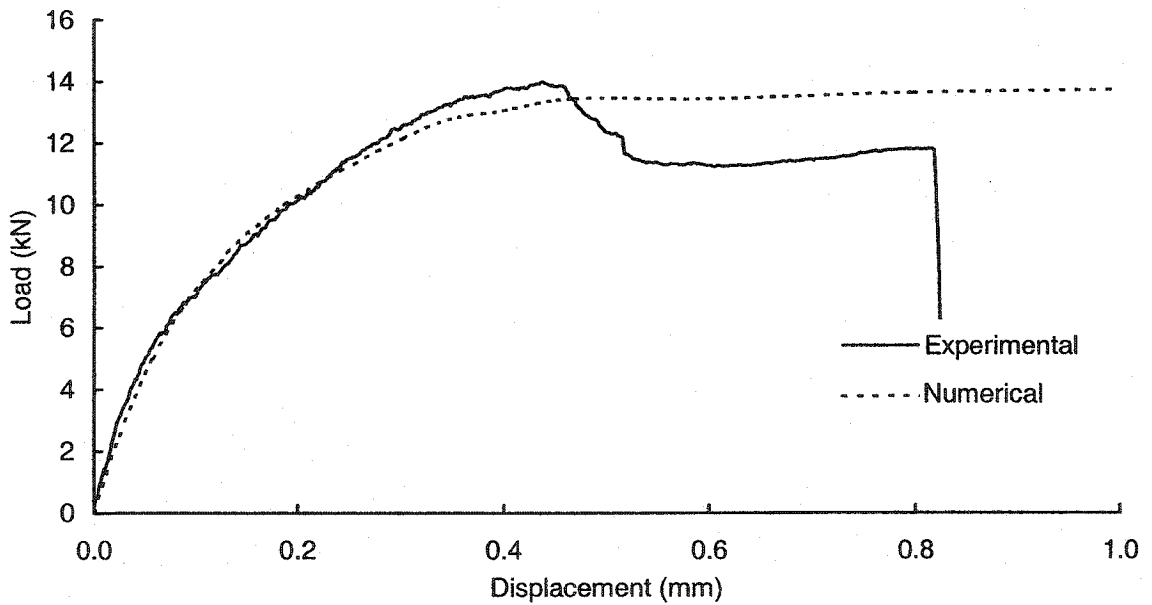


Figure 5-25 Load-displacement for experimental and 2D model of P13

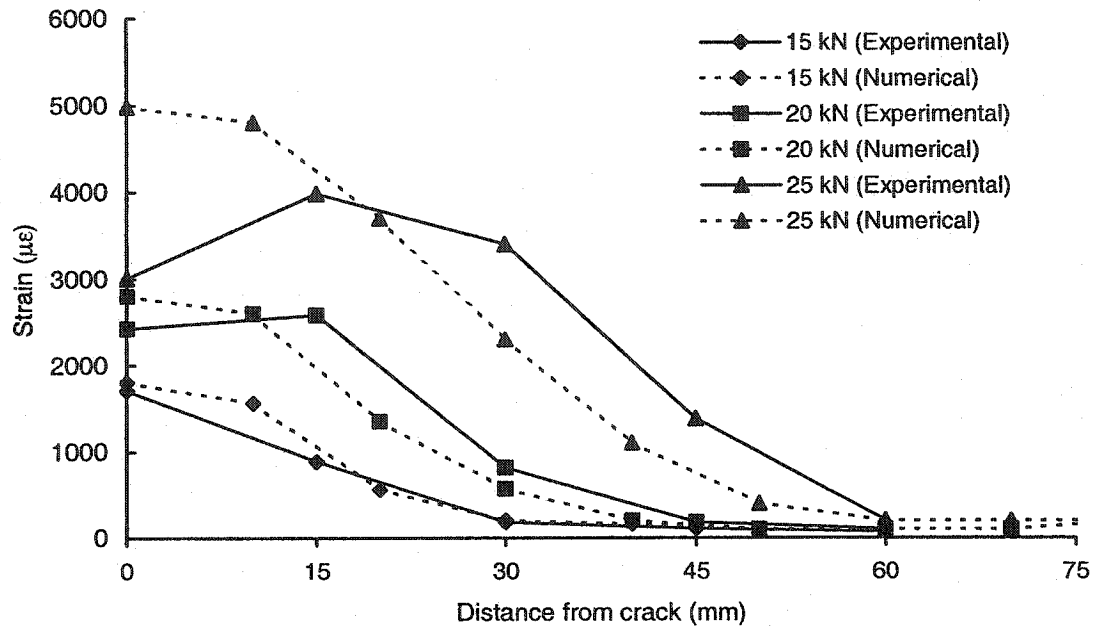


Figure 5-26 Strain distributions for experimental and 2D model of S1

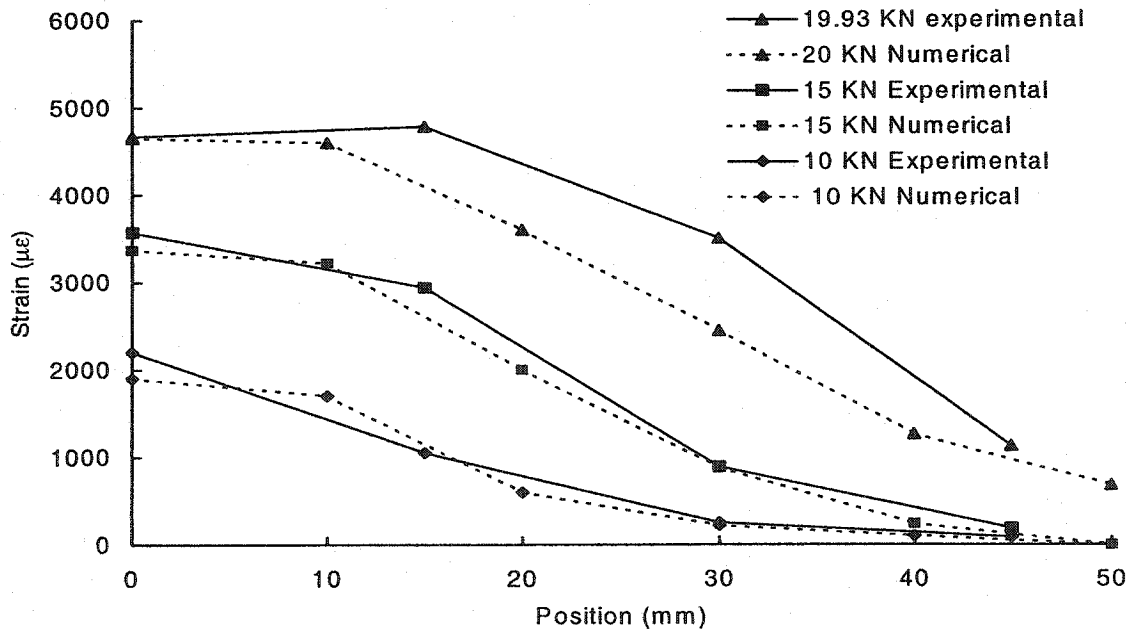


Figure 5-27 Strain distributions for experimental and 2D model of S2

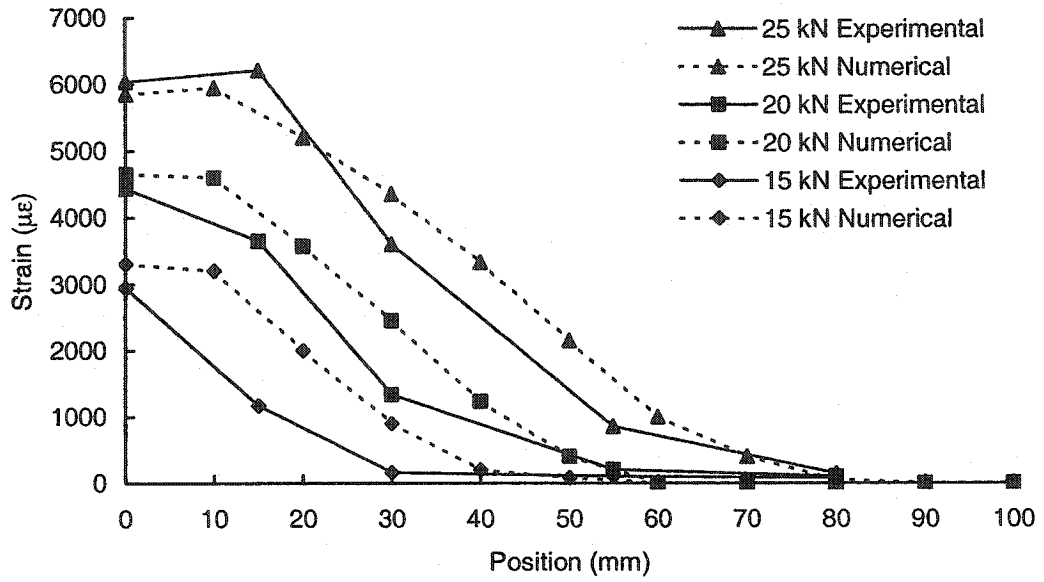


Figure 5-28 Strain distributions for experimental and 2D model of S3

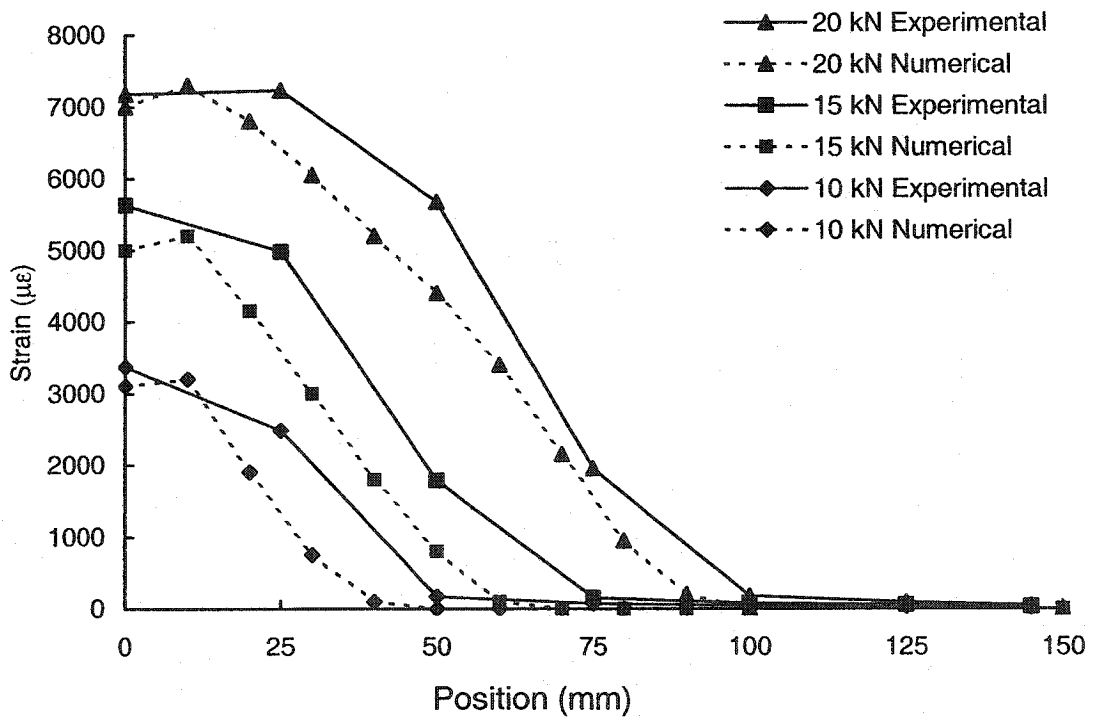


Figure 5-29 Strain distributions for experimental and 2D model of S4

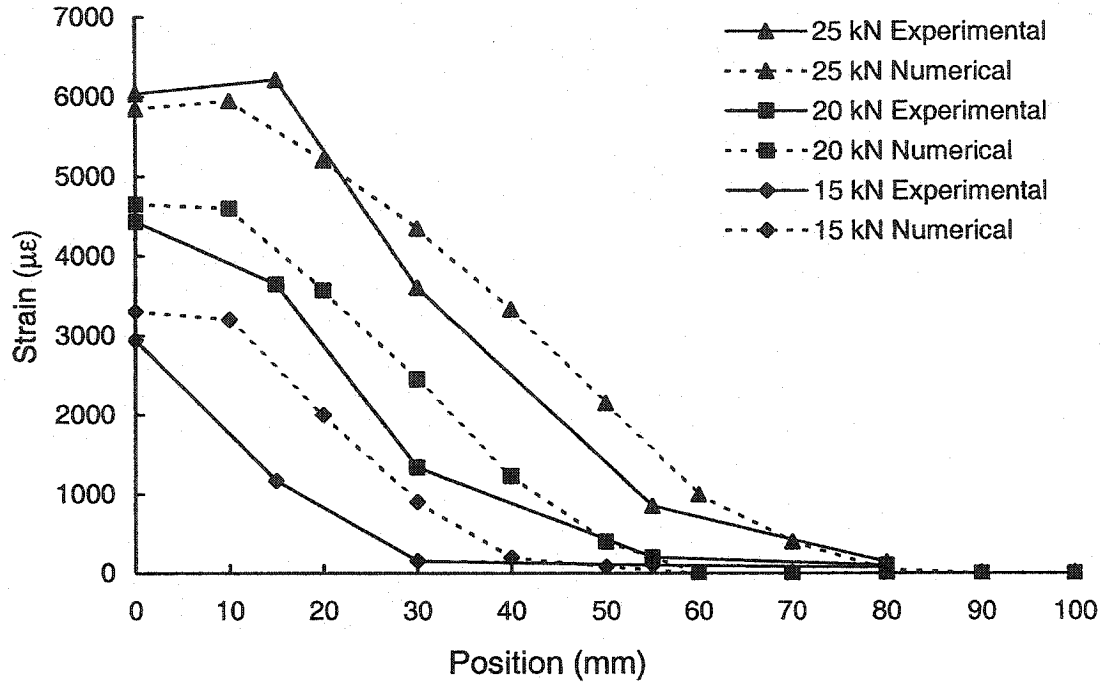


Figure 5-30 Strain distributions for experimental and 2D model of S5

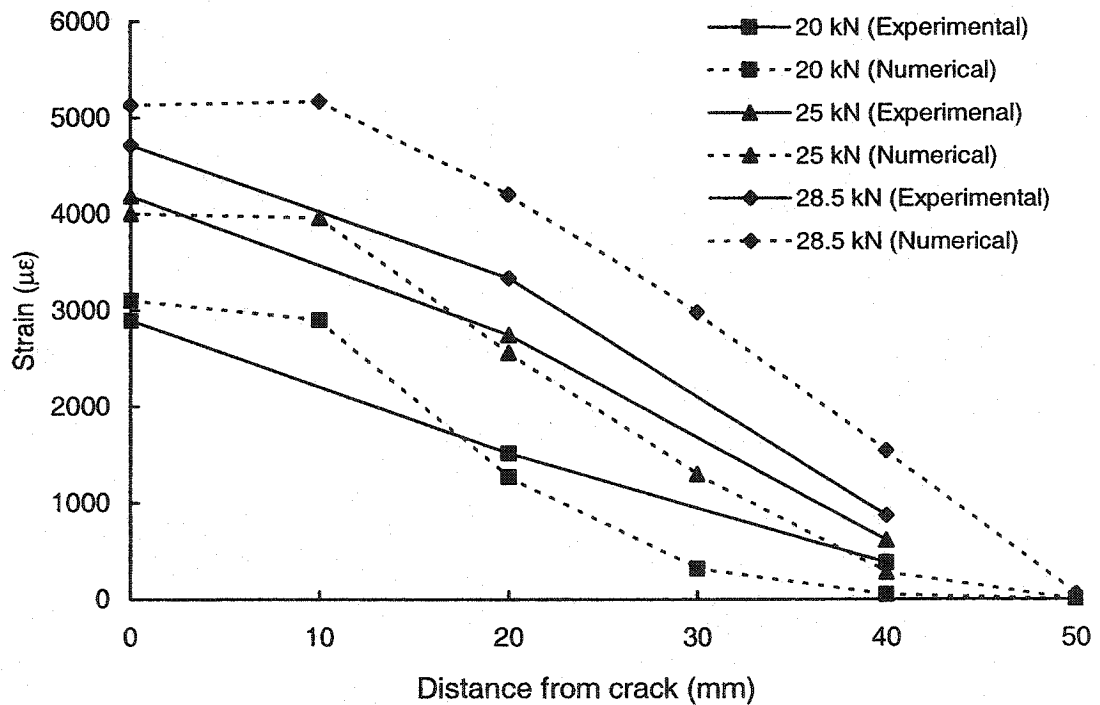


Figure 5-31 Strain distributions for experimental and 2D model of P9

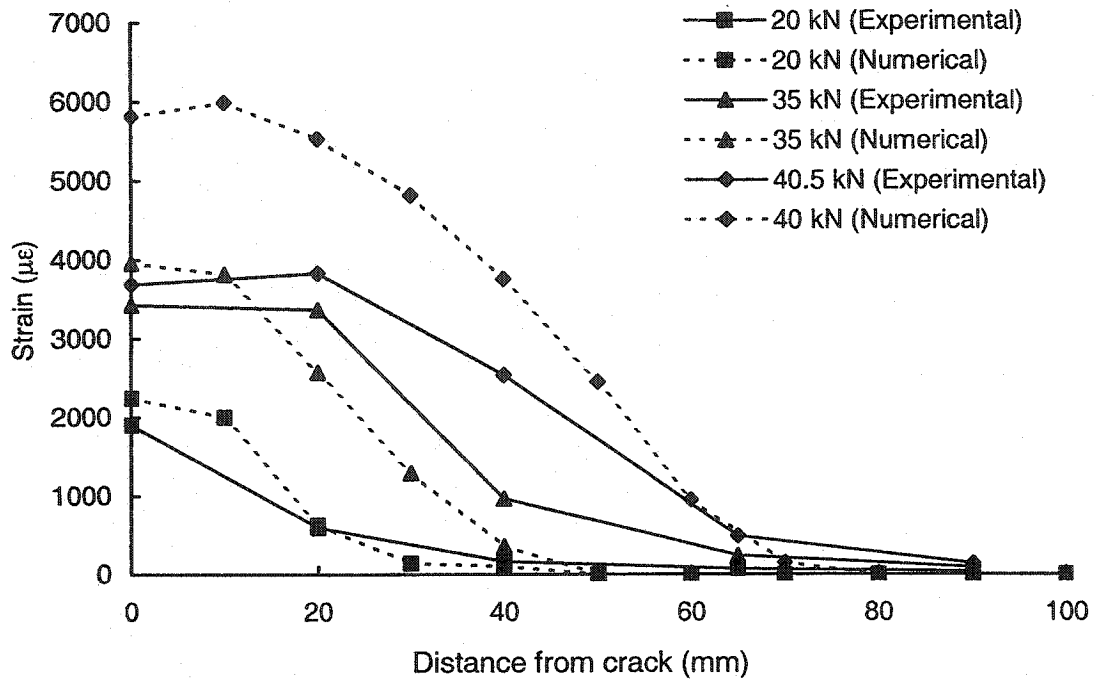


Figure 5-32 Strain distribution for experimental and 2D model of P10

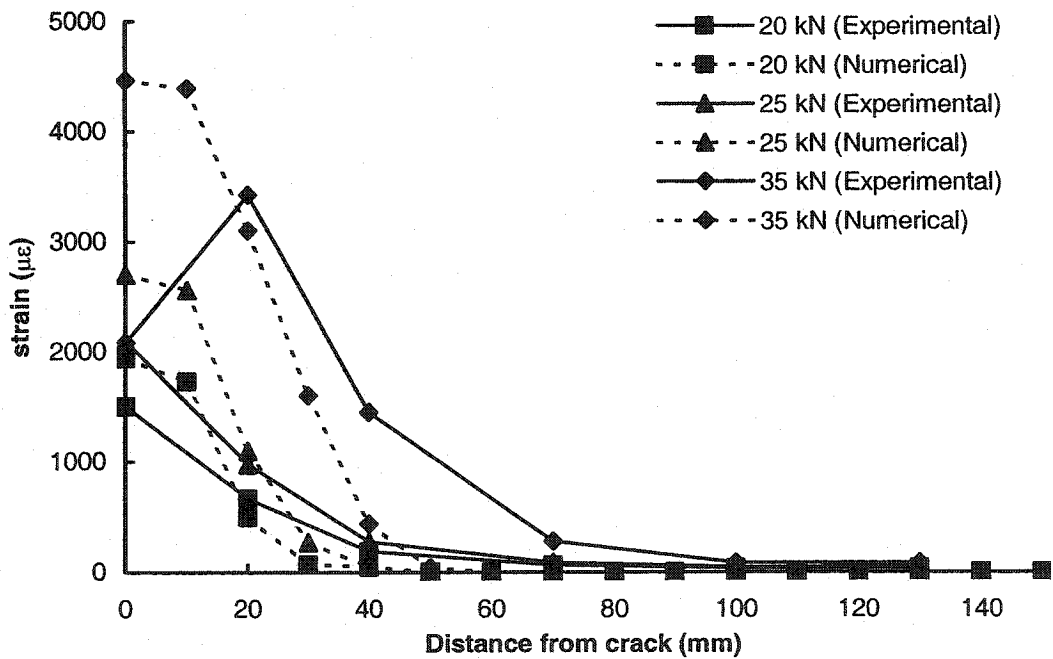


Figure 5-33 Strain distributions for experimental and 2D model of P11

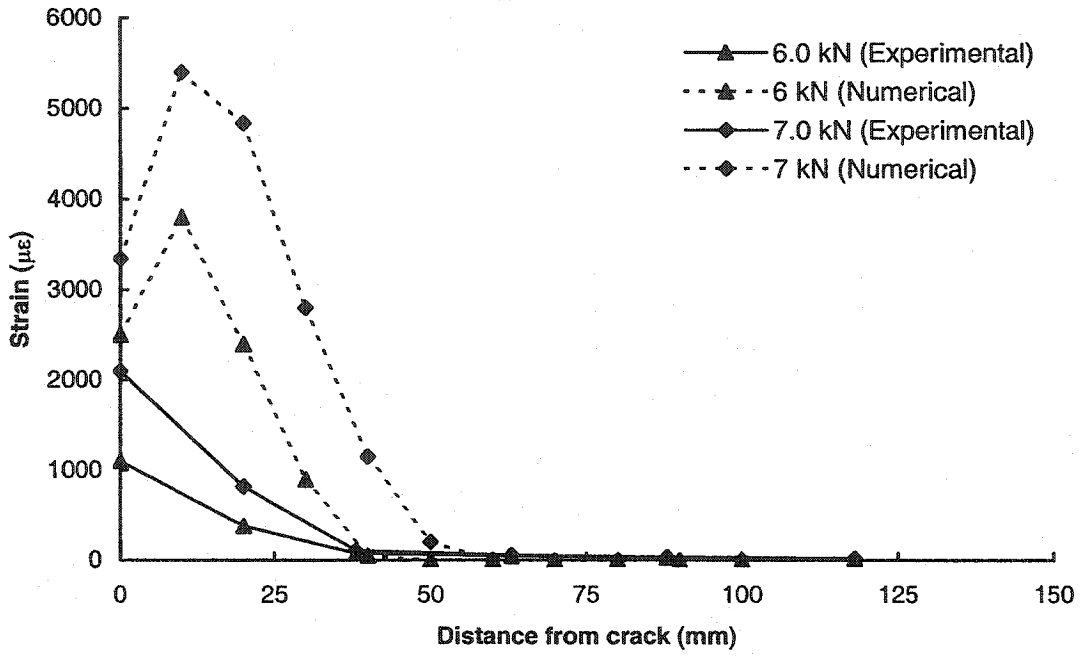


Figure 5-34 Strain distributions for experimental and 2D model of P12

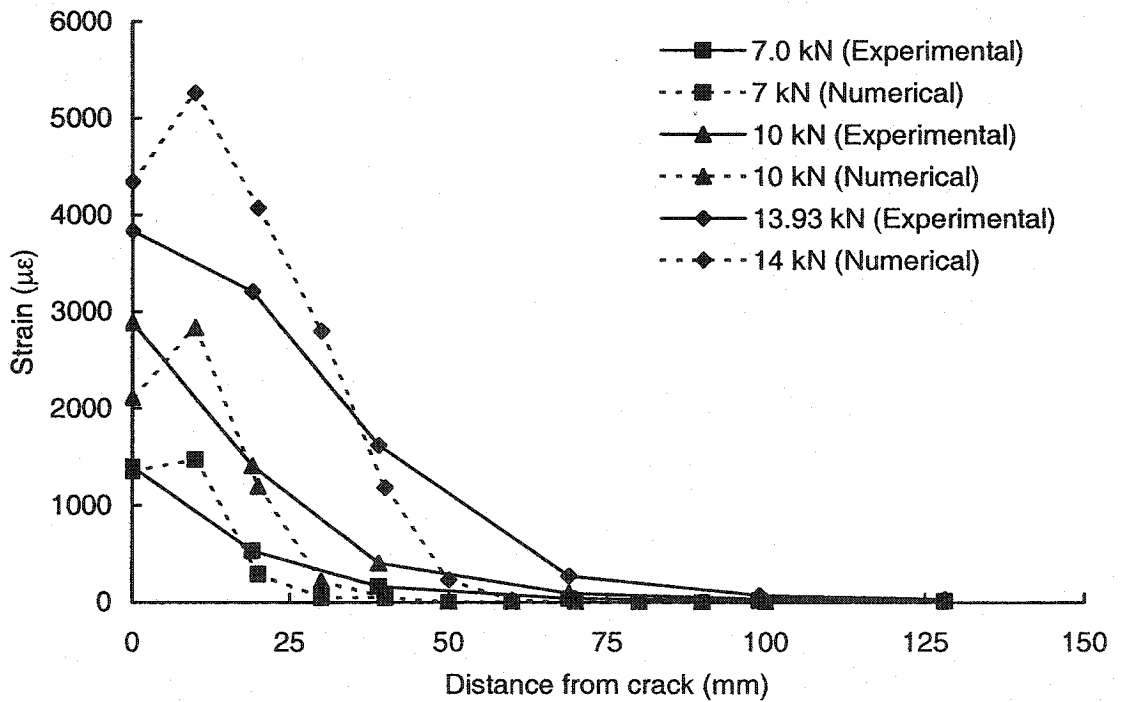


Figure 5-35 Strain distributions for experimental and 2D model of P13

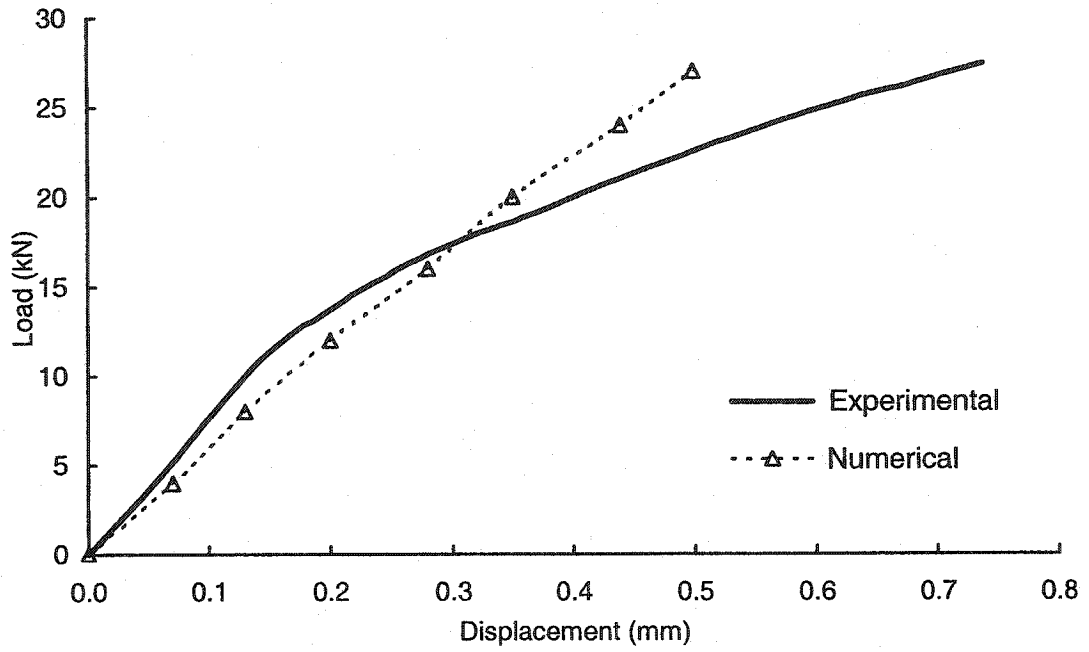


Figure 5-36 Load-displacement for experimental and 3D model of S1

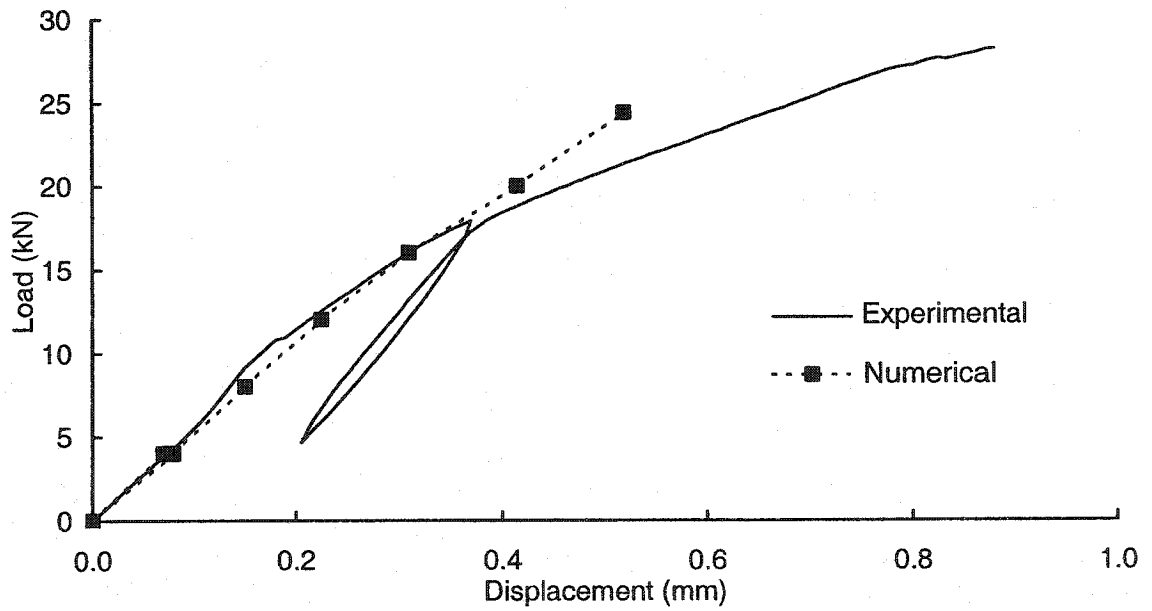


Figure 5-37 Load-displacement for experimental and 3D model of S3

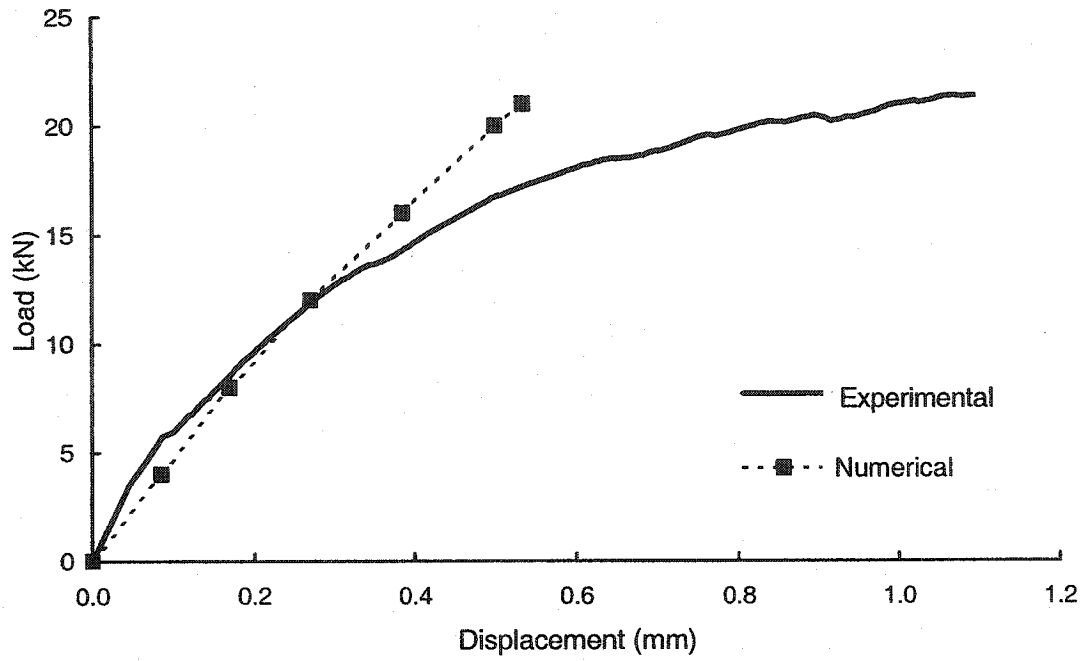


Figure 5-38 Load-displacement for experimental and 3D model of S4

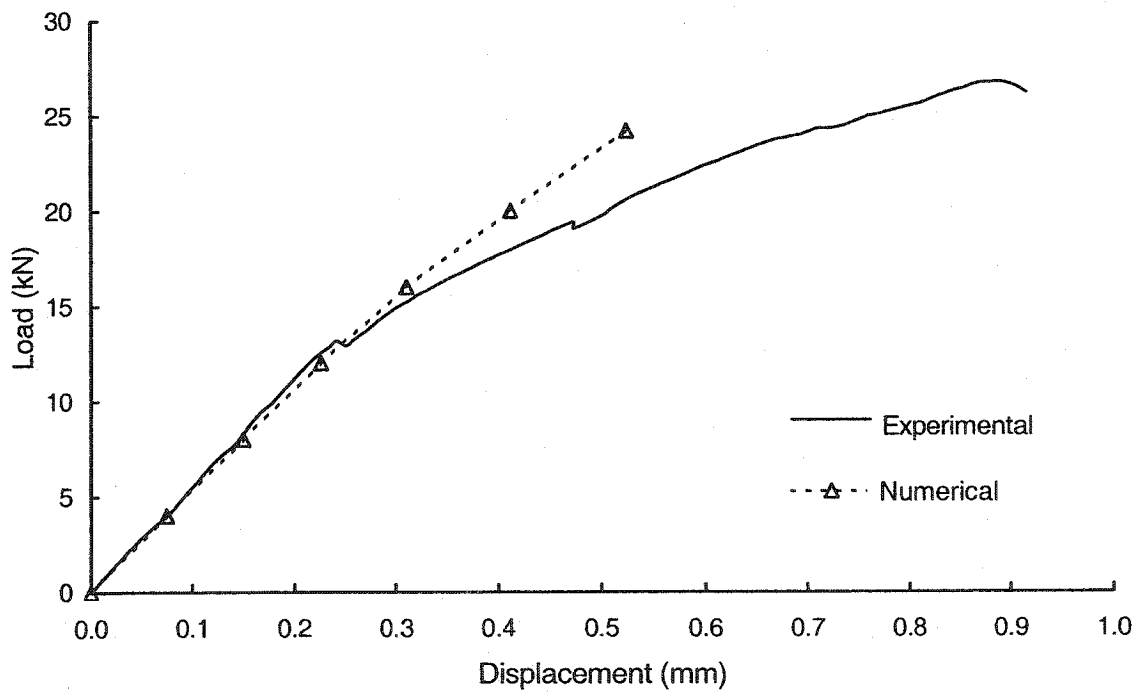


Figure 5-39 Load-displacement for experimental and 3D model of S5

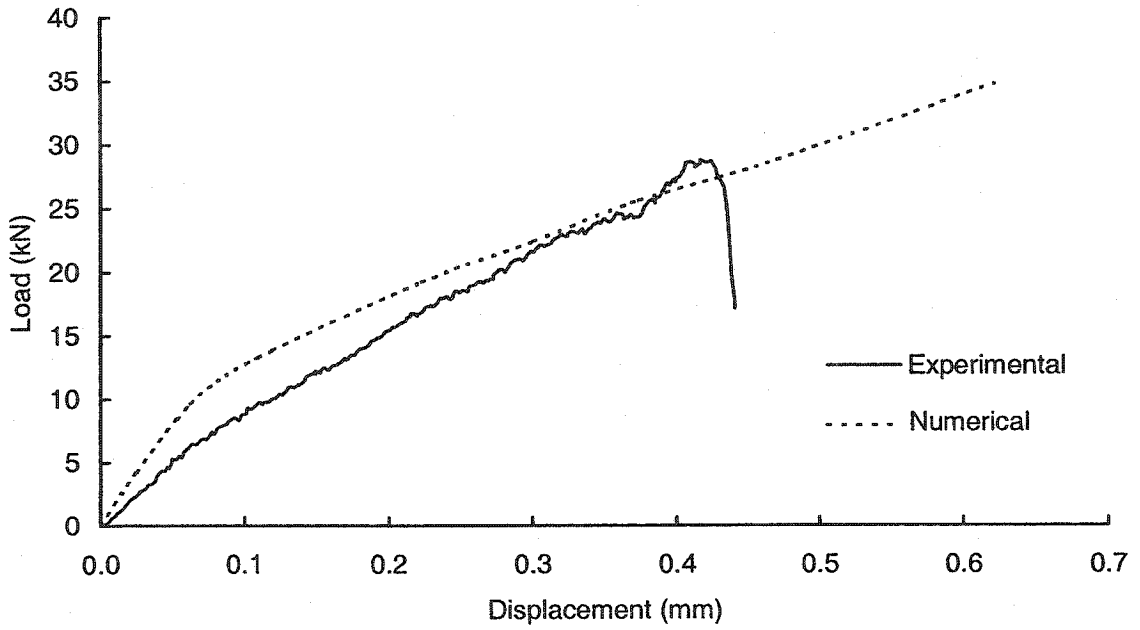


Figure 5-40 Load-displacement for experimental and 3D model of P9

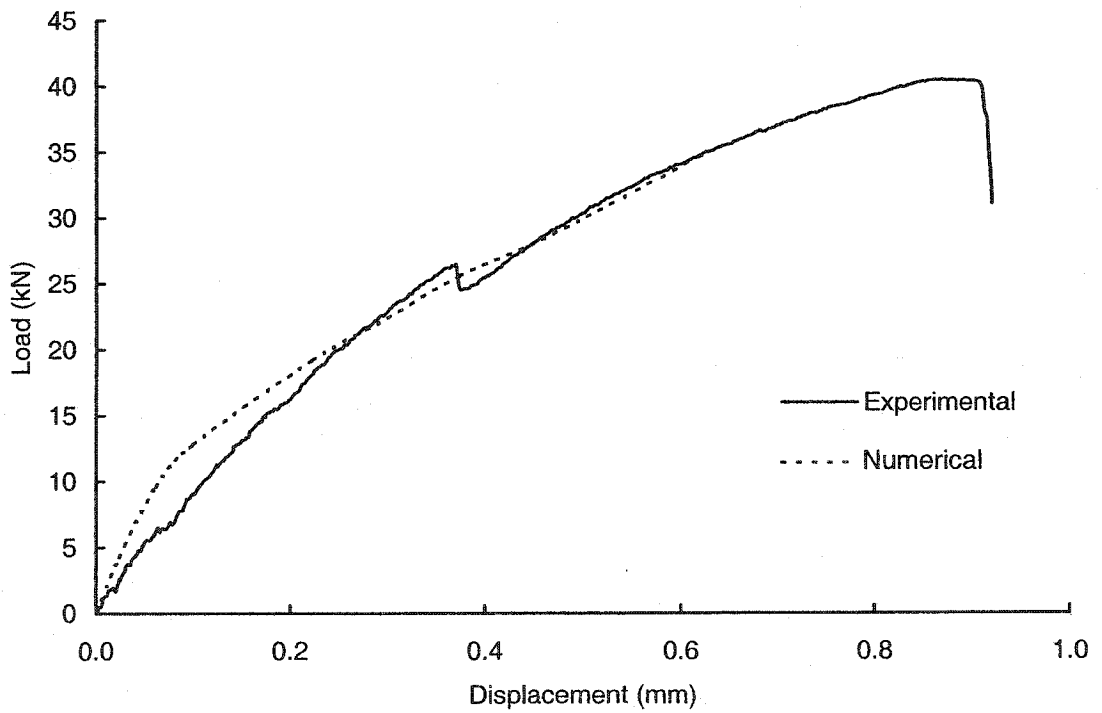


Figure 5-41 Load-displacement for experimental and 3D model of P10

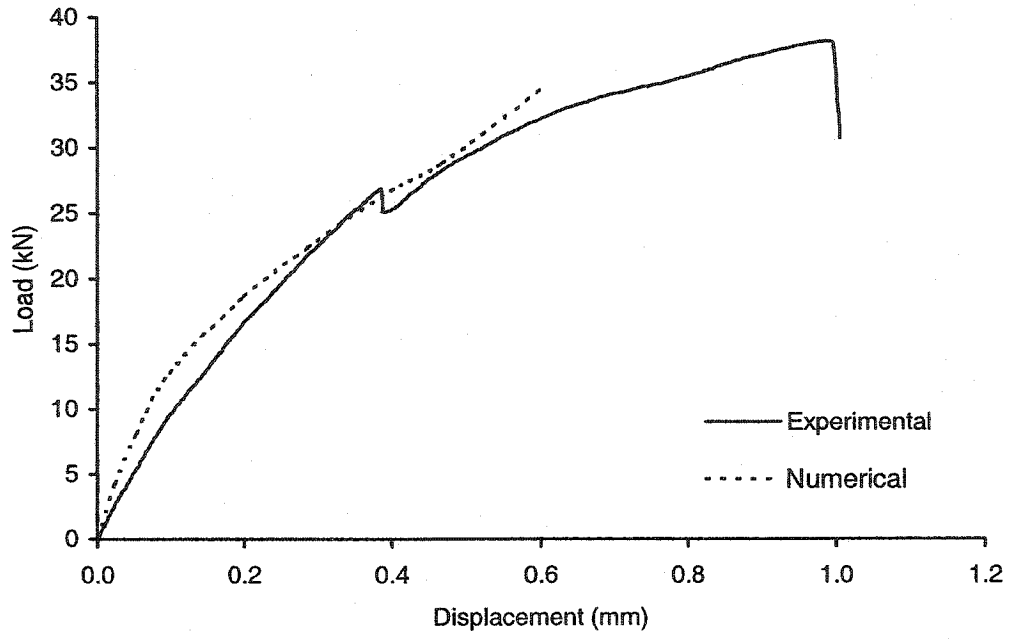


Figure 5-42 Load-displacement for experimental and 3D model of P11

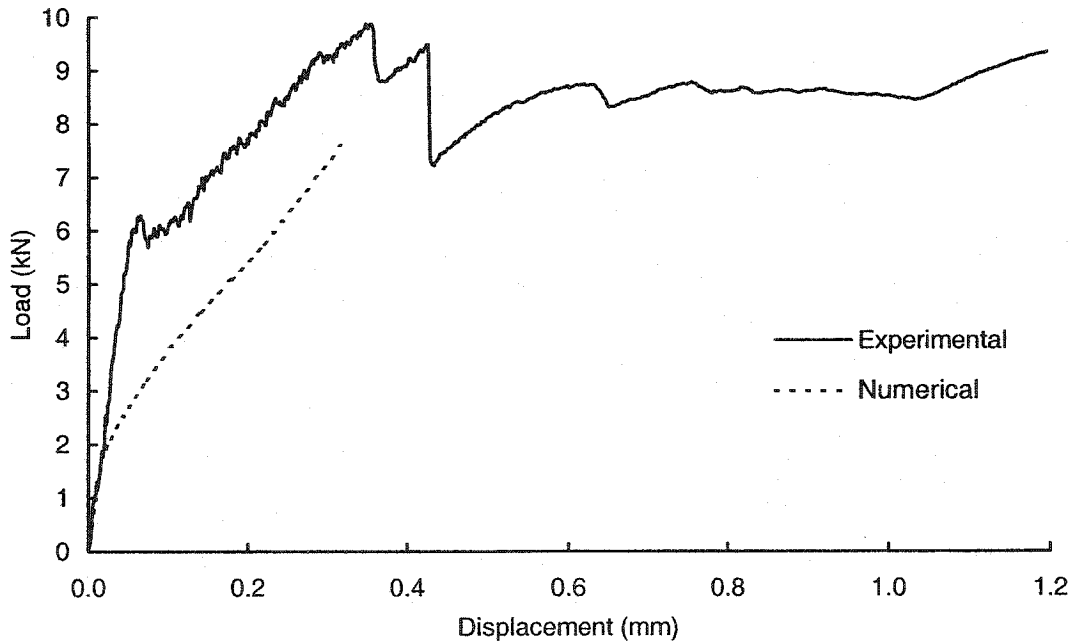


Figure 5-43 Load-displacement for experimental and 3D model of P12

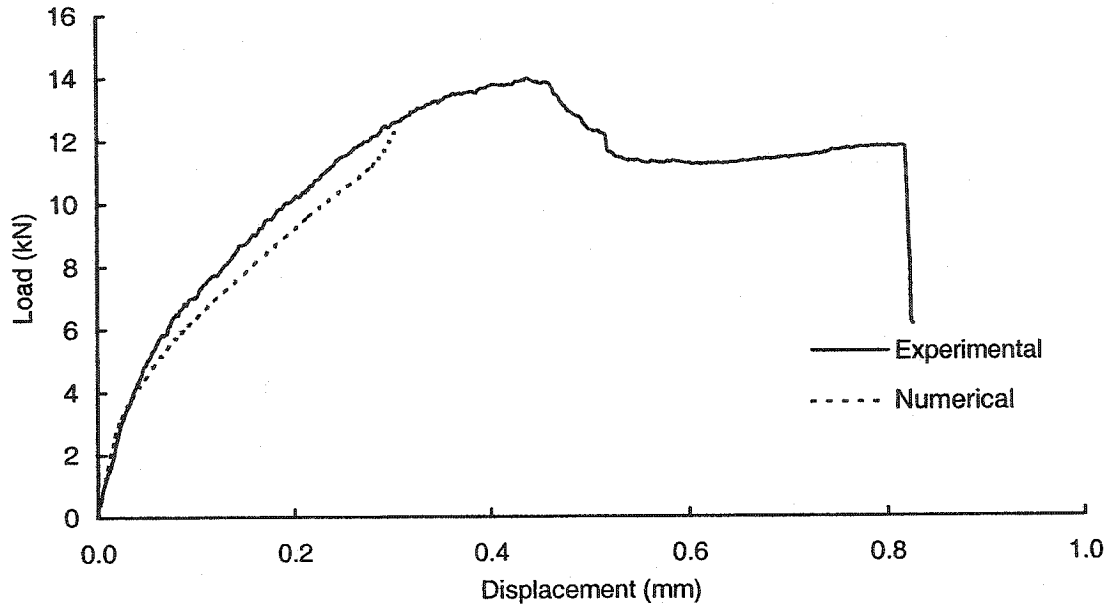


Figure 5-44 Load-displacement for experimental and 3D model of P13

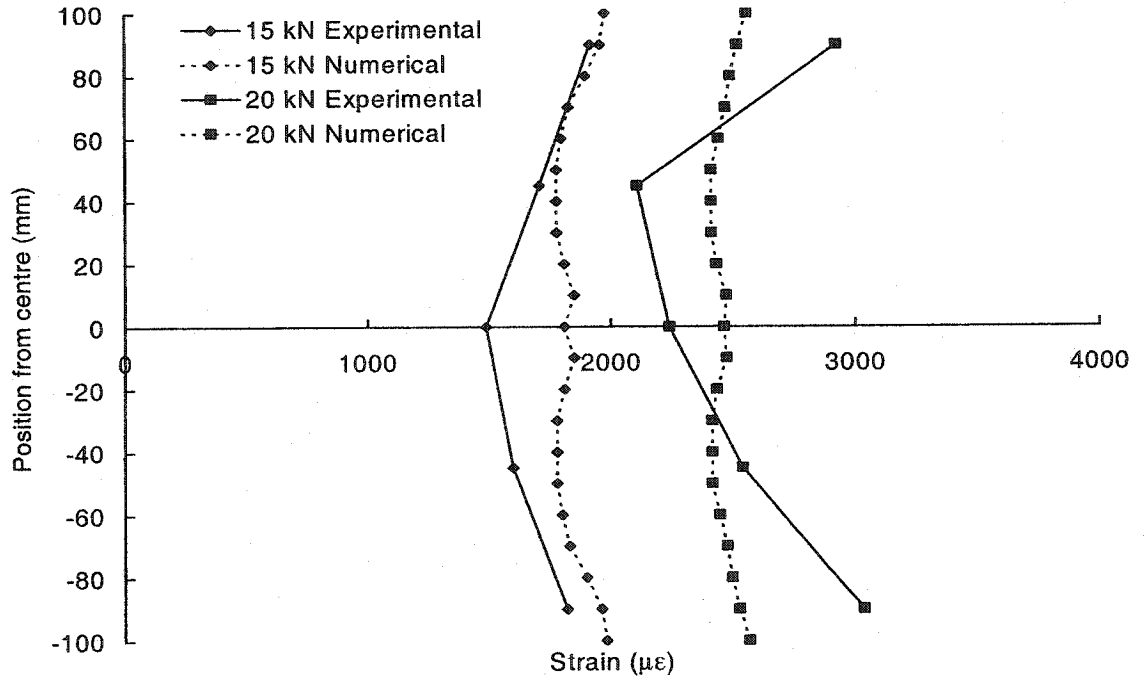


Figure 5-45 Strain distributions across sheet width of S1 at the crack location

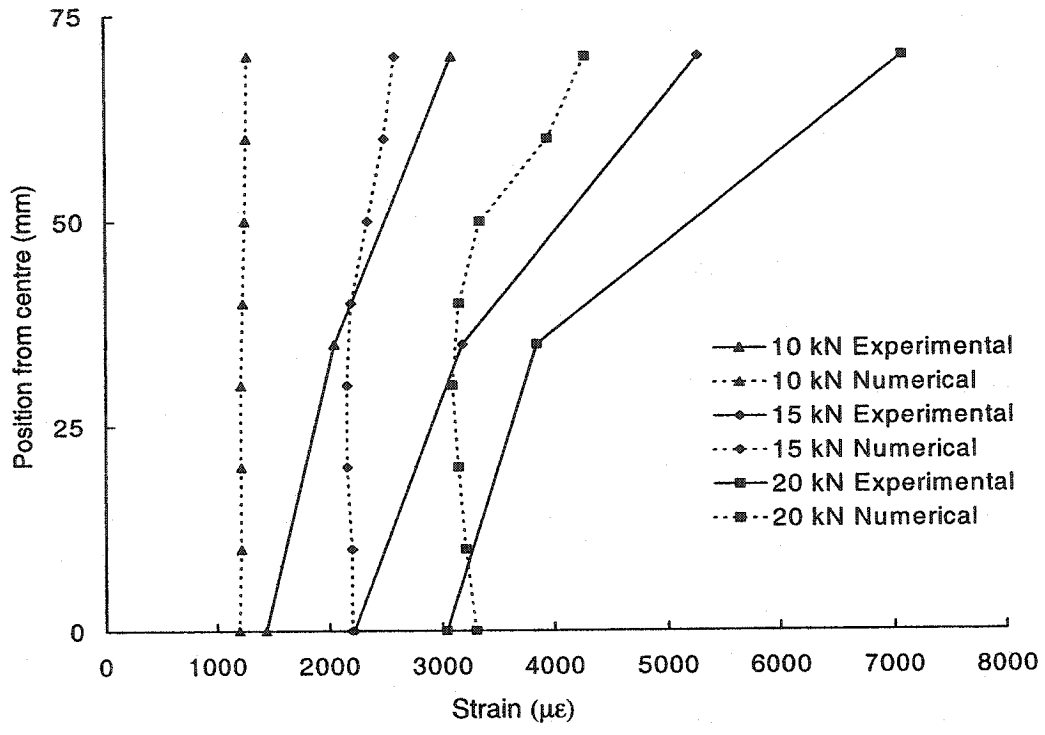


Figure 5-46 Strain distributions across half sheet width of S2 at the crack location

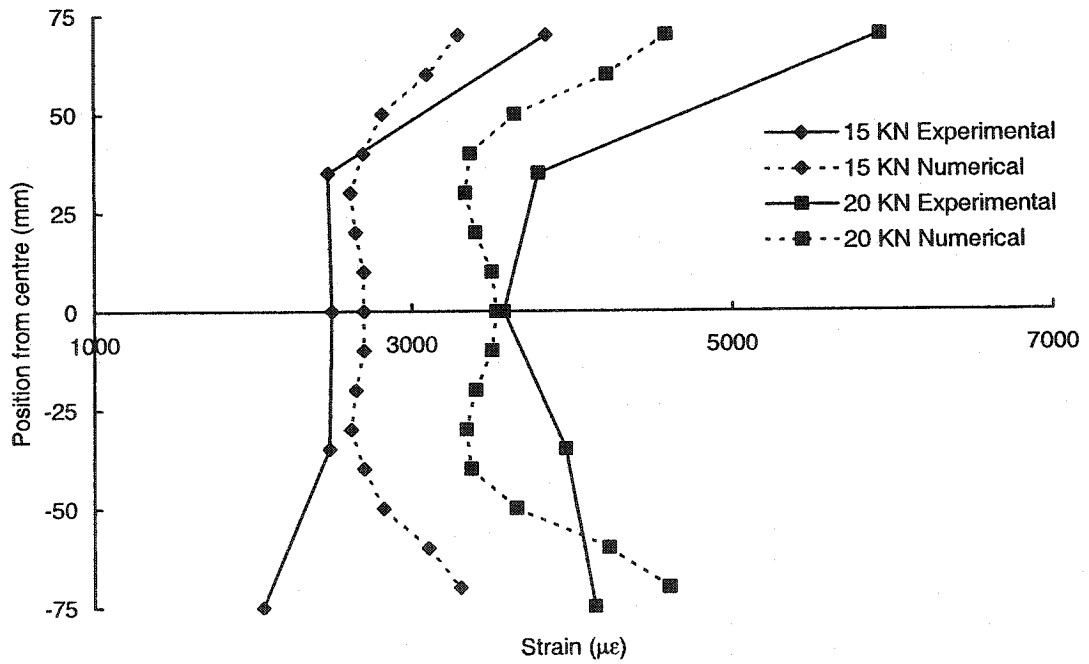


Figure 5-47 Strain distributions across sheet width of S3 at the crack location

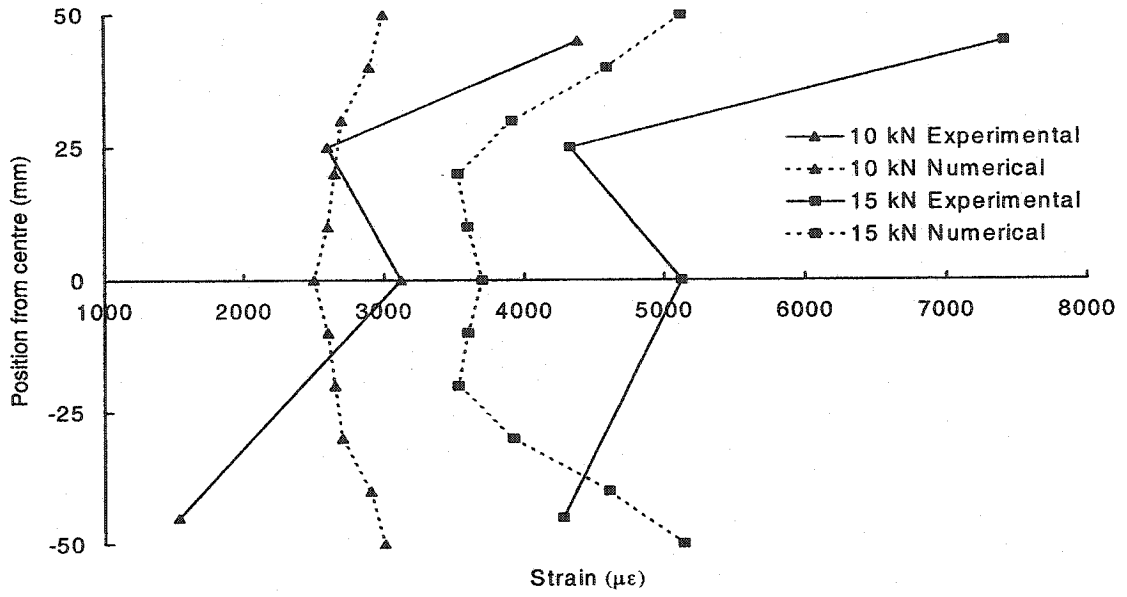


Figure 5-48 Strain distributions across sheet width of S4 at the crack location

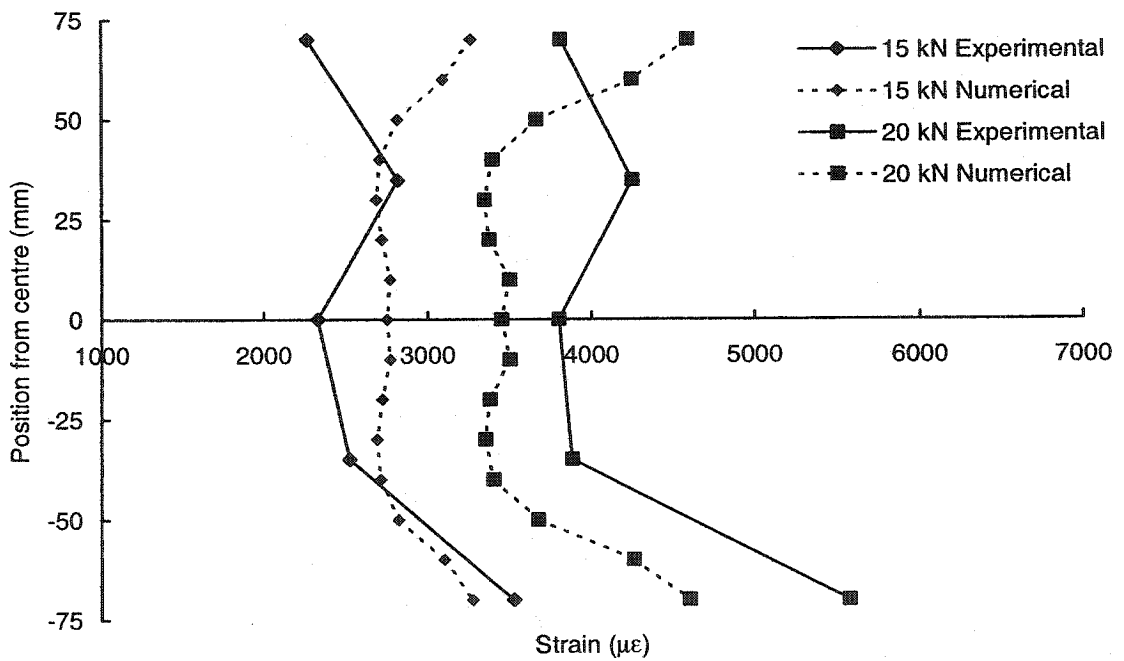


Figure 5-49 Strain distributions across sheet width of S5 at the crack location

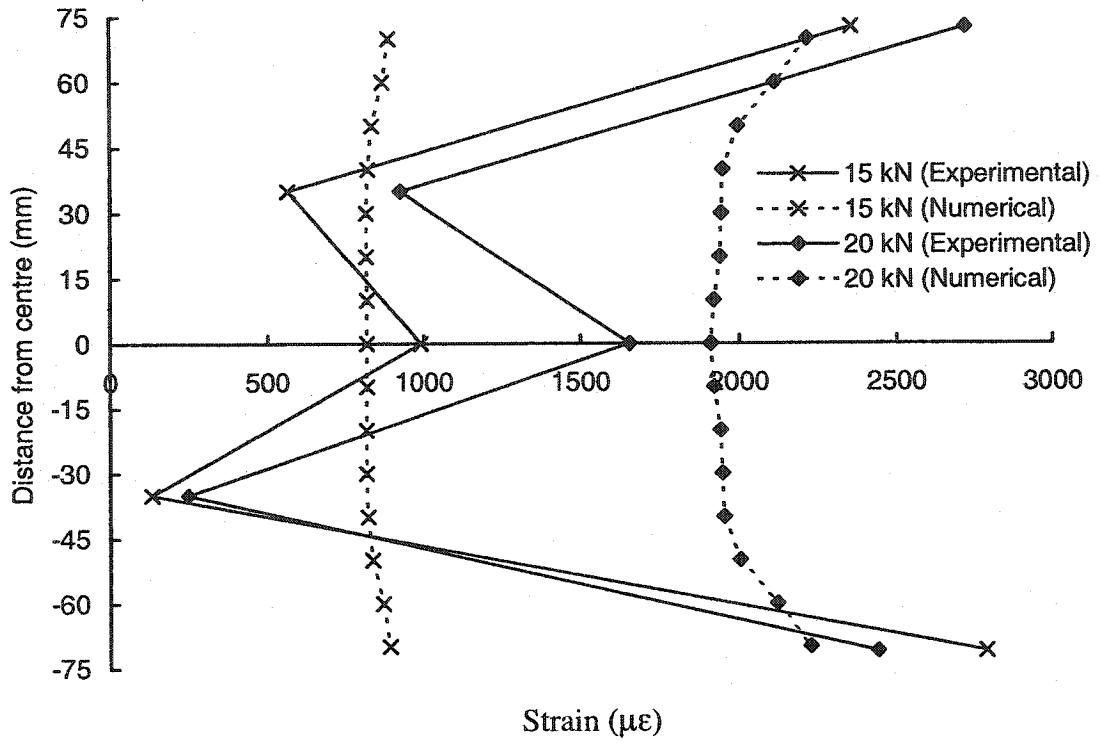


Figure 5-50 Strain distributions across the width of P9 at crack location

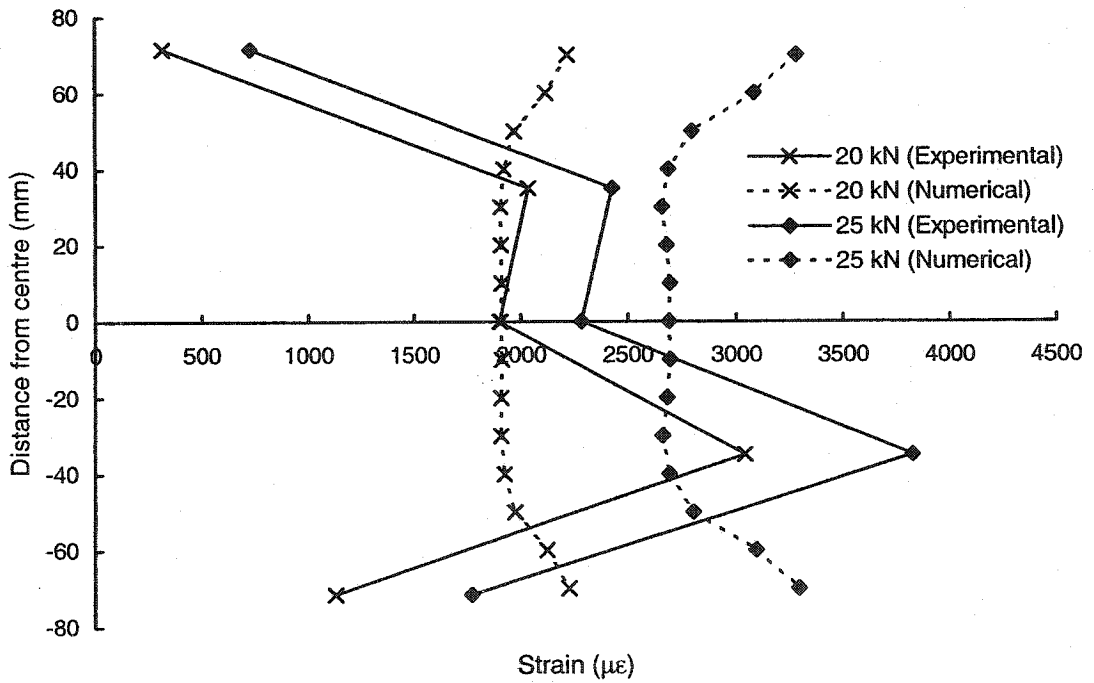


Figure 5-51 Strain distribution across the width of P10 at crack location

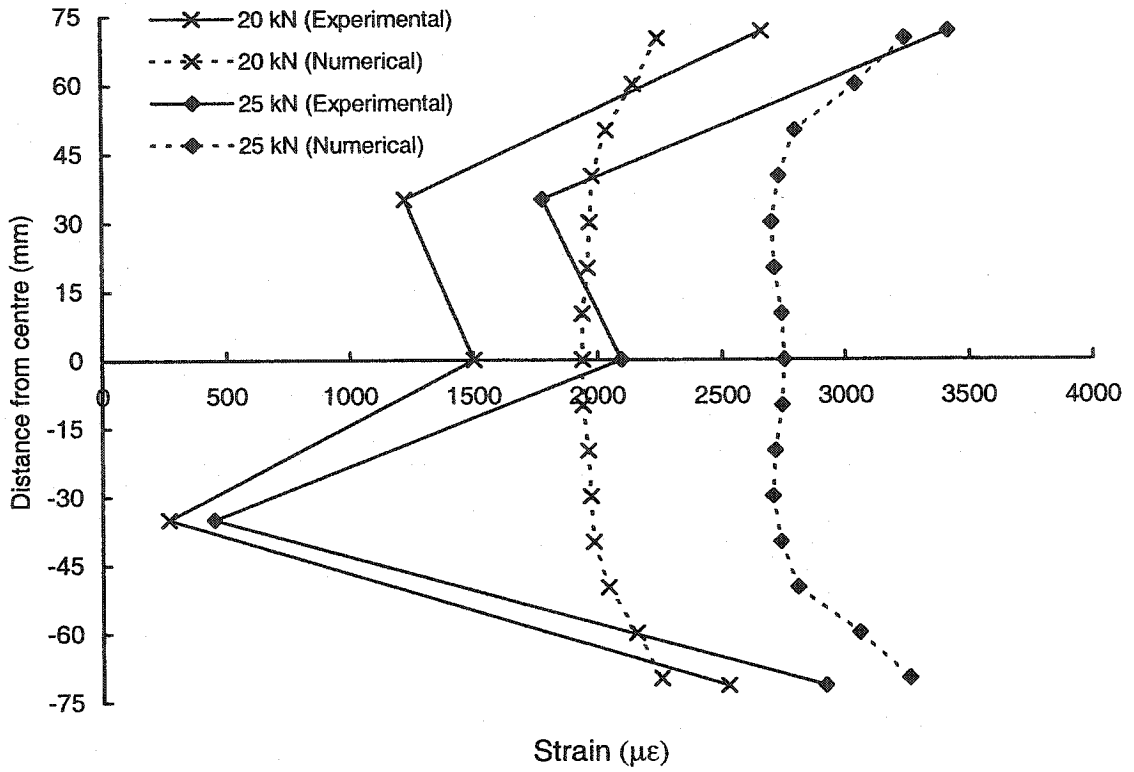


Figure 5-52 Strain distributions across the width of P11 at crack location

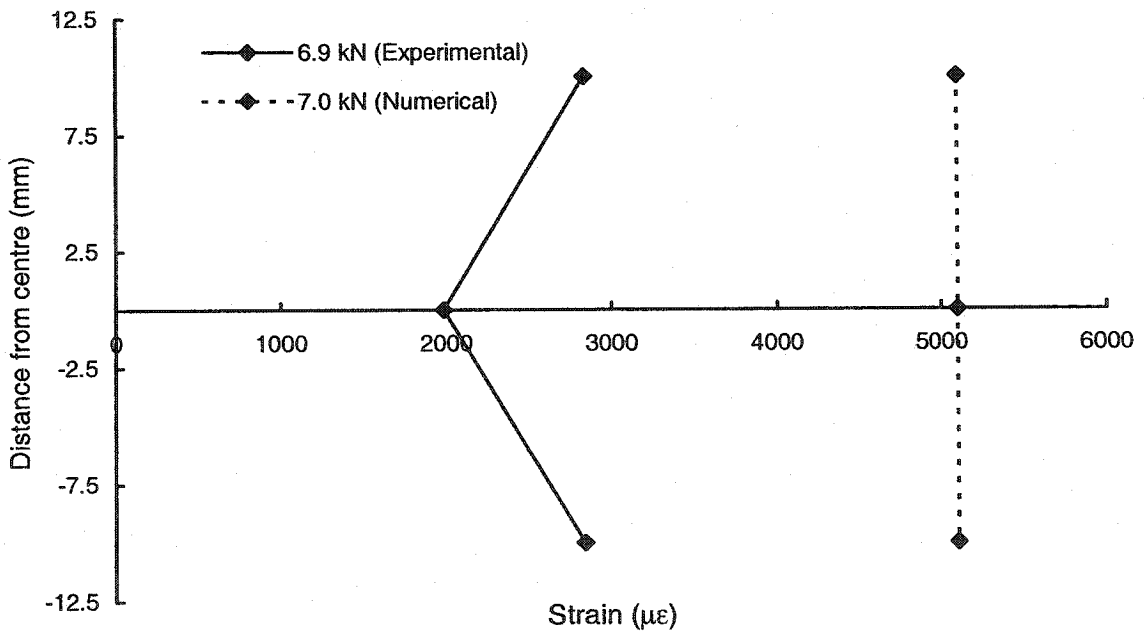


Figure 5-53 Strain distributions across the width of P12 at crack location

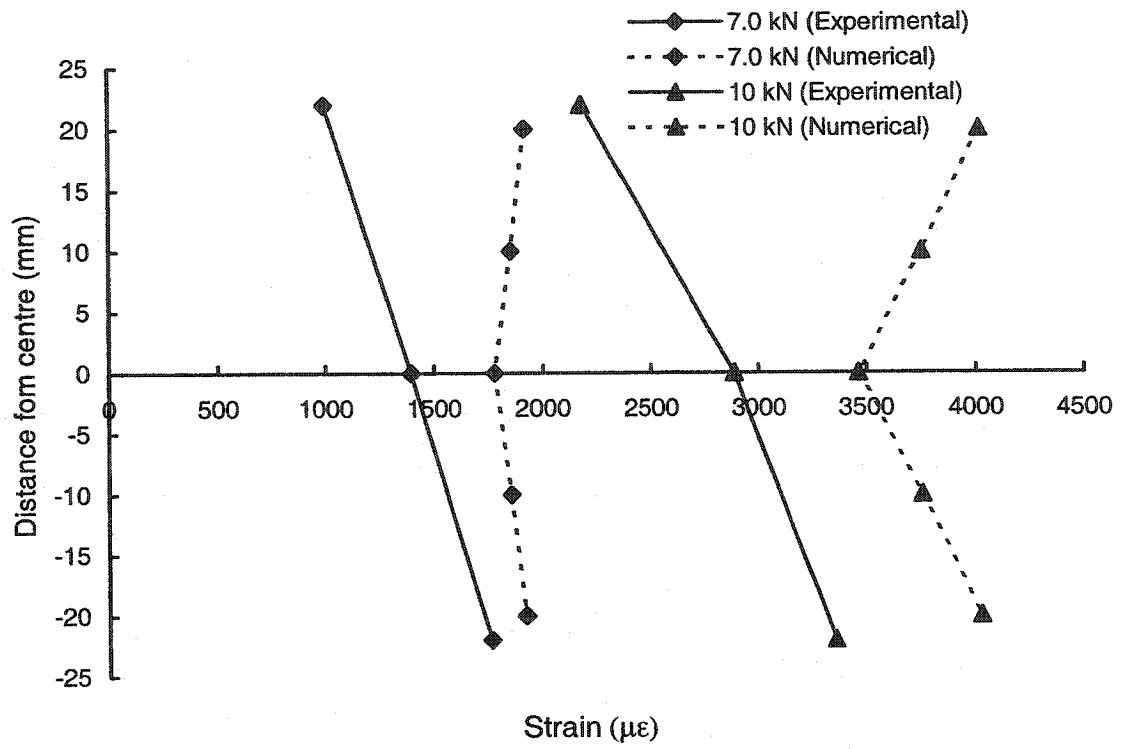


Figure 5-54 Strain distributions across the width of P13 at crack location

6. PARAMETRIC STUDY

6.1 Introduction

Design guidelines are still developing for specific retrofitting requirements using FRP sheets bonded to concrete structures. Such guidelines are to govern how fibre systems should be tailored in order to provide adequate improvements in strength, ductility, or both. Evaluating the effect of externally bonded FRP sheets based on their tensile strength and using guidelines similar to those for conventional steel reinforcement in concrete members is insufficient. The failure modes associated with FRP sheets externally bonded to concrete (see Section 2.5) need to be accounted for in the design. It is difficult, expensive, and time consuming to optimize FRP performance completely experimentally. Alternatively numerical models that consider both concrete and FRP properties through mechanical interaction provide a possible means of extending the available database.

The following subsections will investigate the debonding type failure, which could occur in members strengthened in flexure or shear. The numerical models used are able to investigate this type of failure by allowing the FRP sheet to debond. A discussion and verification of the 2D and 3D numerical models used are detailed in Chapter 5. The good agreement of the model trends with the experimental results were seen as sufficient for the models to be used to conduct a parametric study on the behaviour of FRP sheets bonded to concrete. Debonding is assumed to take place when the normal and shear stresses at the interface reach an interaction function defined by critical values of 6.0 and 3.5 MPa, respectively. These levels are based on values reported in the literature, (Section 2.6.3), and the values used in the numerical models in Chapter 5.

The aim of the parametric study presented in this chapter was to provide further insight into the behaviour of FRP sheets bonded to concrete. The literature review presented in Chapter 2 and the experimental program carried out in this study, presented in Chapters 3 and 4, have both shown that the main parameters affecting the

bond behaviour between concrete and FRP sheets are the FRP sheet bond length, bond width, stiffness, and the concrete strength. These parameters are investigated in the parametric study presented in this chapter. The FRP sheet bond length and width were also investigated in the experimental tests, detailed in Chapters 3 and 4, but with considerably lower values and smaller range than the numerical parametric study. In addition to the previous parameters, the strain distribution across the FRP sheet width and the relative FRP sheet width to the concrete specimen width are investigated.

Table 6-1 shows the concrete and FRP sheet default material properties used in the parametric study unless otherwise stated. A summary of the variables investigated is given in Table 6-2 through Table 6-7. The tables indicate that a total number of 124 specimens were analyzed. For each parameter investigated, the numerical model generated several relationships including load-deflection responses and strain distributions along the length and across the width of the FRP sheet. The relationships generated were further used to plot relationships that provide insight into the bond behaviour. Each parameter investigated is discussed in detail in the following subsections.

6.2 FRP Sheet Bond Length

The effect of the bond length of the FRP sheet on the bond behaviour was studied using the 2D modified push-apart model. The bond length was studied in relation to the bond width, stiffness, and concrete strength; each was varied individually while maintaining the other parameters constant. Ultimate load and average bond strength were plotted against the FRP sheet bond length at different bond width, stiffness, and concrete strength values in order to investigate the bond length effect on the bond behaviour and the effect of each variable on the effective bond length.

The variables in the investigation of the bond length effect with varying bond widths were the FRP sheet bond length and width, while the FRP sheet stiffness and

concrete strength were maintained at 25 GPa·mm and 50 MPa, respectively. The bond lengths (Table 6-2) varied from 50 mm to 200 mm. This range of bond lengths was chosen in order to cover a wide range of bond lengths and was based on the literature value range of the effective bond length. The bond width was varied from 25 to 200 mm, which was 12.5% and 100% of the concrete width, respectively. The smallest width of 25 mm was used in several research investigations, specially the direct pull test, while widths over 100 mm were closer to the widths used in practice.

The ultimate load values for models with various bond lengths were obtained from the load-displacement responses, similar to that shown in Figure 6-1. The figure shows the load-displacement response for models with the same FRP sheet bond lengths of 150 mm. The ultimate load plotted against the bond length at bond width values ranging from 25 mm to 200 mm is shown in Figure 6-2. It is observed from the figure that the ultimate load increases as the bond length increases but beyond a certain bond length, which was different for each bond width, there is no increase in the ultimate load. This bond length is defined as the effective bond length. The reason why the ultimate load does not change can be attributed to the fact that debonding of the FRP sheet propagates without an increase in the applied force in the sheet for the longer bond lengths.

The effective bond lengths are determined for each bond width from Figure 6-2 by estimating the bond length beyond which no increase in the ultimate load is gained. The locations of the estimated effective bond lengths are marked on Figure 6-2 by vertical dotted lines. There is no significant change in the ultimate load as the bond length increases for models with bond widths of 25 mm. The effective bond length, although not clear, is estimated to be 110 mm for bond widths of 25 mm. The effective bond length plotted against the bond width is shown in Figure 6-3. The figure shows that the effective bond length increases as the width increases. The reason for the increase in the effective bond length as the bond width increases is attributed to the decrease in the average bond stress across the FRP sheet as the bond width increases, which requires a larger effective bond length in order to develop the

full bond capacity. This will be discussed in the following subsection. The literature reports effective bond length values ranging from 60 to 275 mm as discussed in Section 2.7.1. To our best knowledge, there has been no research relating the effective bond length to the bond width.

The computed average bond strengths for models investigating the bond length effect with varying bond width values are listed in Table 6-2. The average bond strength was calculated by:

$$\tau_b = \frac{P_u}{L \cdot w} \quad (6-1)$$

in which, P_u is the ultimate load, and L and w are the FRP sheet bond length and width, respectively. The average bond strength plotted against the FRP sheet bond length at bond width values ranging from 25 to 200 mm is shown in Figure 6-4. The figure shows that the average bond strength decreases as the bond length increases. There is also no significant difference in behaviour for bond widths higher than 100 mm. Figure 6-5 shows the average bond strength evaluated on the basis of the effective bond lengths estimated from Figure 6-3. The figure shows that the average effective bond strength values are constant beyond the effective bond lengths and that they decrease as the FRP sheet bond width increases.

Models investigating the bond length effect at various FRP sheet stiffness values are listed in Table 6-3. The table shows that the only variables are the FRP sheet bond length and stiffness, while the bond width and concrete strength are maintained at 100 mm and 50 MPa, respectively. The FRP sheet stiffness, E_t , values range from 25 to 125 GPa·mm, which represent the common values used in the literature and that represent a range of one to five plies of FRP sheets having a ply thickness of 0.38 mm and a modulus of elasticity of 65789 MPa. Figure 6-6 shows the FRP sheet bond length plotted against the ultimate load at the various E_t values listed in Table 6-3. The figure shows that the ultimate load increases as the sheet stiffness increases. Estimating the effective bond lengths for the different E_t values from Figure 6-6 and plotting them against the sheet stiffness in Figure 6-7 shows that the effective bond

length increases as the sheet stiffness increases. This could be attributed to the decrease in the ductility of the FRP sheet with the increase in its stiffness, which delays the occurrence of debonding. This delay also increases the capacity of the joint, where a larger effective bond area resists the applied load. The expression “joint” used here refers to the assembly of concrete, adhesive, and FRP sheet. The figure also shows a constant effective bond length beyond the sheet stiffness of 100 GPa·mm. Maeda et al. (1997) who studied the effect of the number of plies on the bond behaviour using pull-apart specimens, stated that the effective bond length decreases as the sheet stiffness increases, which is contrary to findings of this investigation.

Table 6-4 lists the models investigating the bond length effect at various concrete strength values. The table shows that the only variables were the FRP sheet bond length and the concrete strength, while the FRP sheet bond width and stiffness are maintained at 100 mm of 25 GPa·mm, respectively. The value of the concrete modulus of elasticity, E_c , was calculated in accordance with the CSA Standard A23.3-94, (1995):

$$E_c = 4500 \sqrt{f'_c} \quad (6-2)$$

in which f'_c is the uniaxial concrete compressive strength. The concrete strength values range from 20 to 60 MPa, chosen from practical value ranges for existing and new reinforced concrete structures. The concrete tensile strength was taken equal to $0.53 \sqrt{f'_c}$. The overall load-displacement responses for models with $L=200$ mm, listed in Table 6-4, are plotted in Figure 6-8. Figure 6-9 shows the FRP sheet bond length plotted against the ultimate load diagrams at the various concrete strength values listed in Table 6-4. The figure shows that the ultimate load increases as the bond length increases up to 200 mm, beyond which no increase in the ultimate load is observed. The figure also shows that as f'_c increases, the ultimate load increases and that the curves for different f'_c values are almost parallel, which results in similar effective bond lengths of 200 mm for all f'_c values. Further investigation into the

previous observation is detailed in Section 6.5, which studies f'_c effect on the bond behaviour.

A plot of the average bond strength against the FRP sheet bond length for f'_c values ranging from 20 to 60 MPa for the same models listed in Table 6-4 is shown in Figure 6-10. The figure shows the relationship converging and the average bond strength stabilizing at longer bond lengths. This indicates that the concrete strength does not have a significant effect on the bond behaviour of longer bond lengths. This could be attributed to the debonding type failure simulated in the models, which is dependent on the adhesive strength represented in the interface shear and normal stresses between the FRP sheet and the concrete rather than the concrete strength. This explanation was also stated by De Lorenzis et al. (2000) who studied f'_c effect on bond behaviour using beam specimens. Assuming an effective bond length of 200mm in calculating the average bond strength is plotted in Figure 6-11. The figure shows that the average effective bond strength values beyond the effective bond lengths are constant and range between 1.1 and 1.3 MPa for f'_c values of 20 and 60 MPa, respectively.

From the previous discussion it is concluded that increasing the bond length increases the capacity and bond strength of the joint. There also exists an effective bond length beyond which no increase in the capacity is gained, which is similar to the experimental conclusion. The effective bond length increases as the sheet bond width increases. Increasing the sheet stiffness also increases the effective bond length up to a certain stiffness value of 100 GPa·mm beyond which no increase in the effective bond length is gained. The concrete strength does not appear to have a significant effect on the effective bond length.

6.3 FRP Sheet Bond Width

6.3.1 General

The following presents the effect of the FRP sheet bond width on the bond behaviour with concrete studied using the 2D modified push-apart model as detailed in Chapter 5. As the models developed in Chapter 5 were able to capture the width effect in an average sense, they were seen as sufficient for this investigation. Table 6-2 lists the models and their variables used in investigating the bond width effect. The variables are the FRP sheet bond width and length. The bond width values ranged from 25 to 200 mm, which was 12.5% and 100% of the concrete width, respectively. The bond lengths ranged from 50 to 200 mm, which covered a wide range of development lengths practically used.

Figure 6-12 shows the FRP sheet bond width plotted against the ultimate load relationships for bond length values ranging from 50 to 200 mm while maintaining a constant sheet stiffness and concrete strength of 25 GPa·mm and 50 MPa, respectively. The figure shows that the ultimate load increases as the bond width increases. At bond width values less than 100 mm the percentage increase in ultimate load is almost similar to the percentage increase in the bond width while for bond width values larger than 100 mm the percentage increase in load is significantly lower than the percentage increase in bond width. This behaviour is apparent from the change in slopes at the bond width of 100 mm in Figure 6-12. Increasing the bond width by 100% from 50 to 100 mm increases the ultimate load by 94% while increasing the bond width from 100 to 200 mm increases the ultimate load by 51% on average for bond lengths ranging from 50 to 200 mm. The ultimate load per unit width plotted against the bond length is shown in Figure 6-13. The figure shows that there is no significant difference in P_u/w for bond widths below 100 mm, but beyond this value P_u/w decreases as the bond width increases. This indicates a variation in the stress distribution across the FRP sheet width as the width increases. Figure 6-13 also shows that the P_u/w value increase as the bond length increases, but stabilizes as it reaches lengths over 150 mm.

The previous discussion indicates a reduction in the average bond strength for wider FRP sheets, which is directly proportional to the ultimate load and inversely proportional to the sheet bond width. The FRP sheet bond width plotted against the average bond strength relationship for bond length values ranging from 50 to 200 mm and using constant FRP sheet stiffness and bond width values of 25 GPa·mm and 100 mm, respectively, is shown in Figure 6-14. The average bond strength in the figure was calculated by equation (6-1). The figure shows that the average bond strength decreases as the bond width exceeds 100 mm while there is no significant change in its value at bond widths less than 100 mm.

The first portion of the previous conclusion is consistent with the literature (Ueda et al., 1999) and with the S-series experimental results detailed in Section 4.5, which shows the average bond strength decreasing as the bond length increases from 100 to 150 mm. The second portion agrees with literature research done on narrow bond widths, which indicates that the bond width has no effect on the bond behaviour (Brosen and Van Germert, 1999, and De Lorenzis et al., 2000). On the other hand, the conclusion does not match the results of the P-series, also detailed in Section 4.5, where the average bond strength is seen to decrease as the width increased even for width values lower than 100 mm. The following chapter will investigate if the type of bond test used is the cause of this variation.

Figure 6-15 shows the average bond strength based on an estimated effective bond length of 110 mm. The figure show that using the average effective bond length stabilizes the average bond strength beyond the average effective bond length. This indicates that the bond width is important only when the bond length is less than the effective bond length.

The previous discussion concludes that the average bond strength decreases as the bond width exceeds 100 mm while no significant change occurs at bond width values below 100 mm. This explains the contradictory results in the literature

regarding the influence of the bond width on the bond behaviour, presented in Section 2.7.2. The same conclusion implies that narrow sheets over-estimate the average bond strength. Practical strengthening schemes, however, tend to use wider FRP sheets. This indicates the importance of studying the behaviour of wider sheets on the bond behaviour.

6.3.2 The Effect of FRP Sheet Width to Concrete Width Ratio

Both the 2D and 3D modified push-apart models discussed in Chapter 5 were used to investigate the ratio of the sheet bond width to the concrete width on the bond behaviour. The 3D model was only used to investigate the strain distribution across the FRP sheet width, where it did not have the debonding capability but was seen as sufficient to investigate the strain distribution across the FRP sheet width. On the other hand, the 2D model was shown in Chapter 5 to be able to capture the bond behaviour in an average sense as the bond width varied.

The distance from the edge of the bonded FRP sheet to the specimen edge is analogous to half the spacing between FRP strips in shear strengthening of RC girders or flexural strengthening of RC slabs in practical applications. The ratio of the width of the FRP sheet to the width of the concrete specimen was taken into consideration in the literature in some proposed models predicting the bond strength of bonded FRP sheets to concrete as detailed in Section 2.8. The strain distribution across the FRP sheet width was investigated in the experimental tests detailed in Chapters 3 and 4. The experimental results discussed in Section 4.3.2 showed the strain distribution to vary across the sheet width. This experimental observation pointed out the need to study the strain distribution across the FRP sheet width in more detail using numerical models.

Table 6-5 lists the variables used in this investigation. The variables were the concrete width and FRP sheet bond length, while all the other parameters were maintained constant. The concrete width values considered were 200, 300, and 400

mm, while FRP sheet bond widths were maintained at 200 mm in order to investigate whether the ratio of the FRP sheet to concrete width or the actual value of the concrete width was the effective factor influencing the bond behaviour. FRP sheet lengths of 50 and 150 mm were used in order to study whether the FRP sheet length had any influence on the behaviour.

The load-displacement responses of 2D models with concrete width values of 200, 300, and 400 mm are presented in Figure 6-16 and Figure 6-17 for FRP sheet bond lengths of 50 and 150 mm, respectively. The figures show that as the concrete width increases, both the ultimate load and stiffness of the joint increases, regardless of the bond length value. This shows that the concrete width itself affects the bond behaviour rather than the FRP sheet to concrete width ratio.

Figure 6-18 shows the contour lines of the strain in the main direction of the FRP sheet, E11, in 3D models with sheet width to concrete width ratios, w/w_c , of 0.7 and 1.0. It is clear from the figure that the strain values are higher at the FRP sheet edge than at its centre for the w/w_c of 0.7 case, while the strain is almost uniform across the FRP sheet width in the case of the FRP sheet covering the whole concrete width (w/w_c of 1.0). Figure 6-18b also shows that the strain is distributed in the concrete beyond the bonded width of the FRP sheet, which could explain the reason behind the increase in ultimate load with wider concrete widths.

The strain distribution, E11, across half the concrete width at the crack location in 3D models with FRP sheet bond widths of 100 and 200 mm are plotted in Figure 6-19 at 15 kN and ultimate load. The figure shows that for the model with FRP sheet width of 100 mm, the strain distribution in the concrete is higher underneath the FRP sheets but continues around 30 mm beyond the sheet width at ultimate load. The strain gradient is also high in this case, while in the case of the FRP sheet covering the whole concrete width, the strain distribution in the concrete is almost constant at 15 kN and significantly more uniform at ultimate load.

The distribution of the stress component S11 in the direction of the load across half the concrete width at the crack location for 3D models with FRP sheet widths of 100 and 200 mm are shown in Figure 6-20. The figure shows that the stress distribution in the concrete underneath the 100 mm wide FRP sheet is not uniform and the stresses are compressive, while the stresses in the concrete beyond the FRP sheet are in tension. The compression in the concrete balances the applied tensile stresses in the FRP sheets to satisfy equilibrium, while the tension stresses in the concrete beyond the FRP sheet balance the concrete compressive stress under the FRP sheet. The values of the stresses in Figure 6-20 indicate that the concrete is uncracked. The model with the FRP sheet covering the whole concrete width has a more uniform stress distribution in the concrete.

Figure 6-21 shows the strain distributions at 15 kN across the FRP sheet width at the crack location for 3D models with sheet widths ranging from 60 to 200 mm. The figure shows that the strain at the edge of the sheet is higher than that at its centre. This is similar to the experimental observations in Section 4.3.2. At the same load of 15 kN, the strain difference between the edge and centre of the FRP sheet increases as the bond width decreases. The strain values are also shown to increase as the width decreases. The same behaviour is observed for the strain difference and strain values at loads 50, 70, and 100% of the ultimate load, as shown in Figure 6-22, Figure 6-23, and Figure 6-24, respectively. The figures also show the strain values increasing as the applied load increases.

Figure 6-25 shows the relationship between the FRP sheet width and the difference in strain between the edge and centre of the sheet, $\Delta\epsilon$, at load levels, P/P_u , of 0.5, 0.7, and 1.0 and also at a load of 15 kN. The figure shows that $\Delta\epsilon$ increases as P/P_u increases and the 15 kN curve lies between the P/P_u of 0.5 and 1.0 curves, where the 15 kN load had a different load level value for each sheet width. Figure 6-25 also confirms that $\Delta\epsilon$ increases as the bond width decreases. There are no significant differences in $\Delta\epsilon$ observed when the sheet covers the concrete width (i.e. $w = 200$

mm), except for small $\Delta\varepsilon$ at ultimate load. This was also observed in the experimental tests detailed in Section 4.3.2.

Further investigation was performed into whether the previous behaviour is related to the actual sheet width or, instead, to the sheet-to-concrete width ratio. The strain in the FRP sheets plotted against the ratio of the distance from the specimen centre to half the concrete width for FRP sheet widths of 100, 200, and 400 mm, concrete widths of 200 and 400 mm, and all having bond lengths of 100 mm are shown in Figure 6-26. The figure shows that the strain values and distributions across the width for models with the same sheet widths are more related to each other than the corresponding models with the same w/w_c values. This indicates that the strain values and distributions across the width are related to the actual sheet width rather than the relative sheet to concrete width. This conclusion is important when specifying design guidelines for Reinforced Concrete (RC) beam shear strengthening and RC slab flexure strengthening. It indicates that actual width values should be used rather than relating the distance between the FRP strips to the strip widths. On the other hand, Figure 6-26 shows that the strain difference between the edge and centre of the FRP sheet is higher with wider concrete models as shown for the models with FRP sheet width of 100 mm and w/w_c values of 0.25 and 0.5.

The previous discussions conclude that the strains at the edge of the FRP sheets are higher than those at its centre and the difference between them increases as the FRP sheet bond width decreases and as the concrete width increases. This indicates that the investigations carried out with strain measurements only at the centre of the FRP sheet underestimate the strain values. The strain values are also shown to increase as the width decreases. The actual values of the concrete width and FRP sheet bond width are found to affect the bond behaviour rather than the relative FRP sheet to concrete width. This further indicates that the concrete width effect on the bond behaviour needs to be considered or a unified concrete specimen width needs to be defined and implemented.

6.4 FRP Sheet Stiffness

The literature shows that the FRP sheet stiffness is one of the important variables in determining the bond strength. The product of the FRP sheet modulus of elasticity, E , and its thickness, t , defines its stiffness, Et . A study was performed on models with different E and t values but with the same $E \times t$ value of 100 and 50 GPa·mm as shown in Table 6-7. The results showed no change in behaviour between models with similar $E \times t$ value. In this investigation, the FRP sheet stiffness was changed by changing the sheet thickness, t , to values of 0.38, 0.76, 1.14, 1.52, and 1.9 mm, while maintaining E constant at 65,789 MPa. These values of E and t were taken in order to produce Et values of 25, 50, 75, 100, 125 GPa·mm, respectively.

The effect of the FRP sheet stiffness, Et , on the bond behaviour was studied using the 2D modified push-apart model. The variables used in this investigation are listed in Table 6-3. The FRP sheet stiffness investigated ranged from 25 to 125 GPa·mm while the bond width was sustained at 100 mm. The ultimate load plotted against the FRP sheet stiffness at different bond length values is shown in Figure 6-27. The figure shows that the ultimate load increases as the stiffness increases but the effect is more significant at longer bond lengths. As previously stated this could be attributed to reduction in the elongation of the FRP sheet as the stiffness increases, which in turn causes less strain at the interface. This conclusion agrees with previous findings by other researchers who stated that increasing the sheet stiffness increases the capacity of the joint, as presented in Section 2.7.3. It is also observed from Figure 6-27 that the rate at which the ultimate load increases falls as the stiffness increases.

The average bond strength plotted against the FRP sheet stiffness at different bond length values ranging from 50 to 200 mm is shown in Figure 6-28. The figure shows that there is a stiffness value for every bond length beyond which no change in the average bond strength was observed. This limiting stiffness value will be called the effective stiffness. The effective FRP sheet stiffness estimated from Figure 6-28 and indicated by dotted vertical lines is plotted against the bond length in Figure 6-29. The figure shows that the effective FRP sheet stiffness increases as the bond length

increases. This can be attributed to the limited average bond strength each bond area can resist. The average bond stress will increase as the sheet stiffness increases until the sheet stiffness reaches a value that applies the maximum average bond stress to the bond area. Any increase in the sheet stiffness beyond that value will not increase the average bond strength and this limiting value could be considered the effective sheet stiffness value.

From the previous discussion it is concluded that the ultimate load increases as the FRP sheet stiffness increases. The average bond strength also increases as the FRP sheet stiffness increases but up to a certain limit. This limit is defined as the effective sheet stiffness beyond which no increase in the average bond strength is gained. The effective sheet stiffness changed with the bond lengths. This conclusion has a practical implication of an optimum FRP sheet stiffness or number of plies for every bond length.

6.5 Concrete Strength

The concrete strength, f'_c , effect on the bond behaviour was studied using f'_c values ranging from 20 to 60 MPa and bond lengths ranging from 50 to 200 mm, while the bond width was sustained at 100 mm. The bond length range was chosen in order to capture the influence of the effective bond length on the f'_c effect. The models used to study this effect are listed in Table 6-4. The overall load-displacement responses, measured at the point of load application, for all models listed in Table 6-4 were plotted, similar to that shown in Figure 6-8, which were used in further analysis. Figure 6-30 shows the concrete compressive strength plotted against the ultimate load at different bond length values. The figure shows that the ultimate load increases as f'_c increases, with the effect decreasing at longer bond lengths. The strain distributions along the sheet length of 100 mm at ultimate load plotted in Figure 6-31 also show that the strains increase as f'_c increases. There is no significant increase in the ultimate load or the strain values for f'_c values higher than 40 MPa.

The average bond strength plotted against the concrete compressive strength at various bond length values ranging from 50 to 200 mm and a constant bond width of 100 mm is shown in Figure 6-32. The figure shows that the average bond strength increases as the concrete strength increases. The increase in the average bond strength is more noticeable at shorter bond lengths, where an increase in the concrete strength by 200% from 20 to 60 MPa increases the average bond strength for bond lengths of 50 and 200 mm by 41.2 and 18%, respectively.

Figure 6-8 shows the load-deflection response for models with concrete strengths ranging from 20 to 60 MPa and a constant bond length of 100 mm. The figure shows that the overall load-deflection response is stiffer for higher concrete strengths. To further investigate whether the test method had an effect on the results, the 2D pull-apart models were applied for the same variables and the same material properties as the modified push-apart models listed in Table 6-4. The overall load-deflection responses for pull-apart models with f'_c values ranging from 20 to 60 MPa, similar to those shown in Figure 6-33, were used to plot the ultimate load against the f'_c values. Figure 6-34 shows the ultimate load from the pull-apart models plotted against f'_c for bond lengths of 70, 100, and 200 mm. The figure shows that there is no significant difference in the ultimate load between the different bond lengths. The differences in ultimate load for the various f'_c values were also smaller than those from the modified push-apart model. The strain distributions along a sheet length of 100 mm at ultimate load for the pull-apart models are shown in Figure 6-35. The figure shows that for the pull-apart model the strains also increase as f'_c increases but at f'_c values of 40, 50, and 60 MPa the maximum strain is almost uniformly distributed along the length.

The previous discussion indicates that increasing f'_c stiffens the overall behaviour of the specimen and in return affects the capacity of the joint. The amount of influence will depend on the geometry and loading of the specimen. This shows

the importance of studying the effect of the test method on the bond behaviour. A detailed investigation on the conventional bond test methods and the relationship between their results is presented in the following chapter.

Table 6-1 Main material properties used in the parametric study

Concrete	Width	w_c (mm)	200
	Modulus of Elasticity,	E (MPa)	31820
	Poisson's ratio,	ν	0.15
	Compressive yield strength,	f_y (MPa)	28
	Ultimate comp. Strength,	f'_c (MPa)	50
CFRP Sheet	Thickness	t (mm)	0.38
	Modulus of Elasticity,	E (MPa)	65789
	Poisson's ratio,	ν	0.26
	Ultimate tensile Strength,	f_u (MPa)	2500

Table 6-2 Models with FRP sheet bond lengths varying with bond width

Model No.	L (mm)	w (mm)	eff. τ_b (MPa)	f_c' (MPa)	Et (GPa.mm)	P_u (kN)	τ_b (MPa)
1	50	25	4.36	50	25	5.45	4.36
2	50	50	4.32	50	25	10.80	4.32
3	50	70	4.29	50	25	15.00	4.29
4	50	100	4.08	50	25	20.40	4.08
5	50	150	3.32	50	25	24.90	3.32
6	50	200	2.88	50	25	28.80	2.88
7	70	25	3.31	50	25	5.80	3.31
8	70	50	3.29	50	25	11.50	3.29
9	70	70	3.27	50	25	16.00	3.27
10	70	100	3.24	50	25	22.70	3.24
11	70	150	2.67	50	25	28.00	2.67
12	70	200	2.36	50	25	33.00	2.36
13	100	25	3.43	50	25	6.00	2.40
14	100	50	3.49	50	25	12.20	2.44
15	100	70	3.47	50	25	17.00	2.43
16	100	100	3.43	50	25	24.00	2.40
17	100	150	2.93	50	25	30.80	2.05
18	100	200	2.57	50	25	36.00	1.80
19	130	25	3.49	50	25	6.10	1.88
20	130	50	3.66	50	25	12.80	1.97
21	130	70	3.59	50	25	17.60	1.93
22	130	100	3.53	50	25	24.70	1.90
23	130	150	3.10	50	25	32.50	1.67
24	130	200	2.76	50	25	38.70	1.49
25	150	25	3.60	50	25	6.30	1.68
26	150	50	3.71	50	25	13.00	1.73
27	150	70	3.65	50	25	17.90	1.70
28	150	100	3.57	50	25	25.00	1.67
29	150	150	3.14	50	25	33.00	1.47
30	150	200	2.85	50	25	39.95	1.33
31	200	25	3.60	50	25	6.30	1.26
32	200	50	3.71	50	25	13.00	1.30
33	200	70	3.65	50	25	17.90	1.28
34	200	100	3.57	50	25	25.00	1.25
35	200	150	3.14	50	25	33.00	1.10
36	200	200	2.85	50	25	39.95	1.00

Table 6-3 Models with bond lengths varying with sheet stiffness, Et

Model No.	L (mm)	w (mm)	f'_c (MPa)	Et (GPa.mm)	P_u (kN)	τ_b (MPa)
37	50	100	50	25	20.40	4.08
38	50	100	50	50	24.00	4.80
39	50	100	50	75	25.50	5.10
40	50	100	50	100	26.30	5.26
41	50	100	50	125	26.50	5.30
42	70	100	50	25	22.70	3.24
43	70	100	50	50	26.50	3.79
44	70	100	50	75	28.00	4.00
45	70	100	50	100	28.90	4.13
46	70	100	50	125	29.60	4.23
47	100	100	50	25	24.00	2.40
48	100	100	50	50	29.20	2.92
49	100	100	50	75	30.40	3.04
50	100	100	50	100	31.40	3.14
51	100	100	50	125	32.20	3.22
52	150	100	50	25	25.00	1.67
53	150	100	50	50	31.67	2.11
54	150	100	50	75	34.00	2.27
55	150	100	50	100	35.50	2.37
56	150	100	50	125	37.00	2.47
57	200	100	50	25	25.00	1.25
58	200	100	50	50	32.50	1.63
59	200	100	50	75	36.57	1.83
60	200	100	50	100	38.95	1.95
61	200	100	50	125	40.52	2.03
62	250	100	50	25	24.95	1.00
63	250	100	50	50	32.80	1.31
64	250	100	50	75	37.80	1.51
65	250	100	50	100	40.70	1.63
66	250	100	50	125	43.08	1.72
67	300	100	50	25	24.95	0.83
68	300	100	50	50	32.90	1.10
69	300	100	50	75	37.82	1.26
70	300	100	50	100	41.27	1.38
71	300	100	50	125	43.60	1.45

Table 6-4 Models with bond lengths varying with concrete strength

Model No.	L (mm)	w (mm)	f_c (MPa)	E_c (MPa)	Et (GPa.mm)	P_u (kN)	τ_b (MPa)
72	50	100	20	20125	25	15.30	3.06
73	50	100	30	24648	25	16.62	3.32
74	50	100	40	28460	25	18.30	3.66
75	50	100	50	31820	25	20.40	4.08
76	50	100	60	34857	25	21.59	4.32
77	70	100	20	20125	25	18.00	2.57
78	70	100	30	24648	25	19.60	2.80
79	70	100	40	28460	25	21.20	3.03
80	70	100	50	31820	25	22.70	3.24
81	70	100	60	34857	25	23.20	3.31
82	100	100	20	20125	25	20.10	2.01
83	100	100	30	24648	25	21.80	2.18
84	100	100	40	28460	25	22.90	2.29
85	100	100	50	31820	25	24.00	2.40
86	100	100	60	34857	25	24.50	2.45
87	150	100	20	20125	25	21.75	1.45
88	150	100	30	24648	25	23.00	1.53
89	150	100	40	28460	25	23.80	1.59
90	150	100	50	31820	25	25.00	1.67
91	150	100	60	34857	25	25.50	1.70
92	200	100	20	20125	25	22.10	1.11
93	200	100	30	24648	25	23.50	1.18
94	200	100	40	28460	25	24.30	1.22
95	200	100	50	31820	25	25.20	1.26
96	200	100	60	34857	25	25.90	1.30
97	250	100	20	20125	25	22.05	0.88
98	250	100	30	24648	25	23.60	0.94
99	250	100	40	28460	25	24.50	0.98
100	250	100	50	31820	25	25.30	1.01
101	250	100	60	34857	25	25.98	1.04
102	300	100	20	20125	25	22.06	0.74
103	300	100	30	24648	25	23.60	0.79
104	300	100	40	28460	25	24.50	0.82
105	300	100	50	31820	25	25.30	0.84
106	300	100	60	34857	25	26.00	0.87

Table 6-5 Models with variable concrete width and FRP bond length

model #	w (mm)	L (mm)	w _c (mm)	w/w _c	P _u (kN)	f _c ' (MPa)	Et (GPa.mm)
107	200	50	400	0.50	35.2	50	25
108	200	50	300	0.75	34.5	50	25
109	200	50	200	1.00	28.6	50	25
110	200	150	400	0.50	50.0	50	25
111	200	150	300	0.75	46.9	50	25
112	200	150	200	1.00	40.0	50	25

Table 6-6 3D models with variable concrete width and FRP bond widths

model #	w (mm)	L (mm)	w _c (mm)	w/w _c	f _c ' (MPa)	Et (GPa.mm)
113	60	100	200	0.30	50	25
114	100	100	200	0.50	50	25
115	140	100	200	0.70	50	25
116	180	100	200	0.90	50	25
117	200	100	200	1.00	50	25
118	100	100	400	0.25	50	25
119	200	100	400	0.50	50	25
120	400	100	400	1.00	50	25

Table 6-7 2D models with variable E and t values but with the same Et product

model #	w (mm)	L (mm)	f _c ' (MPa)	E (MPa)	t (mm)	Et (GPa.mm)
121	100	150	50	263158	0.38	100
122	100	150	50	65789	1.52	100
123	100	150	50	131579	0.38	50
124	100	150	50	65789	0.76	50

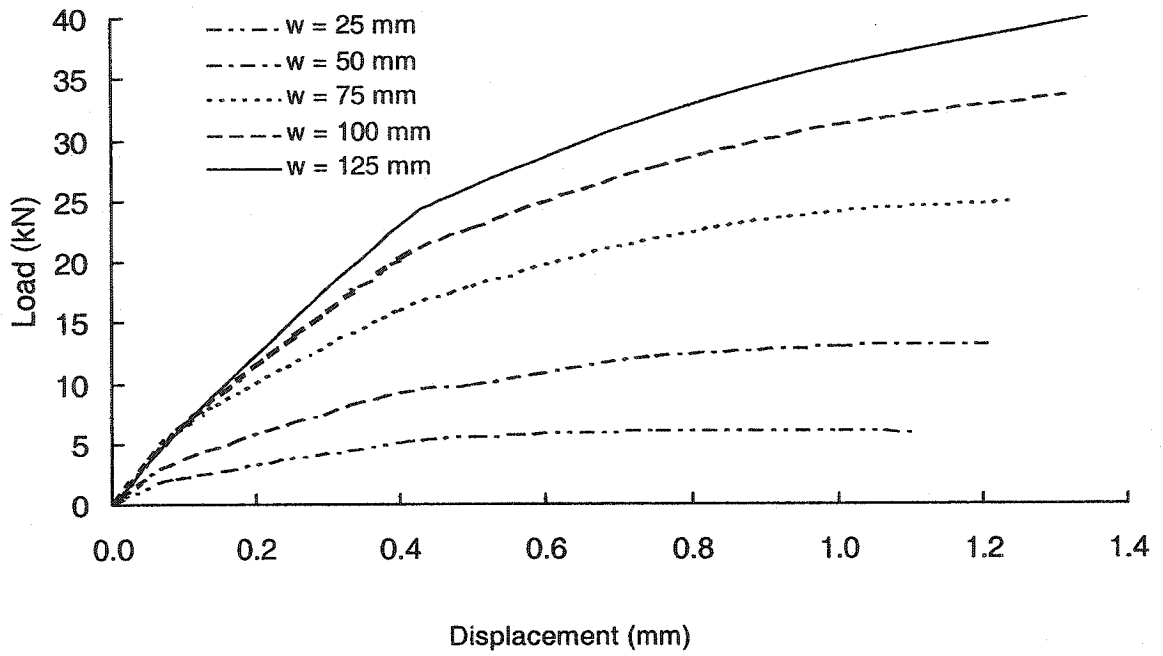


Figure 6-1 Load-displacement response for models with $L = 150$ mm

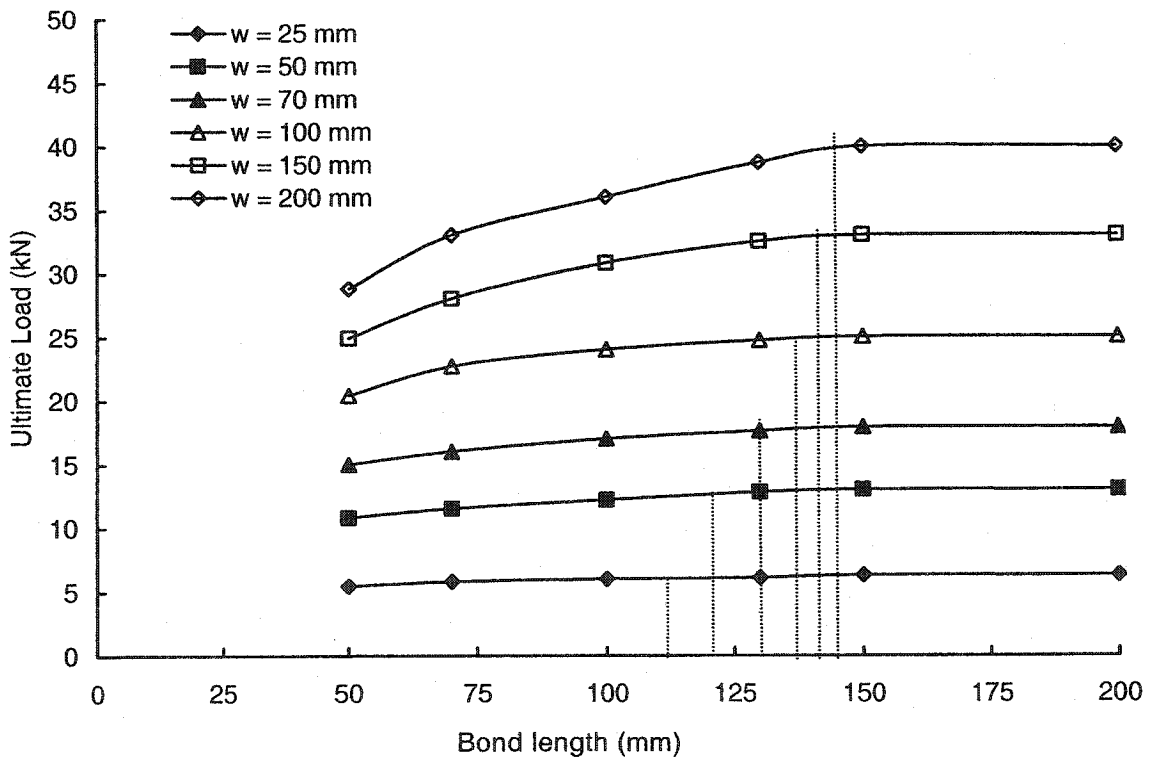


Figure 6-2 Bond length-ultimate load at different w values

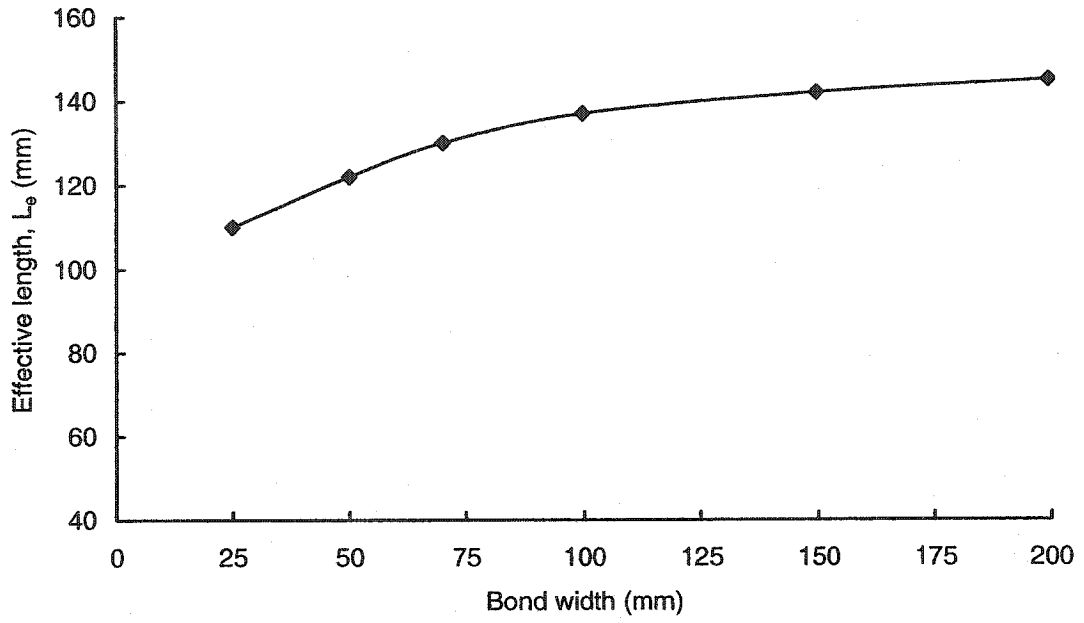


Figure 6-3 Effective length and Bond width relationship

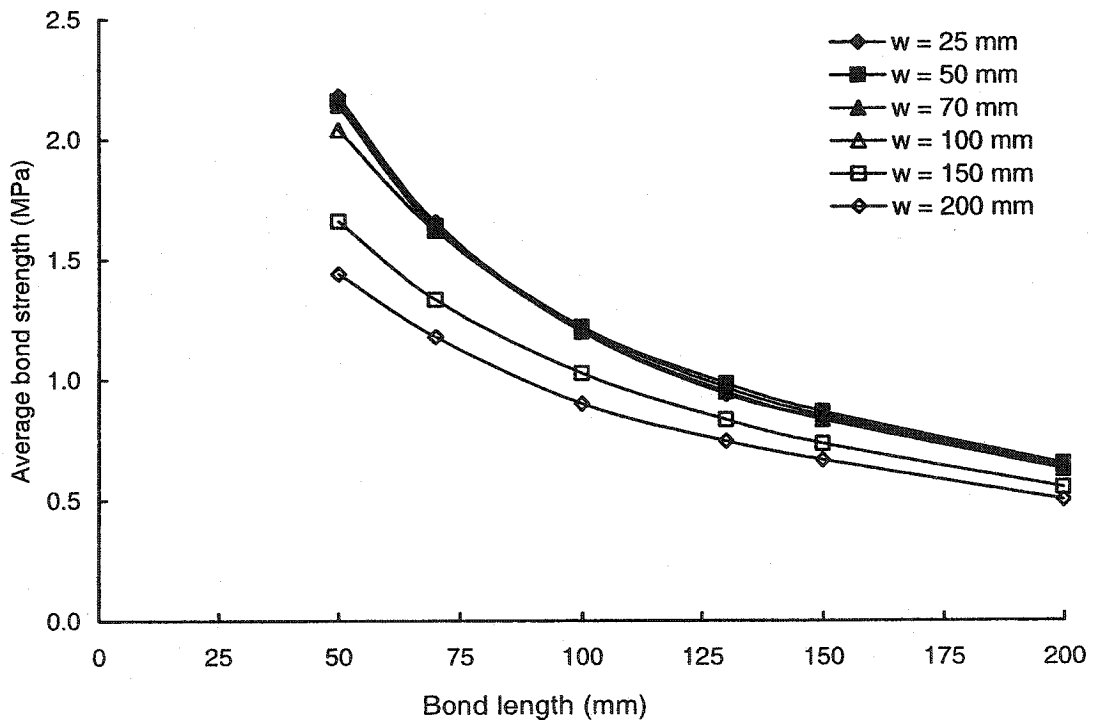


Figure 6-4 Average bond strength and bond length for different w values

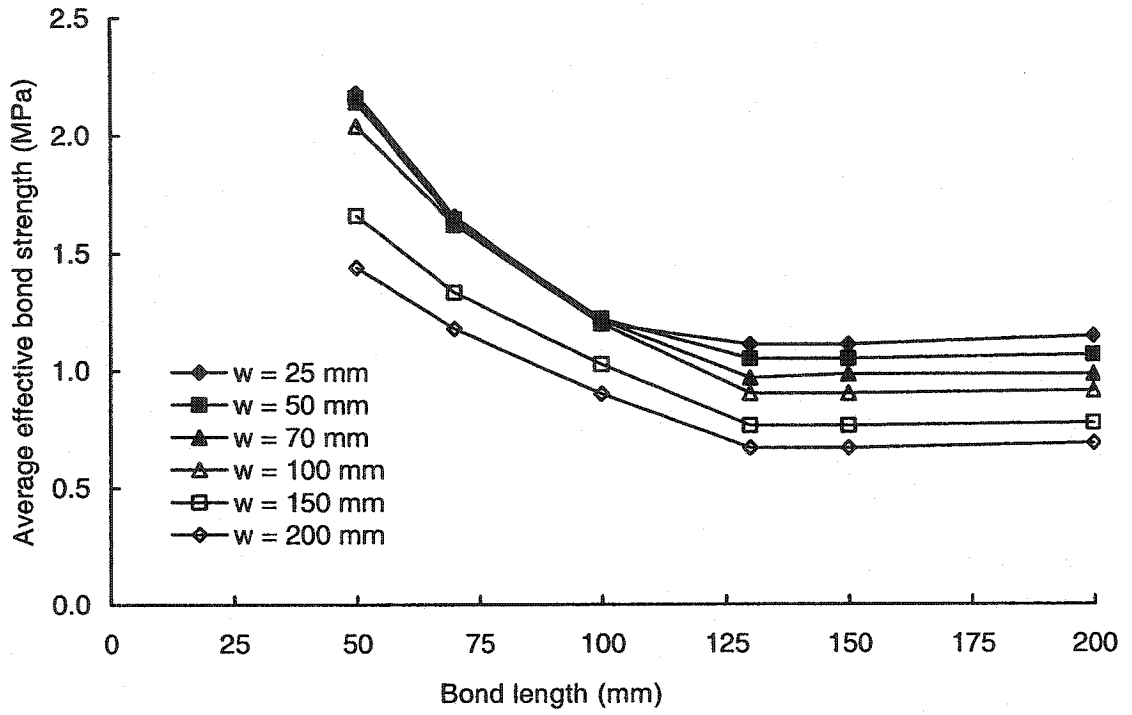


Figure 6-5 Average effective bond strength for different w values

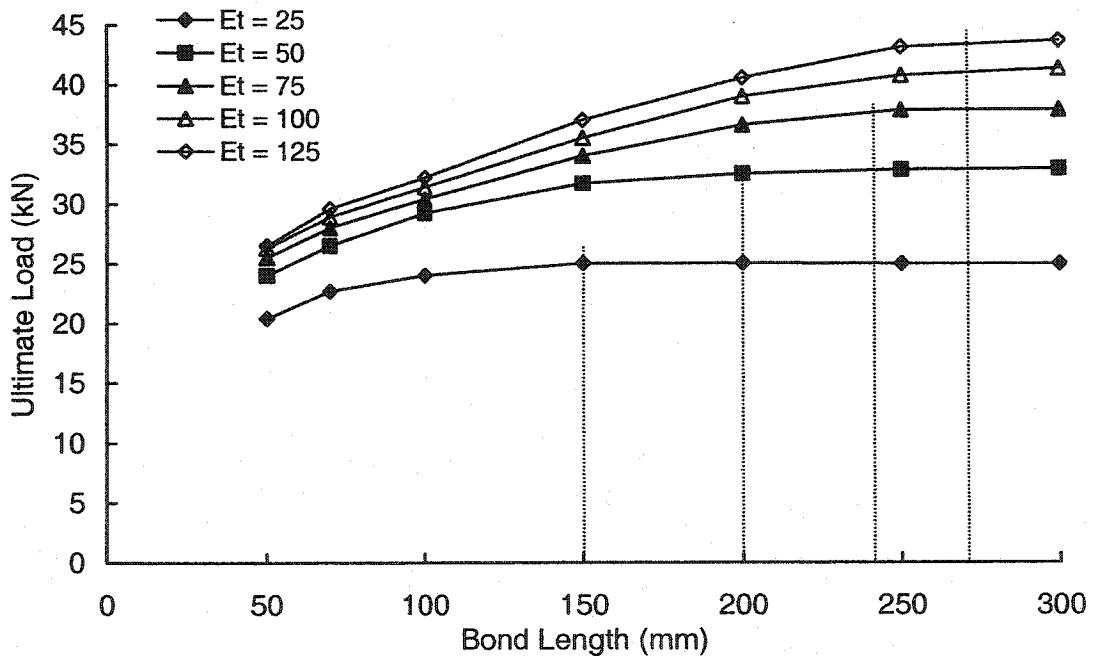


Figure 6-6 Bond length and ultimate load for different E_t values

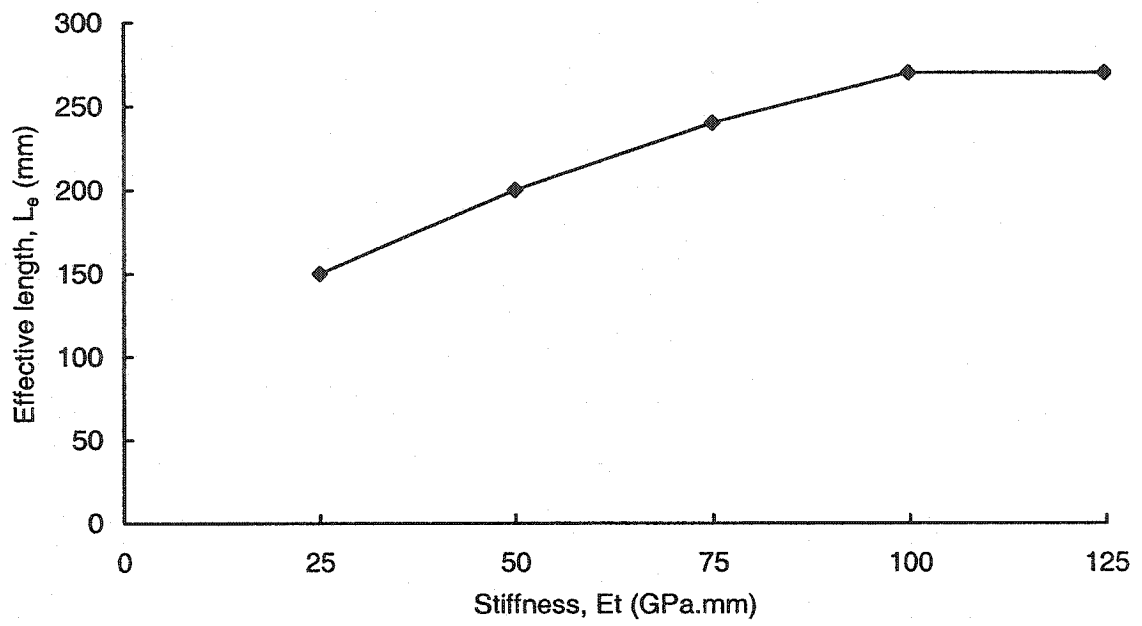


Figure 6-7 Effective length-stiffness for $w = 100$ mm

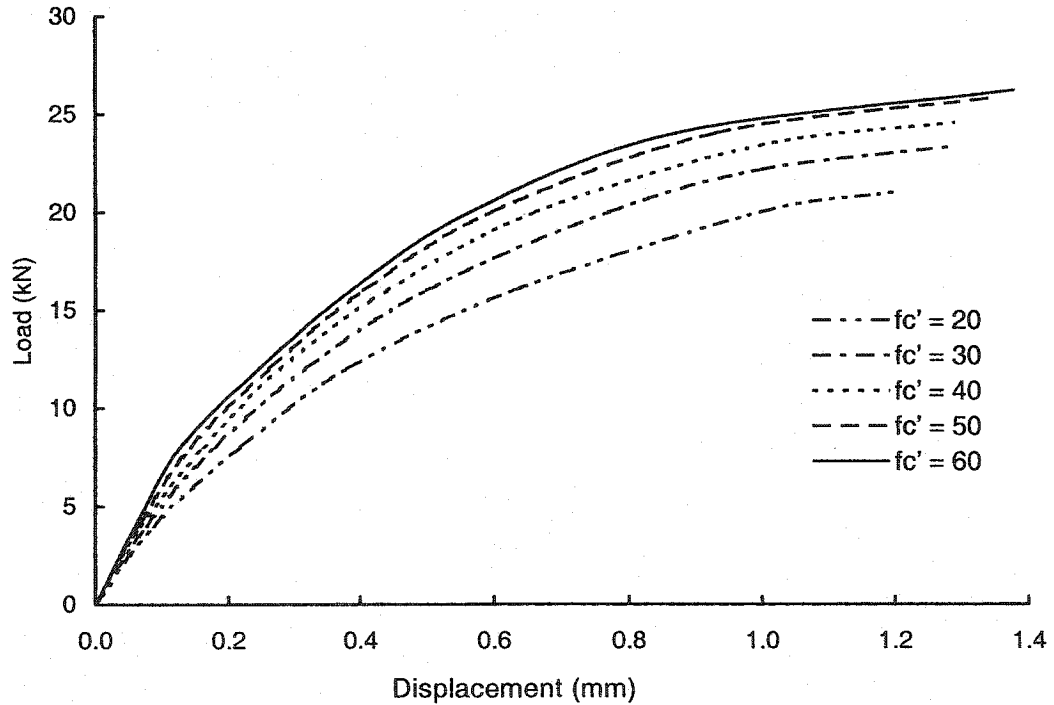


Figure 6-8 Load-displacement response for modified push-apart ($L = 200$ mm)

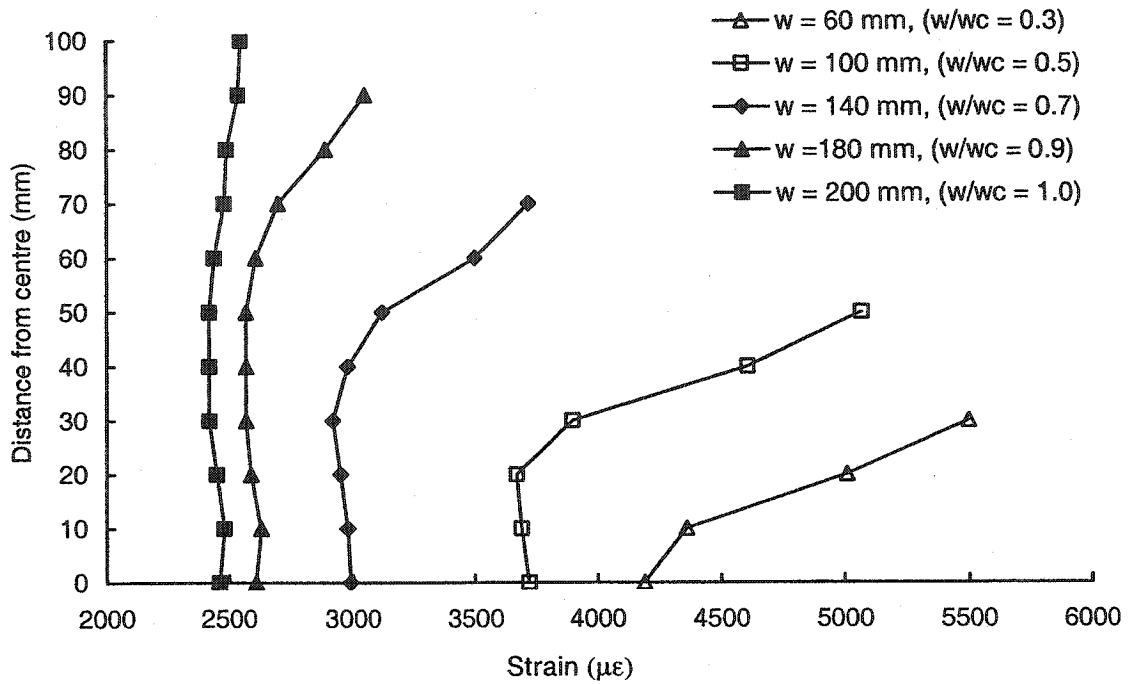


Figure 6-23 Strain distribution across width at crack location, $P/P_u = 0.7$

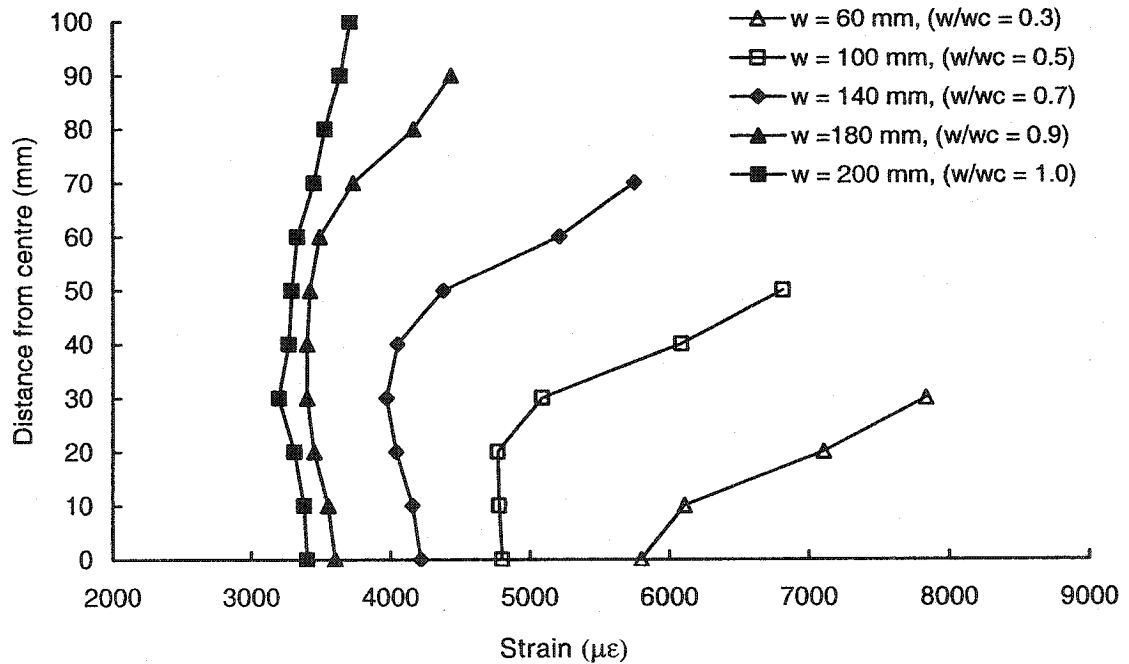


Figure 6-24 Strain distribution across width at crack location, $P/P_u = 1.0$

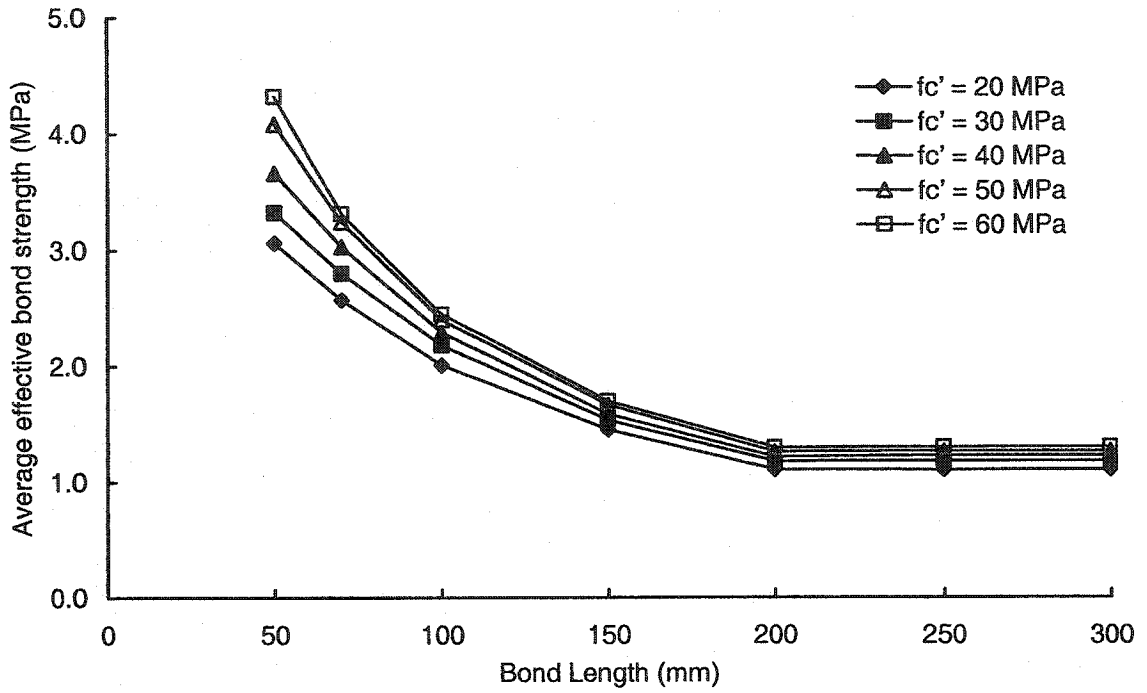


Figure 6-11 Bond length and Average effective bond strength for different f'_c values

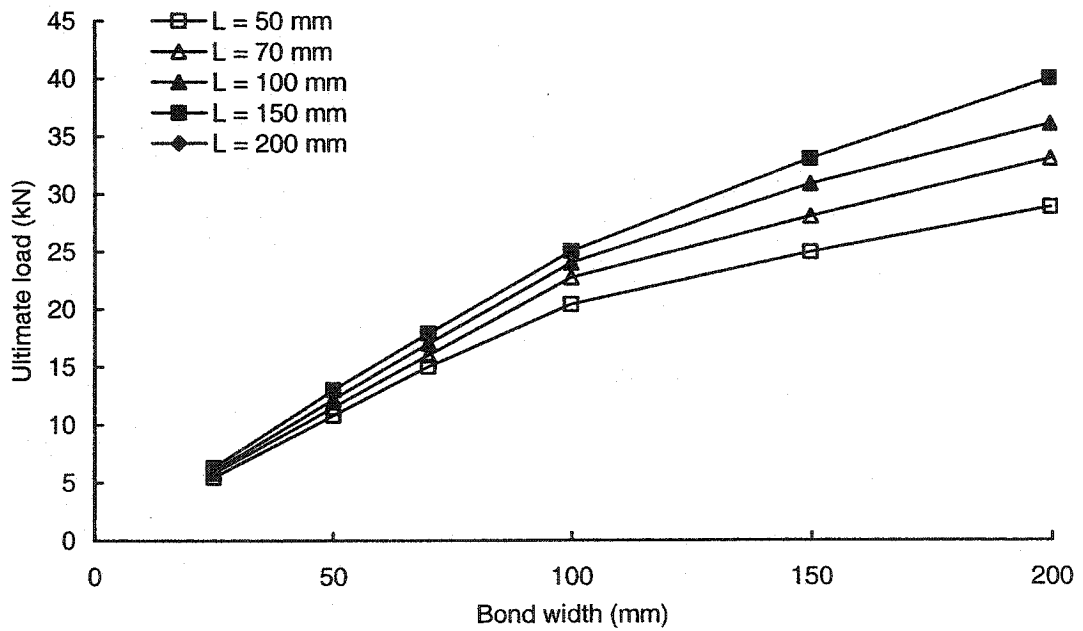


Figure 6-12 Bond width and ultimate load for different L values

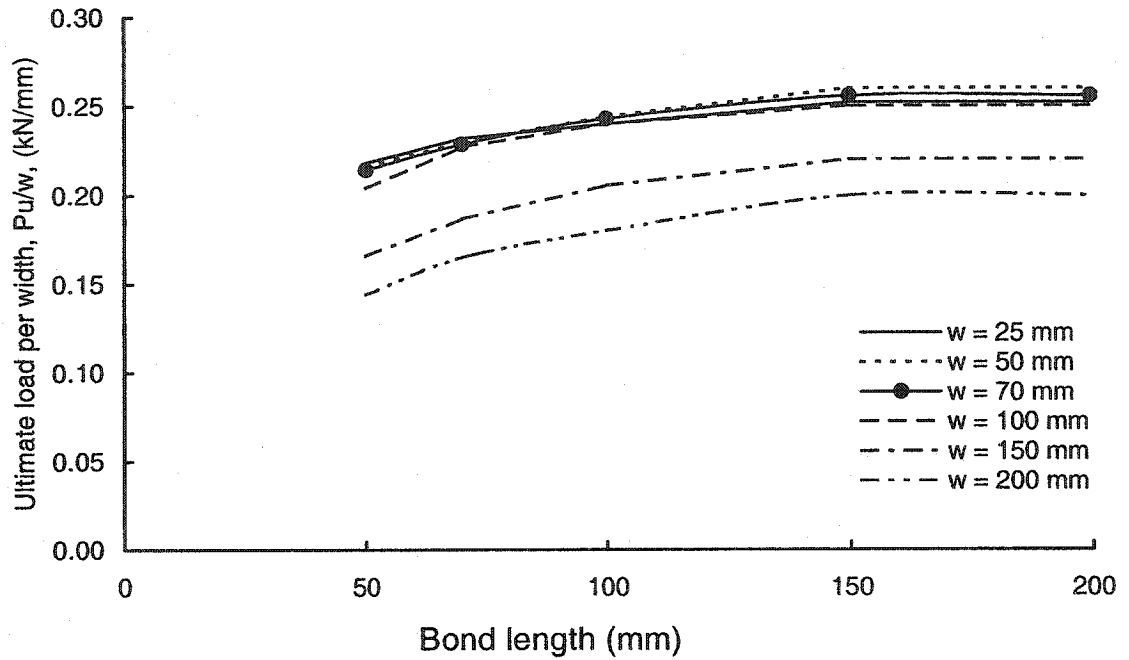


Figure 6-13 Ultimate load per width and bond length for various bond widths

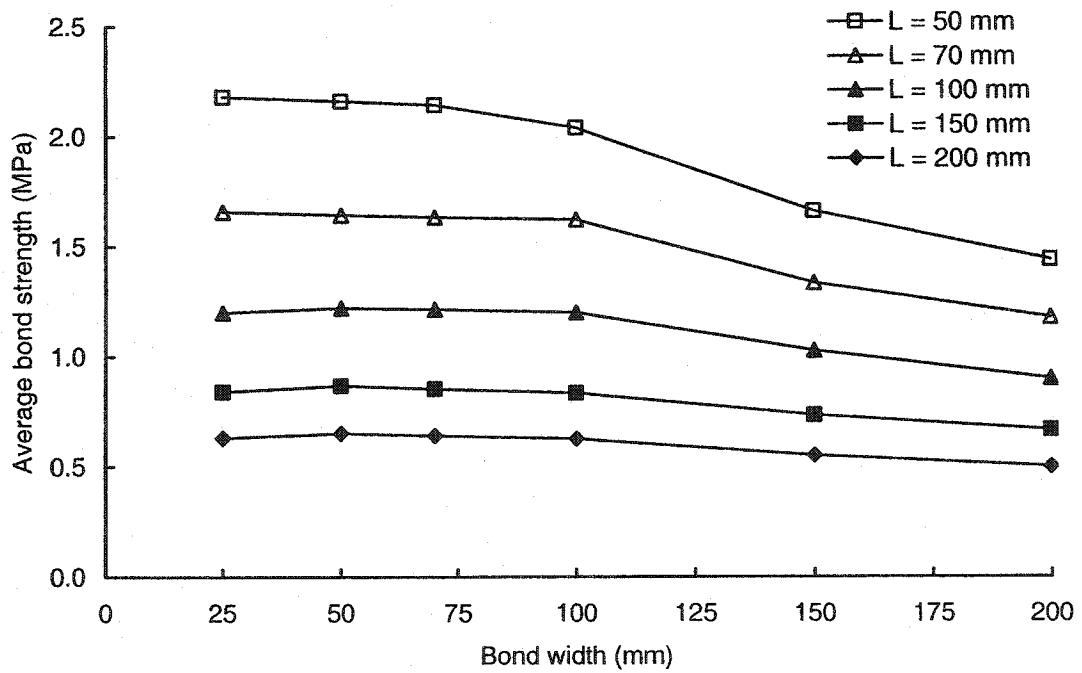


Figure 6-14 Bond width and bond strength for different L values

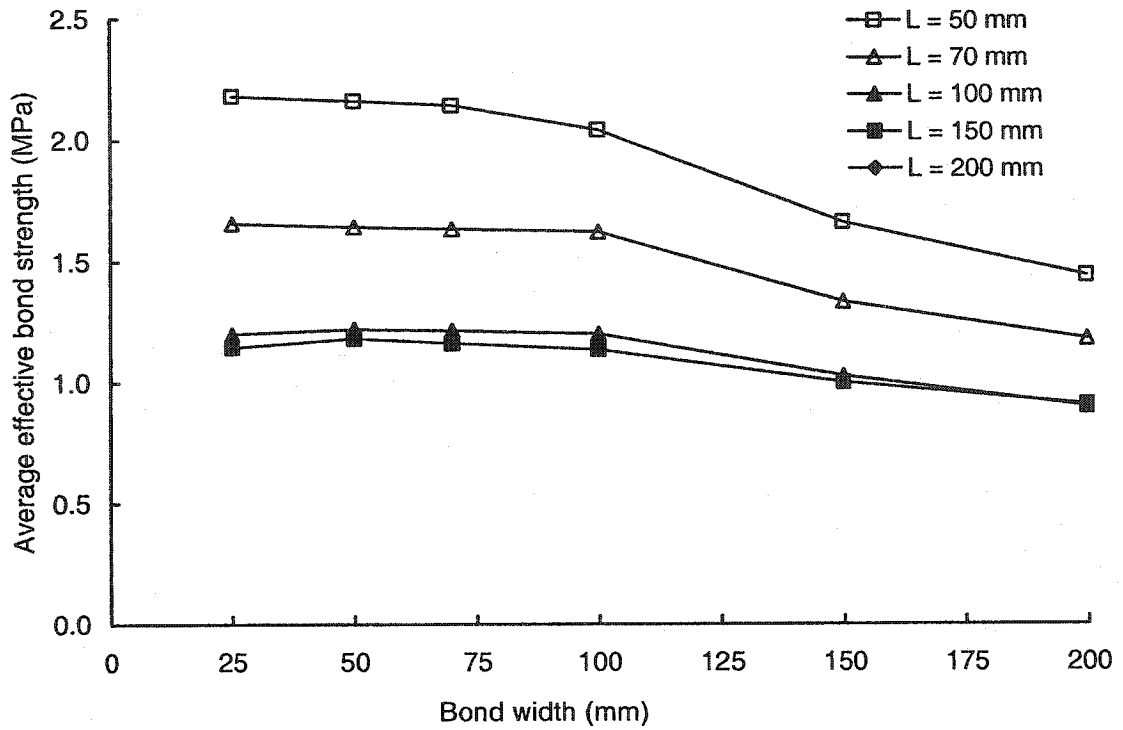


Figure 6-15 Bond width and bond strength for different L values ($L_c = 110$ mm)

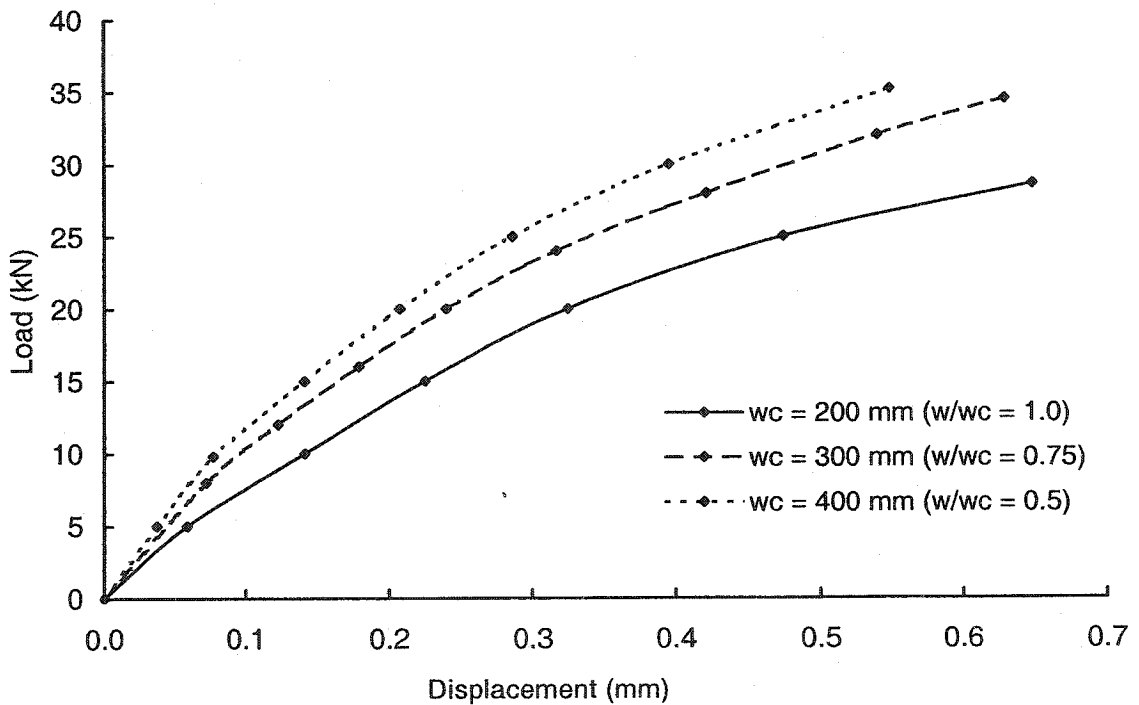


Figure 6-16 Load-Displacement response for different w_c values ($w = 200$ and $L = 50$ mm)

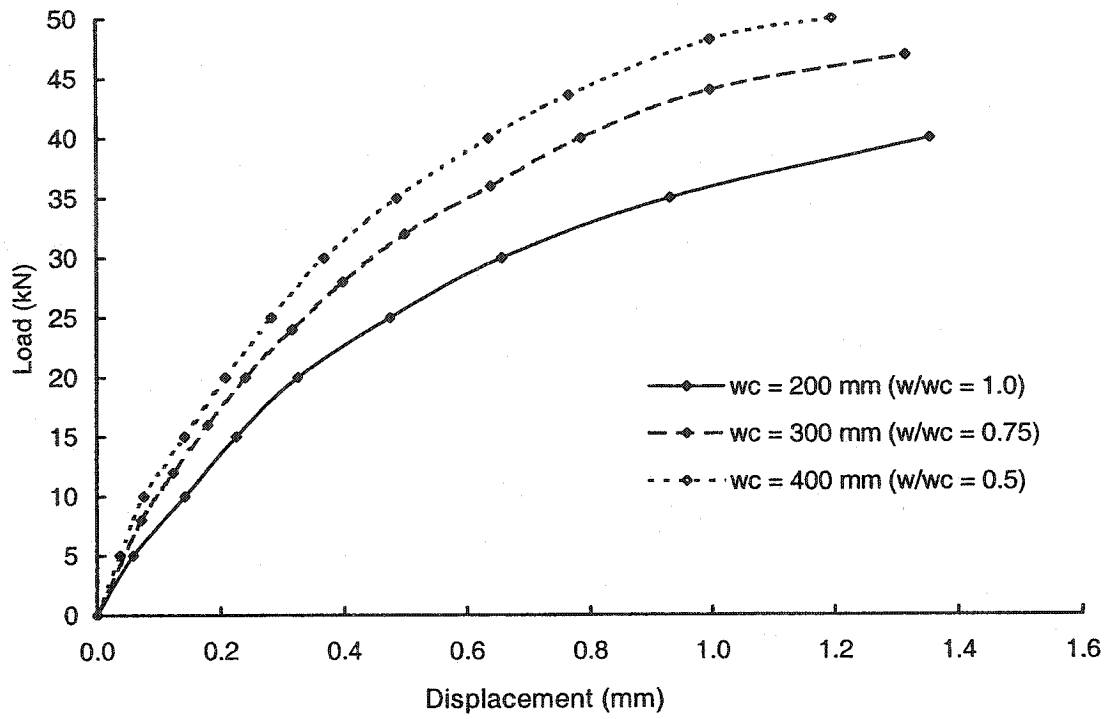


Figure 6-17 Load-Displacement response for different w_c values ($w = 200$ and $L = 150$ mm)

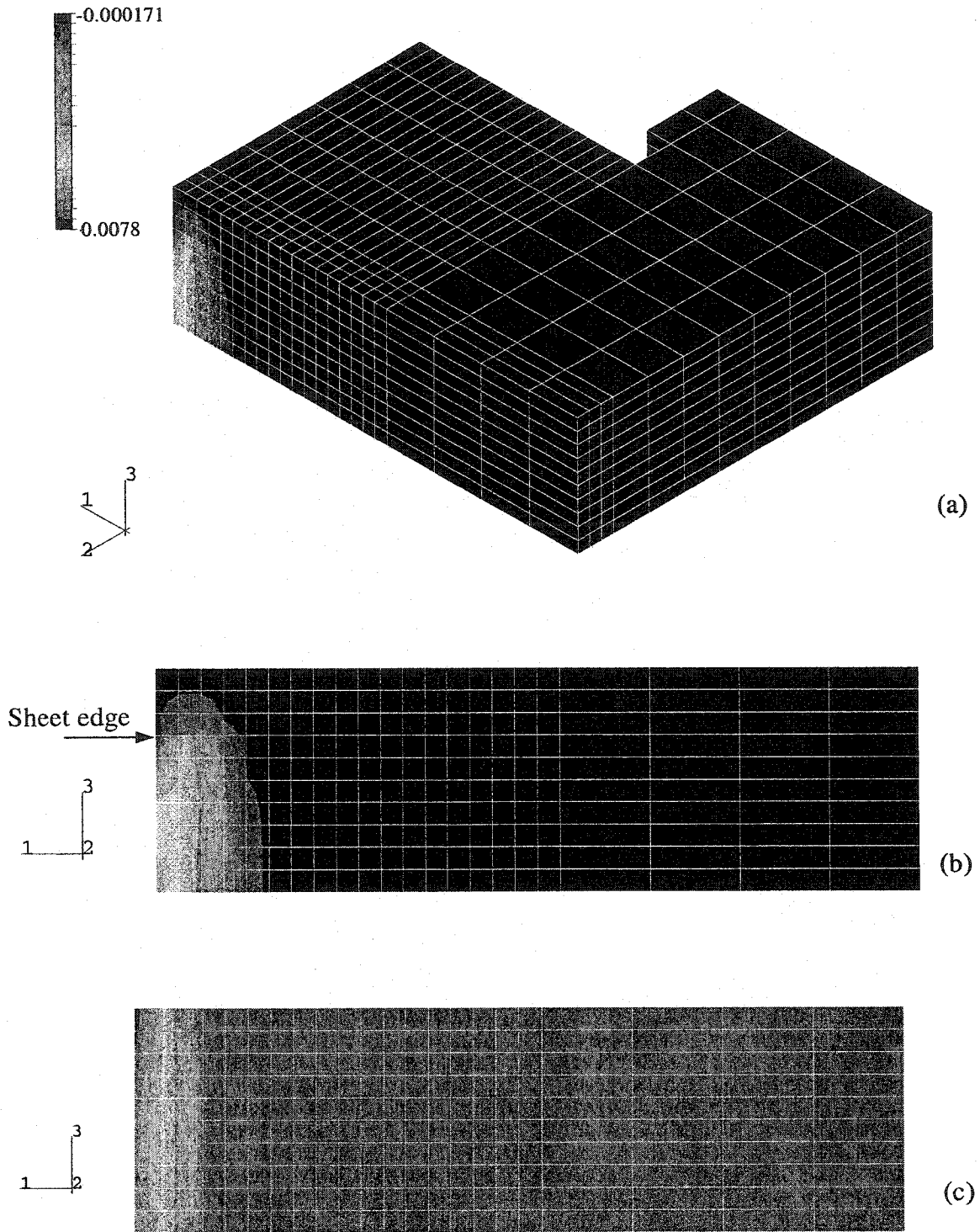


Figure 6-18 Strain E11 contour lines (a) isometric view for $w/w_c = 0.7$ (b) elevation view for $w/w_c = 0.7$ (c) elevation view for $w/w_c = 1.0$

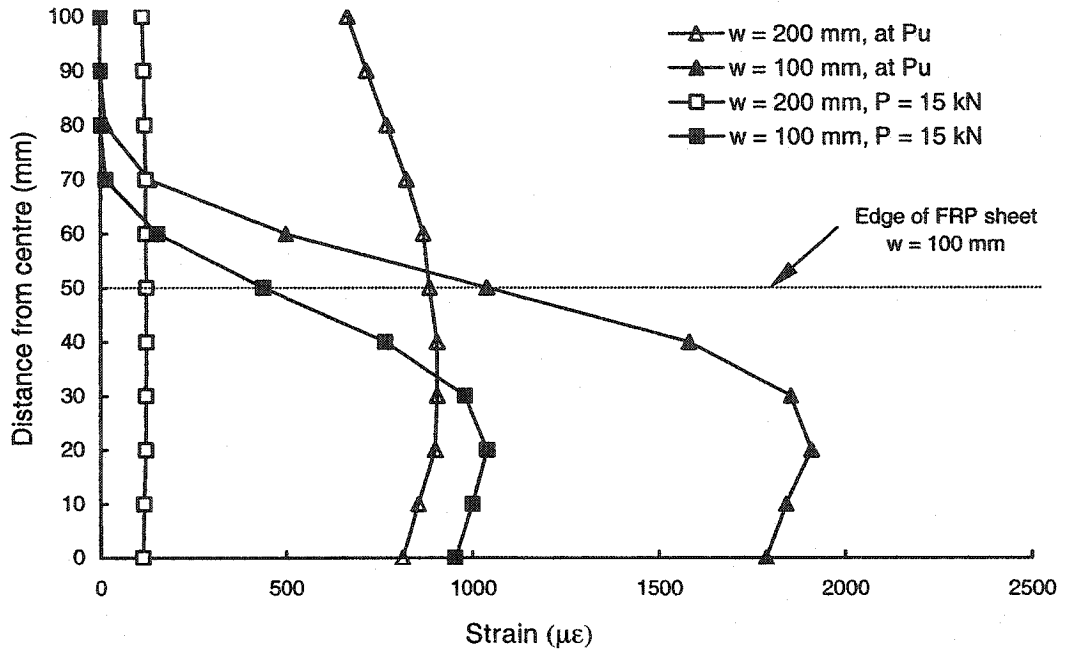


Figure 6-19 Strain distribution across the concrete width

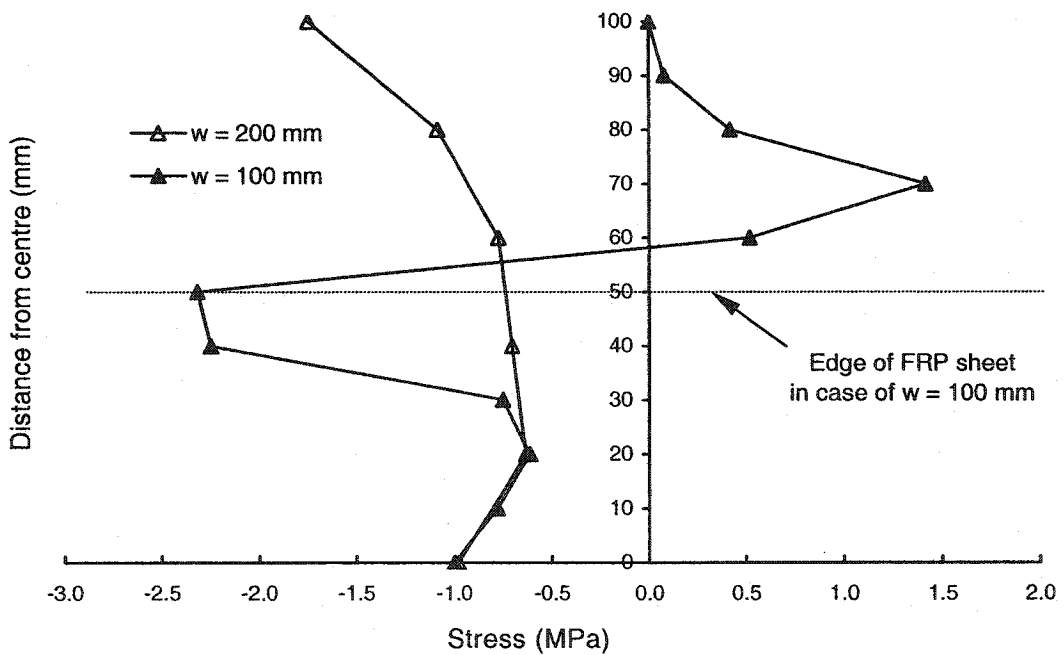


Figure 6-20 Stress distribution across the concrete width at ultimate load

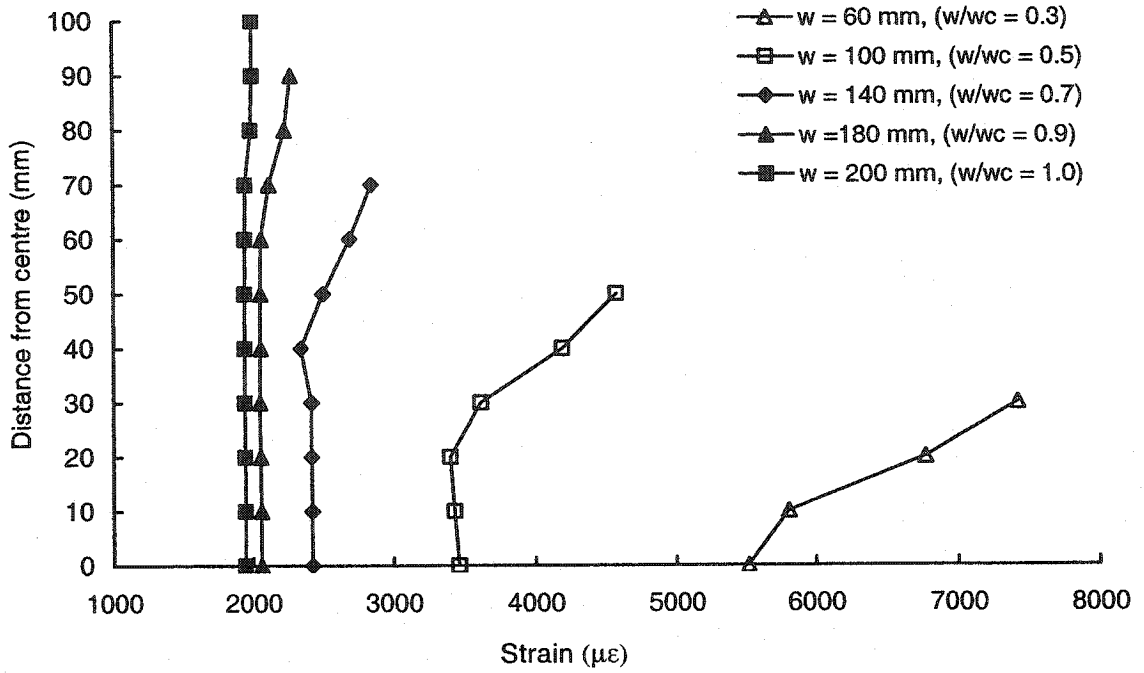


Figure 6-21 Strain distribution across different w values at crack location, 15 kN

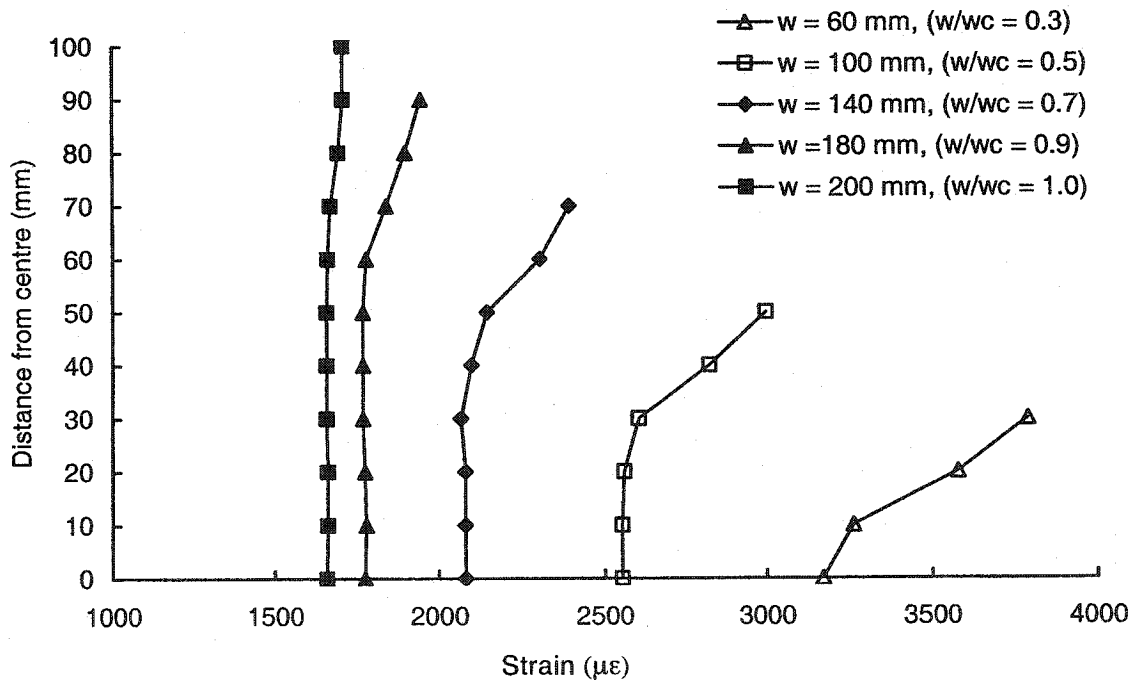


Figure 6-22 Strain distribution across width at crack location, $P/P_u = 0.5$

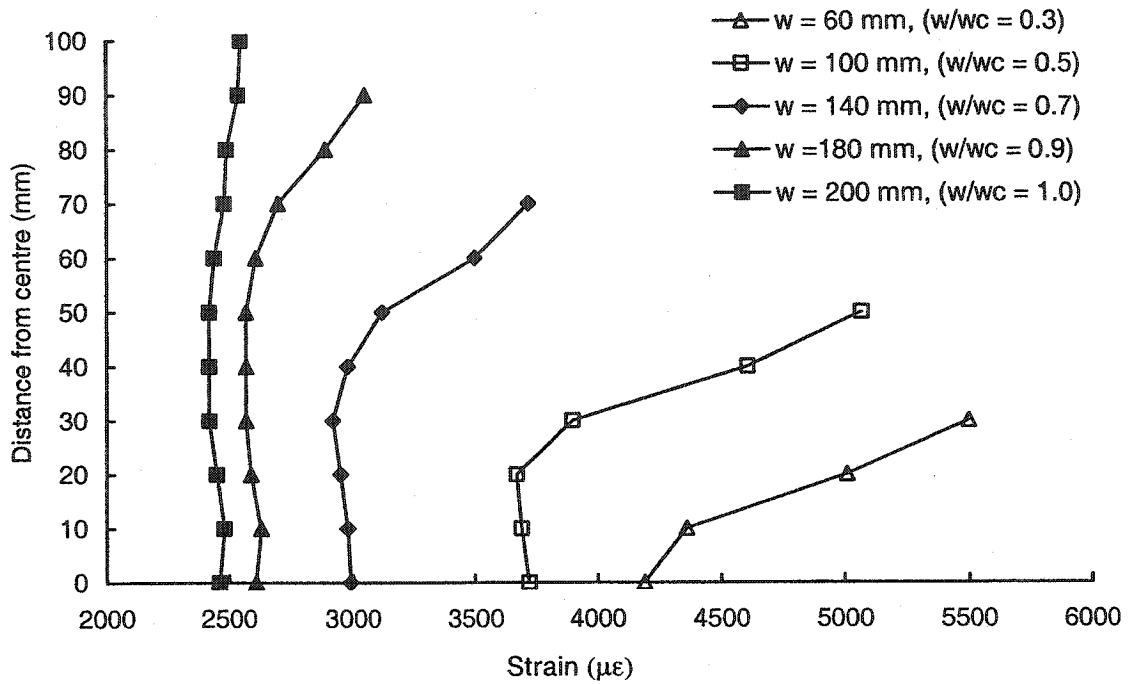


Figure 6-23 Strain distribution across width at crack location, $P/P_u = 0.7$

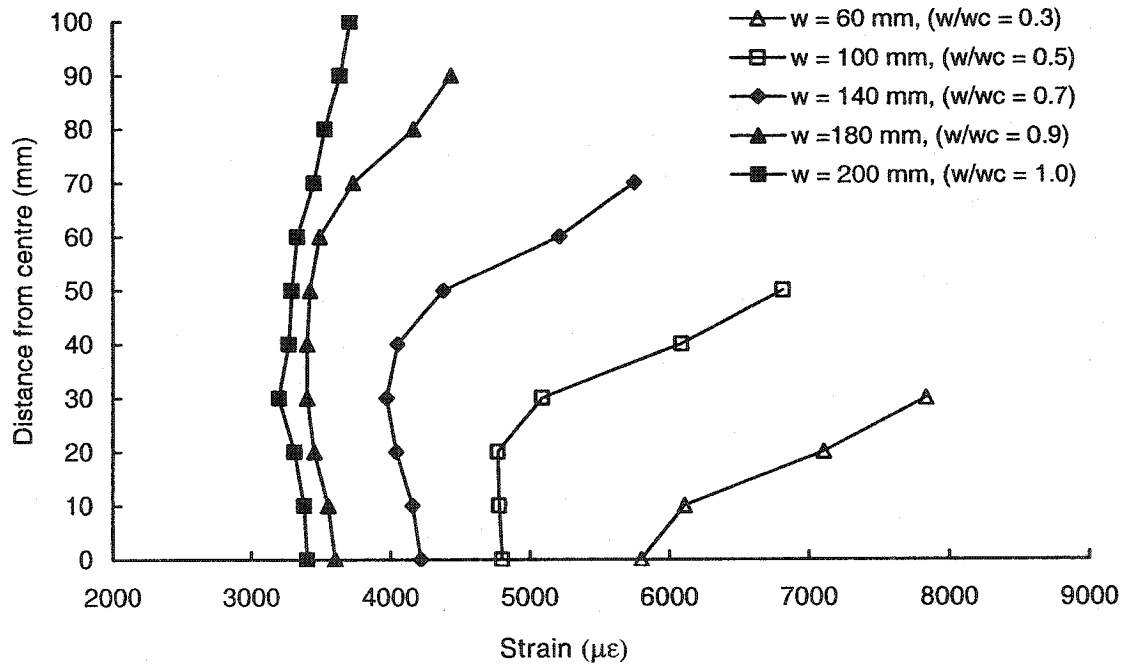


Figure 6-24 Strain distribution across width at crack location, $P/P_u = 1.0$

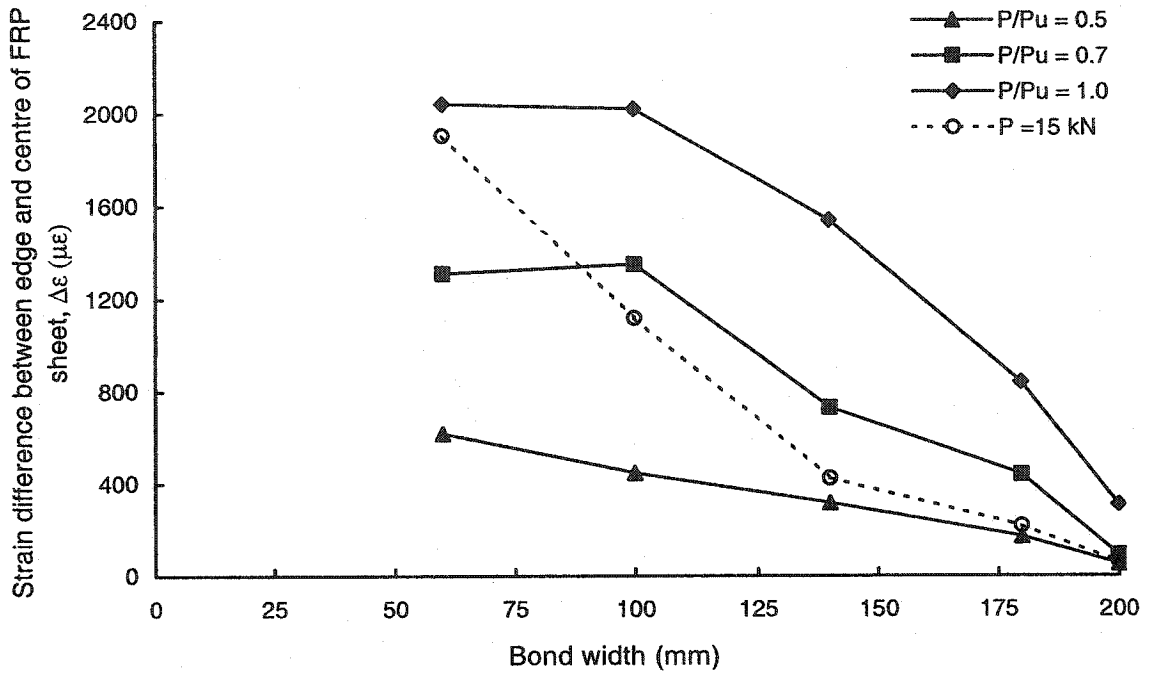


Figure 6-25 Strain difference-bond width response, $w_c = 200$ mm

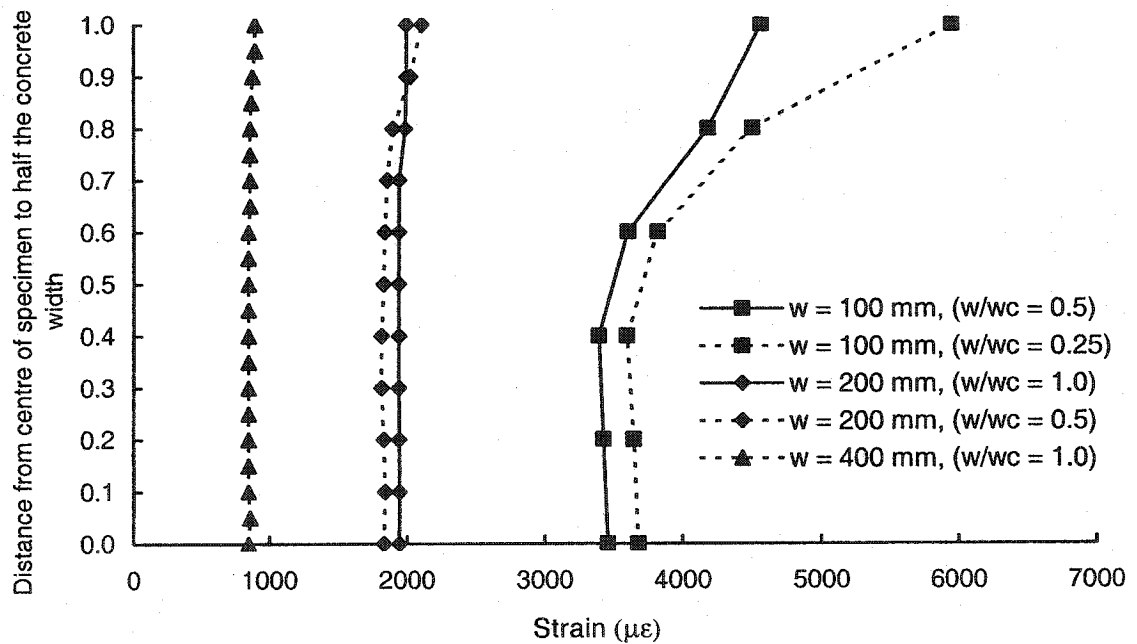


Figure 6-26 Strain distribution across FRP sheet width at 15 kN

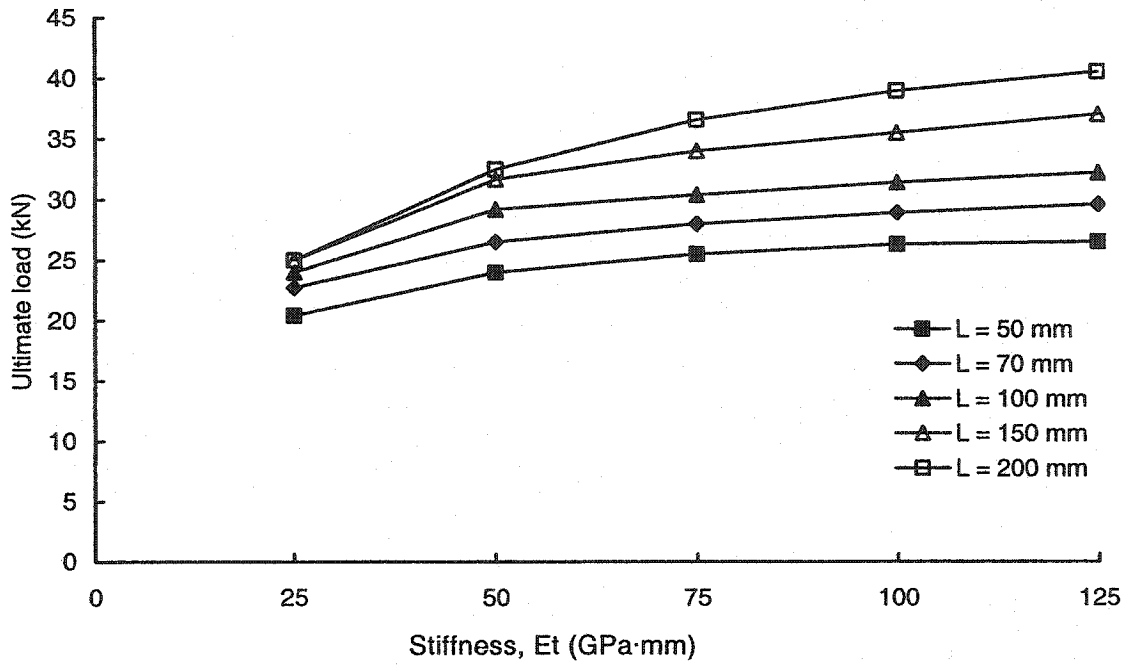


Figure 6-27 FRP stiffness vs. ultimate load for various bond lengths

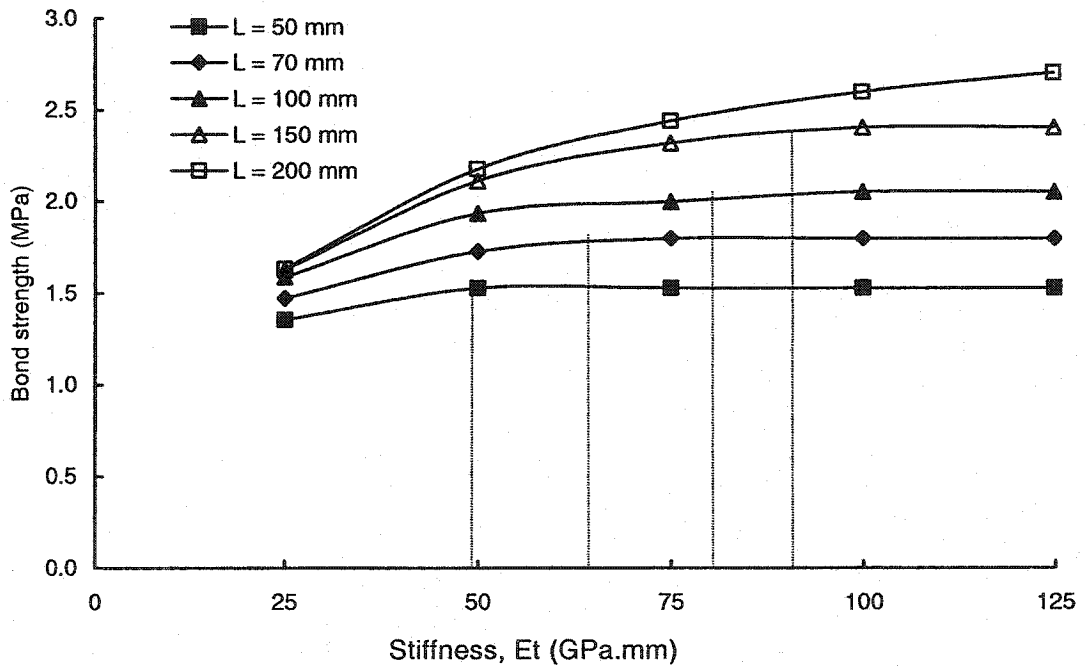


Figure 6-28 FRP stiffness vs. average bond strength for various bond lengths

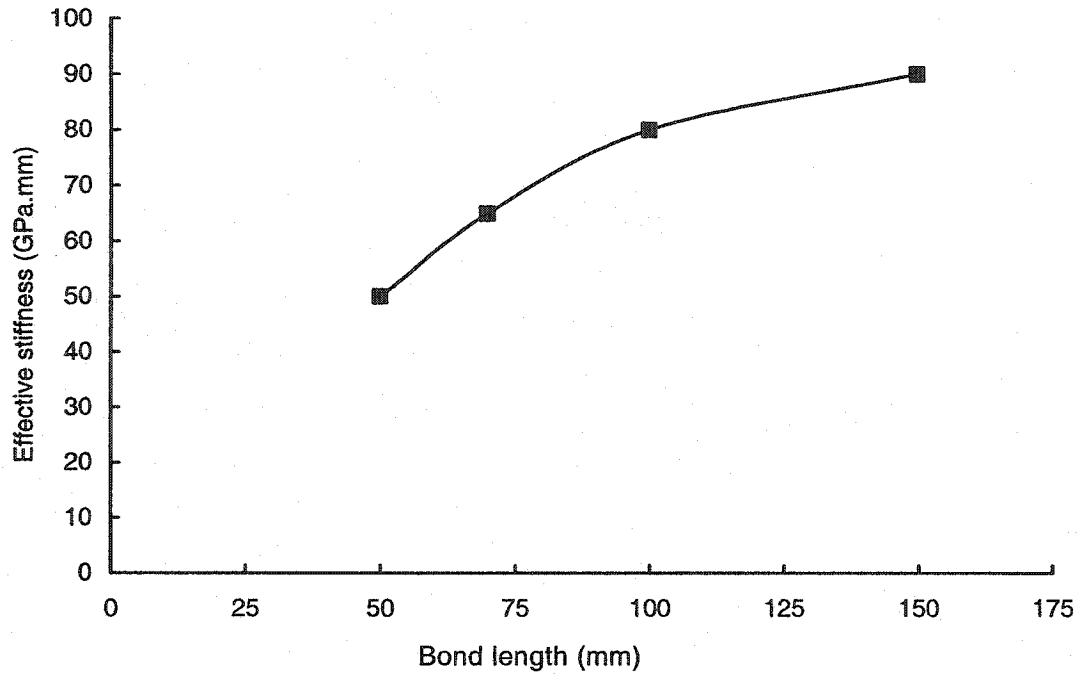


Figure 6-29 Effective FRP stiffness vs. bond length relationship

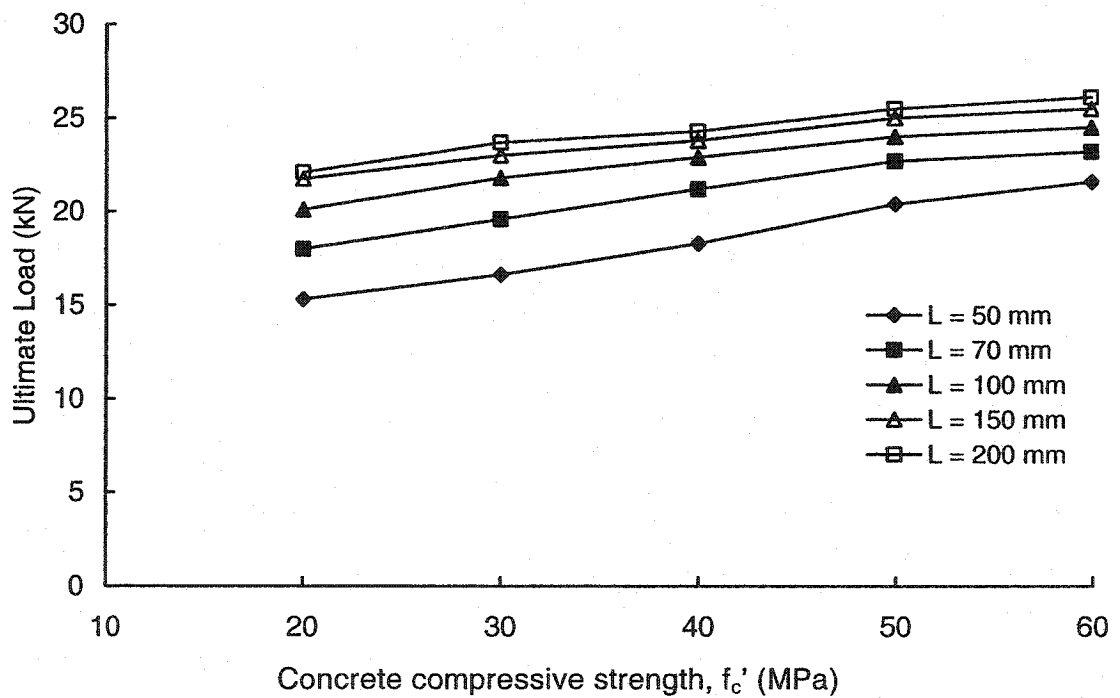


Figure 6-30 Concrete strength vs. ultimate load for various bond lengths

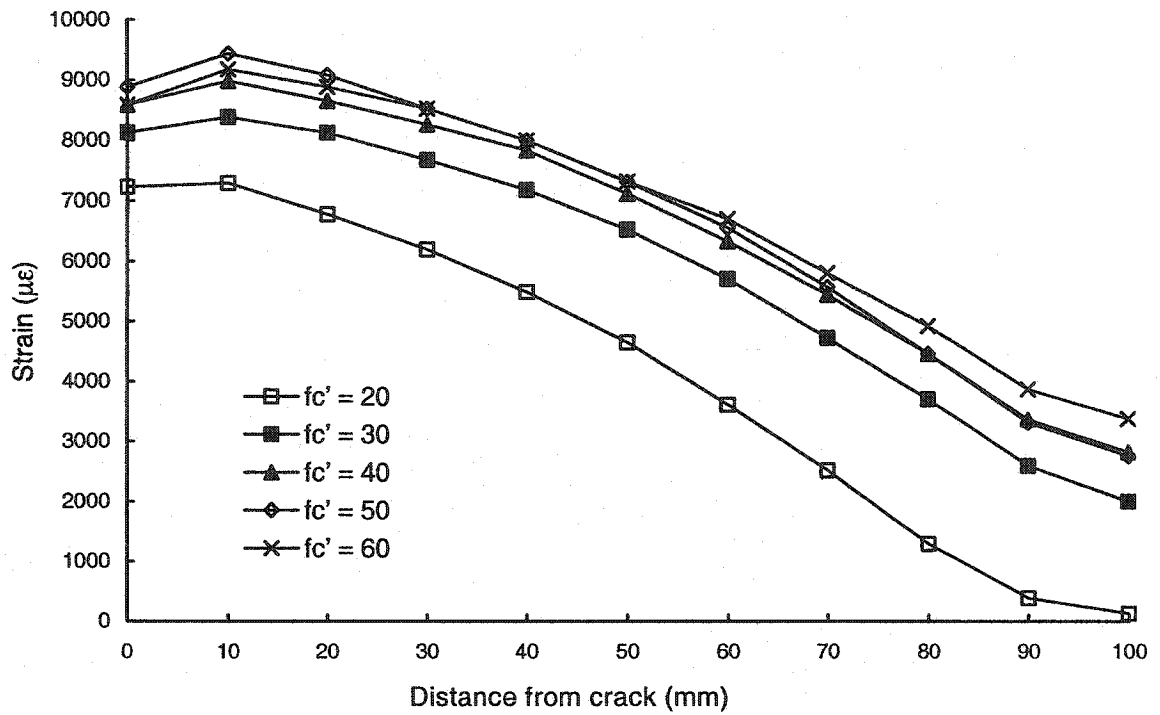


Figure 6-31 Strain distribution for various f'_c values

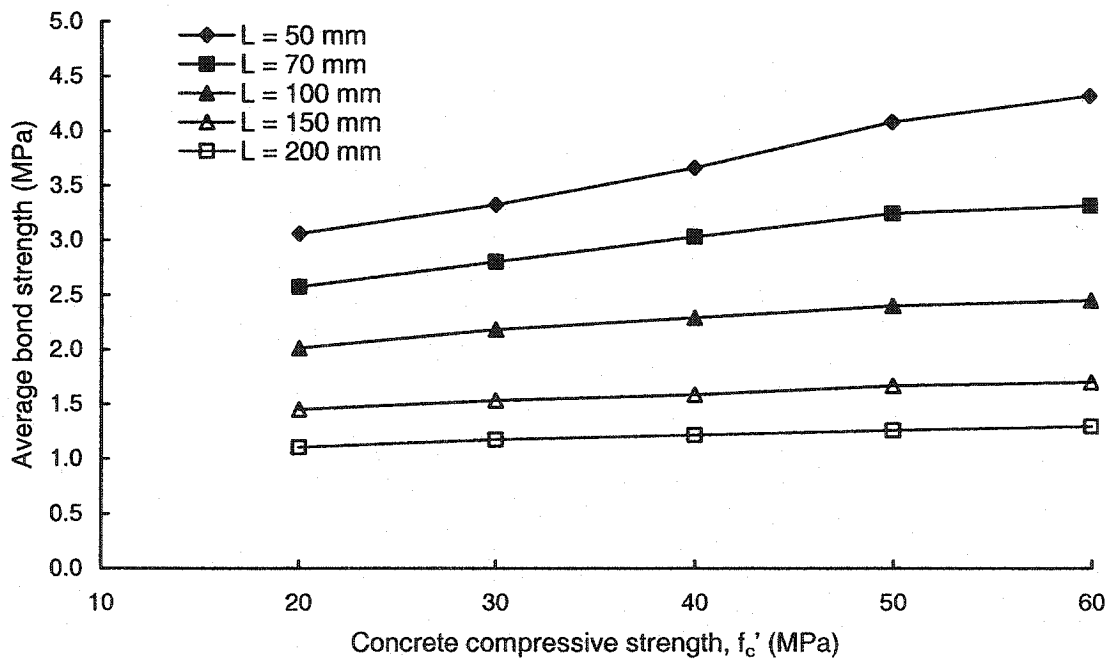


Figure 6-32 Concrete strength vs. ultimate load for various bond lengths

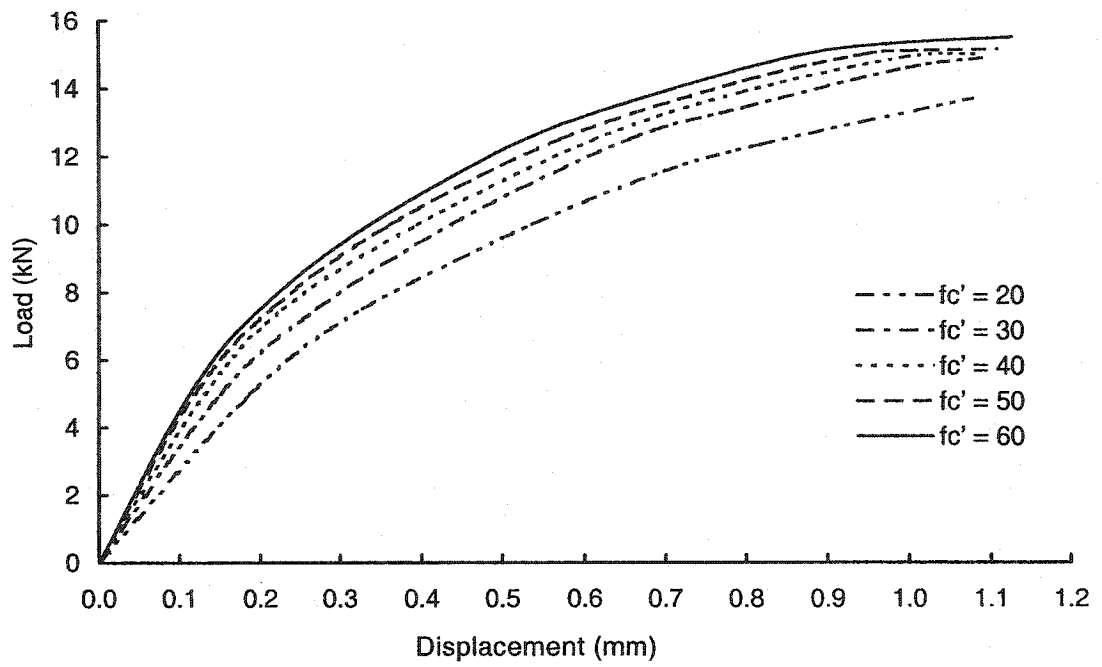


Figure 6-33 Load-displacement response for pull-apart models ($L = 200$ mm)

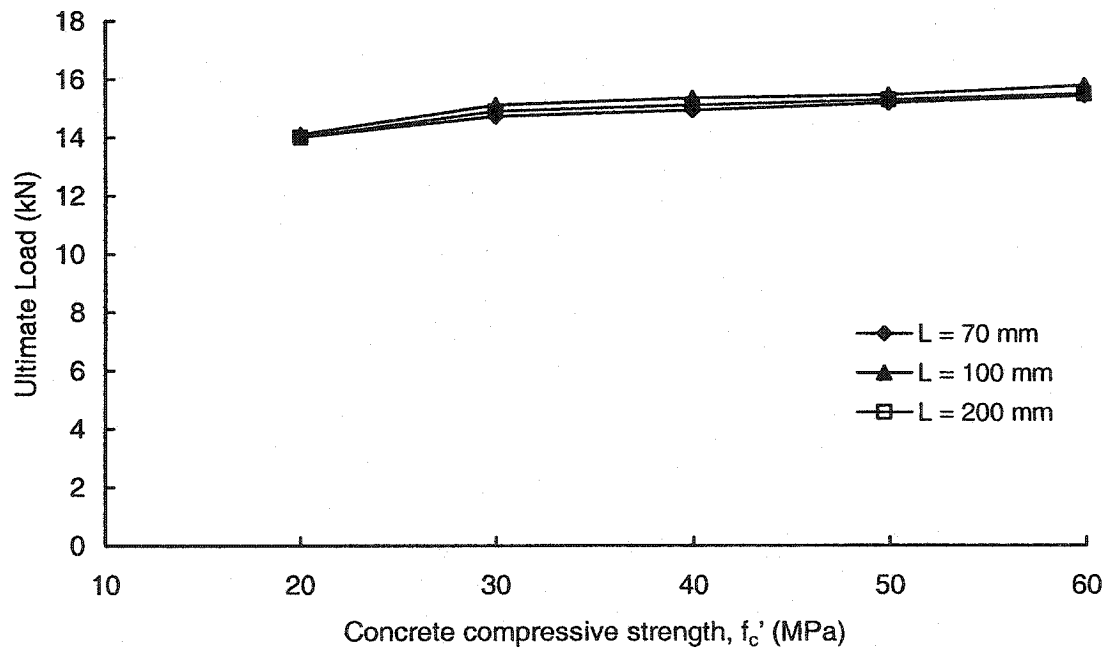


Figure 6-34 Concrete strength vs. ultimate load for push-apart model

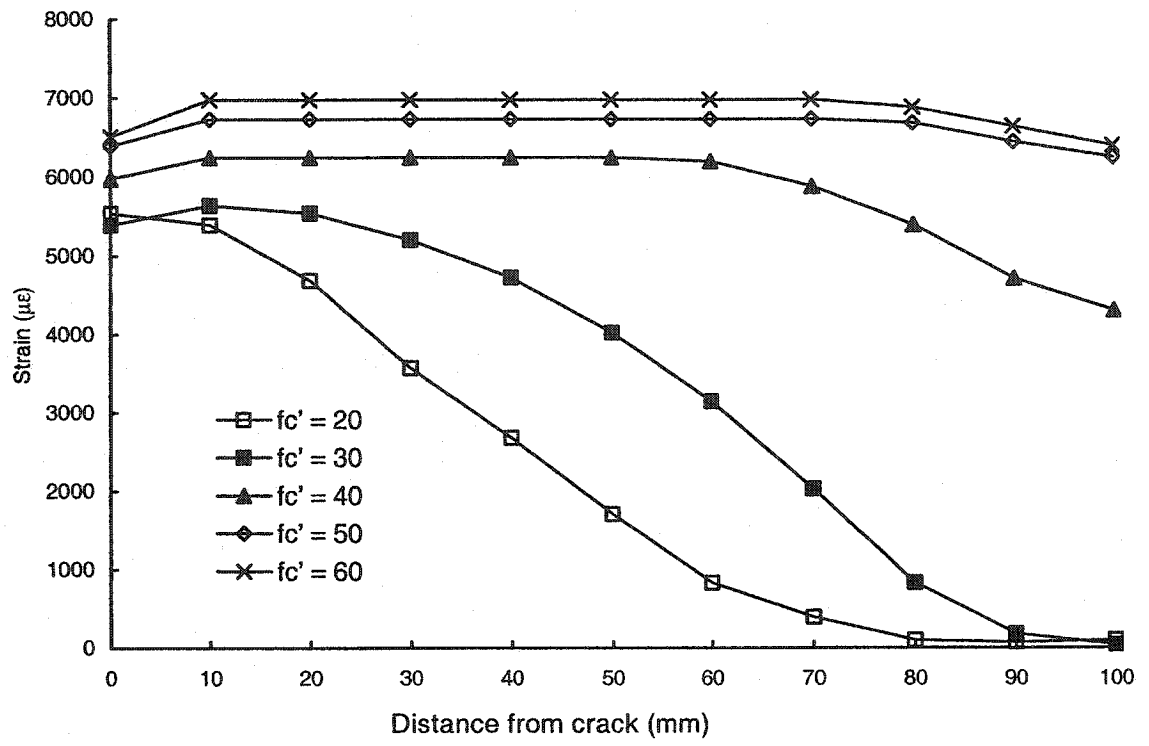


Figure 6-35 Strain distribution for various f'_c at ultimate load for pull-apart model

7 COMPARISON BETWEEN BOND TEST METHODS

7.1 Introduction and Overview

Bond stress curves proposed in the literature describe well the data from which they were defined. However, there are large discrepancy and scattering between these curves. One of the reasons for this discrepancy is the different bond test methods used to conduct the investigations. There are several different test arrangements conventionally used for FRP bond investigations. A brief description of the conventional bond test methods were presented and grouped into categories based on the method of load application in Section 2.6. These include the “Direct pull” method, the “Pull-apart” method, and the “Push-apart” method. The “Modified push-apart” method was also presented in Chapter 3.

There is a need to assess the performance of these methods comparatively in order to develop conversion standards. There is also a need to develop a rational and simplified standard test method for FRP sheets bonded to concrete.

A comparison between bond test methods has been conducted in the form of a parametric study of the effects of the support conditions and loading configurations on the behaviour. In this chapter the different bond test methods, grouped into categories depending on the loading arrangement, are analyzed using 2D nonlinear finite element models. The analysis includes the stress and strain distributions in the concrete and FRP sheet, respectively. The overall load-displacement behaviour and failure mode of each specimen type were also analysed.

In order to initiate the debonding mechanism between the FRP sheet and the concrete surfaces in ABAQUS, the first node in the bonded surfaces is required to be initially debonded. Therefore, the FRP sheet was unbonded from the concrete at the loaded edge node. This prevented the capture of the concrete edge failure reported in the modified push-apart experimental tests in Chapter 4 and stated by Bizindavyi and Neale (1999).

The bond tests investigated in this chapter are those that include the direct pull, indirect pull-apart, push-apart, and the modified push-apart tests. The material properties used in the models are listed in Table 7-1. A relationship between the test methods is proposed based on the numerical study. The relationship is correlated to experimental results from the current study and studies from the literature. Two bond tests are proposed as standard test methods based on the loading apparatus available and comprehensibility, drawn from the analysis in this chapter.

7.2 Direct Pull Bond Test

The direct pull bond test specimen description and the load setup are shown in Figure 7-1a. A brief description of the test was presented in Section 2.6.3.1. The direct pull test is one of the simple bond tests, where an easy to cast concrete block can be used for several tests. The method is conducted using a testing machine, which means it could not be performed on site. The method also restricts the FRP sheet width to a maximum of 50 mm due to gripping problems that could cause slipping of the FRP sheet during testing and premature failure of the FRP sheet. Bizindavyi and Neale (1999) stated that to reduce the risk of sliding and premature failure of the FRP sheets within the grips, the FRP sheets were limited to two plies with bond width of 25.4 mm. Bonding the FRP sheet to the concrete block and impregnating the free unbonded portion of the sheet while maintaining the sheet straight is also difficult. The concrete block is in compression during the test while the FRP sheet is in tension, which is not the stress state in flexure and shear. Special precautions must be taken during testing to ensure that no eccentricity exists in the FRP sheet.

Due to the practical reasons discussed, the direct pull test is limited to one-layer FRP sheet width of 50 mm or two layers 25 mm wide. However, for the sake of comparison, FRP sheet widths ranging from 25 to 150 mm will be investigated. As the direct pull test specimen has only one FRP sheet bonded to a block of concrete, the whole specimen was modeled. The concrete and FRP sheet element meshes were taken as 10×10 mm four-node plain stress solid elements with reduced integration. The 2D

direct pull model mesh, deformed shape, loading, and boundary conditions are shown in Figure 7-1b. The direct pull model represents the perfect case with no eccentricity in loading the FRP sheet.

The length of the unbonded portion of the FRP sheet, which is the sheet length between the concrete face and the machine grip, was investigated. Figure 7-2 shows the load-displacement response for direct pull models with unbonded sheet lengths of 10, 50, 100 mm and constant bond lengths and widths of 150 mm each. The figure shows that the load-displacement response was stiffer as the unbonded length decreased. This is attributed to the fact that the concrete block was fixed, causing the displacement to be only from the extension of the unbonded FRP sheet including the debonded portions of the sheet. This caused higher displacement to occur as the unbonded sheet lengths increased. Figure 7-2 also showed no significant difference in ultimate load values for the different unbonded lengths. In practice the unbonded FRP sheet length must allow for the bearing steel plate and clearance for aligning the sheet into the machine grip. This length is estimated to be at least 50 mm. Based on practical test setup implementation, the direct pull model used in the comparison between the test methods will have an unbonded FRP sheet length of 50 mm. This behaviour cannot be confirmed from the literature, as there are no studies on the effect of the unbonded sheet length.

Figure 7-3 shows the contour lines for the principal stresses at various load increments in the direct pull model. The figure shows the development of the principal stresses, where a compression strut is formed between the bearing steel plate and the loaded (bonded) portion of the FRP sheet. The figure also shows that as the load increases, the compression strut shifts along the sheet. This is attributed to the debonding propagation of the FRP sheet from the concrete, which causes the bonded area to shift away from the loaded end.

The effect of the compression field in the concrete adjacent to the bearing steel plate on the FRP sheet bond behaviour was investigated. The investigation focused on

the distance between the end of the bearing steel plate and the FRP sheet. That distance ranged from 10 to 50 mm. It is found from the numerical investigation that there is no significant effect on the load-displacement behaviour or the strain distribution in the FRP sheet due to the variation of that distance. Therefore, the distance between the bearing steel plate and the FRP sheet used in the comparison between the test methods was arbitrarily chosen to be 30 mm.

Figure 7-4 shows the load-displacement behaviour for direct pull models with FRP sheet widths of 25, 50, 100, and 150 mm. The figure shows that increasing the bond width increases the ultimate load, but the ultimate load per unit width is constant at 0.2 kN/mm for all bond widths. This indicates that the maximum average bond strength across the FRP sheet width is similar for all bond widths. Figure 7-5 shows the load level, P/P_u , plotted against the displacement for models with FRP sheet widths of 25, 50, 100, and 150 mm. The figure shows that there is no significant difference between the responses with the change in bond width.

Figure 7-6 and Figure 7-7 show the strain distribution along the FRP sheet length for bond widths of 25 and 150 mm, respectively. The figures show that the strain increases as the load increases, but at the ultimate load there is a limiting strain value that corresponds to the model ultimate interface normal and shear stresses. The figures also show that for the same load levels, the strain in the model with 150 mm bond width is higher than that in the model with 25 mm bond width. The transfer length, the distance from the crack location to the point where the strain is negligibly small, is also longer in the 150 mm bond width model. At ultimate load both the 25 and 150 mm bond width models have almost the same ultimate strain plateau value, but with the 25 mm model covering more of the bond length and having higher strain values beyond the plateau portion.

7.3 Pull-Apart Test

The pull-apart bond test specimen is illustrated in Figure 7-8a. The specimen description and loading setup were also presented in Sections 2.6.3.2 and 3.3. The pull-

apart test is an indirect bond test that requires a testing machine or a hydraulic jack with a special loading frame. The specimen is an easy to cast concrete prism but special care must be taken to ensure the alignment of the steel rebars and to secure the location of the crack initiator during casting. The number of FRP sheet plies and dimensions are limited by the bond strength of the steel rebar. Aligning the specimen in the testing machine and preventing any inclination of the specimen during testing is very important, where eccentricity has a significant effect on the results.

Although some pull-apart tests have been performed with specimens having a gap between the concrete prisms, the pull-apart model used in this investigation assumes no gap between the prisms. As no anchor sheets are applied to the tested sheets when the specimens are used to determine the bond strength or the development length, one quarter of the pull-apart specimen was modeled, making use of symmetry. The 2D pull-apart numerical model is as described in Chapter 5 with the exception that one quarter of the specimen is modeled rather than one half. The mesh, deformed shape, loading, and boundary conditions of the pull-apart model are shown in Figure 7-8b.

The pull-apart model represents the perfect case with no load eccentricity, where the steel rebars are assumed perfectly aligned and have perfect bond with the concrete. The failure mechanism of the pull-apart specimens in the experimental investigation, detailed in Section 4.2.2, showed that failure occurred on one side of the specimen, causing eccentricity in loading during testing. This behaviour was not represented in the numerical model.

A numerical investigation of the rebar free length effect, which is the length between the machine grip and the concrete specimen, was conducted using lengths of 10, 50, and 100 mm. The investigation showed that the free length of the rebar did not affect the model output. This is because the applied stresses were significantly less than the rebar yield stress and also because perfect alignment was assumed. The free length of the steel rebar in the model used in the comparison between the test methods was taken to be 50 mm. A numerical investigation studying the specimen width separating

the bonding concrete faces also showed no significant effect on the numerical results. The concrete prism dimension between the bonding surfaces was taken as 100 mm in the model used for the comparison between the test methods.

Figure 7-9 shows the applied load plotted against the displacement for pull-apart models with FRP sheet widths of 25, 50, 100, and 150 mm. The figure shows that increasing the bond width increases the ultimate load, but the ultimate load per unit width is constant at 0.21 kN/mm for all bond widths. Figure 7-10 shows the load level, P/P_u , plotted against the displacement for models with FRP sheet widths of 25, 50, 100, and 150 mm. The figure shows that at the same displacement, the load level is higher for smaller bond widths but there is no significant difference between the responses at ultimate load.

Figure 7-11 and Figure 7-12 show the strain distribution along the FRP sheet length at various load levels for models with bond widths of 25 and 150 mm, respectively. The figures show the strain increasing as the load increases, but with no limiting strain plateau. As the value of the ultimate strain is related to the combination of both the interface shear and normal stresses, an inclination between the FRP sheet and the concrete will result in changing the ultimate shear value. The FRP sheet in the pull-apart test debonds and inclines away from the concrete as load progresses, which could explain their descending strain distribution. The figures also show that there is no significant difference between the strain values or the transfer lengths at the same load levels for the bond widths of 25 and 150 mm.

7.4 Push-Apart Test

The push-apart bond test specimen and loading are shown in Figure 7-13a. The specimen description and loading setup are also described and presented in Section 2.6.3.3. Only one quarter of the specimen was modeled making use of symmetry. The concrete, FRP sheet, and bearing steel plate meshes were taken as four-node plain stress solid elements with reduced integration, with dimensions similar to those of the

modified push-apart model detailed in Chapter 5. The 2D indirect push-apart model mesh, deformed shape, loading, and boundary conditions are shown in Figure 7-13b.

The push-apart test is an indirect bond test that only requires the use of a hydraulic jack to apply the load, which makes it suitable for field verifications in retrofit situations. The specimen consists of two concrete blocks that are easy to cast. On the other hand, bonding the FRP sheets to the concrete and impregnating the unbonded portion of the sheet while maintaining the alignment must be done carefully. Special precautions must also be taken to ensure no eccentricity in loading. The concrete is in compression while the FRP is in tension, similar to that in the direct pull test.

The effect of the unbonded FRP sheet length, which is the distance between the two concrete blocks, on the bond behaviour was investigated. Figure 7-14 shows the load-displacement response for models with unbonded FRP sheet lengths of 40, 100, 180, and 200 mm. The figure shows that the behaviour becomes stiffer as the unbonded FRP sheet length decreases. The unbonded length in practice needs to account for a hydraulic jack and two bearing steel plates. The unbonded length was taken as 180 mm in the model used in the comparison between the test methods.

An investigation of the effect of the specimen width separating the two bonding faces on the results was conducted. Numerical investigation of prism dimensions of 120 and 200 mm show that there is no change in behaviour due to the change in the width separating the bonded sheets. The prism dimension between the bonding faces was taken as 200 mm in the comparison between the test methods. The effect of the distance between the bearing steel plate and the bonding faces was also investigated numerically. It was found from the numerical investigation that changing the distance from 20 to 50 mm did not have any significant effect on the results. Therefore, the steel plate distance from the bonding faces was taken as 20 mm in the comparison between the test methods.

Figure 7-15 shows the applied load plotted against the displacement for push-apart models with FRP sheet widths of 25, 50, 100, and 150 mm. The figure shows that increasing the bond width increases the ultimate load, but the ultimate load per unit width is almost constant at 0.175 kN/mm for all bond widths. Figure 7-16 shows the load level, P/P_u , plotted against the displacement for models with FRP sheet widths of 25, 50, 100, and 150 mm. The figure shows that there is no significant difference between the responses for the different bond widths.

Figure 7-17 and Figure 7-18 show the strain distribution along the FRP sheet length for bond widths of 25 and 150 mm, respectively. The figures show that at the ultimate load there is a limiting strain value that corresponded to the ultimate interface normal and shear stresses. The figures also show that for the same load levels, the strain in the model with 150 mm bond width is higher than that in the model with 25 mm bond width but that there is no significant difference in the transfer length between the models. At ultimate load both the 25 and 150 mm bond width models show almost the same ultimate strain plateau value, but with the 25 mm model covering more of the bond length and having slightly higher strain values beyond the plateau portion.

7.5 Modified Push-Apart Test

The modified push-apart bond test specimen is shown in Figure 7-19a. The specimen description and loading setup are also described and presented in Section 3.2. As no anchor sheets are used when the specimens are used to determine the bond strength or the development length, only one quarter of the specimen was modeled making use of symmetry. The 2D modified push-apart numerical model was described in detail in Chapter 5, except that one half of the specimen was modeled rather than one quarter. The mesh, deformed shape, loading, and boundary conditions of the pull-apart model are shown in Figure 7-19b.

Similar to the push-apart test, the modified push-apart test only requires a hydraulic jack to apply the load. Bonding the FRP sheets to the arms of the specimen away from the load application point eliminates the compression in the concrete on

which the sheets are bonded, which is a better simulation of the practical situation. The modified push-apart test is more stable with no free unbonded FRP sheets. It is also easy to bond the FRP sheets to the straight flat concrete surface. On the other hand, the specimen is more difficult to prepare and is relatively large in size.

Figure 7-20 shows the applied load plotted against the displacement for four modified push-apart models with FRP sheet widths of 25, 50, 100, and 150 mm. The figure shows that increasing the bond width increases the ultimate load, but the ultimate load per unit width is almost constant at 0.205 kN/mm for all bond widths. Figure 7-21 shows the load level, P/P_u , plotted against the displacement for models with FRP sheet widths of 25, 50, 100, and 150 mm. The figure shows that at the same displacement, the load level is higher for smaller bond widths but the responses converges at ultimate load.

Figure 7-22 and Figure 7-23 show the strain distribution along the FRP sheet length at various load levels for models with bond widths of 25 and 150 mm, respectively. The figures show the strain increasing as the load increases, but with no limiting strain plateau, where the increase in the angle between the FRP sheet and the concrete as debonding progresses reduces interface shear stresses and in return the ultimate strain along the sheet. The figures also show that there is no significant difference between the strain values or the transfer lengths at the same load levels for the bond widths of 25 and 150 mm.

The effect of the steel rebar in the concrete arms was investigated using models with different arm widths. Figure 7-24 shows the load-displacement response for four specimen arm widths of 60, 100, 150, and 200 mm with and without steel rebar. The figure shows that the existence of the steel rebar in the concrete arms significantly increases the ultimate load for the narrow arm widths, which prevents premature failure of the concrete arm. The effect of the steel rebar decreases as the arm width increases, up to an arm width of 200 mm, at which no significant difference between models with and without rebar occurs.

The effect of the concrete specimen arm width on the bond behaviour was investigated. The concrete specimen arm widths investigated ranged from 40 to 300 mm. The applied load plotted against the deflection at the point of loading for arm widths ranging from 40 to 100 mm is shown in Figure 7-25. The figure shows that the ultimate load increases as the specimen arm width increases. On the other hand, the behaviour for arm widths ranging from 100 to 300 mm shown in Figure 7-26 shows that the ultimate load decreases as the specimen arm width increases above 100 mm. The reason for the lower ultimate load in the case of narrower arm widths is the excessive deformation of the specimen arms, which causes concrete cracking beyond the FRP sheet. The strain concentrations in the concrete arm beyond the FRP sheet of the model with a 40 mm arm width are shown in Figure 7-27. The tensile stress values in the stress distribution in the concrete arm shown in Figure 7-28 also indicate that the concrete is cracked. On the other hand, the reason for the lower ultimate load in the case of wider arm widths is the concrete failure at the outer concrete face. The strain concentrations at the outer concrete face of the model with an arm width of 300 mm are shown in the strain contour in Figure 7-29. The tensile stress values in the stress distribution shown in Figure 7-30 also indicate that the concrete is cracked.

The previous discussion suggests an optimum arm width for the modified push-apart specimen. According to the numerical analysis, this optimum width was 100 mm for the range of material properties used. The optimum arm width is also expected to depend on the dimensions and stiffness of the bonded FRP sheet.

7.6 Comparison Between the Bond Tests

A comparison is performed between the test methods based on the previous discussions and the data generated in order to recommend a test method to be used as a standard test method and to relate the various test methods to each other.

As discussed separately in the previous subsections, each test method has advantages and limitations. The preparation of the specimen, serviceability, performing

the test, and the stability of the test are all factors in deciding on the preferred bond test method for FRP sheets bonded to concrete. On the other hand, relating the different types of tests will enable the use of their experimental results in developing design guidelines and equations.

7.6.1 Specimen Preparation

The concrete preparation for both the direct pull and push-apart tests are the easiest, where the specimens consist of simple concrete square prisms. But on the other hand, bonding the FRP sheets is difficult. The pull-apart test needs special arrangements to ensure that the rebar are concentric and aligned. If the pull-apart concrete specimen is initially intact then bonding the sheets will be on a flat continuous surface. The modified push-apart concrete specimen is the most difficult to prepare but a flat continuous surface makes bonding the sheet a simple task. All the test methods require special precautions when handling in order to preserve the FRP sheet and its connection with the concrete.

7.6.2 Test Serviceability and Execution

The FRP sheet in the direct pull test is limited to 25 mm bond width while the other tests do not have this restriction. Both the direct pull and the pull-apart tests need a testing machine to perform the test, while the push-apart and the direct push-apart tests require a hydraulic jack, which enables the test to be conducted on any flat surface in any location. The modified push-apart specimen size is relatively large, which could cause handling problems and is considered a drawback. The direct pull and push-apart tests require special precautions to ensure that the unbonded FRP sheets are perfectly straight.

7.6.3 Test Stability

The definition of test stability in the context of this discussion is the sensitivity of the test to change in the concrete specimen dimensions, FRP sheet unbonded length, and load eccentricity. The modified push-apart method showed change in the results

due to change in the concrete arm width dimension, which affected the output of the model. The existence of rebar in the modified push-apart specimen arm also affected the results. The unbonded FRP sheet length affected both the direct pull and push-apart results. Eccentricity affects all test methods and special precautions must be taken to ensure that no eccentricity exists.

7.6.4 Relationship Between Test Methods

All the models had the same concrete and FRP material properties as listed in Table 7-1. The FRP sheet bond length and width were also similar in all the models. The only differences between the models were the geometry, loading, and boundary conditions.

The push-apart model had the same load-displacement behaviour as the modified push-apart model when the unbonded FRP sheet length was taken as 40 mm, which is shown in Figure 7-14 and was investigated for the sake of discussion but is not practically possible. For longer unbonded sheet lengths, the push-apart model had a more ductile response and a lower ultimate load than the modified push-apart model. The strain distribution along the FRP sheet in the push-apart model had a limiting plateau regardless of the unbonded length value.

The load-deflection behaviour for all investigated models with bond widths of 25, 50, 100, and 150 mm are shown in Figure 7-31 through Figure 7-34. The figures show that the pull-apart and modified push-apart models have the same trend while the direct pull and push-apart models have a different more ductile trend. The load-deflection relationship between the pull-apart and modified push-apart models is closer at bond widths 25 and 150 mm than at bond widths 100 and 150 mm. On the other hand, for the direct pull and push-apart models is an almost unchanged load-deflection relationship regardless of the bond width.

The ultimate load plotted against the bond width for the results of the models illustrated in Figure 7-31 through Figure 7-34 is shown in Figure 7-35. The figure shows that the relationship in all the models is almost linear with the pull-apart model

having the highest ultimate loads and the push-apart model having the lowest ultimate loads, while there was no significant difference between the modified push-apart and direct pull models. The ultimate load in the pull-apart model was higher than that in the push-apart model by 16.7% at 25 mm and 19.2% at 150 mm.

The ultimate load per unit width is plotted against the bond width in Figure 7-36. The figure shows that the ultimate load per unit width was almost constant in all the models. The average ultimate load per unit width was 0.21 for the pull-apart model, 0.2 for both the modified push-apart and direct pull models, and 0.17 for the push-apart model. This could provide a conversion relationship between the results of the test methods, specially the ultimate load that is used to determine the average bond strength. If one takes the direct pull test as the basis for comparison then the ultimate load for the pull-apart, modified push-apart, and push-apart tests are equal to 0.95, 1.0, and 0.8 of the direct pull test ultimate load, respectively.

The experimental results of modified push-apart and pull-apart tests with bond length of 150 mm listed in Tables 4-1 and 4-2 are also plotted in Figure 7-36. The figure shows that the modified push-apart experimental result is 7.3% higher than the model at bond width 100 mm and 10.9% lower at 150 mm, while both results from the pull-apart test were 16.3 and 20.2% higher. The push-apart experimental result from Alexander and Cheng (1997) shows a 5.8% higher value than the corresponding numerical value. On the other hand the experimental result from the direct pull test done by Bizindavyi and Neale (1999) show a much higher ultimate load per unit width of 70.3%, which could be attributed to the lower bond width of 25 mm used in the tests.

The pull-apart test was the only test with sufficient results including width variations to plot the ultimate load per unit width against the bond width, as shown in Figure 7-37. The figure shows that the ultimate load per unit width is higher when the bond width is less than 50 mm with an average of 0.25, while that for bond widths of 50mm and above is 0.17.

The ultimate load per unit width plotted against the bond length for experimental results from the current study and the literature for the direct pull, pull-apart, push-

apart, and modified push-apart tests are shown in Figure 7-38 through Figure 7-41. The tests chosen had no significant difference in FRP sheet stiffness. The figures show that the experimental results do not have a defined trend relating the ultimate load per unit width to the bond length.

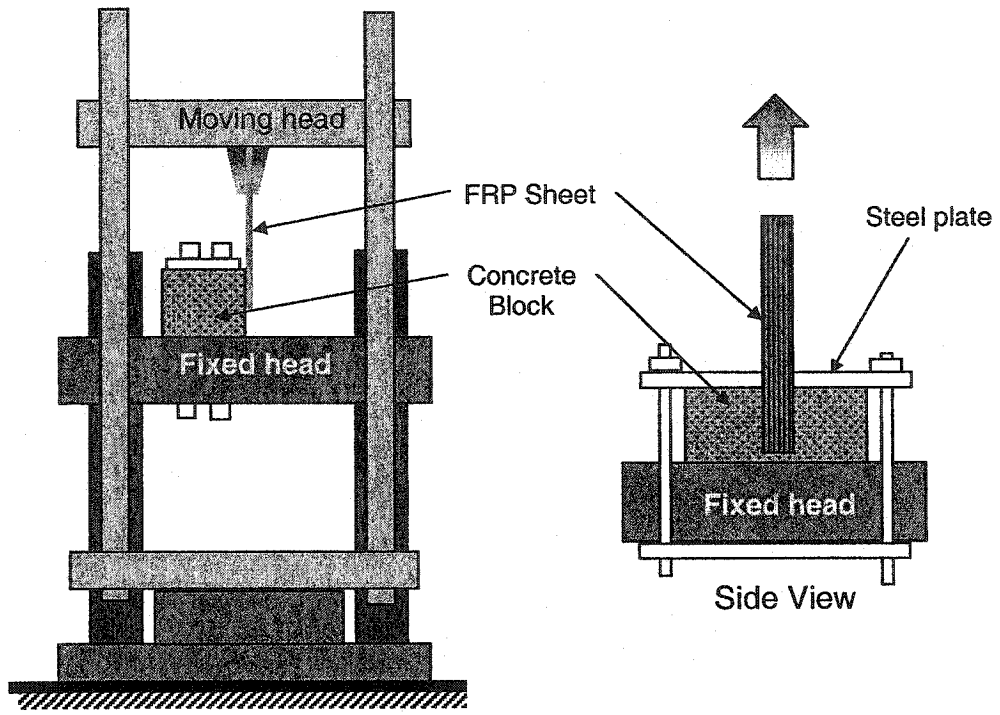
The strain distribution in all test methods at fractions of the ultimate load, $0.6P_u$, $0.8P_u$, $0.9P_u$, and P_u , are shown in Figure 7-42 through Figure 7-45. The figures show that there is no significant difference in the strain distributions at $0.6P_u$, but the differences increase as the load increases. The strain distribution at ultimate load in Figure 7-45 shows two trends, one for the methods with unbonded FRP sheets, namely the direct pull and push-apart tests, and another for the methods without unbonded sheets. The first trend has a maximum limiting strain plateau, which corresponds to the ultimate interface normal and shear stresses. The second trend shows a varying strain along the bond length with a maximum value at the crack location. The same behaviour is recorded for bond widths of 150 mm as shown in Figure 7-46.

The load-deflection responses for models with bond widths of 25 mm at 4 kN are shown in Figure 7-47. The figure shows that the responses are relatively close except for the pull-apart test, which is observed at a relatively higher load level, $0.92 P_u$. Figure 7-48 shows the load-deflection responses for models with bond widths of 150 mm at 24 kN. The figure shows that the previously discussed trends have already been developed although the load levels were almost the same as for the models with 25 mm bond width.

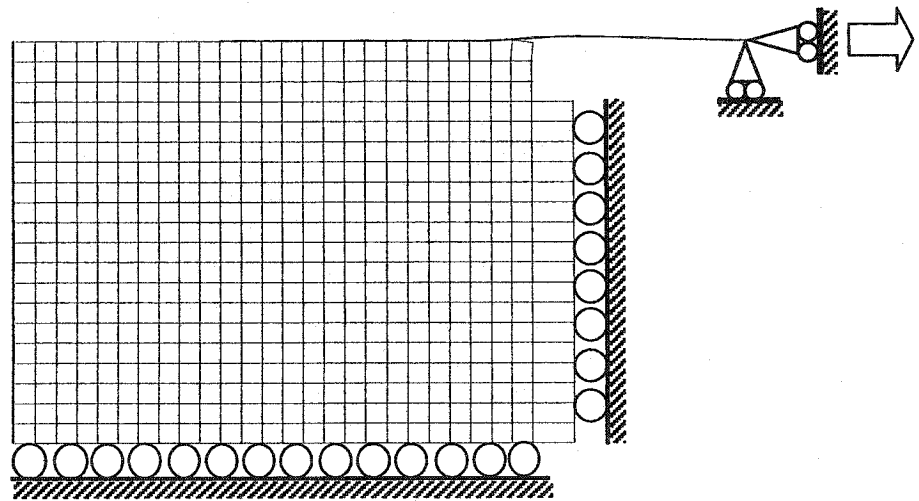
The previous discussion of the numerical analysis and the practical aspects of the different test methods shows that each test method has advantages and limitations. Two bond tests are proposed as standard test methods based on the loading mechanism available and the advantages shown in the analysis in the current investigation. The pull-apart test is recommended over the direct pull test if a testing machine is available for its consistency in results and ease of performing the test. On the other hand, the modified push-apart test is recommended over the push-apart test for its self-confinement and less sensitivity to eccentricity.

Table 7-1 Material properties used in all models

Concrete	Width	w_c (mm)	200
	Modulus of Elasticity	E_c (MPa)	31820
	Poisson's ratio	ν_c	0.15
	Compressive yield strength	f_{cy} (MPa)	28
	Ultimate comp. Strength	f_c (MPa)	50
CFRP Sheet	Thickness	t_p (mm)	0.38
	Bond length	L (mm)	150
	Modulus of Elasticity	E_p (MPa)	65789
	Poisson's ratio	ν_p	0.26



(a) Specimen details and load setup



(b) Mesh, deformed shape, loading, and boundary conditions

Figure 7-1 Direct pull bond test

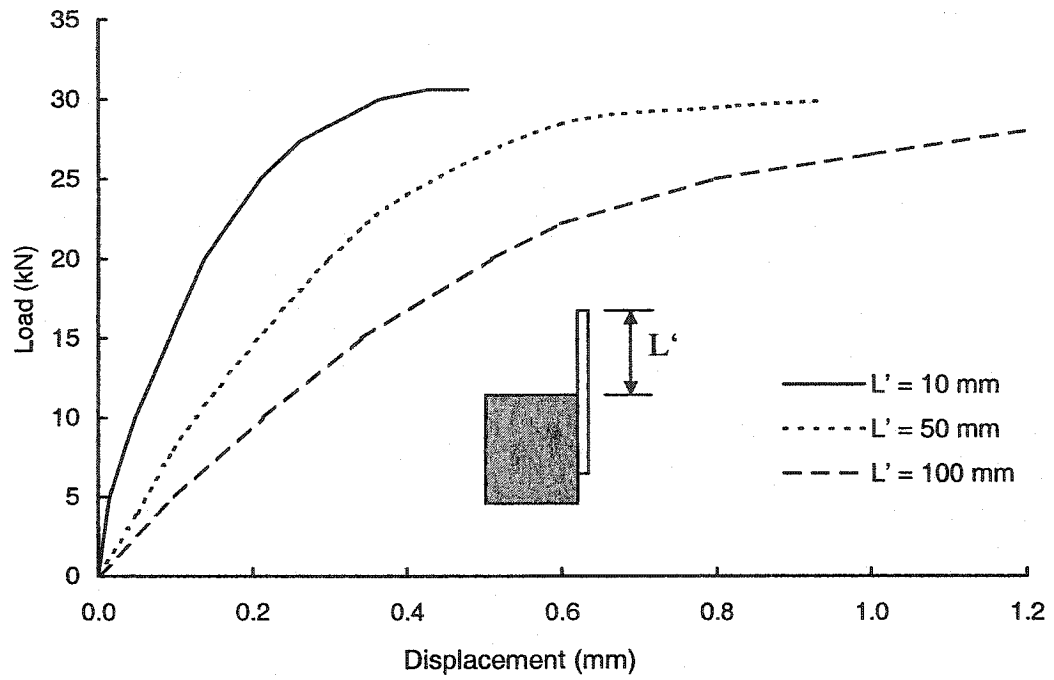
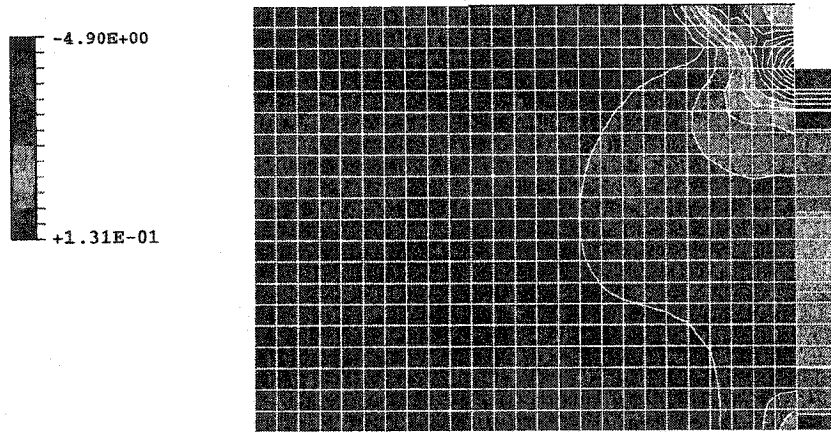
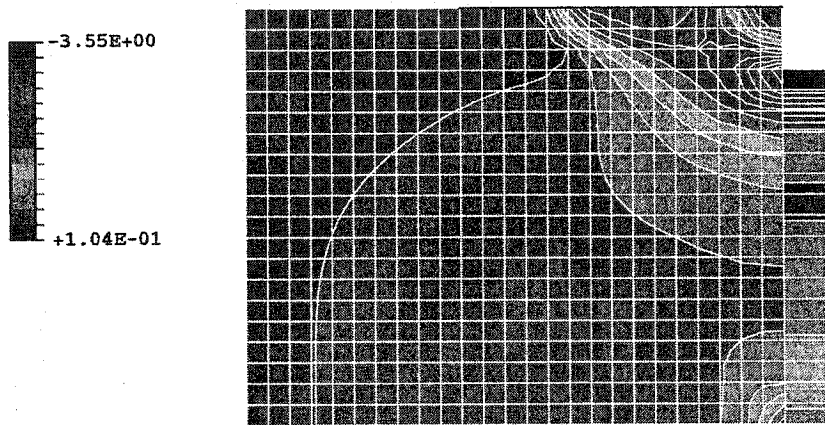


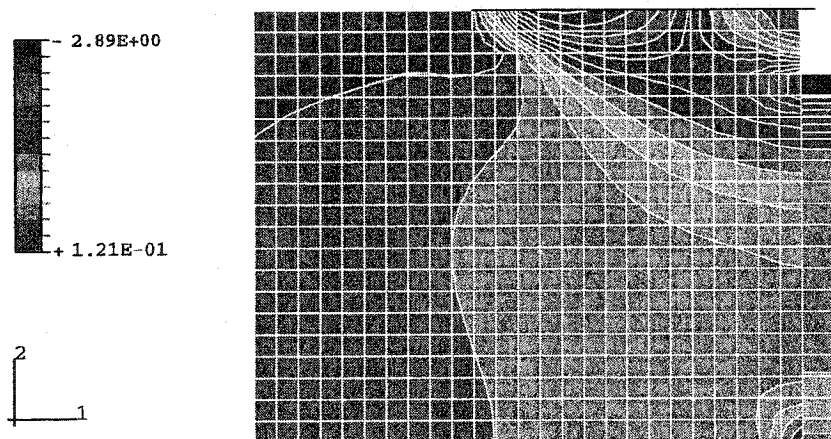
Figure 7-2 Load-displacement for direct pull tests with various unbonded lengths



(a) At 20 kN



(b) At 22 kN



(c) At 24.85 kN

Figure 7-3 Development of principal stresses in direct pull concrete specimen

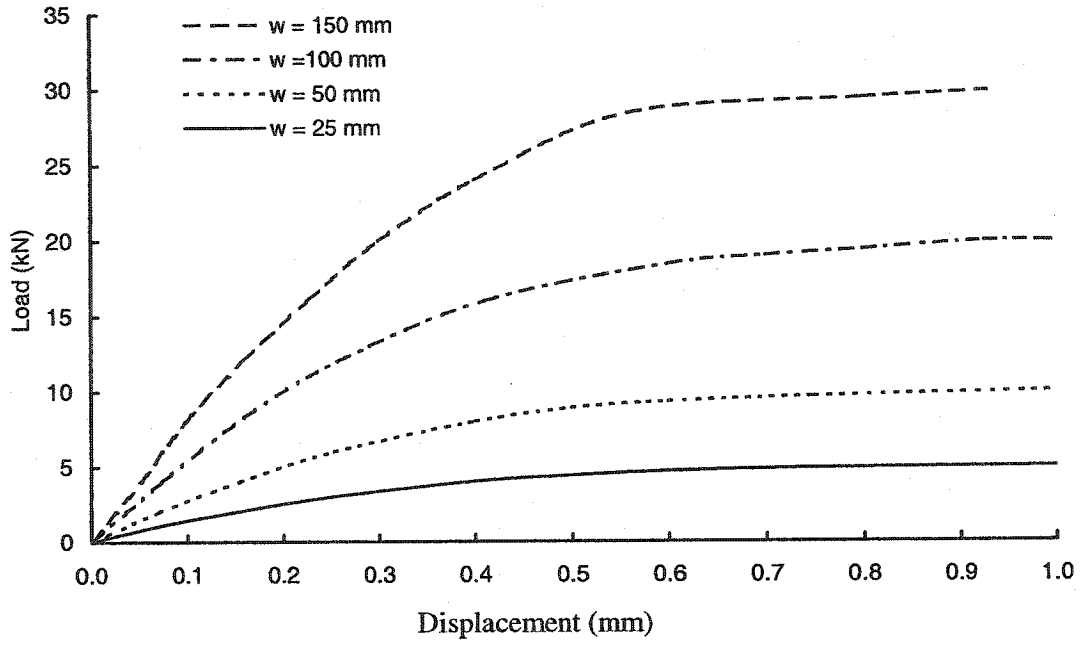


Figure 7-4 Load-displacement for direct pull models

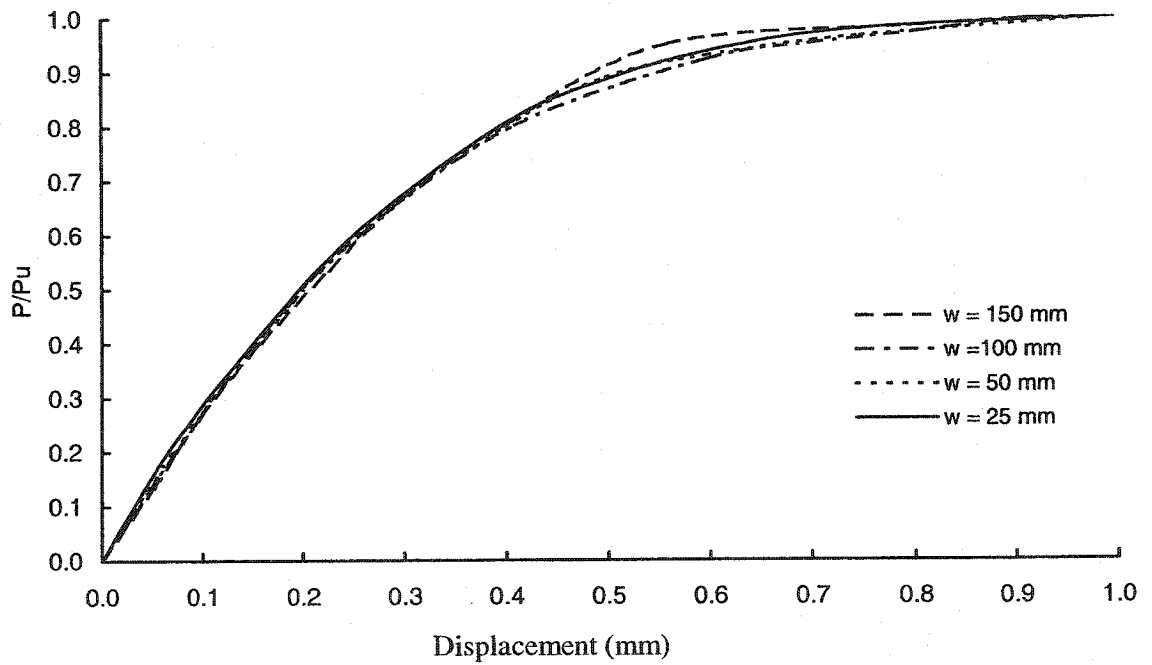


Figure 7-5 Load level-displacement for direct pull models

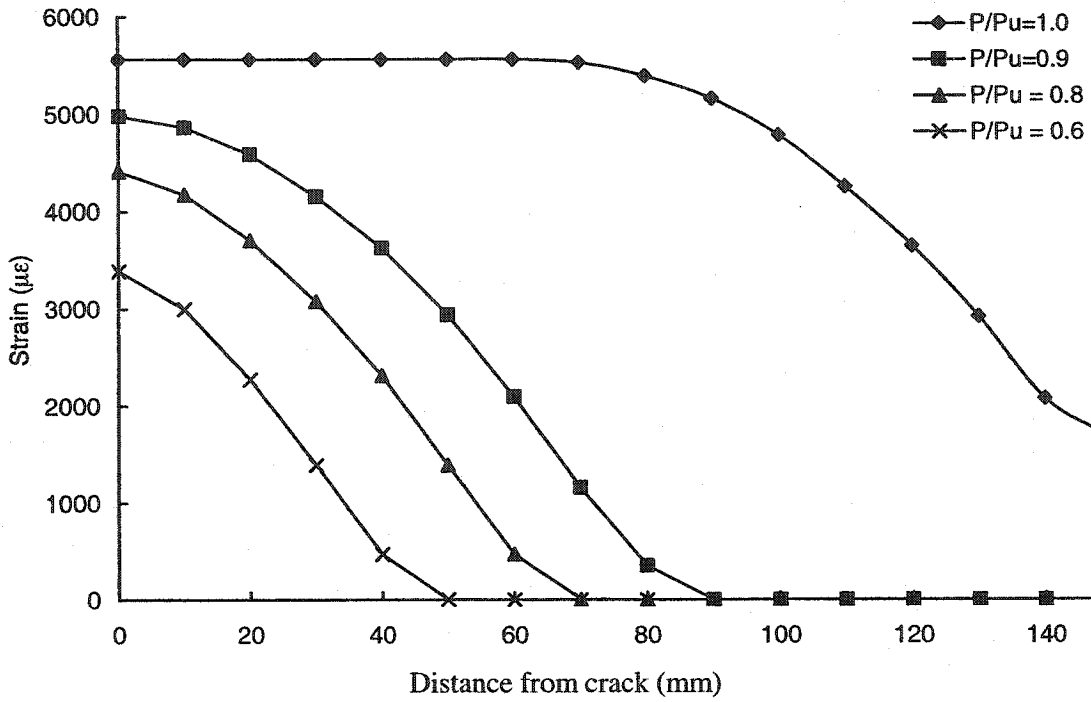


Figure 7-6 Strain distribution for direct pull models with FRP width of 25 mm

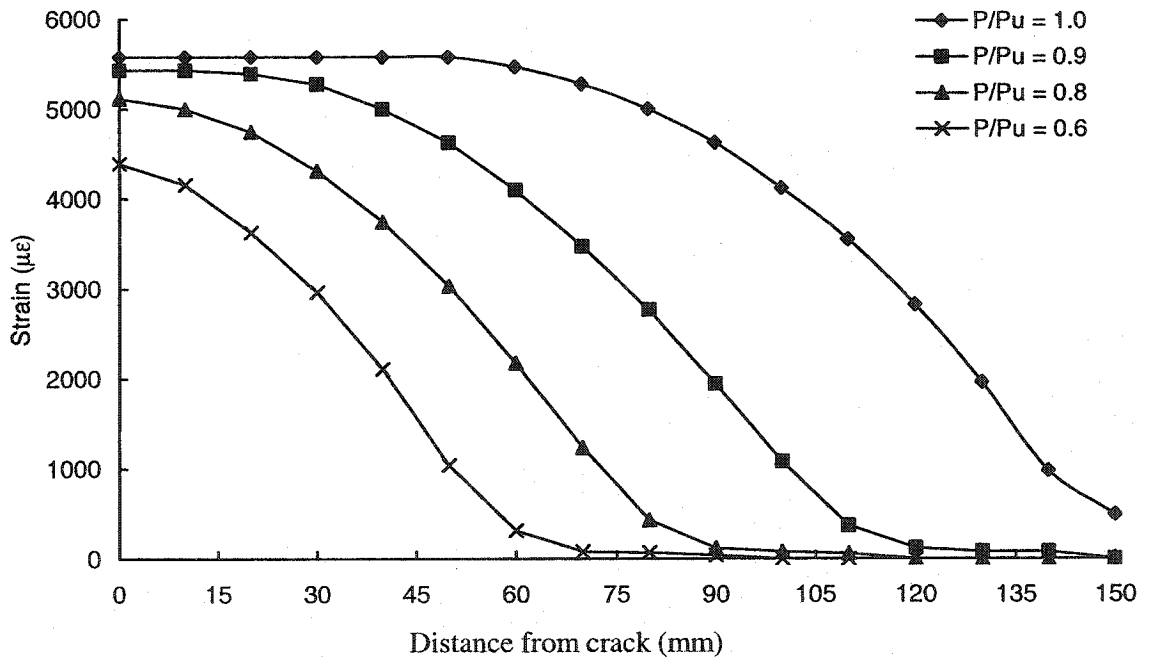
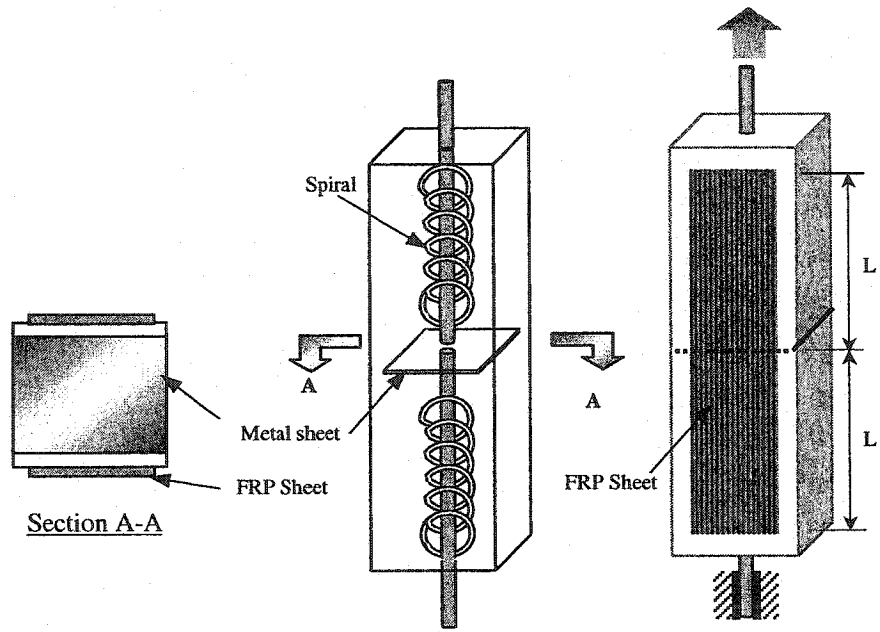
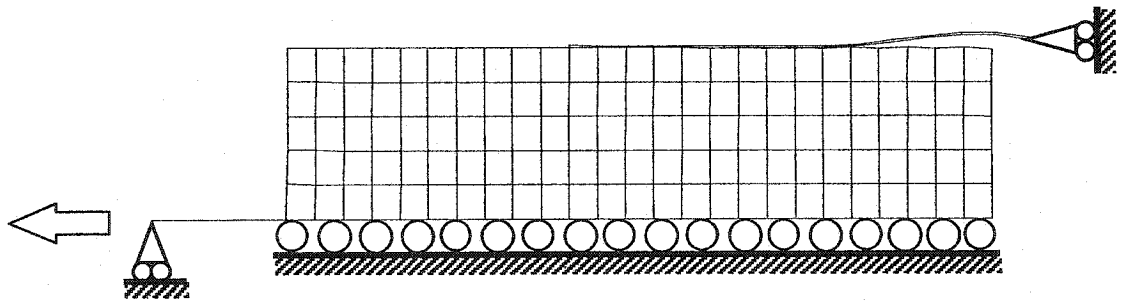


Figure 7-7 Strain distribution for direct pull models with FRP width of 150 mm



(a) Specimen details



(b) Mesh, deformed shape, loading, and boundary conditions

Figure 7-8 Pull-apart bond test

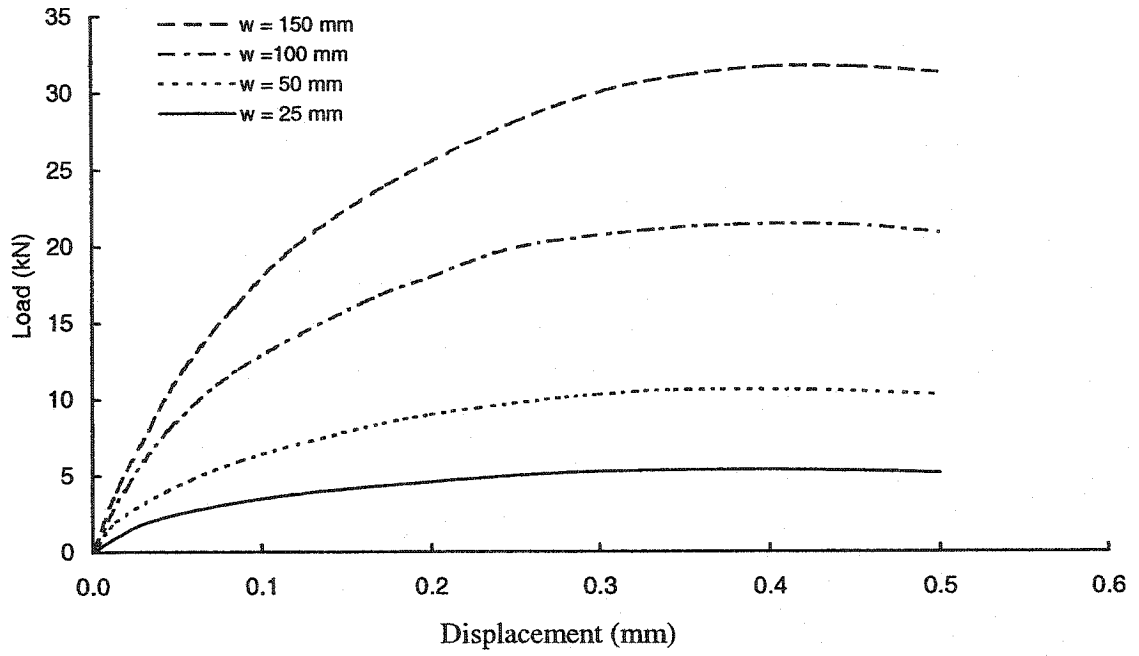


Figure 7-9 Load-displacement for pull-apart models

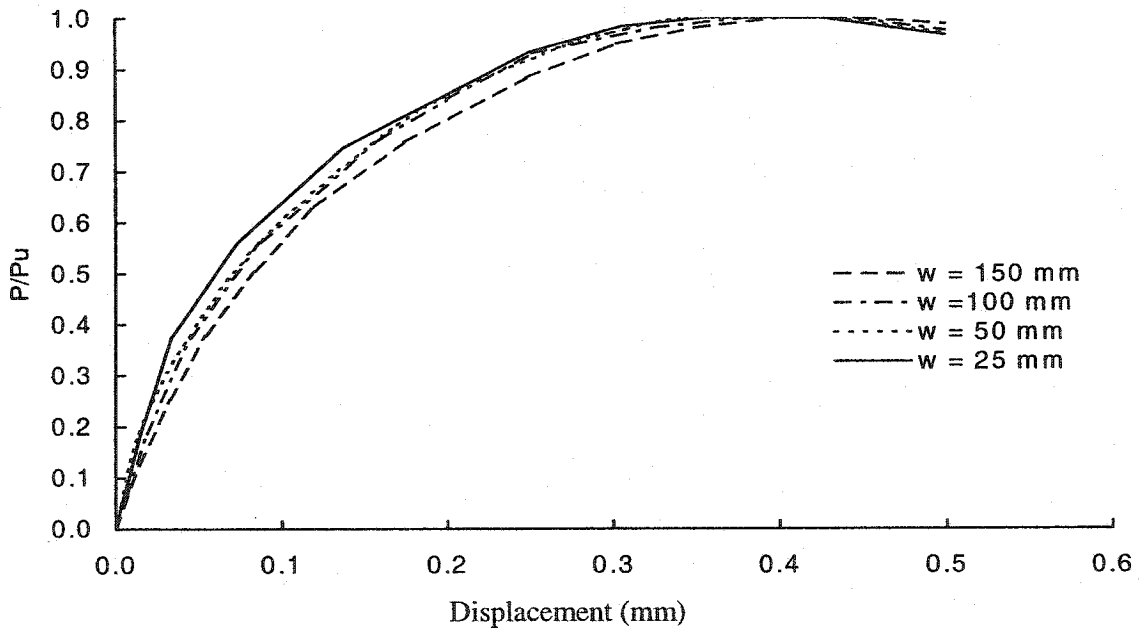


Figure 7-10 Normalized load-displacement response for pull-apart models

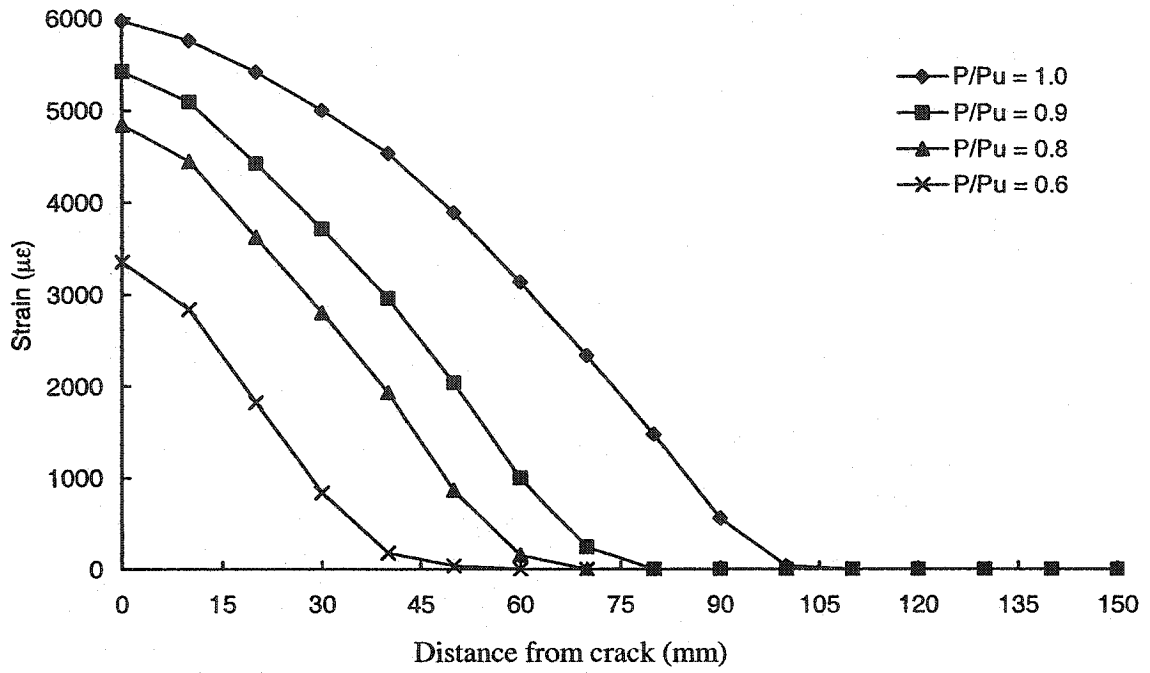


Figure 7-11 Strain distribution for pull-apart models with FRP width of 25 mm

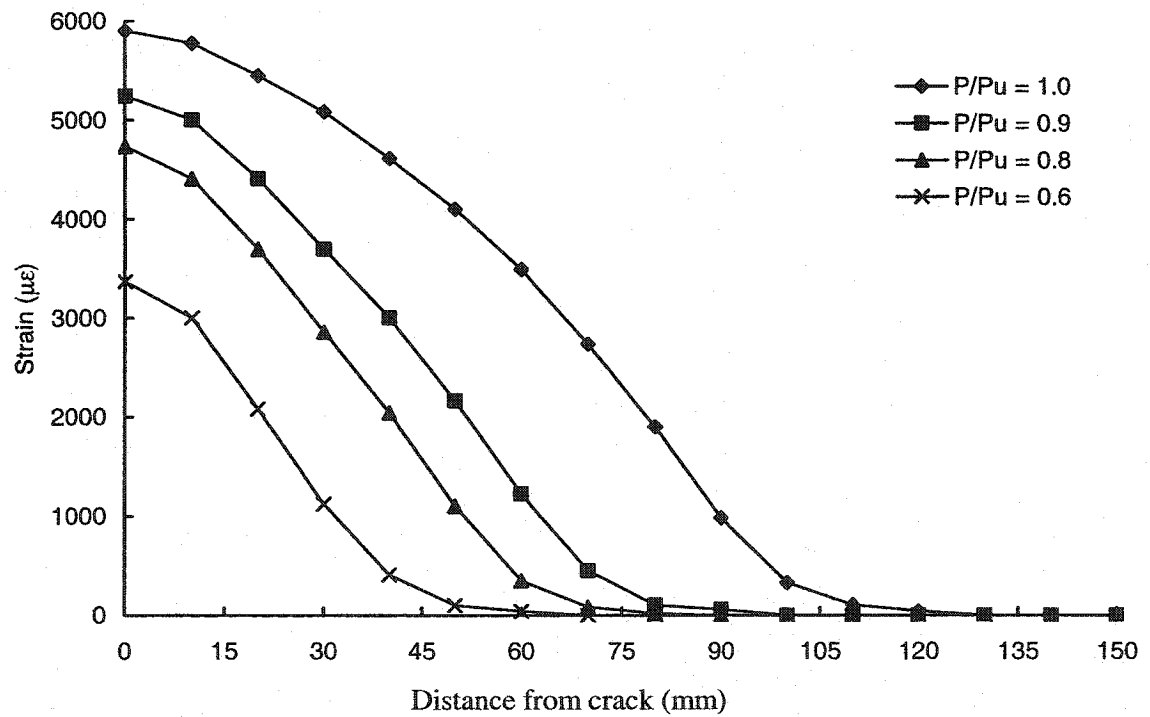
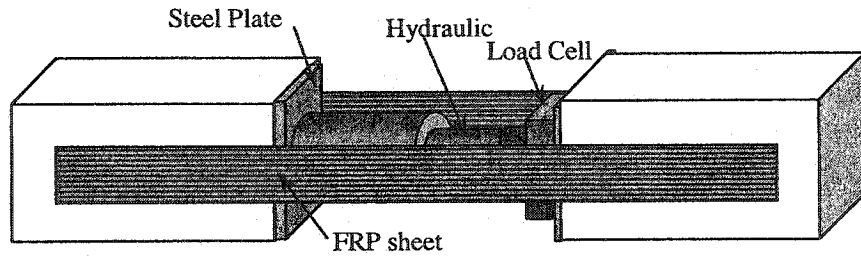
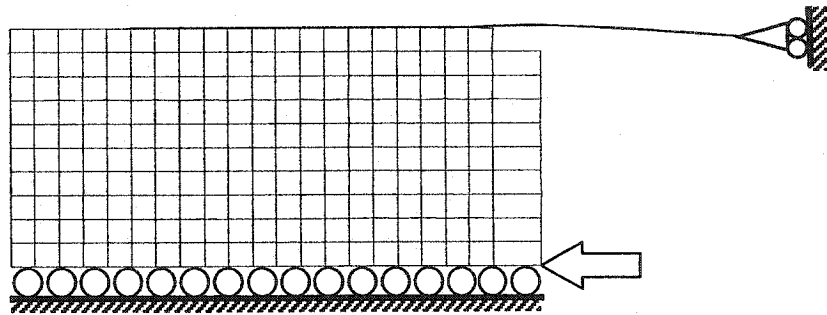


Figure 7-12 Strain distribution for pull-apart models with FRP width of 150 mm



(a) Specimen details and load setup



(b) Mesh, deformed shape, loading, and boundary conditions

Figure 7-13 Push-apart bond test

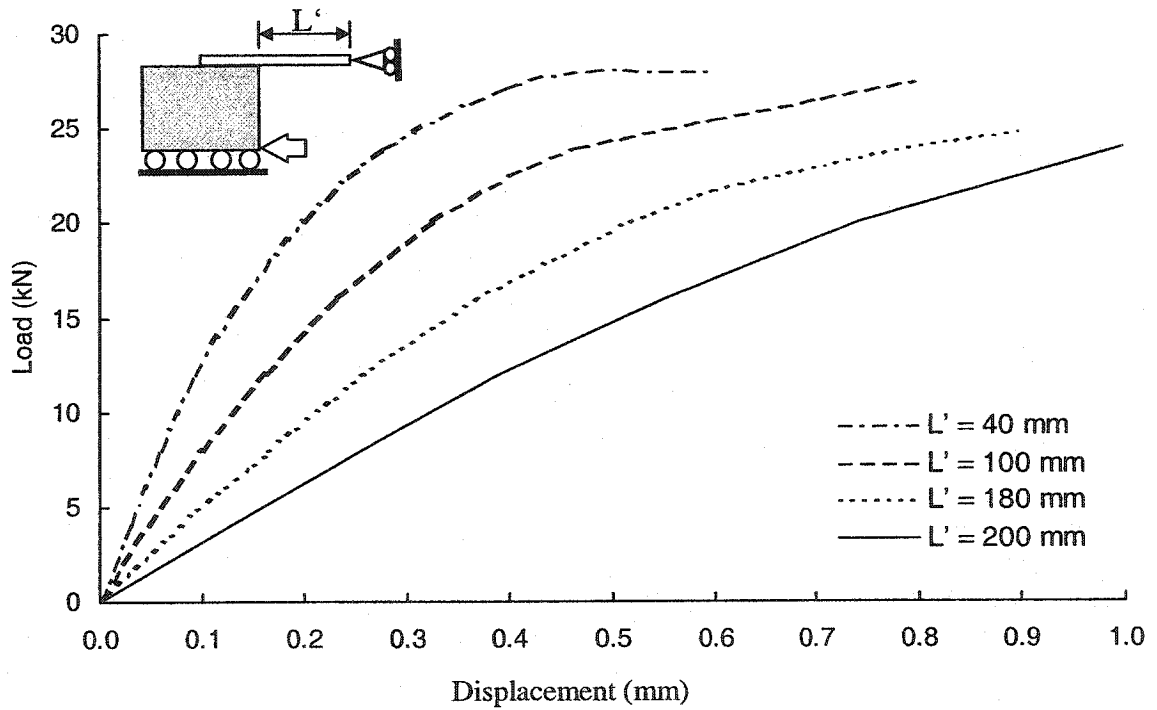


Figure 7-14 Load-displacement push-apart tests with different unbonded lengths

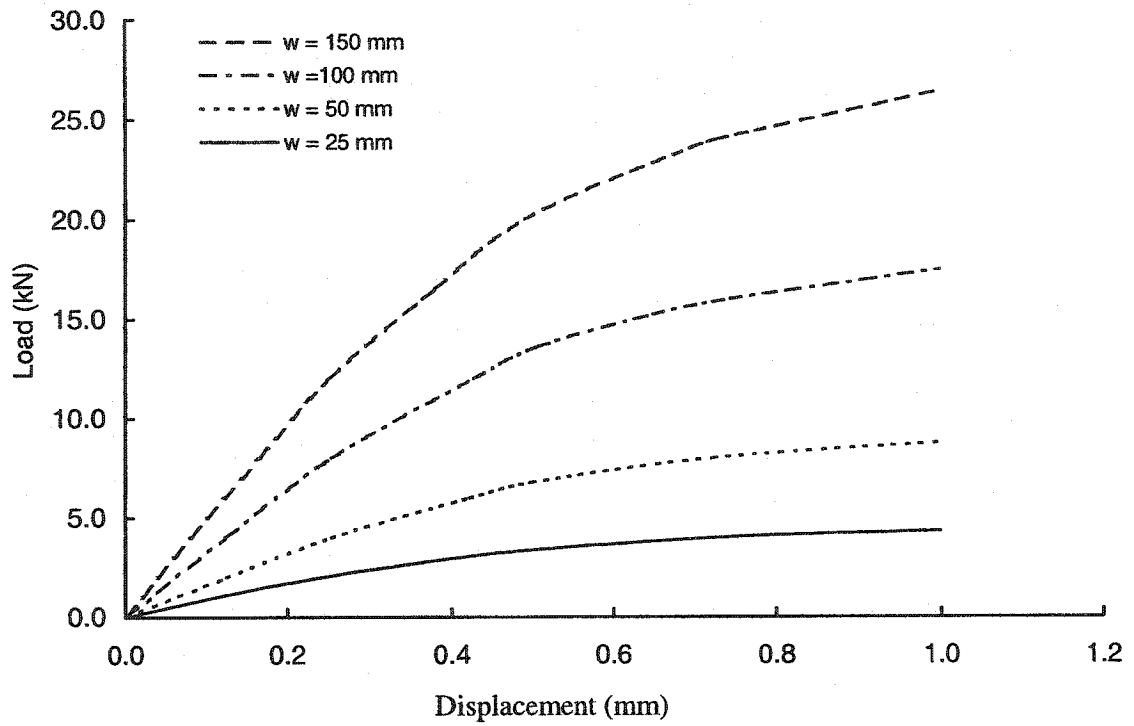


Figure 7-15 Load-displacement for push-apart models

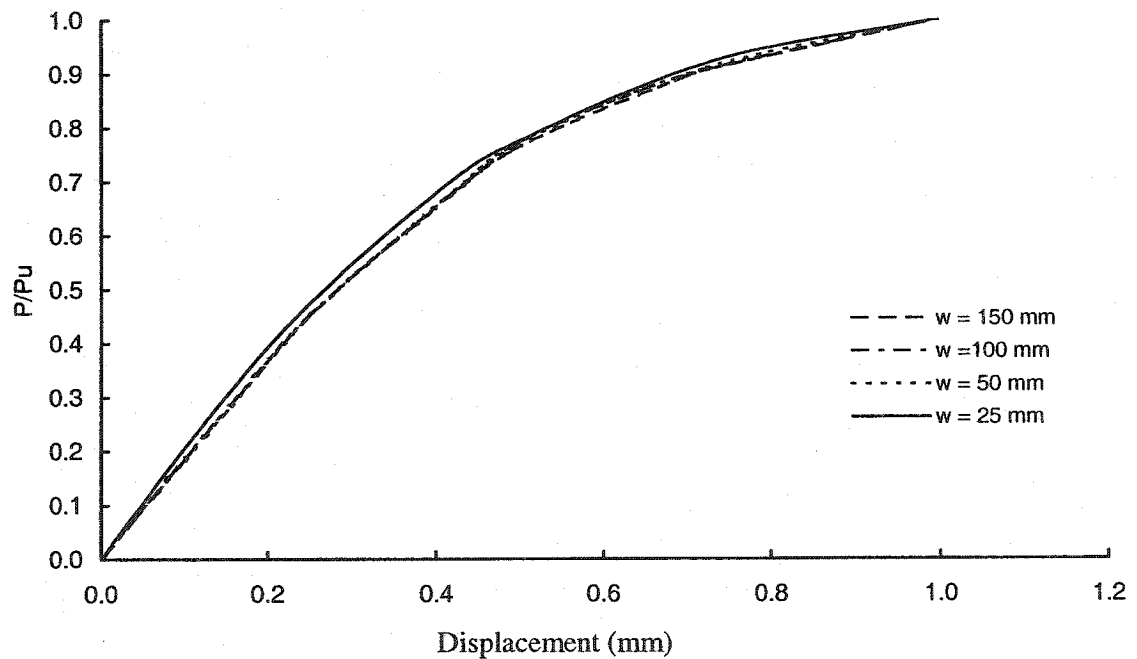


Figure 7-16 Normalized load-displacement response for push-apart models

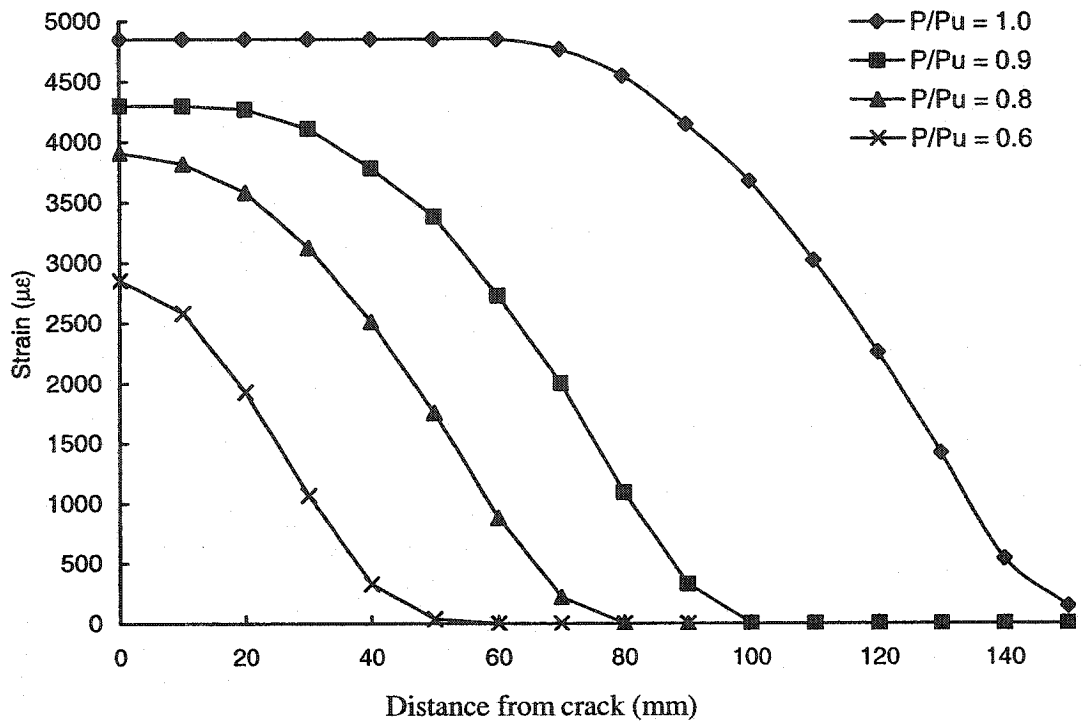


Figure 7-17 Strain distribution for push-apart models with FRP width of 25 mm

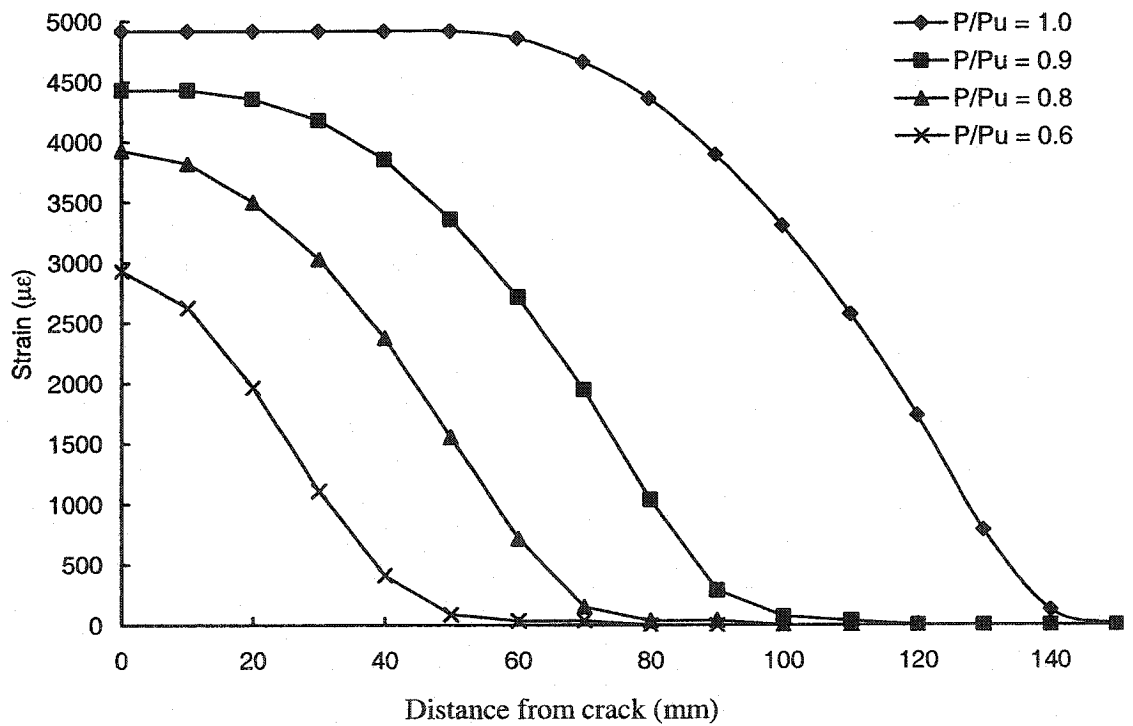
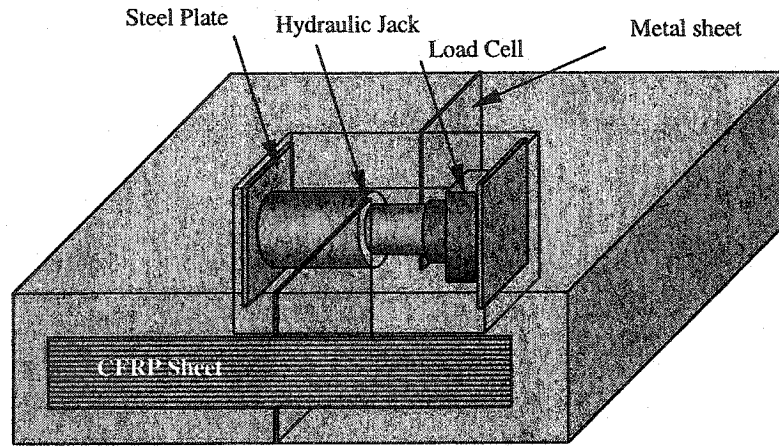
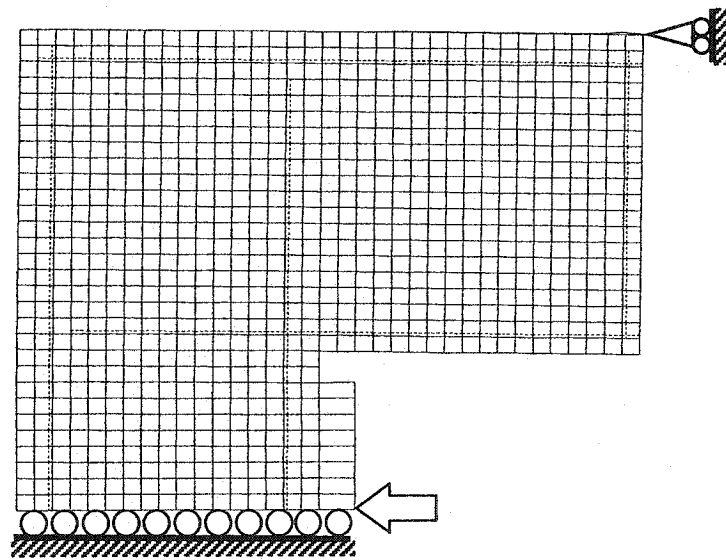


Figure 7-18 Strain distribution for push-apart models with FRP width of 150 mm



(a) Specimen details and load setup



(b) Mesh, deformed shape, loading, and boundary conditions

Figure 7-19 Modified push-apart test

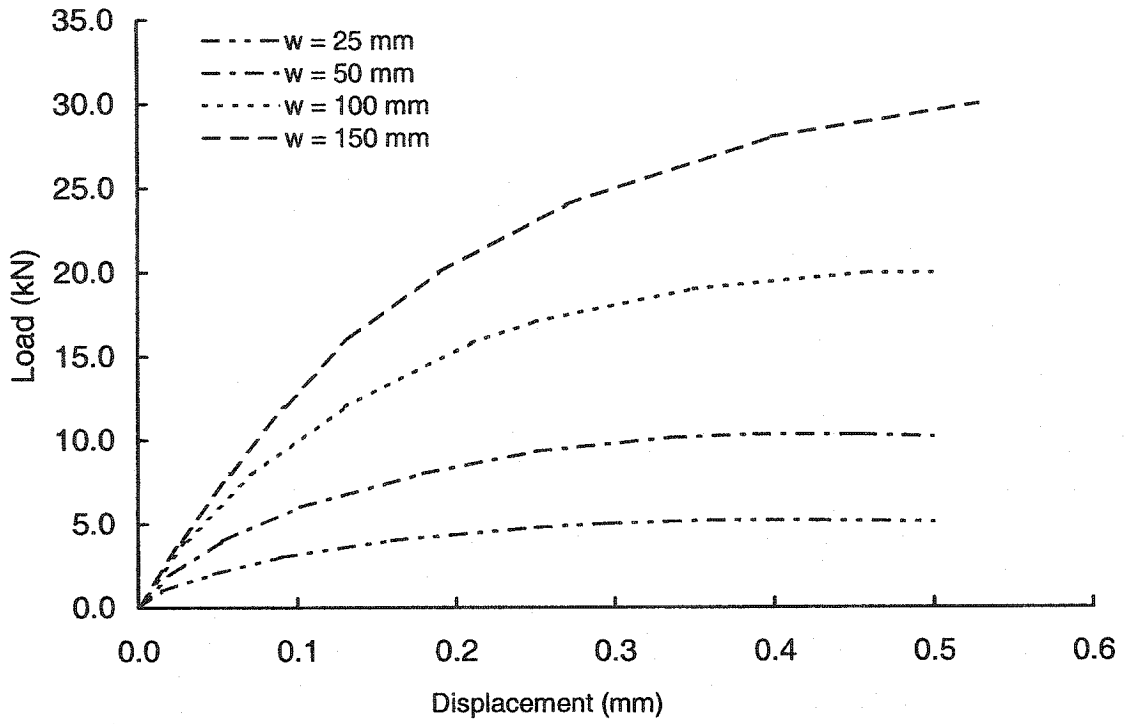


Figure 7-20 Load-displacement response for models with $L = 150$ mm

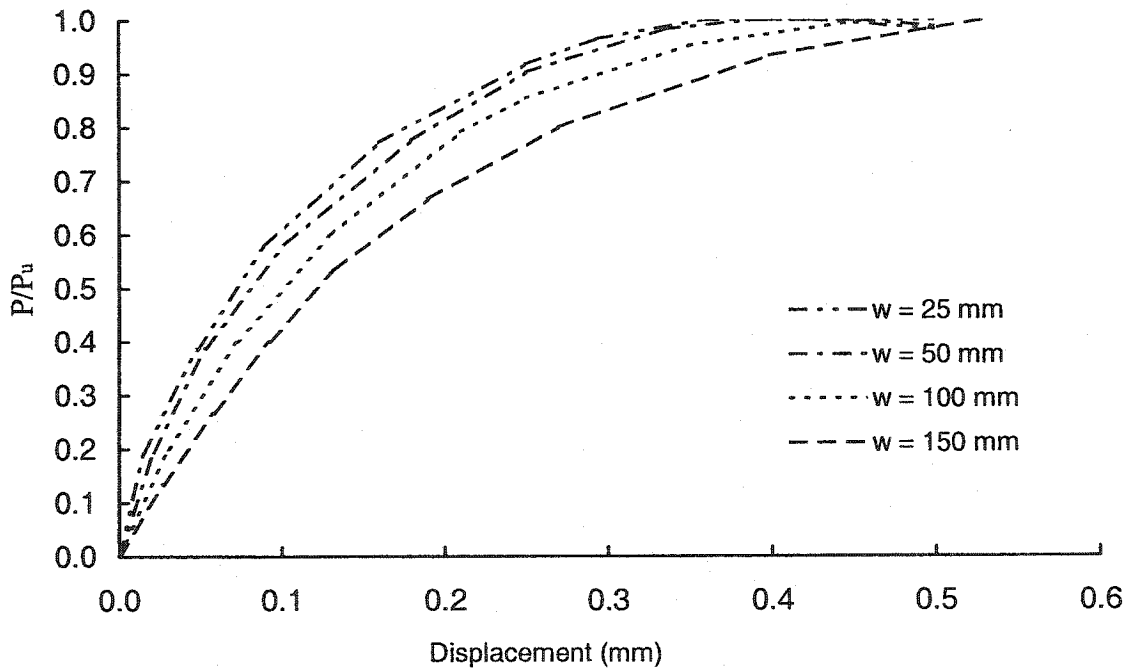


Figure 7-21 Normalized load-displacement response for models with $L = 150$ mm

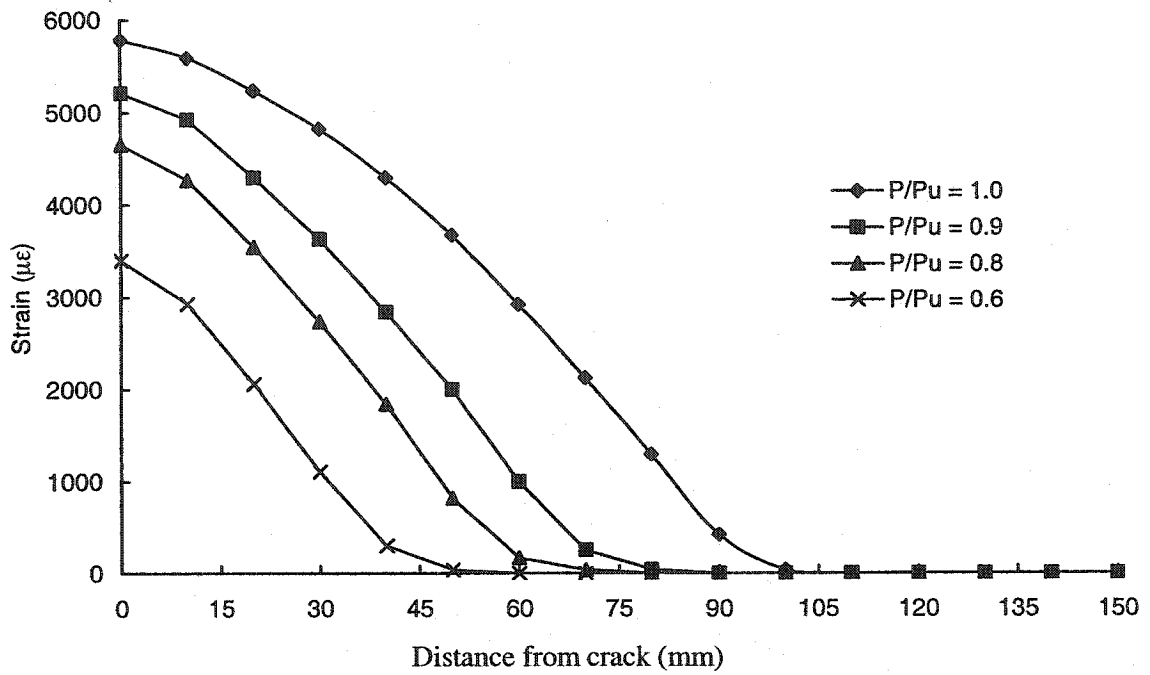


Figure 7-22 Strain distribution for modified push-apart models, $w = 25$ mm

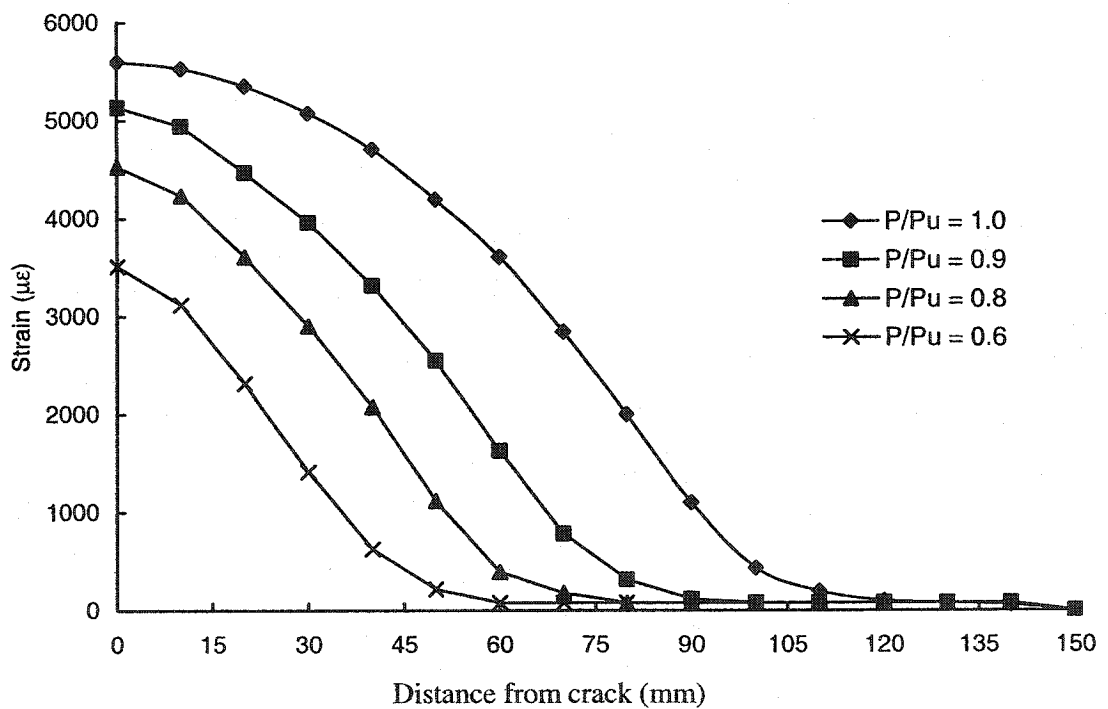


Figure 7-23 Strain distribution for modified push-apart models, $w = 150$ mm

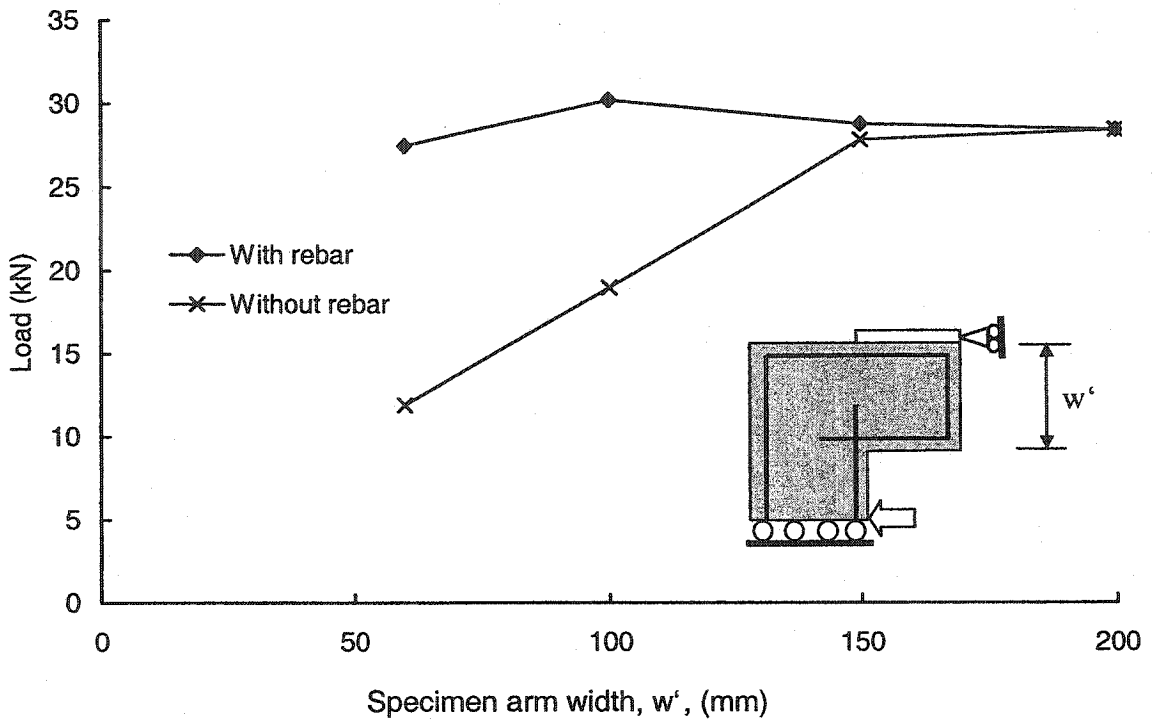


Figure 7-24 Load-displacement, modified push-apart tests, various arm widths

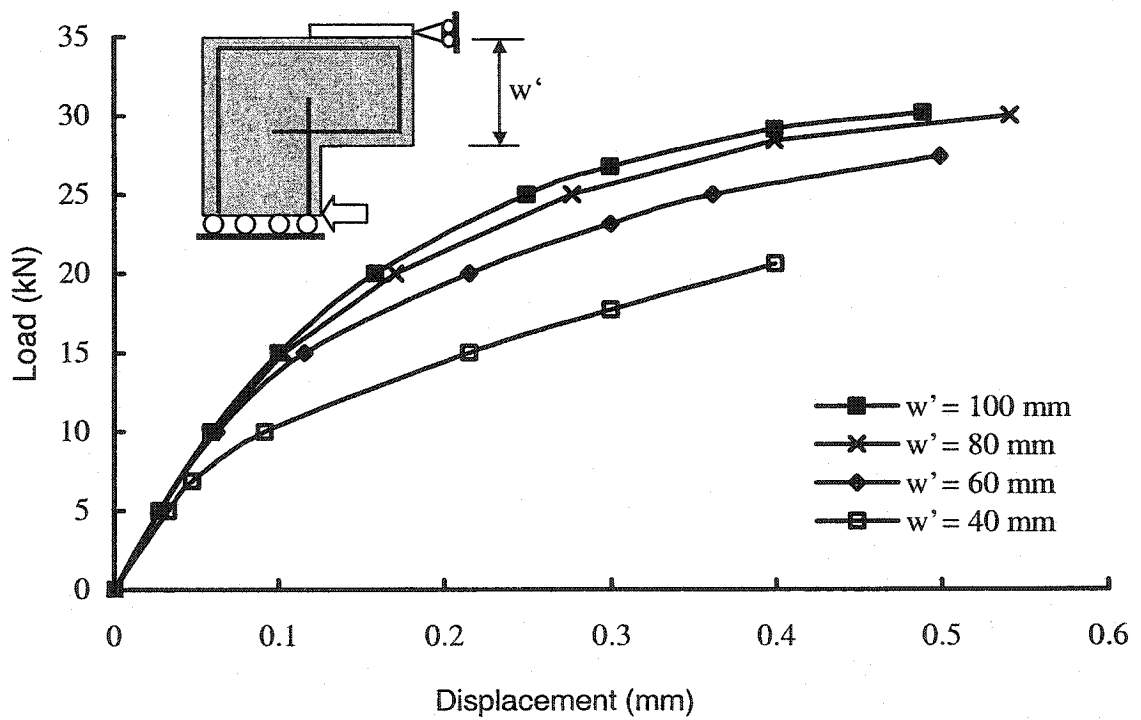


Figure 7-25 Load-displacement behaviour for modified push-apart with arm widths ranging from 40 to 100 mm

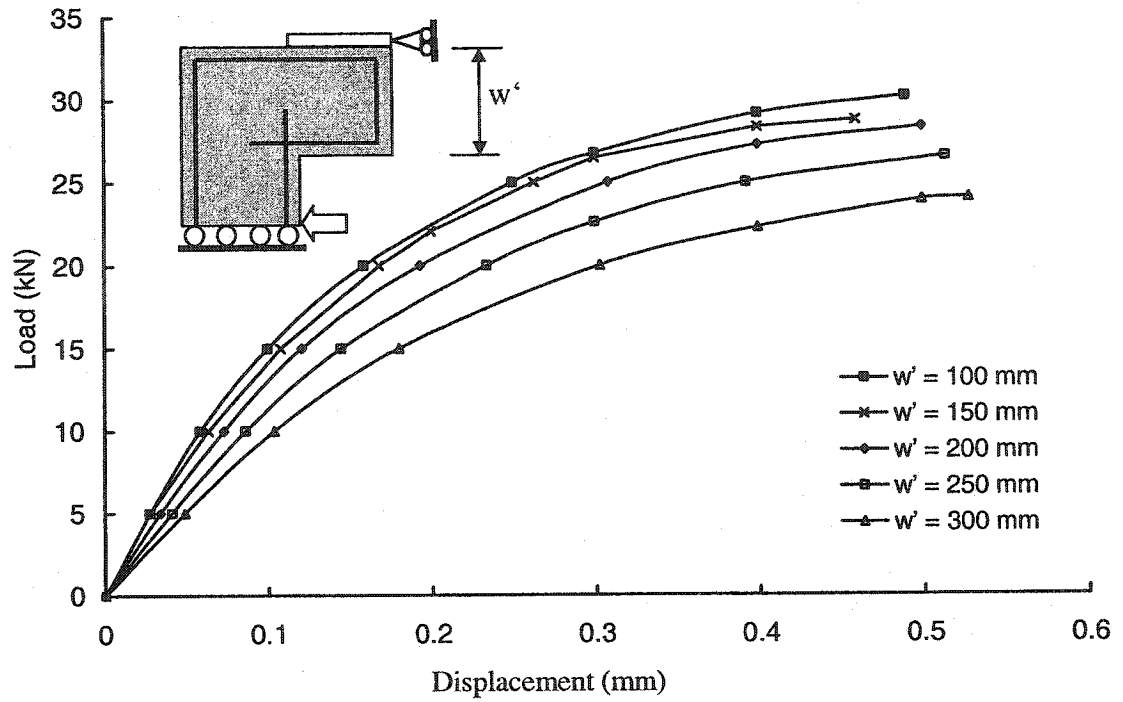


Figure 7-26 Load-displacement behaviour for modified push-apart with arm widths ranging from 100 to 300 mm

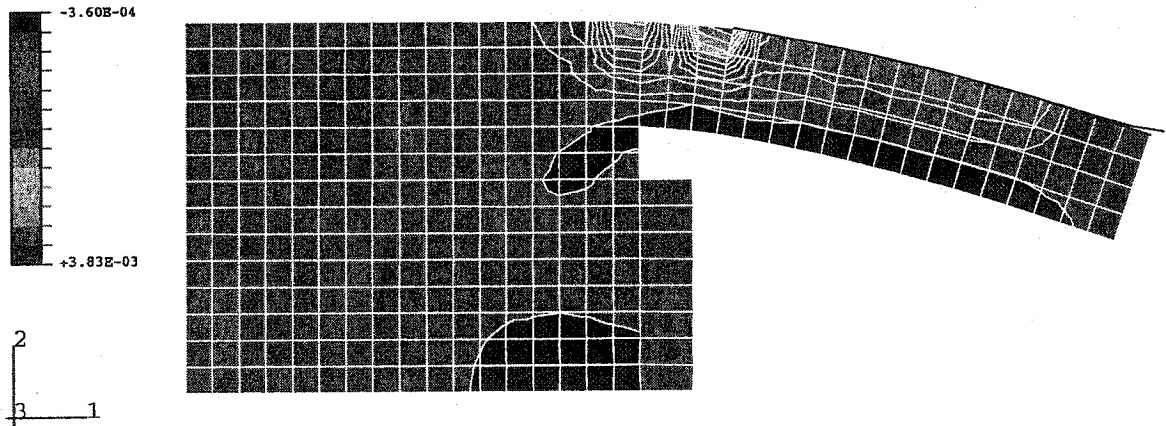


Figure 7-27 Strain distribution in load direction for modified push-part model with 40 mm arm width

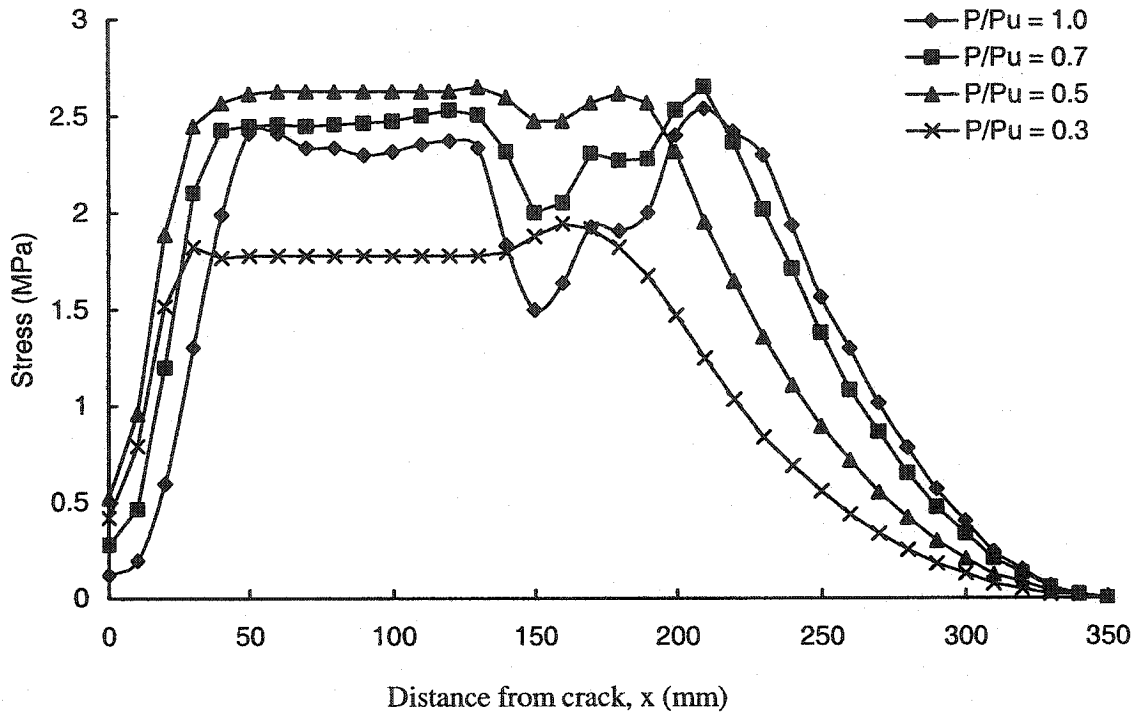


Figure 7-28 Stress distribution along the concrete arm for modified push-part model with 40 mm arm width

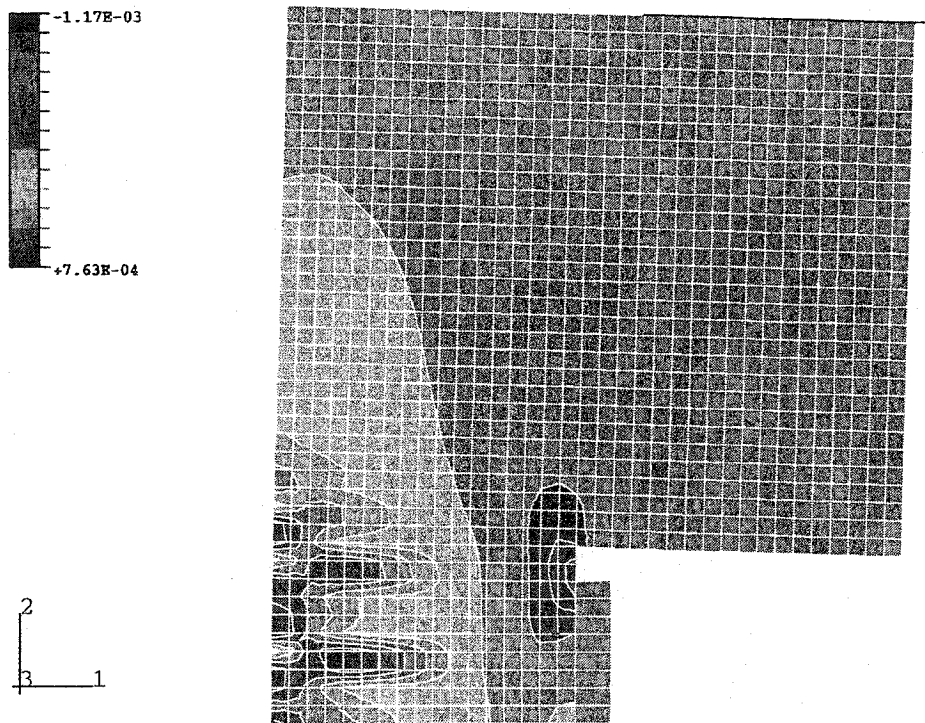


Figure 7-29 Strain distribution in perpendicular direction to loading for modified push-apart model with 300 mm arm width

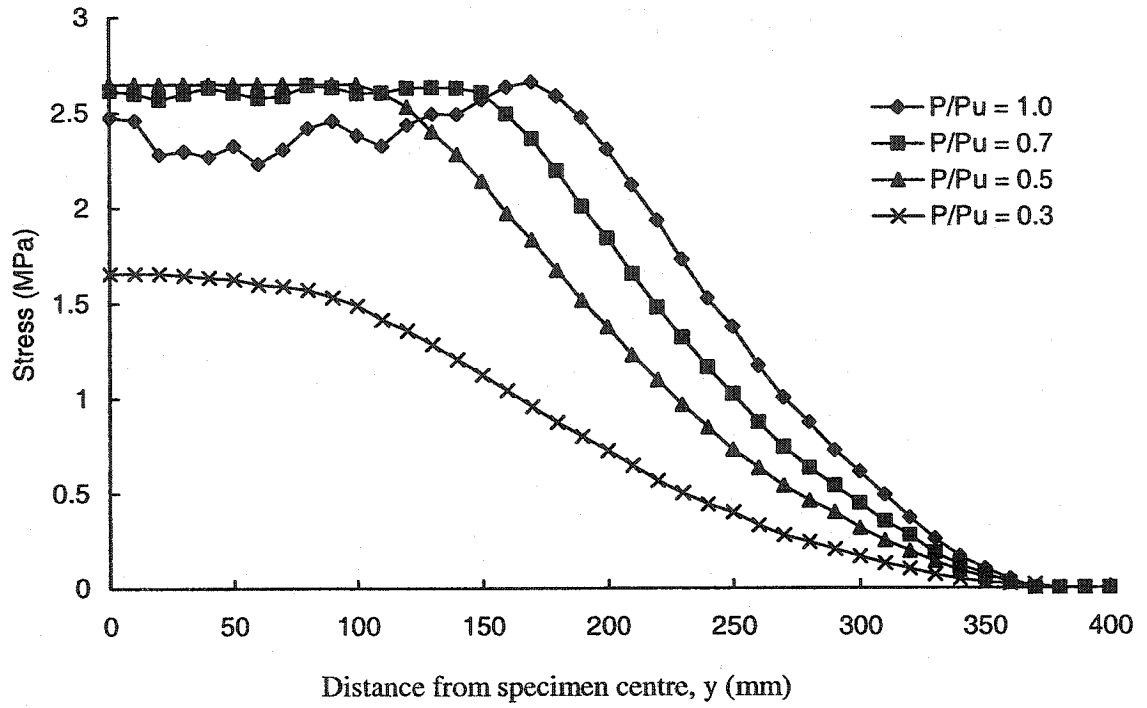


Figure 7-30 Stress distribution across outer concrete for modified push-part model with 300 mm arm width

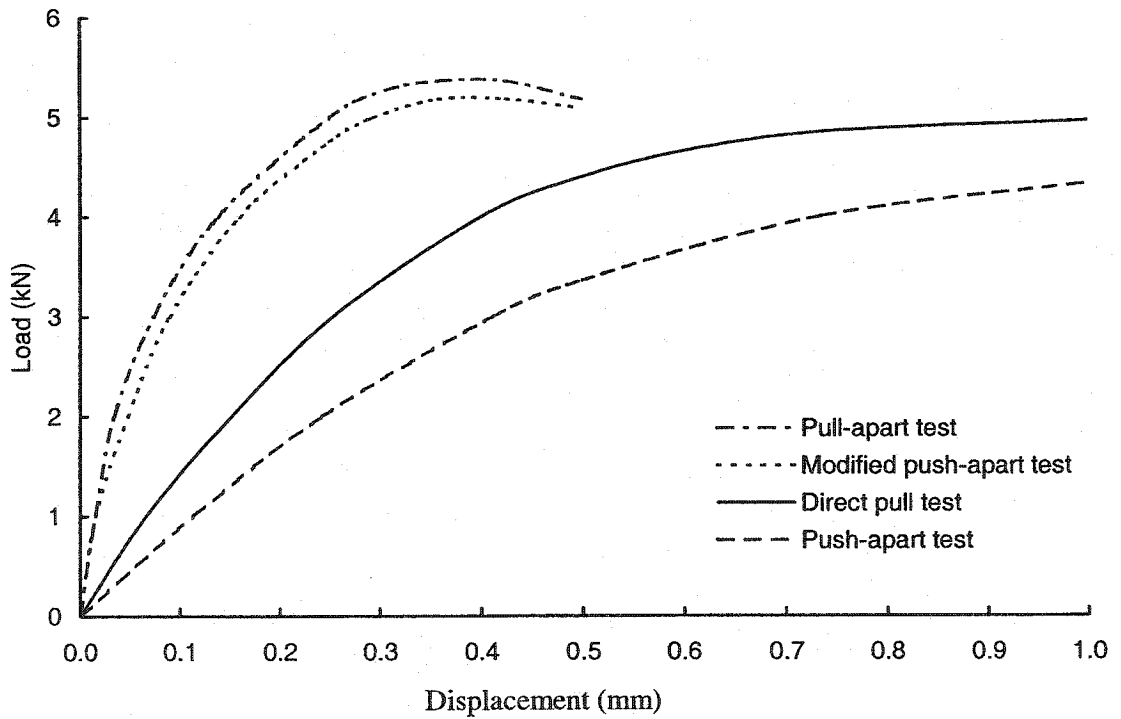


Figure 7-31 Load-displacement for all bond tests, w = 25 mm

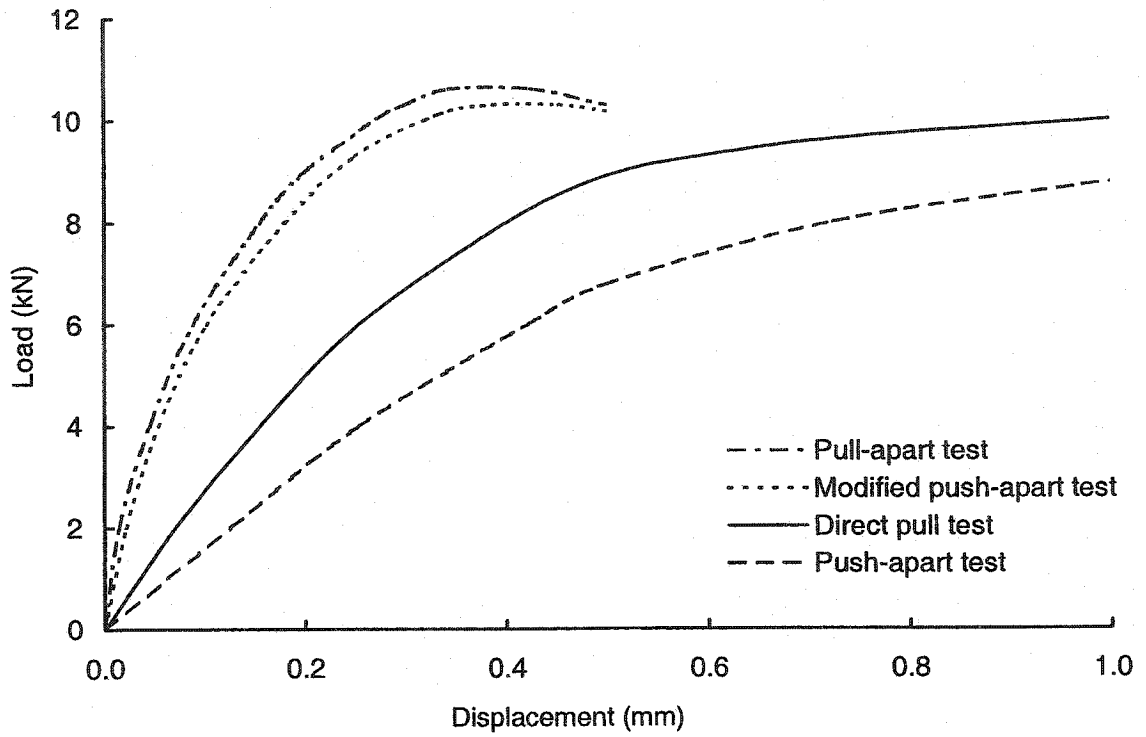


Figure 7-32 Load-displacement for all bond tests, $w = 50$ mm

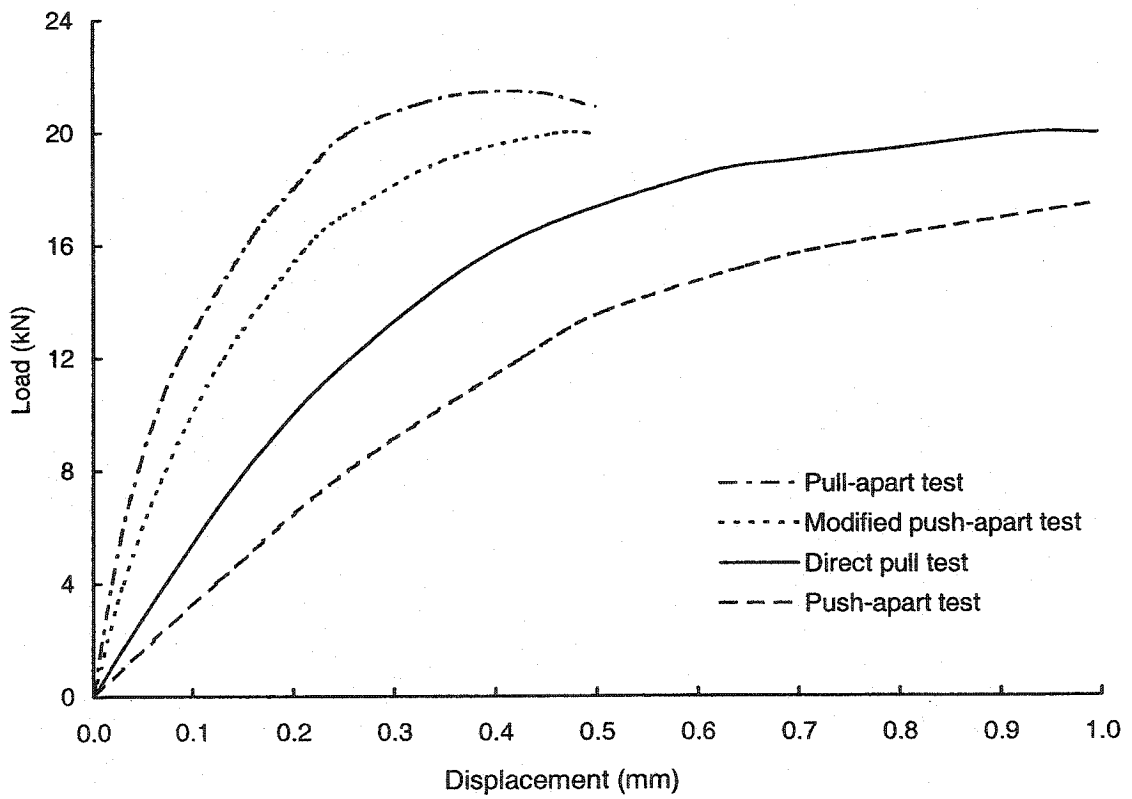


Figure 7-33 Load-displacement for all bond tests, $w = 100$ mm

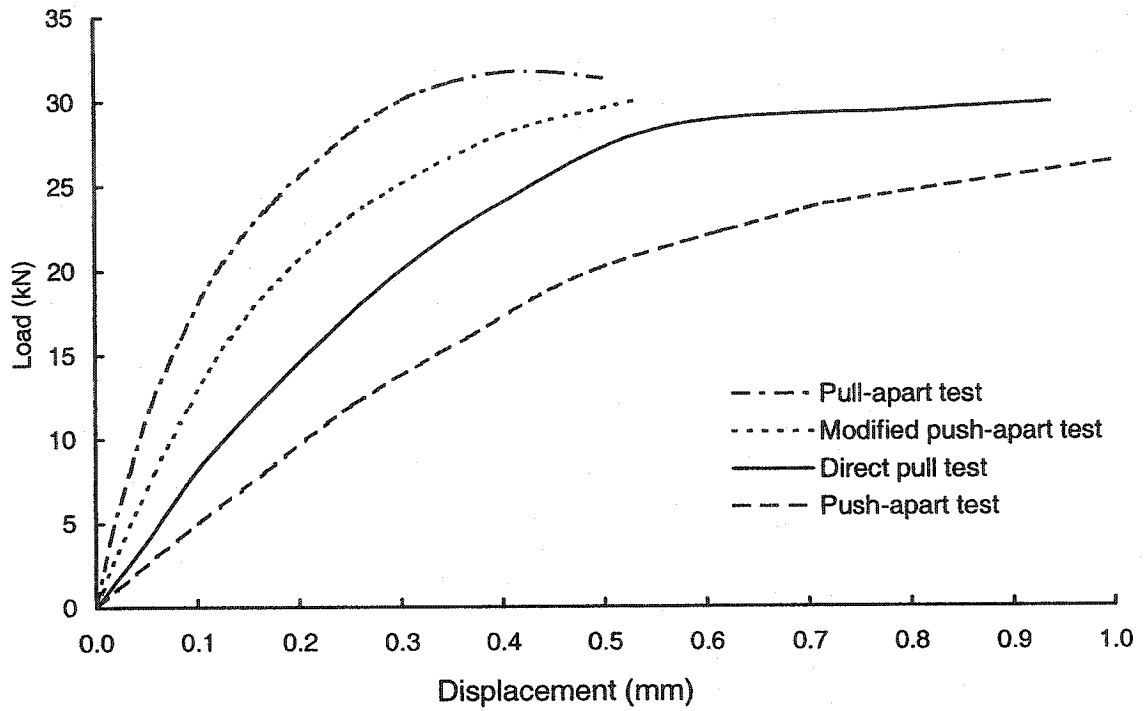


Figure 7-34 Load-displacement for all bond tests, $w = 150$ mm

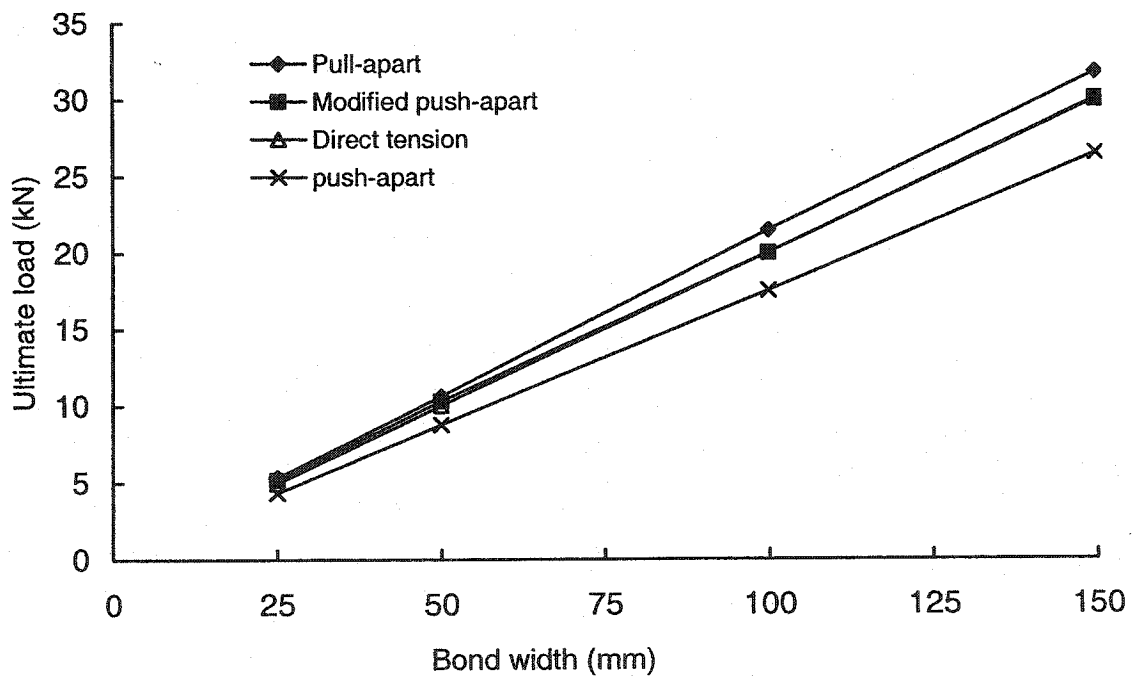


Figure 7-35 Ultimate load vs. bond width for $L = 150$ mm

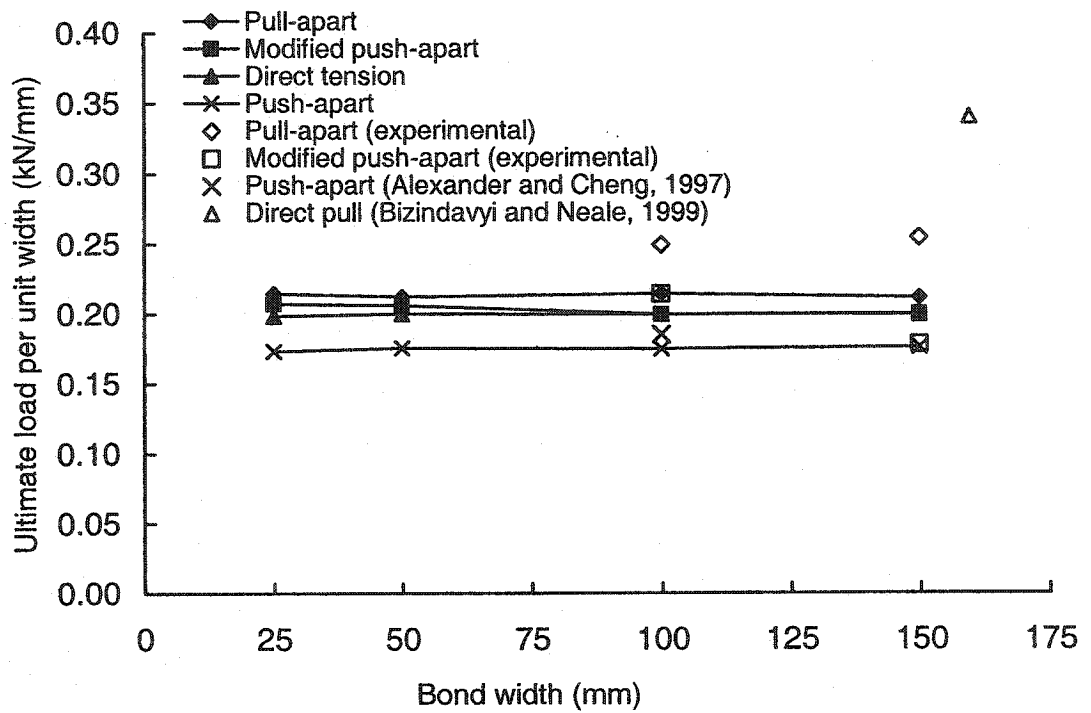


Figure 7-36 Ultimate load per width vs. bond width for L = 150 mm

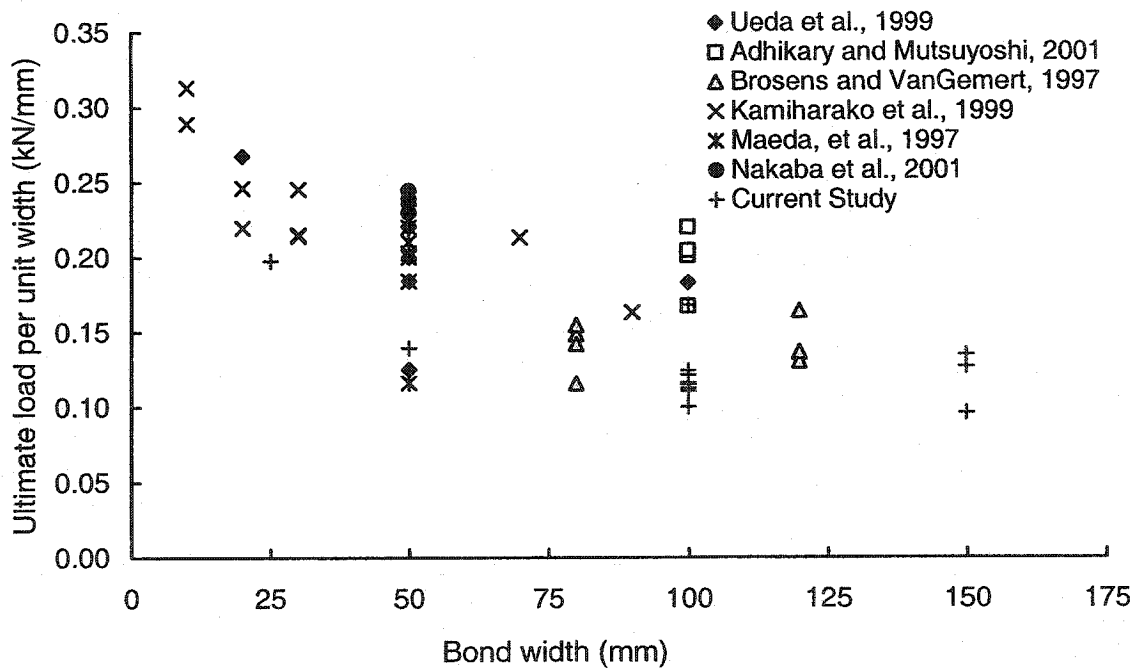


Figure 7-37 Ultimate load per width vs. bond width, pull-apart tests

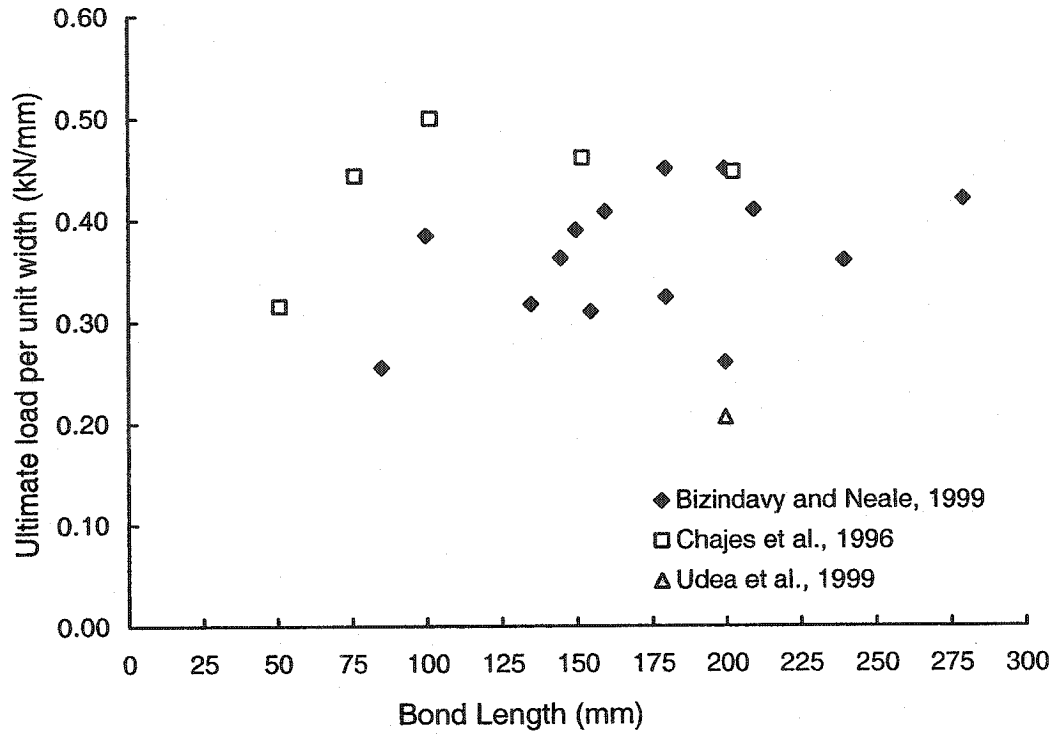


Figure 7-38 Ultimate load per width vs. bond length, direct pull tests

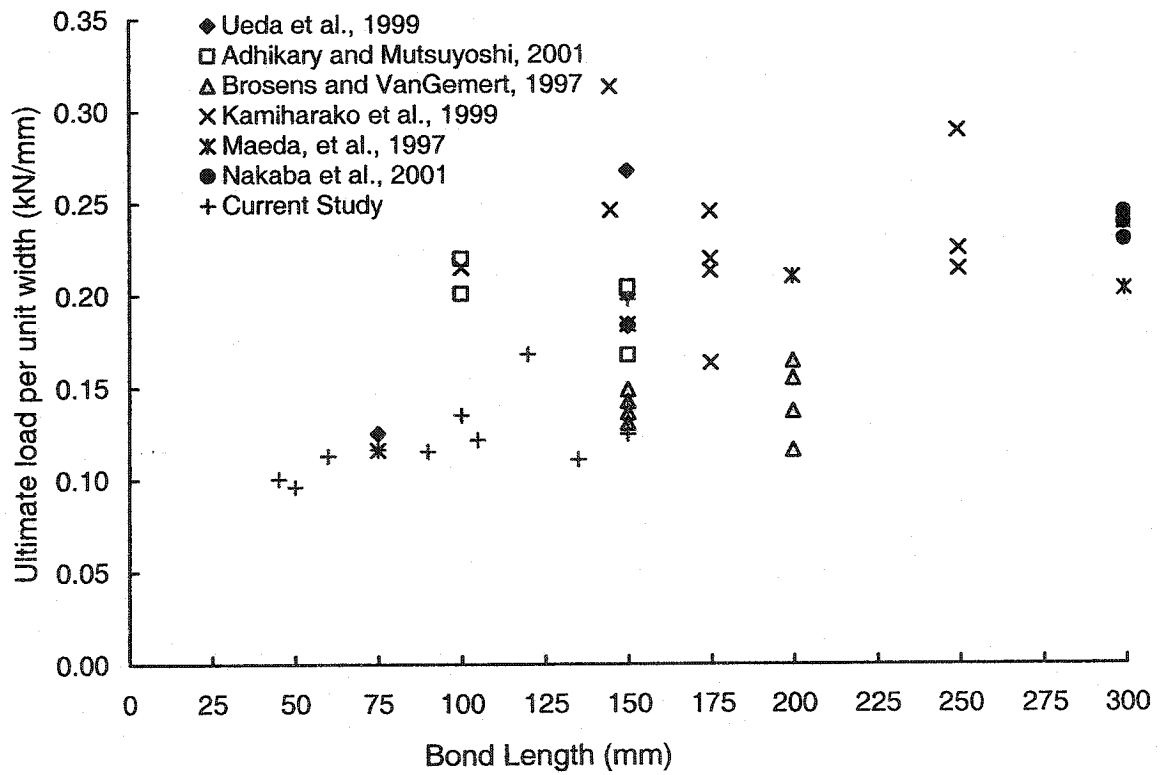


Figure 7-39 Ultimate load per width vs. bond length, pull-apart tests

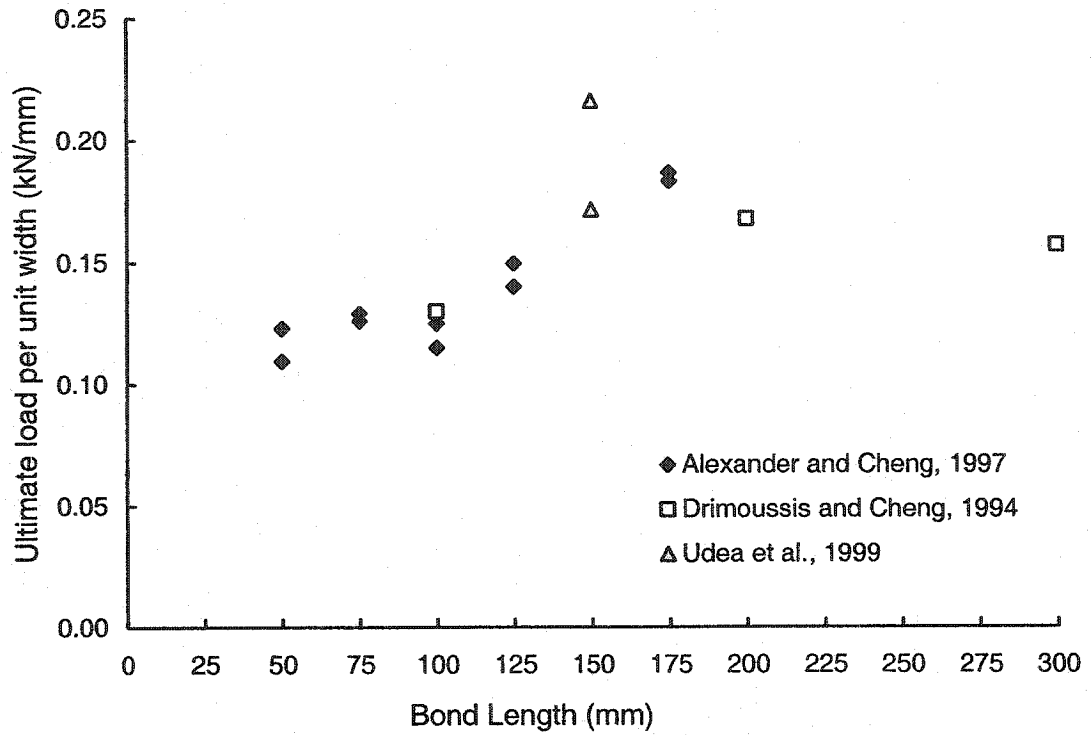


Figure 7-40 Ultimate load per width vs. bond length, push-apart tests

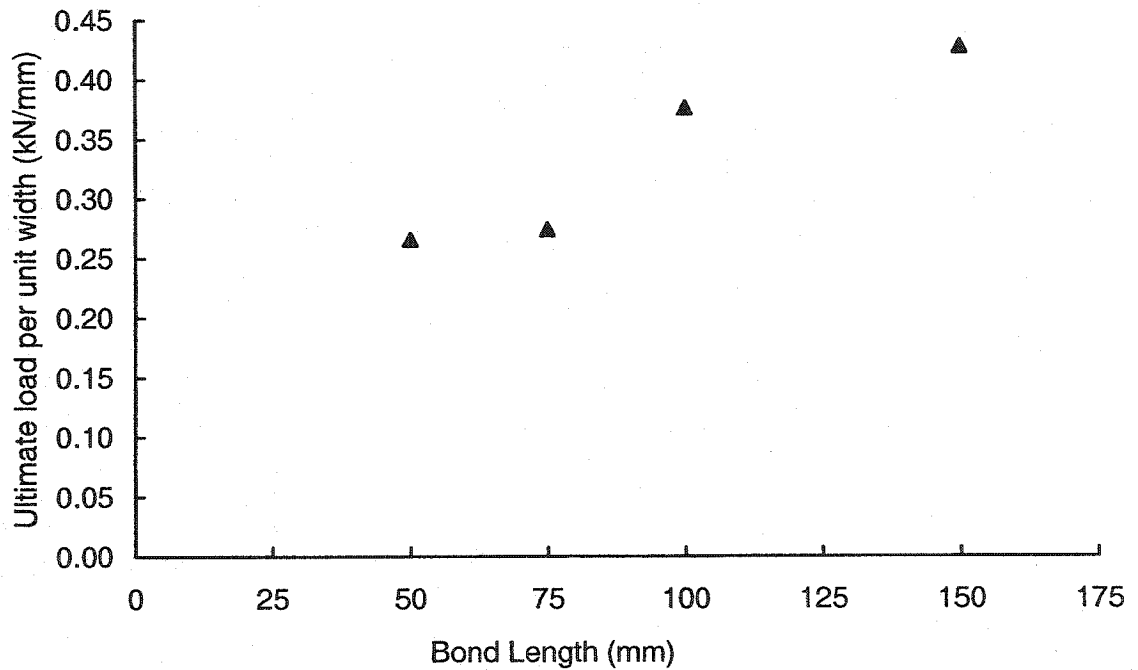


Figure 7-41 Ultimate load per width vs. bond length, modified push-apart test

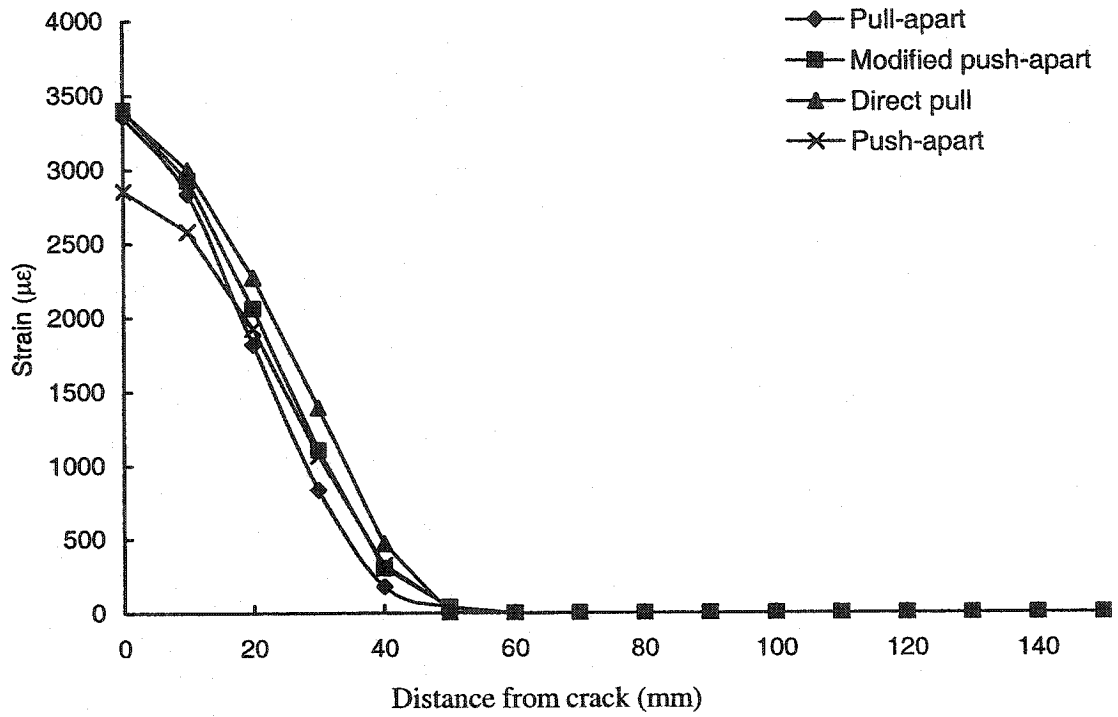


Figure 7-42 Strain distribution for models with FRP width of 25 mm at 0.6 P_u

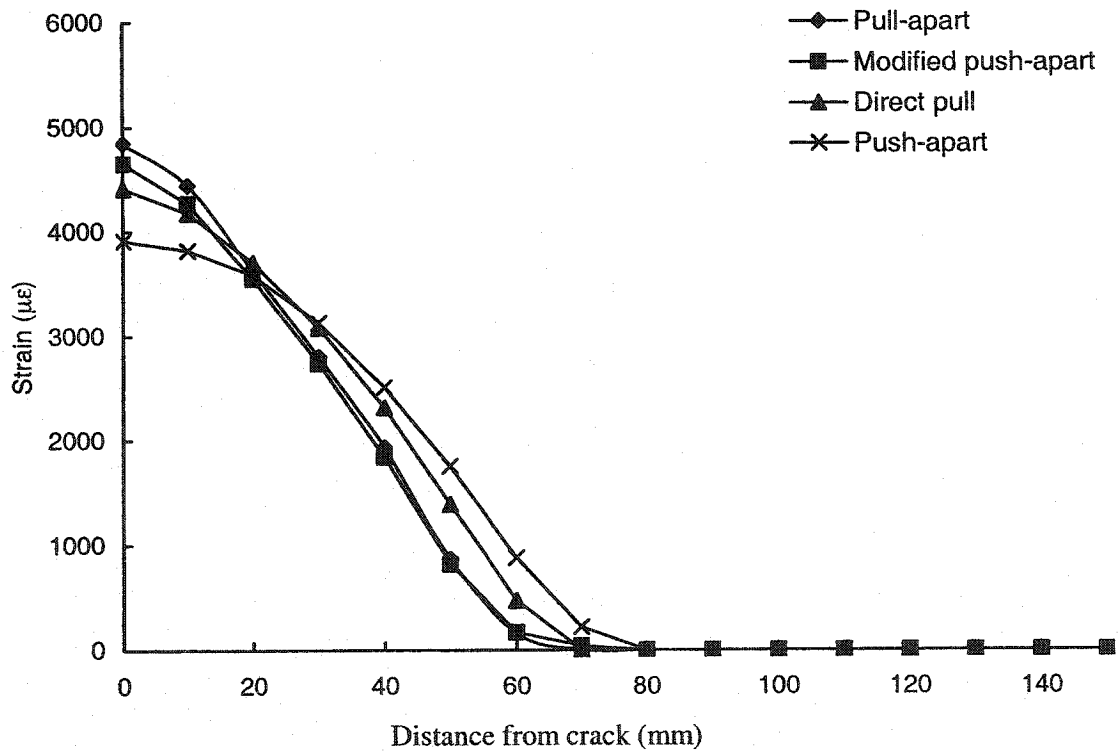


Figure 7-43 Strain distribution for models with FRP width of 25 mm at 0.8 P_u

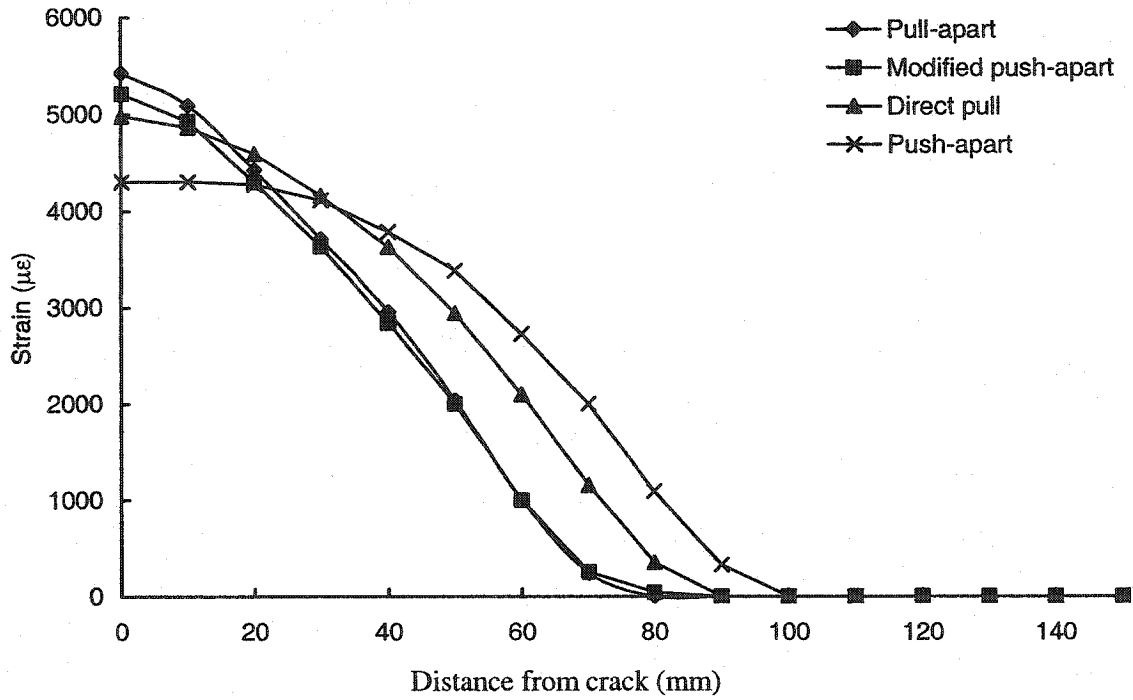


Figure 7-44 Strain distribution for models with FRP width of 25 mm at 0.9 P_u

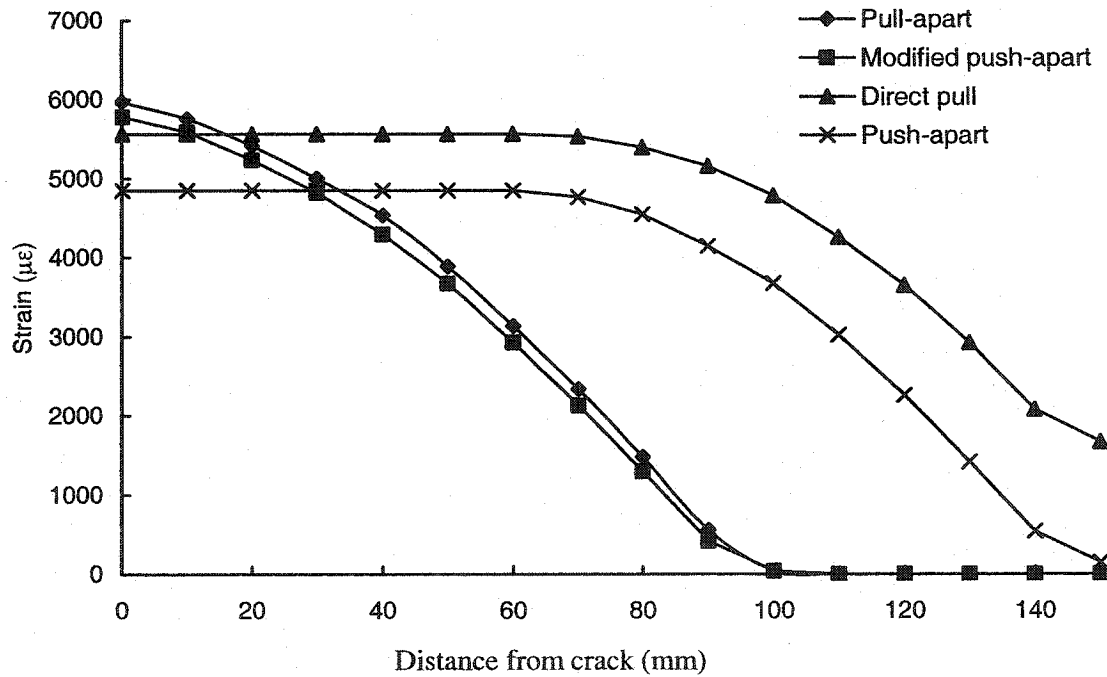


Figure 7-45 Strain distribution for models with $w = 25$ mm at ultimate load

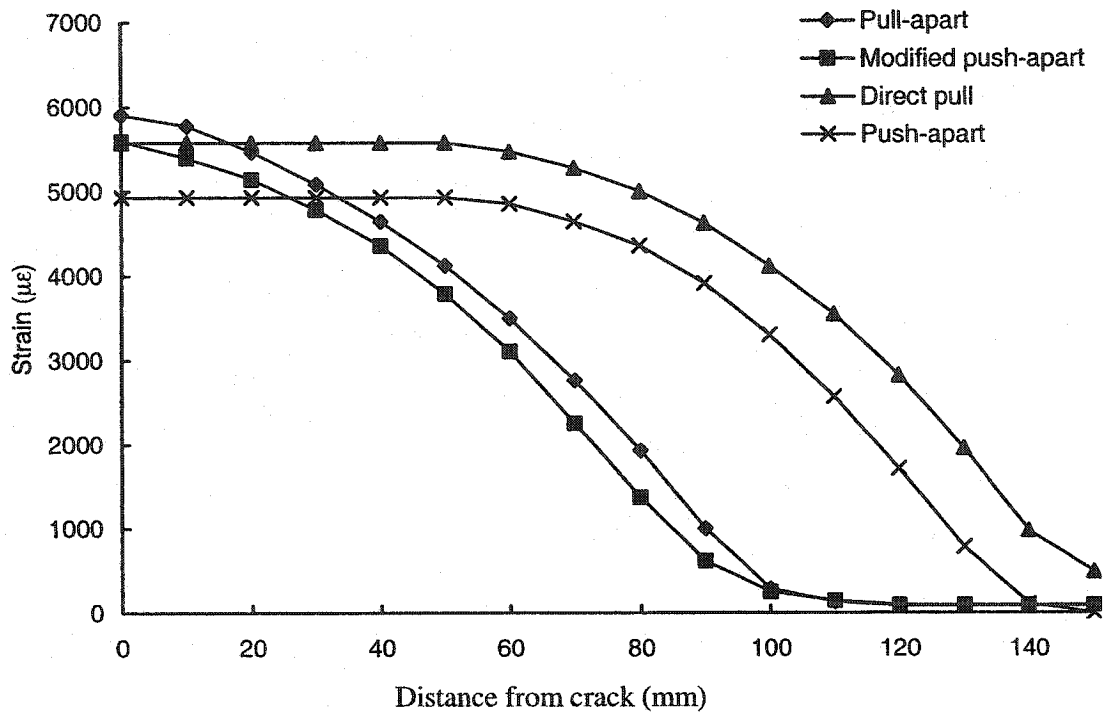


Figure 7-46 Strain distribution for models with $w = 150$ mm at ultimate load

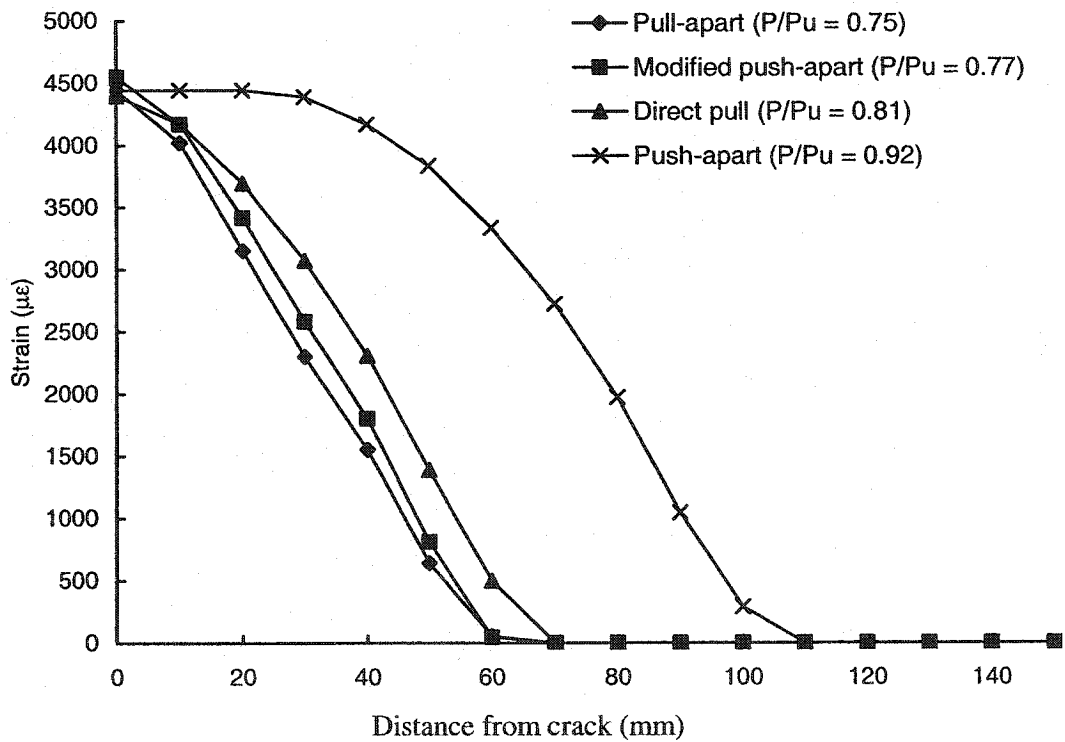


Figure 7-47 Strain distribution for models with FRP width of 25 mm at 4 kN

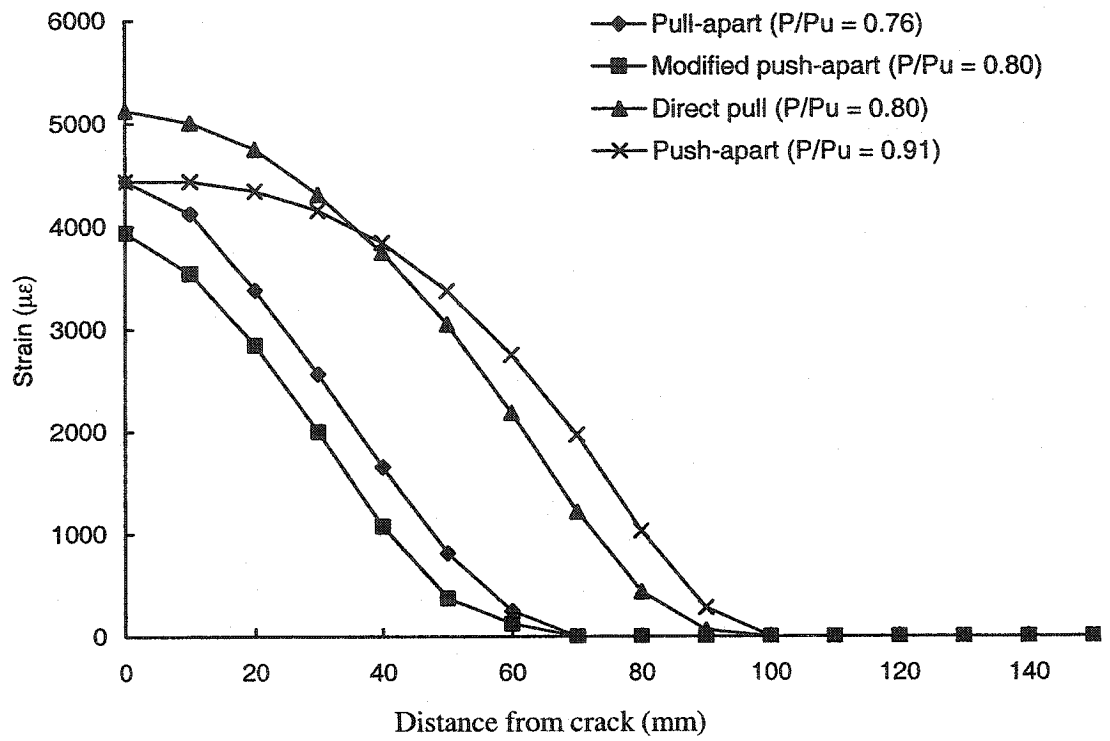


Figure 7-48 Strain distribution for models with FRP width of 150 mm at 24 kN

8. FRP SHEET BOND MODEL

8.1. Introduction and Overview

Since FRP materials are non-corrosive, non-magnetic, and generally resistant to chemicals, they are an excellent option for external reinforcement. Strengthening with externally bonded FRP sheets has been shown to be applicable to many types of reinforced concrete (RC) structural members such as columns, beams, slabs, and walls. This method has also been used to strengthen RC chimneys, tunnels, and silos. External FRP reinforcement is employed for flexural and shear strengthening as well as to improve confinement and ductility of compression members. In all cases, however, both the fibres as well as the concrete substrate in the direction of the fibres are all subjected to tensile strain.

Despite the diversity of reinforcing materials used, the different concrete strengths investigated, and the different specimen geometries and loading employed, there is a rather general agreement on the main factors affecting the capacity of the bond between the FRP sheets and concrete. These factors are the FRP sheet bond length, width, and stiffness, and the concrete tensile strength and width.

One of the difficulties with verifying the bond strength of FRP sheets is the various bond test methods used, which generally produce different results. These test methods were presented in Section 2.6 and analyzed in Chapter 7. The analysis of the test methods proposed a simple linear relationship between the results of these methods. Analytical studies such as this and their experimental verification are necessary for the development of sound design guidelines. These linear relationships will not be used in the regression analysis in this study.

8.2. Design Implementations of the Analytical Model

Limit state design demands that the axial force capacity, flexural capacity, and shear capacity of members in a structure are not exceeded. Evaluating the contribution

of externally bonded FRP sheets based on their tensile strength and using guidelines similar to those for conventional steel reinforcement in concrete members is insufficient. The failure modes associated with externally bonded FRP sheets to concrete, detailed in Section 2.5, need to be accounted for in the design. The following subsections will deal with implementation of the debonding type failure mode in both flexure and shear. Proposed equations to predict the average bond strength and the effective bond length may be used to quantify the capacity available of the FRP sheets at delamination.

Once shear forces develop inclined cracks in the concrete, high tensile stresses are developed in the portions of FRP sheet that bridge these cracks. The tensile stresses in vertically oriented FRP sheets are a result of the separation of rigid bodies of concrete on either side of the crack. These tensile stresses must be transferred to the concrete on each side of the crack by interfacial bond stresses. If this interfacial bond is compromised before rupture of the FRP sheet, a debonding failure occurs. Similarly, the use of FRP in direct flexural application is obvious.

In order to address the debonding failure mode in shear design, the bond characteristics of FRP sheets with concrete is considered including concrete strength effect and bonded surface conditions. The use of shear bond tests to characterize the bond mechanism for shear strengthening is reasonable considering the mechanism of force transfer in a shear strengthening configuration. The proposed equations used to predict the average bond strength and effective bond length may also be used to quantify the ultimate capacity of FRP sheets at debonding.

A design approach based on the tensile strength of the FRP sheet assumes perfect bond with the concrete surface. In order to assure the previous conditions, it is necessary to provide a development length, L_d , calculated from:

$$L_d = \frac{\sigma_f \cdot n \cdot t_f}{\tau_f} \quad (8-1)$$

where σ_f is the maximum stress in the FRP sheet, n is the number of plies, t_f is the thickness of one FRP sheet, and τ_f is the average bond strength. The derivation of equation (8-1) is illustrated in Figure 8-1. This evaluation cannot be applied in the case where there is not enough development length, available physically. A case in point is shear reinforcement, where the depth of the web and the end distances are typically small.

8.3. Design Model

The parametric study in Chapter 6 illustrated the relationship between the ultimate load and the main parameters affecting the bond behaviour. The main parameters directly proportionate to the ultimate load are the bond length, width, and stiffness of the FRP sheet, and the width available and strength of concrete. There are limiting values for all parameters beyond which they no longer contribute to the bond capacity. In the following two equations are proposed. First the effective bond length, then the ultimate bond capacity is defined.

8.3.1. Effective Bond Length Model

The expression predicting the effective bond length proposed by Maeda et al. (1997), which is used in the CSA S806-02 (2002) takes the form:

$$L_e = \frac{25350}{(t_p \cdot E_p)^{0.58}} \quad (8-2)$$

in which, E_p and t_p are respectively tensile modulus of elasticity in MPa and thickness in mm of the FRP sheet. Equation (8-2) shows that $E_p t_p$, which represents the FRP sheet stiffness, is inversely proportional to the effective bond length. This is contradictory to the conclusion derived from the parametric study presented in Section 6.2, which showed that the effective bond length increases with an increase in the FRP sheet stiffness. Chen and Teng (2001) compared five tests with predicted effective bond lengths, and also found that the expression proposed by Maeda et al. (1997) predicted the wrong trend for the effect of $E_p t_p$ on the effective bond length.

Neubauer and Rostásy (1999) and Chen and Teng (2001) proposed expressions based on fracture mechanics similar to that developed by Holzenkämpfer (1994):

$$L_e = \sqrt{\frac{E_p t_p}{4f_{ct}}} \quad (\text{Holzenkämpfer, 1994}) \quad (8-3)$$

in which, f_{ct} is the concrete tensile strength. Equation (8-3) lets the effective bond length be proportional to the FRP sheet stiffness and inversely proportional to the concrete strength. This also does not agree with the conclusion from the parametric study that showed the effective bond length increasing as the concrete strength increases. The expression proposed by Chen and Teng (2001) takes the form:

$$L_e = \sqrt{\frac{E_p t_p}{\sqrt{f'_c}}} \quad (8-4)$$

Figure 8-2 shows the effective length plotted against the FRP sheet stiffness, $E_p t_p$, for results from the parametric study detailed in Section 6.2. The regression line for the data in the figure shows a relationship between the effective bond length and the stiffness to the power of 0.39. Plotting the effective bond length against the square root of the FRP sheet stiffness for simplicity resulted in an almost linear relationship as compared to the linear regression line of the data points, as shown in Figure 8-3.

Figure 8-4 shows the effective bond length plotted against the FRP sheet bond width for results from the parametric study detailed in Section 6.2. The power regression line for the data in the figure shows a relationship between the effective bond length and the bond width to the power of 0.14. Plotting the effective bond length against the bond width to the power of 0.14 shows an almost linear relationship, as shown in Figure 8-5.

Based on the previous discussion and the trends derived from the parametric study, an expression predicting the effective bond length is proposed:

$$L_e = 0.25w^{0.14} \sqrt{E_p t_p} \quad (\text{mm}) \quad (8-5)$$

in which E_p , t_p , and w are the FRP sheet modulus of elasticity in MPa, thickness in mm, and width in mm, respectively.

The proposed expression (8-5) predicting the effective bond length is compared with the experimentally evaluated effective bond lengths by Bizindavyi and Neale (1999), Brosens and VanGermert (1997), and the current study. The expressions (8-2) and (8-4) proposed by Maeda et al. (1997) and Chen and Teng (2001), respectively, are also used to evaluate the accuracy of the expression proposed in this study relative to other expressions from the literature. Figure 8-6 shows the effective bond length from test results plotted against the predicted values using Equation (8-2), (8-4), and (8-5). The figure shows that the expression proposed in this study, Equation (8-5), is more accurate and reliable in predicting the effective bond length, where the test to predicted values are gathered around the 45° line. The figure also clearly shows that the proposed expression by Maeda et al. (1997) predicts the wrong trend.

Table 8-1 shows the experimental test values used in the comparison. The table also shows the test to predicted ratio of the effective bond length and the values predicted by the proposed expressions. Table 8-2 shows the mean, coefficient of variation (COV), and minimum and maximum values of the test to predicted effective bond length ratios. The table shows that the expression proposed in the current study has the closest mean value to unity and the smallest COV and range between the minimum and maximum values, which is an indication of the better accuracy of the expression proposed in this study.

8.3.2. Bond Capacity Model

The bond force is used as a measure of strength rather than the bond stress because the bond stress is usually expressed as an average value at failure, when in fact bond stress varies significantly over the length of the FRP sheet as discussed in Section 4.3.2. Since the bond stress is a structural, rather than material property, the bond force provides a better measure of member response than bond stress.

To improve the accuracy of the analysis, test results from various studies are used representing the different bond test methods. The results used for the modified push-apart method are those from this study, while the results from Udea et al. (1999), Alexander and Cheng (1997), and Drimoussis and Cheng (1994) are used for the push-apart method. The results used for the direct pull method are those by Bizindavy and Neale (1999), Udea et al. (1999), Taljsten (1997), and Chajes et al. (1996), while the results from Adhikary and Mutsuyoshi, (2001), Kamiharako et al. (1999), Udea et al. (1999), Brosens and VanGemert (1997), Horiguchi and Saeki (1997), Maeda et al. (1997), and the current study are used for the pull-apart method.

Figure 8-7 shows the concrete compressive strength, f_c' , plotted against the ultimate bond capacity. The figure shows that in the numerical model, f_c' had no significant effect on the ultimate bond capacity in the debonding type failure. The literature indicates that f_c' is directly proportional to the bond capacity if the failure was shear in the concrete below the FRP sheet.

The concrete width, w_c , represents the distance between FRP strips in shear strengthening or beam width in flexure strengthening. The numerical analysis in Section 6.3.2 showed that the concrete specimen width, w_c , is directly proportional to the bond capacity of the bonded FRP sheet. In order to simplify the equation predicting the ultimate bond capacity, w_c effect was disregarded.

Using the results of the parametric study in Section 6.3.1, Figure 8-8 shows the ultimate load plotted against the FRP sheet bond width. The figure shows that there is an almost bilinear relationship between the ultimate load and the bond width with a change in trend at 100 mm. Linear regression lines are shown in the figure and the relationship was approximated as linear.

Figure 8-9 shows the ultimate load plotted against the FRP sheet bond length for the results from Section 6.2. The figure shows that the ultimate bond capacity increases

as the bond length increases up to an effective bond length. Linear regression lines are shown in the figure and the relationship was also approximated as linear.

To help reduce the effect of bias in the data and to isolate the effects of bond length, width, stiffness, and concrete width, the first approximation of bond capacity in this study uses the following expression:

$$P_u = r \cdot w L_e \quad (8-6)$$

in which L_e is the smaller of the FRP sheet bond length and the effective bond length calculated from Equation (8-5), and r is a factor analogous to the average bond stress. Figure 8-10 shows the ultimate load plotted against the effective bond area, with the effective bond area being equal to the bond width times the effective bond length calculated from Equation (8-5). The linear trend line of the relationship was $y = 0.0013x + 7.537$, which resulted in the expression:

$$P_u = 0.0013w L_e + 7.5 \quad (8-7)$$

Figure 8-11 shows the ultimate load test to predicted values using Equation (8-7), where the experimental data used were those from this study and from the literature as detailed previously. The figure shows the results scattered around the 45° line.

Figure 8-12 shows the load plotted against the square root of the FRP sheet stiffness. The figure shows that there is an almost linear relationship between the ultimate load and the square root of the FRP sheet stiffness as shown from the proximity of the linear regression lines to the curves.

Using Equation (8-7) as the predicted bond capacity, the next step is to determine the effect of the FRP sheet stiffness. To do this the ratio of the test to predicted ultimate load ratio is plotted against the sheet stiffness per unit effective area, $\sqrt{E_p t_p} / w L_e$, as shown in Figure 8-13. The best fit expression for the ratio of the test to predicted values versus $\sqrt{E_p t_p} / w L_e$, excluding the exceptionally high values, was as follows:

$$\frac{(P_u)_{\text{test}}}{0.0013wL_e} = 1.36 + 636 \frac{\sqrt{E_p t_p}}{wL_e} \quad (8-8)$$

Rewriting and rounding equation (8-8) to include the higher ratio values gives an expression for the bond capacity of FRP sheets bonded to concrete, as follows:

$$P_u = 0.0016w L_e + 0.75\sqrt{E_p t_p} \quad (8-9)$$

where the first term represents the effect of the bond area and the second term represents the effect of the FRP sheet stiffness.

Figure 8-14 shows the ultimate load from test results plotted against those predicted by Equation (8-9). The figure shows the 45° line and a linear regression line that shows the proximity of the predicted values to the test results. Table 8-3 shows the ratio of the test ultimate bond load results to those predicted using Equations (8-7) and (8-9). The table includes the ultimate bond capacity test over predicted ratio mean, coefficient of variation (COV), and the minimum and maximum values for each individual research and also for all the tests combined. The predicted ultimate bond capacity values are more accurate if the mean value of the test to predicted ratio is closer to unity, the lower the COV, and the smaller the difference between the maximum and minimum values. Table 8-3 shows the improvement of Equation (8-9) over (8-7) in 12 out of 15 researches that make up 143 out of 155 test results. The table also shows the summary for 126 test results, excluding results by Bizindavyi and Neale (1999) and Chajes et al. (1996), which showed unexpected higher test results. The overall test results using Equation (8-9) showed improvement over that by Equation (8-7) for the 126 test results.

In order to assess the performance of the proposed equation, a comparison with other proposed equations in the literature was performed. The models chosen for comparison are those from Chen and Teng (2001) and Maeda et al. (1997).

The ultimate bond capacity model proposed by Chen and Teng (2001) was based on existing fracture mechanics analysis and experimental observations, which took the form:

$$P_u = 0.427 \times 10^{-3} k_p k_L \sqrt{f'_c} w L_e \quad (\text{kN}) \quad (8-10a)$$

$$k_L = \begin{cases} 1 & \text{if } L \geq L_e \\ \sin \frac{\pi L}{2L_e} & \text{if } L < L_e \end{cases} \quad (8-10b)$$

$$k_p = \sqrt{\frac{2 - w/w_c}{1 + w/w_c}} \quad (8-10c)$$

in which, w is the FRP sheet bond width in mm, L_e is the effective bond length in mm calculated by (8-4), f'_c and w_c are the concrete width in mm and compressive strength in MPa, respectively, and k and k_p are the length factor and width ratio factor, respectively.

The proposed model by Maeda et al. (1997) is an empirical model based on the experimental results obtained from pull-apart test specimens using CFRP sheets.

$$P_u = 110.2 \times 10^{-9} E_p t_p L_e w \quad (\text{kN}) \quad (8-11)$$

in which, t_p , L_e , w and E_p are the FRP sheet thickness in mm, effective bond length in mm, bond width in mm, and modulus of elasticity in MPa, respectively.

Figure 8-15 and Figure 8-16 show the bond capacity test values plotted against the predicted values using Equation (8-10) and (8-11), respectively. Comparing the figures together with Figure 8-14 shows that Equations (8-9) and (8-10) are more accurate than (8-11), where the data points in Figure 8-16 are more scattered.

Table 8-4 contains the summary of the ratio of the ultimate load predicted by equations (8-9), (8-10), and (8-11) to that from the test results. The table includes the mean, COV, and the minimum and maximum values for each individual research and also for all the tests combined. Equation (8-11) showed improved prediction over Equation (8-9) and (8-10) in 3 researches and gives equivalent results in 2 others. Due to the limited prediction accuracy by Equation (8-11), the comparison will be between Equation (8-9) and (8-10).

Equation (8-10) gives better predictions than (8-9) in the current study modified push-apart tests, Ueda et al. (1999) pull-apart tests, Kamiharako et al. (1999), Ueda et al. (1999), and Taljsten (1997), which amount to 24 out of 155 test results. Equation (8-9) gives better predictions than (8-10) in the seven research series by Ueda et al. (1999) pull-apart tests, Adhikary and Mutsuyoshi (2001), Brosens and VanGermert (1997), Maeda et al. (1997), Drimoussis and Cheng (1994), Bizindavyi and Neale (1999), and Chajes et al. (1996), which amount to 96 out of 155 test results. The two equations have no significant difference in prediction accuracy and reliability in the remaining three research series, which amount to 35 out of 155 test results. Table 8-4 also shows that the model proposed in this study, Equation (8-9), gives an overall better match with the test data and has more reliable results than Equations (8-10) and (8-11) proposed by Chen and Teng (2001) and Maeda et al. (1997), respectively. Excluding the results of Bizindavyi and Neale (1999) and Chajes et al. (1996), shown in brackets in Table 8-4, also shows that Equation (8-9) gives more accurate predictions and is more reliable than Equations (8-10) and (8-11).

In summary, the proposed equations predicting the effective bond length and ultimate bond capacity developed in the current study give more accurate predictions and are more reliable than the proposed equations in the literature. This is clear from the mean value that is closer to unity, the COV values closer to zero, and with smaller range between the minimum and maximum values. For practical applications, the proposed equations must be modified to include knockdown factors to account for long-term loading and cyclic loading as well as durability issues such as freeze and thaw.

Table 8-1 Effective bond length comparison details

w mm	f _c MPa	E _t GPa,mm	L _e (Test) mm	Current Study		Maeda et al., 1997		Chen and Teng, 2001	
				Test/Pred	Test/Pred	Test/Pred	Test/Pred	Test/Pred	Test/Pred
25.4	42.5	29.2	75.0	1.12	1.15	1.12	1.15	1.12	1.12
25.4	42.5	58.4	100.0	1.05	2.29	1.05	2.29	1.06	1.06
25.4	42.5	25.0	55.0	0.88	0.77	0.88	0.77	0.89	0.89
25.4	42.5	50.0	70.0	0.80	1.47	0.80	1.47	0.80	0.80
50	57.6	87.19	133.5	1.05	3.86	1.05	3.86	1.25	1.25
50	57.6	70.14	120.3	1.05	3.07	1.05	3.07	1.25	1.25
50	57.6	43.6	95.7	1.06	1.85	1.06	1.85	1.26	1.26
50	57.6	21.8	63.5	0.99	0.82	0.99	0.82	1.18	1.18
120	47.9	38.4	96.9	1.01	1.74	1.01	1.74	1.30	1.30
120	47.9	76.8	136.2	1.01	3.66	1.01	3.66	1.29	1.29
120	47.9	115.2	165.9	1.00	5.64	1.00	5.64	1.29	1.29
80	47.9	38.4	96.1	1.06	1.73	1.06	1.73	1.29	1.29
80	47.9	76.8	135.4	1.06	3.64	1.06	3.64	1.28	1.28
80	47.9	115.2	165.2	1.05	5.62	1.05	5.62	1.28	1.28
100	47	25.0	75.0	1.00	1.05	1.00	1.05	1.24	1.24
Current Study				1.01	2.56	1.01	2.56	1.19	1.19
Mean				0.08	0.63	0.08	0.63	0.13	0.13
COV				0.80	0.77	0.80	0.77	0.80	0.80
Min.				1.12	5.64	1.12	5.64	1.30	1.30
Max.									

Table 8-2 Test vs. predicted effective bond length summary

		Current Study	Maeda et al., 1997	Chen and Teng, 2001
Bizindavi and Neale, 1999 (4)	Mean	0.96	1.42	0.97
	COV	0.15	0.46	0.15
	Min.	0.80	0.77	0.80
	Max.	1.12	2.29	1.12
Nakaba et al., 2001 (4)	Mean	1.04	2.40	1.24
	COV	0.03	0.56	0.03
	Min.	0.99	0.82	1.18
	Max.	1.06	3.86	1.26
Brosens and VanGemert, 1997 (6)	Mean	1.03	3.67	1.29
	COV	0.03	0.47	0.01
	Min.	1.00	1.73	1.28
	Max.	1.06	5.64	1.30
Current Study (1)	Mean	1.00	1.05	1.24
All tests	Mean	1.01	2.67	1.18
	COV	0.08	0.61	0.14
	Min.	0.80	0.77	0.80
	Max.	1.12	5.64	1.30

Table 8-3 Evolution of proposed model

	Eq.	8-7	8-9		Eq.	8-7	8-9
Current Study	Mean	1.16	1.19	Alexander and Cheng, 1997	Mean	0.84	0.93
Modified push-apart (5)	COV	0.08	0.11	Push-apart test (10)	COV	0.17	0.17
	Min.	1.02	0.97		Min.	0.67	0.73
	Max.	1.23	1.34		Max.	1.09	1.18
Ueda et al., 1999	Mean	0.88	1.02	Drimoussis and Cheng, 1994	Mean	0.88	0.96
Pull-apart test (11)	COV	0.23	0.18	Push-apart test (3)	COV	0.13	0.13
	Min.	0.52	0.67		Min.	0.76	0.82
	Max.	1.18	1.28		Max.	0.98	1.06
Adhikary and Mutsuyoshi, 2001	Mean	1.14	1.11	Udea et al., 1999	Mean	1.21	1.23
Pull-apart test (7)	COV	0.13	0.09	Push-apart tests (2)	COV	0.04	0.13
	Min.	0.96	1.01		Min.	1.18	1.12
	Max.	1.38	1.31		Max.	1.25	1.35
Brosens and VanGemert, 1997	Mean	0.88	0.84	Bizindavyi and Neale, 1999	Mean	1.26	1.67
Pull-apart test (28)	COV	0.12	0.10	Direct pull tests (24)	COV	0.34	0.23
	Min.	0.61	0.70		Min.	0.68	1.03
	Max.	1.11	1.05		Max.	2.05	2.39
Kamiharako et al., 1999	Mean	0.65	0.85	Chajes et al., 1996	Mean	1.16	1.76
Pull-apart test (10)	COV	0.35	0.23	Direct pull tests (5)	COV	0.15	0.13
	Min.	0.35	0.57		Min.	0.87	1.37
	Max.	1.02	1.15		Max.	1.33	2.01
Maeda, et al., 1997	Mean	0.92	0.97	Taljsten, 1997	Mean	1.42	1.07
Pull-apart test (18)	COV	0.25	0.18	Direct pull tests (4)	COV	0.16	0.16
	Min.	0.49	0.62		Min.	1.24	0.92
	Max.	1.31	1.28		Max.	1.74	1.32
Nakaba et al., 2001	Mean	1.29	1.36	Udea et al., 1999	Mean	1.38	1.29
Pull-apart test (12)	COV	0.20	0.11	Direct pull tests (3)	COV	0.13	0.05
	Min.	0.99	1.04		Min.	1.19	1.22
	Max.	1.72	1.57		Max.	1.55	1.36
Current Study	Mean	0.73	0.82	Summary of all tests 155 Specimens (126 Specimens)	Mean	1.00 (0.95)	1.12 (0.99)
Pull-apart test (13)	COV	0.17	0.12		COV	0.31 (0.28)	0.33 (0.22)
	Min.	0.52	0.69		Min.	0.35 (0.35)	0.57 (0.57)
	Max.	0.97	1.05		Max.	2.05 (1.74)	2.39 (1.57)

Table 8-4 Summary of comparison with all test results

	Eq.	8-9	8-10	8-11		Eq.	8-9	8-10	8-11
Current Study	Mean	1.19	1.14	0.92	Alexander and Cheng, 1997	Mean	0.93	0.93	0.77
Modified push-apart (5)	COV	0.11	0.07	0.15	Push-apart test (10)	COV	0.17	0.17	0.18
	Min.	0.97	1.04	0.70		Min.	0.73	0.74	0.59
	Max.	1.34	1.23	1.09		Max.	1.18	1.21	0.96
Ueda et al., 1999	Mean	1.02	1.28	1.11	Drimoussis and Cheng, 1994	Mean	0.96	1.08	0.78
Pull-apart test (11)	COV	0.18	0.20	0.26	Push-apart test (3)	COV	0.13	0.13	0.13
	Min.	0.67	0.73	0.64		Min.	0.82	0.92	0.67
	Max.	1.28	1.53	1.51		Max.	1.06	1.19	0.86
Adhikary and Mutsuyoshi, 2001	Mean	1.11	1.22	0.90	Udea et al., 1999	Mean	1.23	1.18	0.99
Pull-apart test (7)	COV	0.09	0.08	0.09	Push-apart tests (2)	COV	0.13	0.01	0.16
	Min.	1.01	1.12	0.82		Min.	1.12	1.18	0.87
	Max.	1.31	1.37	1.07		Max.	1.35	1.19	1.10
Brosens and VanGemert, 1997	Mean	0.84	0.83	0.73	Bizindavyi and Neale, 1999	Mean	1.67	1.92	2.17
Pull-apart test (28)	COV	0.10	0.12	0.11	Direct pull tests (24)	COV	0.23	0.23	0.25
	Min.	0.70	0.65	0.59		Min.	1.03	1.18	1.30
	Max.	1.05	1.10	0.92		Max.	2.39	2.75	3.20
Kamiharako et al., 1999	Mean	0.85	1.16	1.11	Chajes et al., 1996	Mean	1.76	2.08	2.33
Pull-apart test (10)	COV	0.23	0.10	0.18	Direct pull tests (5)	COV	0.13	0.08	0.05
	Min.	0.57	0.99	0.77		Min.	1.37	1.85	2.25
	Max.	1.15	1.33	1.48		Max.	2.01	2.31	2.54
Maeda, et al., 1997	Mean	0.97	1.06	0.94	Taljsten, 1997	Mean	1.07	1.00	1.13
Pull-apart test (18)	COV	0.18	0.18	0.19	Direct pull tests (4)	COV	0.16	0.12	0.27
	Min.	0.62	0.68	0.59		Min.	0.92	0.88	0.73
	Max.	1.28	1.38	1.24		Max.	1.32	1.15	1.48
Nakaba et al., 2001	Mean	1.36	1.36	1.36	Udea et al., 1999	Mean	1.29	0.97	1.12
Pull-apart test (12)	COV	0.11	0.11	0.12	Direct pull tests (3)	COV	0.05	0.06	0.08
	Min.	1.04	1.04	1.07		Min.	1.22	0.91	1.05
	Max.	1.57	1.57	1.64		Max.	1.36	1.01	1.21
Current Study	Mean	0.82	0.84	0.70	Summary of all tests	Mean	1.12	1.21	1.17
Pull-apart test (13)	COV	0.12	0.16	0.18	155 Specimens	(0.99)	(1.02)	(1.04)	
	Min.	0.69	0.70	0.56	(126 Specimens)	COV	0.33	0.370	0.504
	Max.	1.05	1.08	1.01		(0.219)	(0.220)	(0.223)	
						Min.	0.57	0.65	0.56
						(0.57)	(0.67)	(0.65)	
						Max.	2.39	2.75	3.20
						(1.57)	(1.63)	(1.57)	

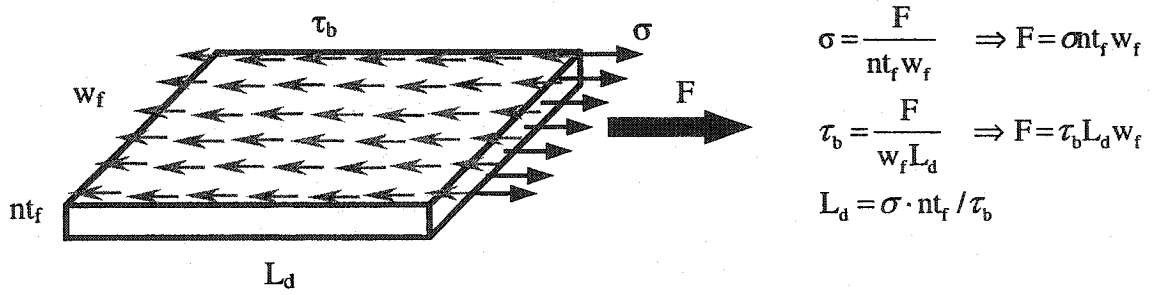


Figure 8-1 Schematic sketch and derivation of development length

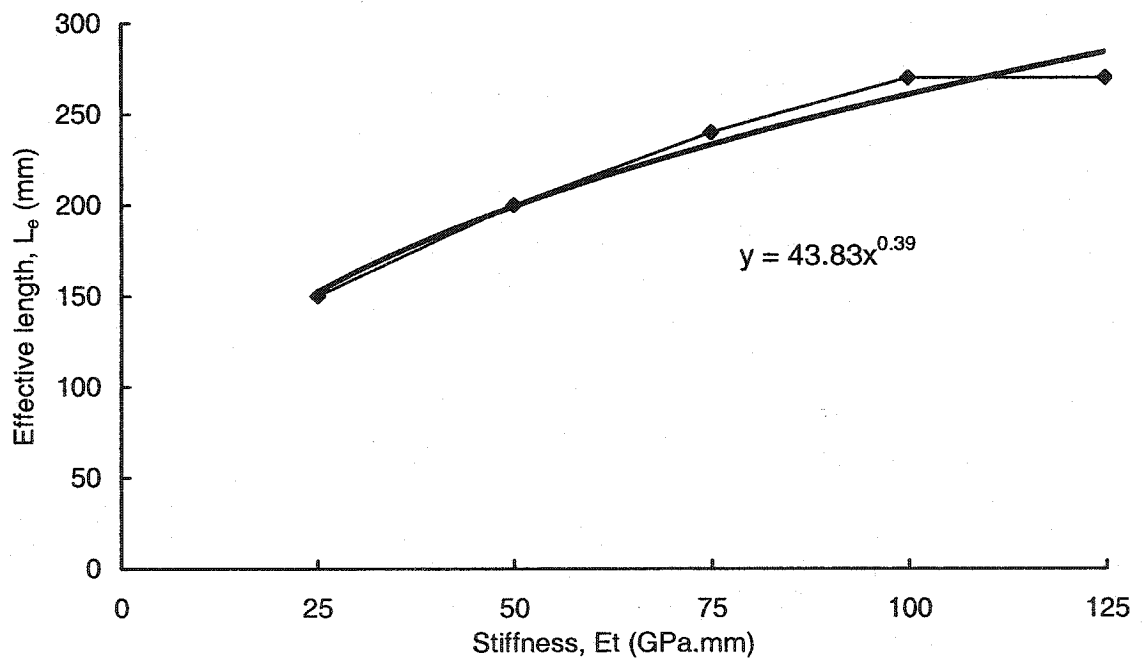


Figure 8-2 Effective length-stiffness for w = 100 mm (Section 6.2)

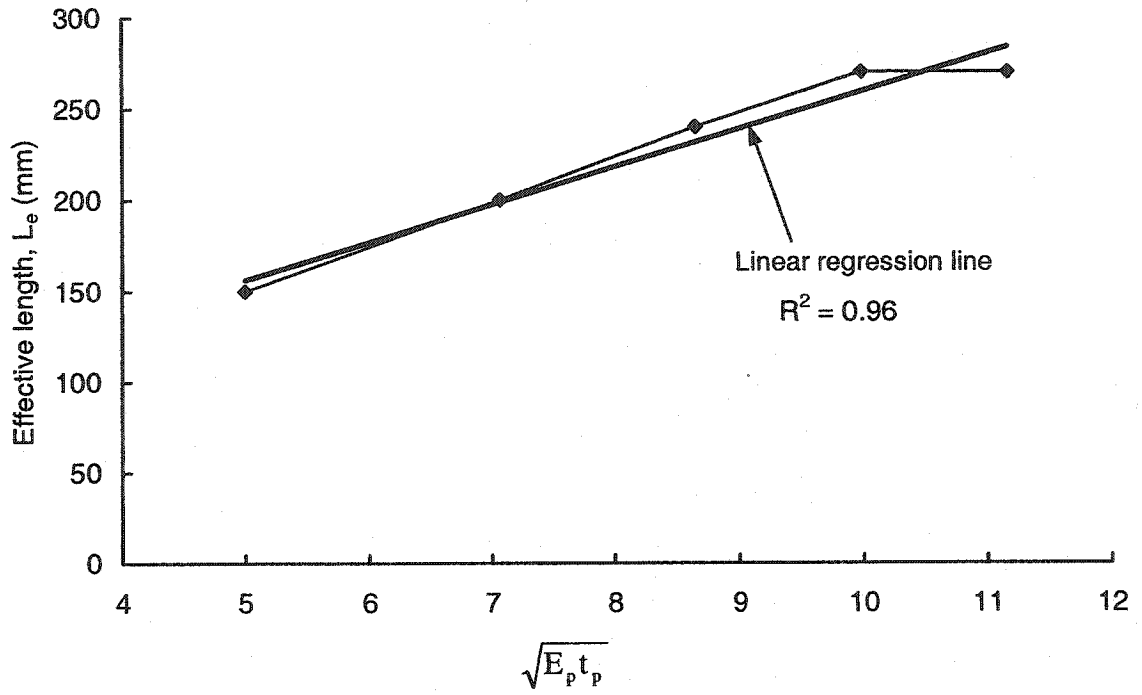


Figure 8-3 Effective length-stiffness for $w = 100$ mm

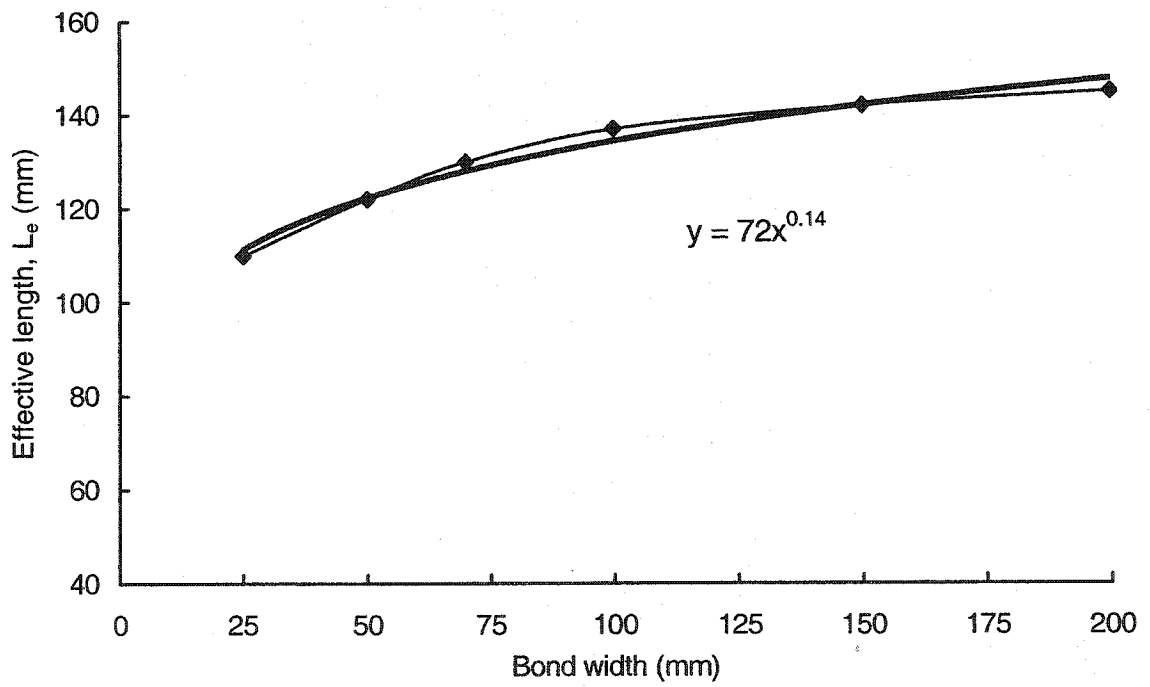


Figure 8-4 Effective length-Bond width relationship (Section 6.2)

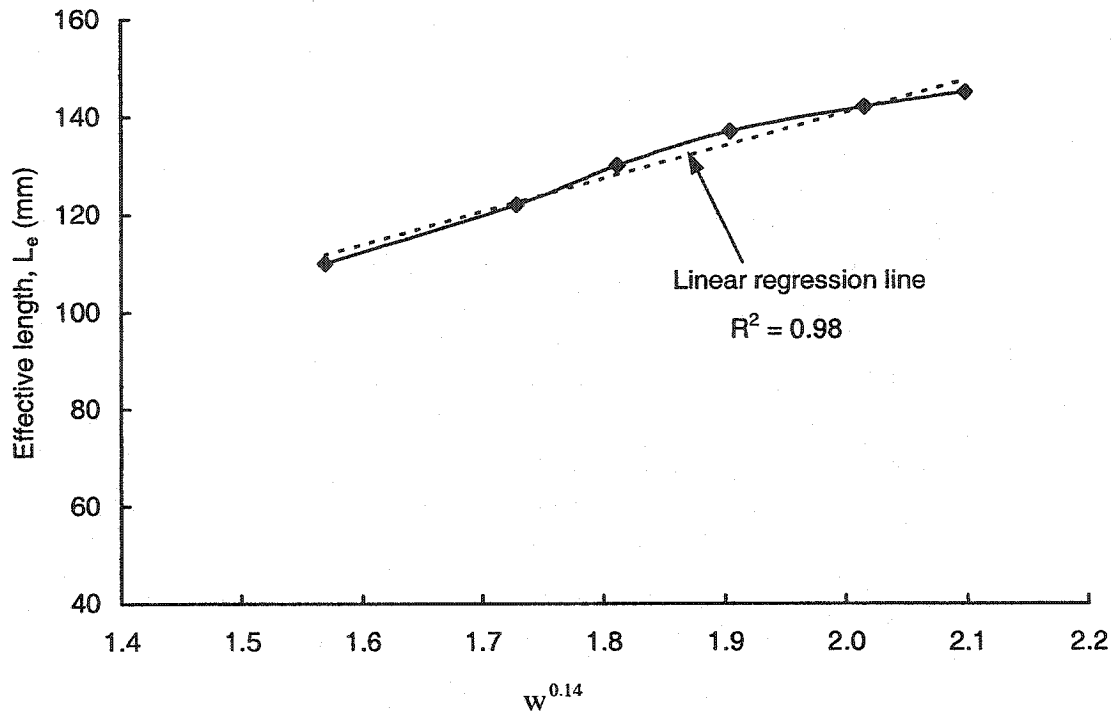


Figure 8-5 Effective length vs. square root of bond width relationship

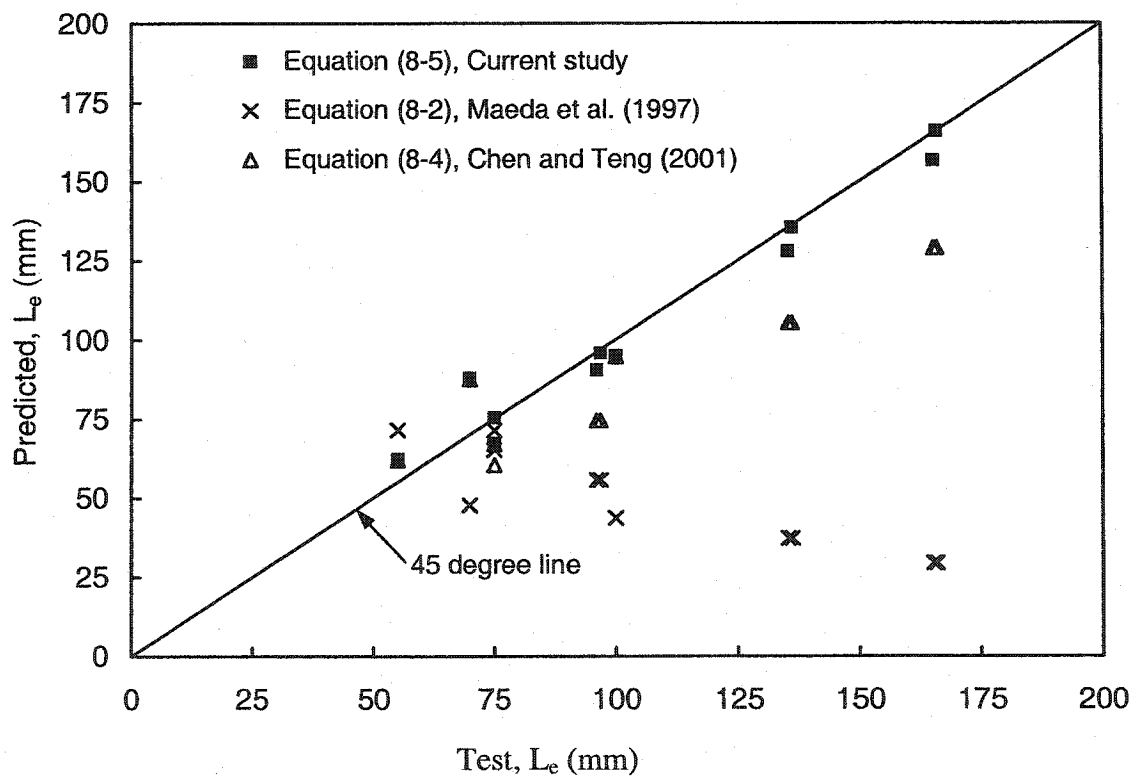


Figure 8-6 Test vs. predicted effective length

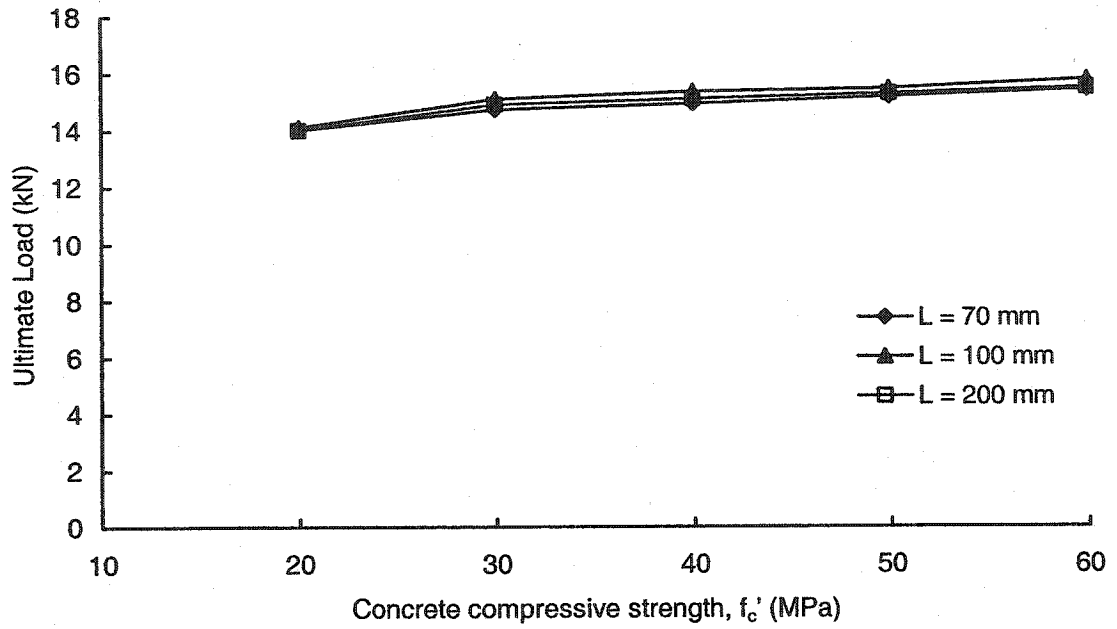


Figure 8-7 Concrete compressive strength vs. ultimate load (Section 6-5)

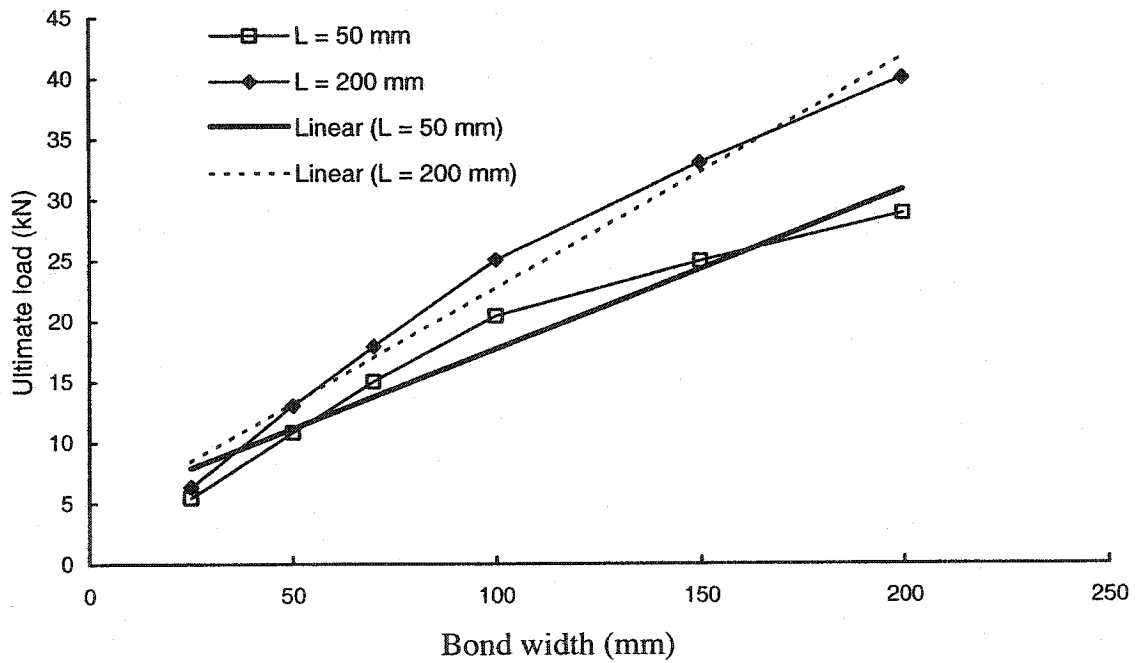


Figure 8-8 Ultimate load vs. FRP sheet bond width (Section 6.3.1)

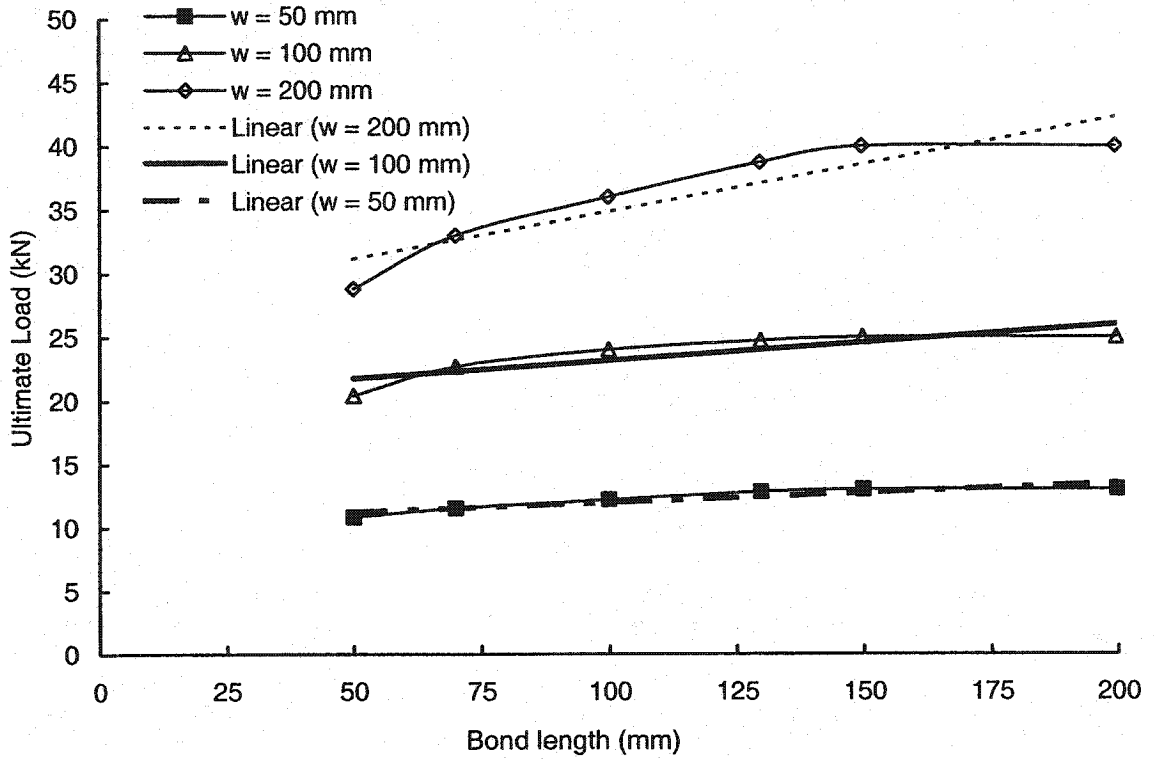


Figure 8-9 Ultimate load vs. Bond length (Section 6.2)

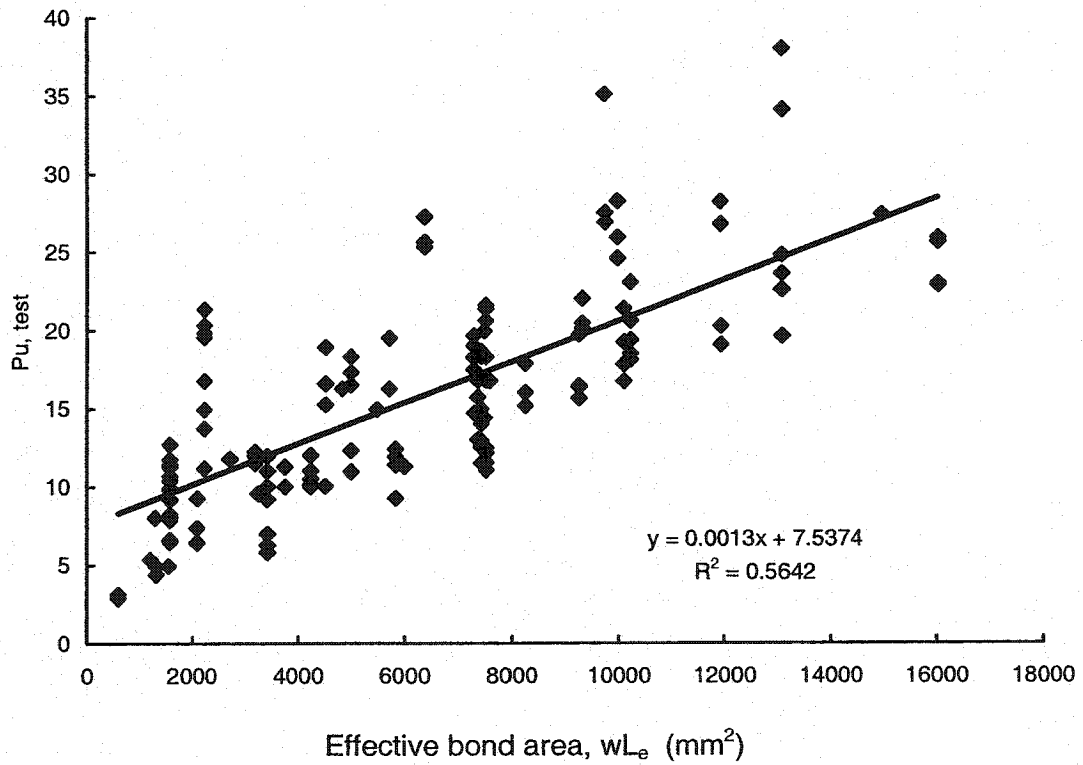


Figure 8-10 Ultimate load vs. bond area

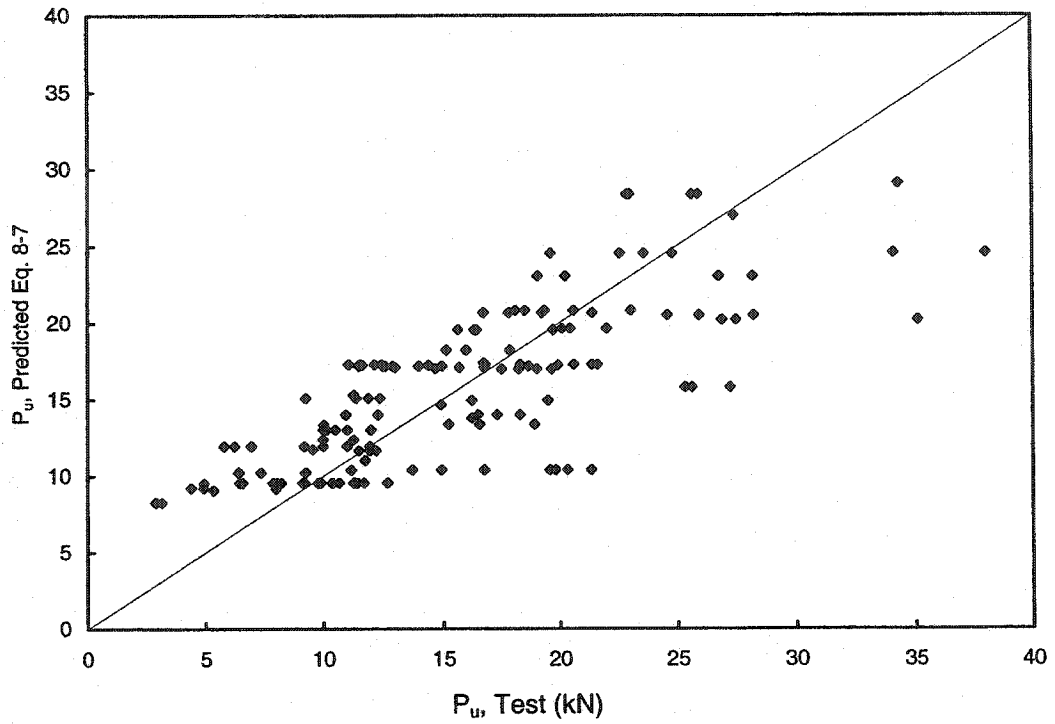


Figure 8-11 Ultimate load test to predicted values, Equation 8-7

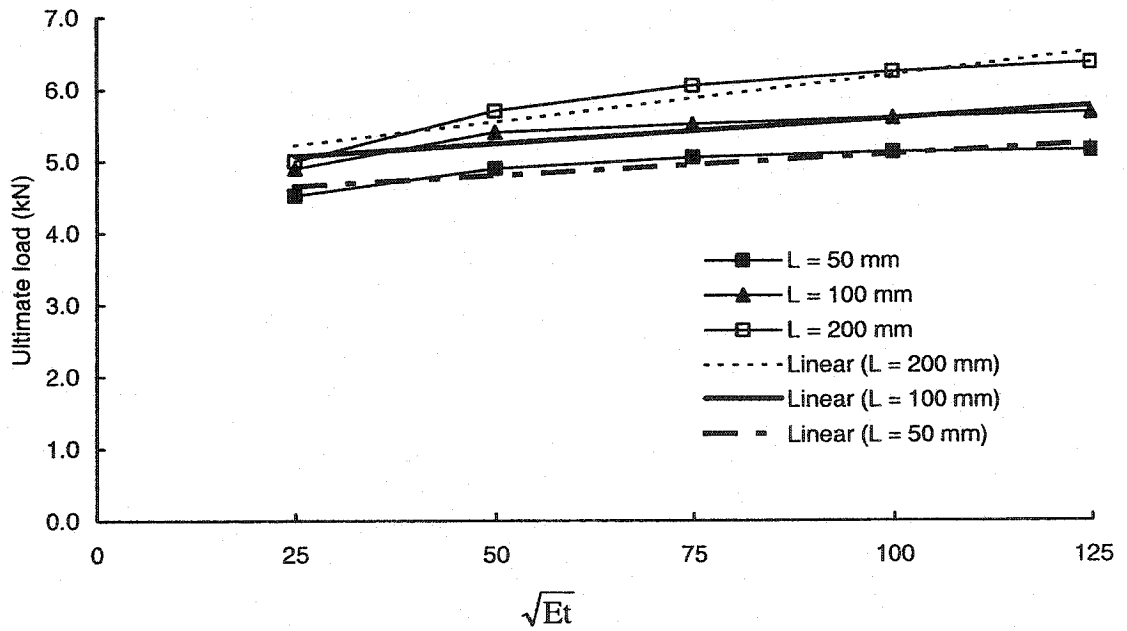


Figure 8-12 Ultimate load vs. square root of stiffness (Section 6-4)

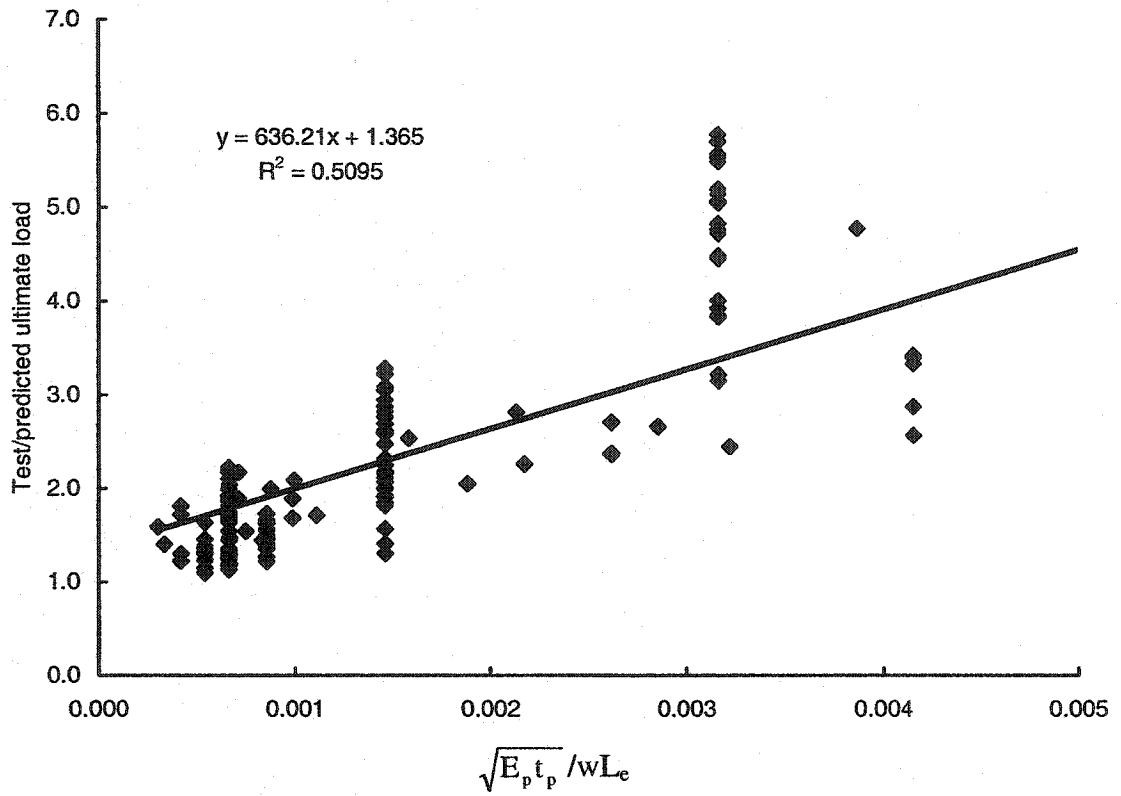


Figure 8-13 Ultimate load test to predicted ratio vs $\sqrt{E_p t_p} / wL_e$, all tests

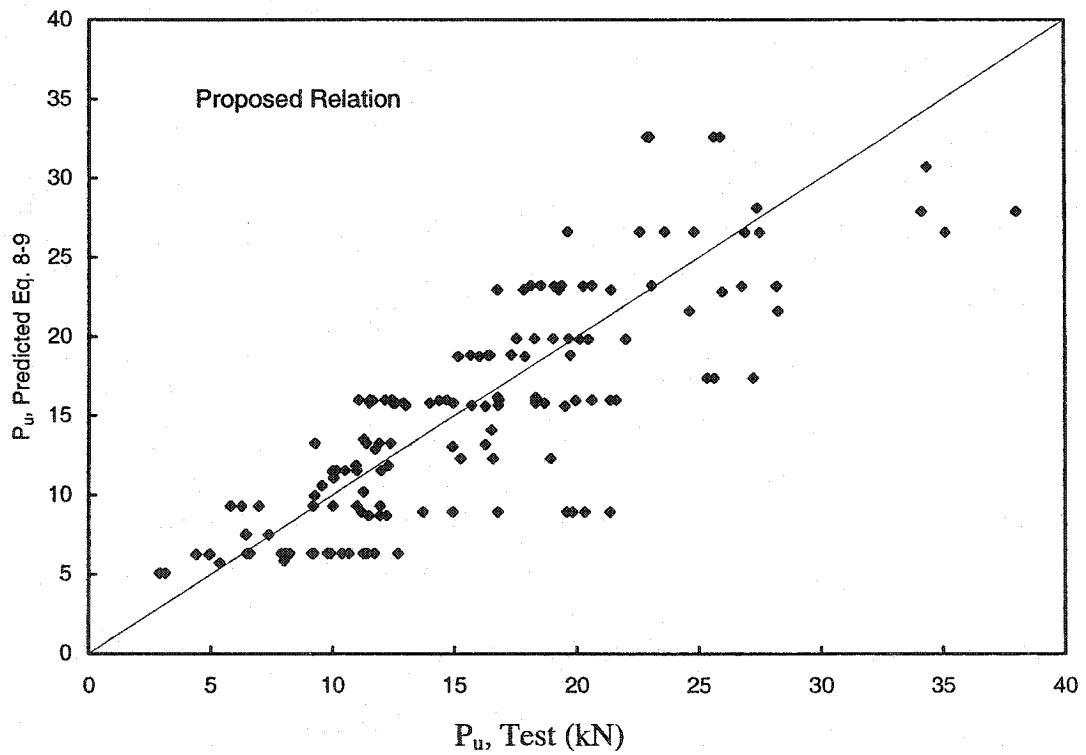


Figure 8-14 Ultimate load test to predicted values, Equation 8-9

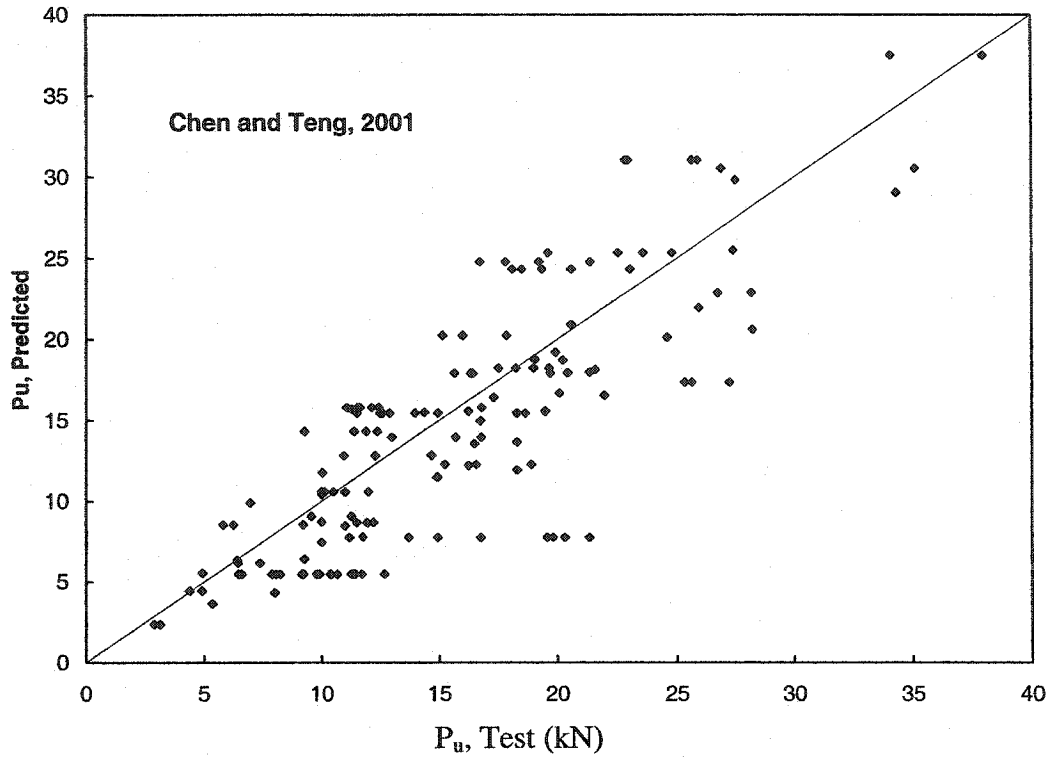


Figure 8-15 Ultimate load test to predicted values, Equation 8-10

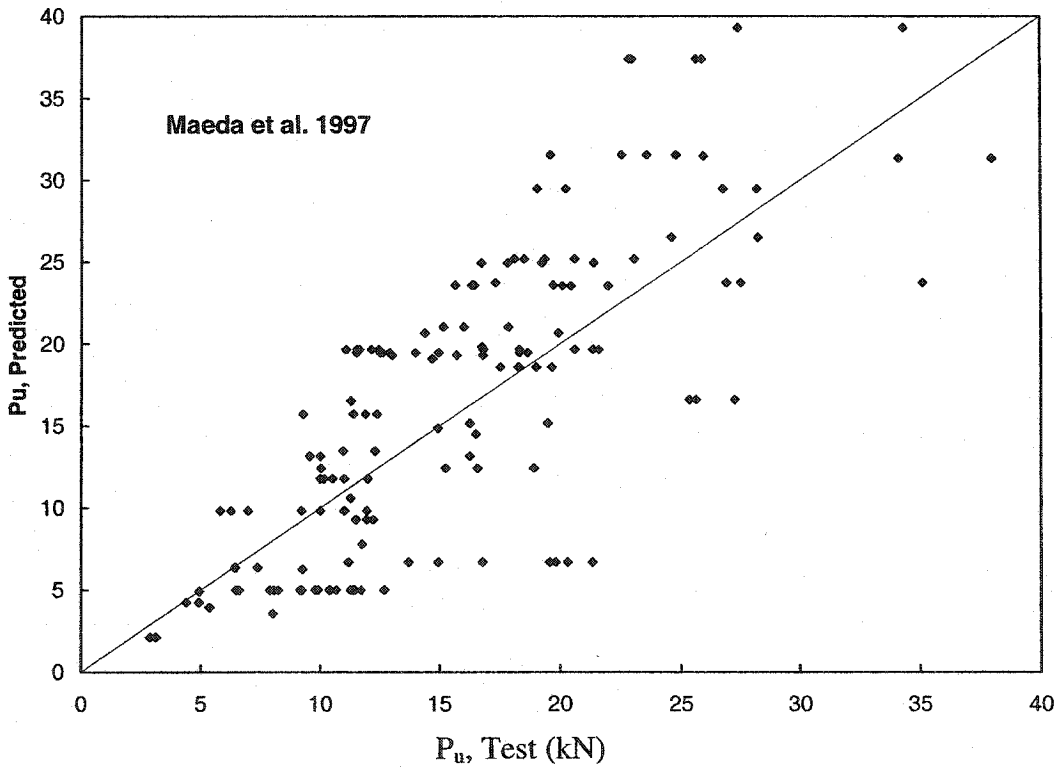


Figure 8-16 Ultimate load test to predicted values, Equation 8-11

9 SUMMARY, CONCLUSIONS, AND RECOMMENDATIONS

9.1 Summary

The FRP strengthening schemes for flexure and shear and the possible failure mechanisms show the existence of a premature type failure caused by debonding of the FRP sheets. Incomplete understanding of the parameters affecting the bond behaviour was seen from the literature review. The literature review also showed the need for reliable experimental test results to investigate the effect of the different parameters on the bond behaviour. In an attempt to provide insight into the behaviour of the FRP to concrete bond, an experimental and numerical investigation was undertaken.

Two experimental test series were conducted in this research using two different types of bond test methods. The first series used a proposed modified push-apart test and the other used a pull-apart test. The experimental tests were also used to verify a number of numerical models, which were then used to conduct further numerical analysis. A parametric study was conducted using numerical models in order to investigate the effect of the different parameters on the bond behaviour.

Reviewing the different conventional bond test methods used in different bond studies pointed out the need to develop a rational standard test method for FRP sheets bonded to concrete. A numerical investigation was conducted in order to investigate the bond test methods and recommend a method to be used as a standard test method. A conversion standard between the test methods was also proposed.

Several researchers have proposed different models to predict the effective length and the ultimate bond capacity. A model was proposed based on evaluation of the proposed models in the literature, the extensive parametric study mentioned above, and test results from the current study and the literature.

9.2 Conclusions

Observations were recorded and conclusions drawn from the experimental study that were further investigated using numerical analysis. The conclusions for both the experimental and numerical analysis are listed separately for more clarity in the following subsections. These conclusions are of course subject to the scope stated in Section 1.2.

9.2.1 Conclusions from the Experimental Analysis

In all tests conducted debonding propagates from the crack location towards the free end of the CFRP sheet and the resisting bonded area of the sheet increases as the applied load increases. For a constant bond width, bond lengths above 100 mm caused no increase in the ultimate capacity of joints tested in this study. This agrees with previous findings by other researchers of the existence of an effective bond length, above which no contribution to the capacity of the joint will be obtained.

The tests also showed that the strain distribution across the width of the CFRP sheet had different behaviour depending on whether the specimen was precracked or not. In general, however, the strain values at the edge of the CFRP sheet are higher than those in the centre throughout the sheet length. The difference in strain increases as the load increases and as the distance from the crack decreases. At the ultimate load at the crack location, the difference between the strain values at the edge and those at the centre of the sheet was 35% on average. The difference also increases as the sheet width increases. This is likely due to a shear lag effect in the concrete substrate. There was also no significant difference in the strain distributions between the pull-apart test method and the modified push-apart test method at the same load value. But the ultimate loads were different in the two methods, which could be attributed to the different loading arrangements and boundary conditions.

The tests also showed that the width of a perpendicular unidirectional CFRP anchor sheet that is bonded outside the tested sheet is ineffective. It was also observed

that placing the anchor sheet above or below the test sheet makes no difference to the failure mechanism. However, a perpendicular unidirectional CFRP anchor sheet located below the tested CFRP sheet showed better or equivalent overall bond behaviour compared to anchor sheets located above the tested sheet. The anchor distance from the crack did not appear to affect the load capacity or the ductility of the joint, except when the anchor sheet was at the crack face in which case there was an increase in the load capacity and ductility of the joint.

The individual values of the CFRP sheet bond length, L , and bond width, w , are the governing factors in the bond behaviour rather than the L/w ratio. Increasing the bonded width of the FRP sheet decreases the average bond strength and the ductility of the joint. The effective bond length governs the ultimate load while the effective bond width governs the average bond strength.

9.2.2 Conclusions from the Numerical Analysis

A comparison between the output of the numerical models and the experimental results proved that it is possible to predict the load-displacement behaviour, the debonding type failure, and the strain distribution in FRP sheets bonded to concrete members using simple numerical models. This allowed a number of generalized conclusions

The results of the numerical models confirmed the existence of an effective bond length beyond which no increase in the capacity is gained for a wide range of parameters. The FRP sheet effective bond length increased as the bond width increased. Increasing the sheet stiffness also increased the effective bond length up to a certain stiffness value of 100 GPa·mm beyond which no increase in the effective bond length was gained. The concrete strength did not appear to have a significant effect on the effective bond length.

The numerical analysis showed also that the average bond strength decreases as the bond width exceeds 100 mm while no significant change occurs at bond width

values below 100 mm. This explains the contradictory conclusions in the literature regarding the effect of the bond width on the bond behaviour. The same conclusion implies that results from narrow sheets over-estimate the average bond strength.

The strains at the edge of the FRP sheets are higher than those at its centre and the difference increases as the FRP sheet width increases and as the concrete width increases. This indicates that the investigations carried out with strain measurements only at the centre of the FRP sheet underestimate the strain values. The strain values are also shown to increase as the width decreases.

The actual values of the concrete specimen width and FRP sheet width affect the bond behaviour rather than the ratio of the FRP sheet to concrete width. This further indicates that the concrete width effect on the bond behaviour needs to be considered or a unified specific concrete specimen width defined and implemented in the standards.

The average bond strength increases as the FRP sheet stiffness increases but up to a certain limit. This limit is defined as the effective sheet stiffness and marks the point beyond which no increase in the average bond strength is gained. The effective sheet stiffness changed with the bond lengths. This conclusion has a practical implication of an optimum number of FRP sheet plies for every bond length.

The expression used to predict the effective bond length in the CSA S806-02 (2002) was shown to be inaccurate at higher FRP sheet stiffness values. New expressions based on regression are proposed to predict the effective bond length and the ultimate bond capacity of the FRP sheets bonded to concrete:

$$L_e = 0.25w^{0.14} \sqrt{E_p t_p} \quad (\text{mm}) \quad (9-1)$$

$$P_u = 0.0016w L_e + 0.75 \sqrt{E_p t_p} \quad (\text{kN}) \quad (9-2)$$

These expressions are shown to be more accurate and reliable than those proposed in the literature to date.

It is necessary that the debonding effect be introduced in the 3D numerical models to numerically study the anchor sheet effect on the behaviour of FRP sheets bonded to concrete.

9.3 Recommendations for code changes

Based on the experimental, numerical, and regression analysis, some recommendations are proposed. For example, it is necessary to introduce refinements to the procedure in Annex P in CSA S806-02 (2002) for determining the value of the FRP sheet effective bond length. These are explained in detail below

Due to the relatively high variability in bond related test results, taking the average of two tests for each bond length together with the expected trend generated by the data points will safeguard for any inconsistent results. The length factor is proposed to range from 0.6 to 1.6 with increments of 0.2 in order to optimize the number of specimens tested. In this proposed change an overall number of twelve specimens would be tested with two specimens for each variable.

The proposed expression (9-1) that predicts the effective bond length for FRP sheets bonded to concrete developed in this study is recommended to replace the existing expression in the CSA S806-02 (2002) and the ISIS Design Manual (2001), where the expression used in these guides was shown to predict the wrong trend.

Test procedures should employ a constant concrete specimen length rather than changing the specimen length with the change in the FRP sheet length. This is to use a constant mould sizes. The proposed concrete specimen length is 500 mm for up to three plies of FRP sheets, where the effective length increases as the number of plies. The specimen length shall be increased by 100 mm for each extra ply.

9.4 Recommendations for Future Research

Based on the experimental and numerical analysis, some recommendations are proposed for future research. For example, studying different anchorage systems and their effect on the bond behaviour in order to propose a rational standard anchor system is recommended.

Experimental test results used to compare and relate bond test methods are from different research studies, which vary in material properties and test conditions. Investigating the effect of the test method experimentally is therefore recommended. This would help develop a conversion standard for the test methods in order to relate the test results from the different bond tests.

The numerical analysis showed that the actual values of the FRP sheet width and the concrete specimen width affect the bond behaviour rather than the FRP sheet width to the concrete specimen width ratio value. Investigating experimentally the effect of the FRP sheet width relative to the concrete specimen width is recommended. The concrete width is analogous to beam width in beam flexure strengthening or the distance between FRP strips in shear strengthening.

The bond test methods investigated in this study involved applying the load in the direction of the fibre. Studying a different state of stress, where the load is applied at an angle to the FRP sheets or the crack is inclined relative to the applied load and its effect on the bond behaviour is also recommended.

REFERENCES

- ABAQUS Standard (1998), Version 5.8. Habbitt, Karlsson, and Sorenson Inc., Pawtucket, RI.
- Adhikary, B. B. and Mutsuyoshi, H. (2001) "Study on the Bond between Concrete and Externally bonded CFRP Sheet," FRPPCS-5, Thomas Telford, London, 371-378.
- Alexander J. S. and Cheng, J. J. R. (1997) "Shear Rehabilitation of G-Girder Bridges Using CFRP Sheets." Structural Engineering Report No. 218, Department of Civil and Environmental Engineering, University of Alberta, October, 181 p.
- Ali, M, Oehlers, D.J. (1997) "Enhancing the Shear Capacity of Reinforced Concrete Beams by Bonding Steel Plates to their Sides" 15th ACMSM '97, Melbourne.
- Arduini M. and Nanni A. (1997) "Behavior of Pre-cracked RC Beams Strengthened with Carbon FRP Sheets." ASCE, Journal of Composites in Construction, Vol. 1, No. 2, May, pp. 63-70.
- Arduini M. and Nanni A. (1997) "Parametric Study of Beams with Externally Bonded FRP Reinforcement." ACI Structural Journal, 94 (5): 493-501.
- Arduini M., Di Tommaso A., Manforoni O., and Nanni A. (1996) "Failure Mechanisms of Concrete Beams Reinforced with FRP Flexible Sheets." Advanced composite materials in bridges and structures, M. El-Badry, Editor, Canadian Society for Civil Engineering, Montreal, Quebec.
- Arduini, M., Di Tommaso, A., and Manfroni, O. (1995) "Fracture mechanisms of concrete beams bonded with composite plates. Non-metallic (FRP) reinforcement for concrete structures. Edited by L. Taerwe. RILEM, London, U.K., pp. 483-491.
- ASTM D-3039/D 3039M-95a (1995) "Standard Test Method for Tensile Properties of Polymer Matrix Composite Materials." American Society for Testing and Materials, West Conshohocken, Pennsylvania, Vol. 15.03.
- Bathe, K. J. (1996) "Finite Element Procedures" Prentice Hall.
- Bizindavyi, L. and Neale, K. W. (1999) "Transfer Lengths and Bond Strengths for Composites Bonded to Concrete," Journal of Composites for Construction, 153-160.
- Bonacci, J. F. (1996) "Strength, Failure Mode and Deformability of Concrete Beams Strengthened Externally with Advanced Composites." Advanced composite materials in bridges and structures, M. El-Badry, Editor, Canadian Society for Civil Engineering, Montreal, Quebec.

- Brozens, K. and Van Gemert, D. (1997) "Anchoring Stresses Between Concrete and Carbon Fibre Reinforced Laminates," Non-Metallic (FRP) Reinforcement for Concrete Structures, proceedings 3rd International Symposium.
- Chaallal, O., Nollet, M. J., and Perraton, D. (1998) "Strengthening of Reinforced Concrete Beams with Externally Bonded Fiber-Reinforced-Plastic Plates: Design Guidelines for Shear and Flexure." *Canadian Journal of Civil Engineering*, 25, 692-704.
- Chajes M.J., Finch W.W., Januszka T.F., Thomson T.A., and Mertz D.R. (1996) "Bond and Force Transfer of Composite Material Plates Bonded to Concrete." *ACI Structural Journal*, 92, 295-303.
- Chajes M.J., Januszka T.F., Mertz D.R., Thomson T.A. and Finch W.W. (1995) "Shear Strengthening of Reinforced Concrete Beams using Externally Applied Composite Fabrics." *ACI Structural Journal*, 92, 295-303.
- Chen, J. F. and Teng J. G. (2001) "Anchorage Strength Models for FRP and Steel Plates Bonded to Concrete." *Journal of Structural Engineering*, Vol. 127, No. 7, 784-791.
- Chen, W. F. (1982) "Plasticity in Reinforced Concrete" McGraw Hill.
- Cheng R.J.J. (1998) "Strengthening of Concrete Beams with FRP Materials." ISIS Alberta workshop, Edmonton, Alberta.
- Collins, M. P. and Mitchell, D. (1987) "Prestressed Concrete Basics". Canadian Prestressed Concrete Institute, CPCI, 1st edition.
- CSA A23.3-94 (1994) "Design of Concrete Structures." Canadian Standards Association, Rexdale, Ontario.
- CSA S6-88 (1988) "Design of Highway Bridges." Canadian Standards Association, Rexdale, Ontario.
- CSA S806-02 (2002), "Design and Construction of Building Components with FRP." Canadian Standards Association, Rexdale, Ontario.
- Deniaud C. and Cheng J. J. R. (2000) "Behaviour of Reinforced Concrete Beams Strengthened in Shear with FRP Sheets." University of Alberta, Structural Engineering Report No. 234.
- De Lorenzis L., Miller B., and Nanni A. (2000) "Bond of FRP Laminates to Concrete." *ACI Structures Journal*, July.
- Dolan B. E., Hamilton H. R., Dolan C. W. (1998) "Strengthening with Bonded FRP Laminate." *Concrete International*, Vol. 20, No. 6, 51-55.

- Donnet, J-P, and R. C. Bansal, (1990) "Carbon Fibers," Marcel Dekker, Inc., New York.
- Drimoussis E.H. and Cheng J.J.R. (1994) "Shear Strengthening of Concrete Girders using Carbon Fiber Reinforced Plastic Sheets." Structural Engineering Report No 205, University of Alberta, Department of Civil Engineering, Edmonton, Alberta, 177 p.
- Erki, M.A., and Heffernan, P.J. (1995) "Reinforced concrete slabs externally strengthened with fiber-reinforced plastic materials," Non-metallic (FRP) reinforcement for concrete structures. *Edited by L. Taerwe.* RILEM, London, U.K., pp. 509-516.
- Fashole-Luke P. S. (1999) "Strengthening of Reinforced Concrete Structures; using externally-bonded FRP composites in structural and civil engineering" Edited by L. C. Holloway and M. B. Leeming, Woodhead publishing limited, 222-241.
- Hiroyuki, Y., and Wu, Z. (1997). "Analysis of debonding fracture properties of CFS strengthened member subjected to tension." Non-Metallic (FRP) Reinforcement for Concrete Structures, 3rd International Symposium, Vol. 1., 287-294.
- Hollaway, L. C. and Leeming, M. B. (1999) "Strengthening of Reinforced Concrete Structures; using Externally Bonded FRP Composites in Structural Engineering." Woodhead publishing Ltd, Cambridge, England.
- Holzenkämpfer, O. (1994) "Ingenieurmodelle des verbundes geklebter bewehrung für betonbauteile." Dissertation, TU Braunschweig (in German).
- Horiguchi, T. and Saeki, N. (1997) "Effect of Test Methods and Quality of Concrete on Bond Strength of CFRP Sheet," Non-Metallic (FRP) Reinforcement for Concrete Structures, 3rd International Symposium, Vol. 1., 265-270.
- ISIS Canada Design Manual (2001) "strengthening Reinforced Concrete Structures with Externally Bonded Fibre Reinforced Polymers" The Canadian Network of Centres of Excellence on intelligent Sensing for innovative Structures, Part 4.
- Kamiharako, A., Shimomura, T., Maruyama, K., and Nishida, H. (1999) "Analysis of Bond and Debonding Behavior of Continuous Fiber Sheet Bonded on Concrete," Journal of Materials, concrete Structures and pavements, Japan Society of Civil Engineers, V.634, 197-208. (in Japanese)
- Khalifa, W. J. Gold, A. Nanni, and M. I. Abdel Aziz (1998) "Contribution of Externally Bonded FRP to Shear Capacity of RC Flexural Members." Journal of composites in construction, Vol. 2. No 4., 195-202.
- Kobayashi K., Fujii, S. Yabe, Y. Tsukagoshi, H. and Sugiyama, T. (2001) "Advanced wrapping system with CF-anchor – stress transfer mechanism of CF-anchor" FRPRCS-5 Conference Cambridge, 379-388.

- Maeda T., Asano Y., Sato Y., Ueda T., and Kakuta Y. (1997) "A Study on Bond Mechanism of Carbon Fiber Sheet." *Non-Metallic (FRP) Reinforcement for Concrete Structures*, 3rd International Symposium, Vol. 1., 279-286.
- MBrace (1998) "Composite Strengthening System Design Guide." Master Builders Inc.
- Microsoft® Excel 2000 (1999), Microsoft corporation.
- Mitsubishi Chemical (1994), "*REPLARK: Carbon Fiber Prepreg for Retrofitting and Repair Method*," Manufacturer Publication, Tokyo, Japan, 18 pp.
- Nakaba K., Kanakubo T., Furuta T., and Yoshizawa H. (2001) "Bond Behavior Between Fiber-Reinforced Polymer Laminates and Concrete." *American Concrete Institute Structural Journal*, 98, No. 3, 359-367.
- Nanni A. (1997) "CFRP Strengthening." *Concrete International*, Vol. 19, No 6.
- Neubauer, u., and Rostásy, F. S. (1999) "Bond Failure of Concrete Fiber Reinforced Polymer Plates at Inclined Cracks-Experiments and fracture Mechanics Model," 4th International Symposium, FRP Reinforcement for RC structures, Editors: Dolan C.W., Rizkalla S.H., and Nanni A, Baltimore.
- Ritchie P.A., Thomas D.A., Lu L.W. and Connelly G.M. (1991) "External Reinforcement of Concrete Beams using Fiber Reinforced Plastics." *ACI Structural Journal*, 88, 490-500.
- Roberts, T.M. and Haji-Kazemi, H. (1989), "*Theoretical Study of the Behavior of Reinforced Concrete Beams Strengthened by Externally Bonded Steel Plates*," Proc. Inst. Civ. Engrs, Part 2, 39-55.
- Saadatmanesh H., and Ehsani M.R. (1991a) "RC Strengthened with GFRP Plates: I: Experimental Study." *Journal of Structural Engineering Division*, ASCE, 117, 3417--3433.
- Saadatmanesh H., and Ehsani M.R. (1991b) "RC Strengthened with GFRP Plates: II: Analysis and Parametric Study." *Journal of Structural Engineering Division*, ASCE, 117, 3434-3455.
- Sato Y., Kakuta Y., and Ono S. (1997a) "Shear Strengthening of Existing Reinforced Concrete Beams by CFRP Sheets." *Proceedings of the Non-Metallic FRP Reinforcement for Concrete Structures (3rd International Symposium)*, Sapporo, Japan, pp. 507-514.
- Sato Y., Ueda T., Kakuta Y. and Tanaka T. (1996) "Shear Reinforcing Effect of Carbon Fiber Sheet Attached to Side of reinforced Concrete Beams." *2nd International Conference on Advanced Composite Materials in Bridges and Structures*, M. El-Badry, ed., CSCE, Montréal, Québec, 621-628.

- Sharif, A. Al-Sulaimani, G.J., Basunbul, I.A., Baluch, M.H., and Ghaleb, B.N. (1994). "Strengthening of Initially loaded Reinforced Concrete Beams using FRP Plates." *ACI Structural Journal*, V. 91, No. 2, pp. 160-168.
- Spadea G, Bencardino F, and Swamy R. N. (1998) "Structural Behavior of Composite RC Beams with Externally Bonded CFRP." *Journal of Composites in Construction*, ASCE, 132-137.
- Swamy R.N., Jones R. and Charif, A. (1986) "Shear Adhesion Properties of Epoxy Resin Adhesives." *Proceedings of an International Symposium on Adhesion between Polymers and Concrete*, pp. 741-755.
- Tadros G., Abdelrahman A., and Rizkalla S. (1998) "Design of Concrete Members with FRP Materials." *ISIS Alberta workshop*, Edmonton, Alberta.
- Täljsten, B., (1994) "Plate Bonding. Strengthening of existing concrete structures with epoxy bonded plates of steel or fibre reinforced plastics," *Doctoral Thesis*, Lulea university of technology, Sweden.
- Täljsten, B., (1997) "Defining Anchor Lengths of Steel and CFRP Plates Bonded to Concrete," *International Journal of Adhesives*, Vol. 17, No. 4.
- Tanaka, T. (1996) "Shear Resisting Mechanism of Reinforced Concrete Beams with CFS as Shear Reinforcement." *Graduation thesis*, Hokkaido University, Japan (in Japanese).
- Triantafillou, T.C. (1998) "Shear Strengthening of Reinforced Concrete Beams Using Epoxy-Bonded FRP Composites." *ACI Structural Journal*, 95 (2), 107-115.
- Tumialan, G., Serra, P., Nanni, A., and Belarbi, A. (1999) "Concrete Cover Delamination in RC Beams Strengthened with FRP Sheets," *SP-188, ACI Proceedings*, 4th International Symposium on FRP for Reinforcement of Concrete Structures, Editors: Dolan C.W., Rizkalla S.H., and Nanni A, Baltimore, 725-735.
- Ueda T., Sato Y., and Asono Y. (1999) "Experimental Study on Bond Strength of Continuous Carbon Fiber Sheet." 4th International Symposium, FRP Reinforcement for RC Structures. Editors: Dolan C.W., Rizkalla S.H., and Nanni A, Baltimore.
- Van Gemert, D. (1980) "Force Transfer in Epoxy Bonded Steel-Concrete Joints", *International Journal of Adhesion and Adhesive*, 2, pp. 67-72.
- Varastehpour, H., and Hamelin, P. (1996) "Analysis and Study of Failure Mechanism of RC Beams Strengthened with FRP Plate." *2nd International Conference on Advanced Composite Materials in Bridges and Structures*, M. El-Badry ed., CSCE, Montréal, Québec, 527-537.

Yoshizawa H., Myojo T., Okoshi M. Mizukoshi M., and Kliger H.S. (1996) "Effect of Sheet Bonding Condition on Concrete Members Having Externally Bonded Carbon Fiber Sheet." 4th Materials Engineering Conference, ASCE annual convention, Washington D.C.